

JS
MAY 29 1962

UNCLASSIFIED

MASTER

COMPREHENSIVE TECHNICAL REPORT

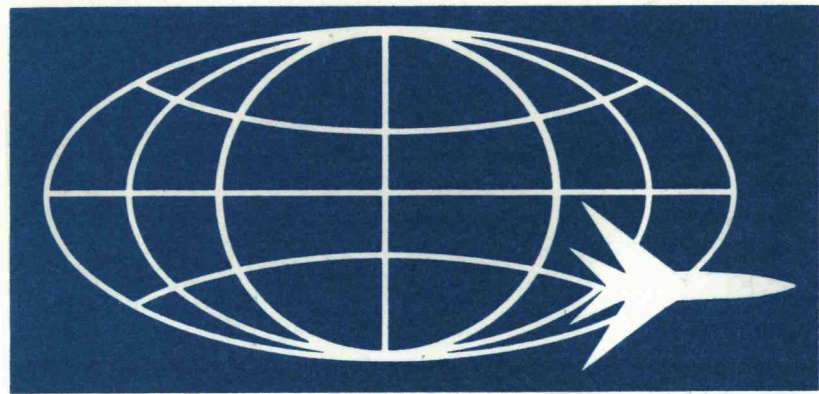
CONFIDENTIAL

**DIRECT
AIR CYCLE**

**AIRCRAFT NUCLEAR
PROPULSION PROGRAM**

APEX 908

PART B



DISTRIBUTION OF THIS DOCUMENT IS UNLIMITED

Classification cancelled (or changed to)
by KA.C. TIC, date SEP 12 1973

Exempt from CCRP Re-review Requirements
(per 7/22/82 Duff/Caudle memorandum)

XNJ 140E NUCLEAR TURBOJET

~~Classification Cancelled~~
~~Or Changed To~~
~~By Authority Of~~ DOC
10/29/71

FLIGHT PROPULSION LABORATORY DEPARTMENT

GENERAL  ELECTRIC

**CONFIDENTIAL
RESTRICTED DATA**

THIS DOCUMENT CONTAINS RESTRICTED DATA AS DEFINED IN THE ATOMIC ENERGY ACT OF 1954. ITS TRANSMITTAL OR THE DISCLOSURE OF ITS CONTENTS IN ANY MANNER TO AN UNAUTHORIZED PERSON IS PROHIBITED.

DISCLAIMER

This report was prepared as an account of work sponsored by an agency of the United States Government. Neither the United States Government nor any agency Thereof, nor any of their employees, makes any warranty, express or implied, or assumes any legal liability or responsibility for the accuracy, completeness, or usefulness of any information, apparatus, product, or process disclosed, or represents that its use would not infringe privately owned rights. Reference herein to any specific commercial product, process, or service by trade name, trademark, manufacturer, or otherwise does not necessarily constitute or imply its endorsement, recommendation, or favoring by the United States Government or any agency thereof. The views and opinions of authors expressed herein do not necessarily state or reflect those of the United States Government or any agency thereof.

DISCLAIMER

Portions of this document may be illegible in electronic image products. Images are produced from the best available original document.

LEGAL NOTICE

This report was prepared as an account of Government sponsored work. Neither the United States, nor the Commission, nor any person acting on behalf of the Commission
A. Makes any warranty or representation, expressed or implied, with respect to the accuracy, completeness, or usefulness of the information contained in this report, or that the use of any information, apparatus, method, or process disclosed in this report may not infringe privately owned rights, or
B. Assumes any liabilities with respect to the use of, or for damages resulting from the use of any information, apparatus, method, or process disclosed in this report.
As used in the above, "person acting on behalf of the Commission" includes any employee or contractor of the Commission, or employee of such contractor, to the extent that such employee or contractor of the Commission, or employee of such contractor prepares, disseminates, or provides access to, any information pursuant to his employment or contract with the Commission, or his employment with such contractor.

~~CONFIDENTIAL~~

~~CONFIDENTIAL~~

APEX - 908
PART B

UNCLASSIFIED

COMPREHENSIVE TECHNICAL REPORT GENERAL ELECTRIC DIRECT-AIR-CYCLE AIRCRAFT NUCLEAR PROPULSION PROGRAM

XNJ 140E NUCLEAR TURBOJET

SECTION 4. REACTOR

~~DATA~~

ected data as
y Act of 1954.
losure of its
unauthorized
ed.

Confidential-Re-
sian applica-
ty.

Author: D. C. LAYMAN
Contributors: D. P. FLITNER
J. G. WOIKE
Editor: D. C. LAYMAN


NOTICE
This report was prepared as an account of work sponsored by the United States Government. Neither the United States nor the United States Energy Research and Development Administration, nor any of their employees, nor any of their contractors, subcontractors, or their employees, makes any warranty, express or implied, or assumes any legal liability or responsibility for the accuracy, completeness or usefulness of any information, apparatus, product or process disclosed, or represents that its use would not infringe privately owned rights.

MAY 15, 1962

~~Guidance (as appropriate)~~

United States Air Force Contract No AF33(600)-38062
United States Atomic Energy Commission Contract No AT(11-1)-171

~~AEC RESEARCH AND DEVELOPMENT REPORT~~

GENERAL  ELECTRIC
NUCLEAR MATERIALS AND PROPULSION OPERATION
(Formerly Aircraft Nuclear Propulsion Department)
FLIGHT PROPULSION LABORATORY DEPARTMENT
Cincinnati 15, Ohio

~~CONFIDENTIAL~~

~~DISTRIBUTION OF THIS DOCUMENT IS UNLIMITED~~

~~CONFIDENTIAL~~

1 826

UNCLASSIFIED

DISTRIBUTION

INTERNAL

C. L. Chase
D. Cochran
E. B. Delson
M. C. Leverett
W. H. Long
H. F. Matthiesen
A. J. Rothstein (6)
D. R. Shoults
G. Thornton
Library (6)

EXTERNAL DISTRIBUTION

Col. Ola P. Thorne
Pentagon, Washington 25, D. C.

Capt. Hendricks
Andrews AFB, Md.

Lt. Col. Stanley Valcik (2)
A. S. D.
Wright-Patterson AFB, Ohio

Dr. Frank Pittman
AEC
Washington 25, D. C.

DTIE (14) plus reproducible master
Oak Ridge, Tennessee

UNCLASSIFIED

~~CONFIDENTIAL~~

ABSTRACT

This volume is one of twenty-one summarizing the Aircraft Nuclear Propulsion Program of the General Electric Company. It is a comprehensive technical report of the design and development activities of the XNJ140E Project. Included are a presentation of the design objectives and requirements, an engineering description of the XNJ140E-1 nuclear turbojet engine, supporting analytical design data and methods of calculation, and a brief review of three design studies preceding, and directly applicable to the XNJ-140E program.

Beginning early in 1960, a major phase of the national effort leading to the achievement of nuclear powered flight was the design and development of the XNJ140E-1 nuclear turbojet engine to be utilized in an Advanced Core Test program. This program was to demonstrate the capabilities of a ceramic reactor coupled with the appropriate associated components of a direct-air-cycle nuclear turbojet engine. Descriptive material contained in this report is based upon the status of the XNJ140E Project at the time of contract termination.

The XNJ140E-1 engine was designed with a reactor of sufficient capability to provide engine performance equivalent to that specified in Department of Defense guidance, which required a speed of Mach 0.8 at an altitude of approximately 35,000 feet in a Convair Model NX 2 aircraft, or equivalent, and an engine life potential of 1000 hours. During this flight condition, the estimated minimum net thrust of the engine was 8120 pounds.

The engine contained a reactor-shield assembly coupled with a single set of X211 turbomachinery and arranged in an integral, in-line configuration. The compressor and turbine were separated, but connected by a long coupling shaft. An annular combustor system, using JP-4 jet fuel, was placed in-line between the reactor rear shield and the turbine inlet, and was arranged concentrically around the coupling shaft.

The reactor-shield assembly was a prototype of comparable components to be used in subsequently planned flight versions of the engine. Turbomachinery components of improved design and an operational afterburner also would have been used.

The reactor fuel elements were made of a beryllium oxide matrix impregnated with enriched uranium dioxide ($\sim 93\%$ U^{235}); the uranium dioxide was stabilized with yttrium oxide to limit the conversion of uranium dioxide to higher states of oxidation. Fuel element surfaces exposed to high velocity

~~CONFIDENTIAL~~

~~CONFIDENTIAL~~

cooling air were coated with zirconium oxide stabilized with yttrium oxide; this coating eliminated water vapor corrosion of the beryllium oxide. The maximum operating temperature was 2530°F.

Beryllium oxide was used in the front, rear, and outer reflectors. Aluminum oxide was used as the inner reflector and served as thermal insulation between the core and the coupling shaft. Beryllium and stainless steel were used as shielding material in the endshields; each material was used both borated and unborated. Lithium hydride, sealed in stainless steel cans, was used as shielding material in the side shield.

This over-all report is divided into four parts. Part A contains section 1., a summary of the report and significant terminology; section 2., precedent studies leading to the selection of the XNJ140E power plant; and section 3., a description of the over-all power plant. Part B contains section 4., a description of the reactor. Part C contains section 5., a description of the shield; section 6., a description of the turbomachinery; and section 7., a description of the control system. Part D contains section 8., a description of test planning, special engineering data instrumentation, and test installations for the Advanced Core Test program; section 9., a discussion of remote handling and maintenance; and section 10., a discussion of on-site and off-site hazards associated with the operation of the engine during the Advanced Core Test program.

ACKNOWLEDGEMENTS

Acknowledgement is made of technical contributions from many members of the Department's engineering staff and of the many reviews and suggestions of J. I. Trussell.

4
~~CONFIDENTIAL~~

CONTENTS

	Page
PART B	
4. Reactor.....	17
4.1 Introduction	17
4.2 Description of Reactor Components	24
4.2.1 Fuel Elements	24
4.2.2 Outer Reflector	24
4.2.3 Inner Reflector.....	26
4.2.4 Transition Pieces	26
4.2.5 Radial Arches.....	26
4.2.6 Core Liner	26
4.2.7 Shaft Tunnel	26
4.2.8 Forward Reflector.....	27
4.2.9 Aft-Retainer Assembly.....	27
4.2.10 Radial-Support-Structure	28
4.2.11 Control Rod Assemblies.....	28
4.3 Performance Requirements	29
4.4 Over-All Reactor Design.....	29
4.4.1 Nuclear Design.....	29
4.4.1.1 Reactivity Requirements.....	29
4.4.1.2 Factors Affecting Reactivity	29
4.4.1.3 Reactivity Effect of Control Rods.....	38
4.4.1.4 Reactor Kinetics.....	38
4.4.2 Secondary Heating.....	38
4.4.2.1 Distribution of Secondary Heating in Reactor Components.....	43
4.4.2.2 Reactor Afterheat.....	43
4.4.2.3 Analytical Methods.....	43
4.4.3 Aerothermal Design	48
4.4.3.1 Distribution of Cooling Air.....	48
4.4.3.2 Influence of Reactor Design Parameters on Engine Thrust and Fuel Element Surface Temperatures.....	52
4.4.3.3 Generalized Equations for Reactor Pressure Ratio and Fuel Element Surface Temperature	66
4.4.3.4 Utilization of X211-E3 Turbomachinery	72
4.4.4 Mechanical Design.....	72
4.4.4.1 Core Definition.....	72
4.4.4.2 High-Temperature Frictional Studies	76
4.5 Fuel Element Component Design Data	77
4.5.1 Nuclear Design	77
4.5.1.1 Reactivity Requirements.....	79

~~CONFIDENTIAL~~

	Page
4.5.1.2 Critical Experiment.....	81
4.5.1.3 Choice of Reflector Control Configuration	85
4.5.2 Aerothermal Design of Fuel Elements	85
4.5.2.1 Fuel Element Sizing.....	87
4.5.2.2 Aerothermal Characteristics of the Active Core.....	91
4.5.2.3 Fuel Element Temperature Deviations	95
4.5.2.4 Aerothermal Characteristics at Off-Design Points...	102
4.5.2.5 Effects of Critical Experiment Data on Radial Temperature Distributions.....	102
4.5.3 Mechanical Design of Fuel Elements.....	109
4.5.3.1 Design Criteria.....	109
4.5.3.2 Mechanical Stresses in Fuel Elements	117
4.5.3.3 Thermal Stress in Fuel Elements.....	123
4.5.3.4 Stress Relaxation and Residual Stresses.....	135
4.6 Outer Reflector Component Design Data	136
4.6.1 Mechanical Design.....	136
4.6.1.1 Mechanical and Thermal Stresses	137
4.6.2 Aerothermal Design	139
4.6.2.1 Design Requirements.....	139
4.6.2.2 Characteristics of System	139
4.6.2.3 Assumptions and Methods of Analysis.....	141
4.7 Inner Reflector Component Design Data	147
4.7.1 Mechanical Design	147
4.7.2 Aerothermal Design	149
4.7.2.1 Design Criteria	149
4.7.2.2 Design Results	151
4.8 Transition Pieces Component Design Data	152
4.8.1 Mechanical Design.....	152
4.8.2 Aerothermal Design	157
4.9 Radial Arches Component Design Data	157
4.9.1 Mechanical Design.....	157
4.9.1.1 Description of Component	157
4.9.1.2 Mechanical and Thermal Stresses	159
4.9.2 Aerothermal Design	161
4.9.2.1 Design Criteria.....	161
4.9.2.2 Design Results	161
4.10 Core Liner and Shaft Tunnel Component Design Data.....	166
4.10.1 Mechanical Design.....	166
4.10.1.1 Core Liner.....	166
4.10.1.2 Shaft Tunnel.....	168
4.10.2 Aerothermal Design	169
4.11 Forward Reflector Component Design Data	170
4.11.1 Mechanical Design.....	170
4.11.1.1 Mechanical Stresses	172
4.11.1.2 Thermal Stresses	172
4.12 Aft-Retainer Assembly Component Design Data.....	173
4.12.1 Mechanical Design.....	173
4.12.1.1 Loading Criteria	177
4.12.1.2 "Worst Case" Design Condition	178
4.12.1.3 Design Results	179

6
~~CONFIDENTIAL~~

	Page
4. 12. 2 Aerothermal Design	182
4. 12. 2. 1 Methods of Analysis.....	182
4. 12. 2. 2 Design Results	185
4. 13 Radial-Support-Structure Component Design Data.....	187
4. 13. 1 Mechanical Design	187
4. 13. 2 Aerothermal Design	197
4. 14 Control Rod Assembly Component Design Data	198
4. 14. 1 Mechanical Design.....	198
4. 14. 1. 1 Design Results	200
4. 14. 2 Aerothermal Design	205
4. 14. 2. 1 Design Results	205
4. 14. 2. 2 Pressure Loss Calculations	212
4. 14. 2. 3 Computer Programs	214
4. 15 Reactor Aftercooling Studies	214
4. 15. 1 Basis of Studies.....	214
4. 15. 2 Rotor Seizure.....	217
4. 15. 3 Engine Coastdown	223
4. 15. 3. 1 Normal Engine Coastdown	223
4. 15. 3. 2 Engine Coastdown Following Compressor Stall.....	223
4. 15. 4 Reactor Pressure Drop	226
4. 15. 5 Fuel Element Temperature Rise with Low Aftercooling-Air Flow Rates	226
4. 15. 6 Effects of Delay in Engine Scram Time	228
4. 15. 7 Control Rod Aftercooling Considerations.....	228
4. 15. 8 Long Duration Reactor Aftercooling Considerations	228
4. 15. 9 Results of Aftercooling Study	230
4. 16 Product Handbook.....	231
4. 17 References.....	234

~~CONFIDENTIAL~~

An abridged table of contents for other parts of this volume is presented below to establish the relationship of this part to the total volume.

PART A

1. SUMMARY
 - 1.1 INTRODUCTION
 - 1.2 PRECEDENT CERAMIC REACTOR AND ENGINE CONFIGURATION STUDIES
 - 1.3 XNJ140E PROJECT
 - 1.4 TERMINOLOGY
 - 1.5 DESIGN SPECIFICATIONS
 - 1.6 HANDBOOKS
 - 1.7 REFERENCES
2. PRECEDENT DESIGN STUDIES
 - 2.1 INTRODUCTION
 - 2.2 D101E REACTOR DESIGN STUDY
 - 2.3 CERAMIC CORE TEST DESIGN STUDY
 - 2.4 ADVANCED CONFIGURATION STUDY
 - 2.5 REFERENCES
3. OVER-ALL POWER PLANT
 - 3.1 INTRODUCTION
 - 3.2 DESIGN REQUIREMENTS
 - 3.3 DESCRIPTION OF THE XNJ140E-1 ENGINE
 - 3.4 PERFORMANCE DATA
 - 3.5 ENGINE COOLING
 - 3.6 JET WAKE AND NOISE DATA
 - 3.7 EFFECTS OF REMOVING CHEMICAL INTERBURNER SYSTEM
 - 3.8 HANDBOOKS
 - 3.9 REFERENCES

PART C

5. SHIELD
 - 5.1 INTRODUCTION
 - 5.2 OVER-ALL SHIELD
 - 5.3 OVER-ALL DESIGN DATA
 - 5.4 FRONT SHIELD COMPONENT DESIGN DATA
 - 5.5 REAR SHIELD COMPONENT DESIGN DATA
 - 5.6 SIDE SHIELD COMPONENT DESIGN DATA
 - 5.7 MISCELLANEOUS COMPONENT DESIGN DATA
 - 5.8 COMPONENT TESTING
 - 5.9 NUCLEAR ANALYSIS
 - 5.10 PRODUCT HANDBOOK
 - 5.11 REFERENCES
6. TURBOMACHINERY
 - 6.1 INTRODUCTION
 - 6.2 DESIGN REQUIREMENTS
 - 6.3 DESCRIPTION OF COMPONENTS
 - 6.4 MAINTENANCE AND REMOTE HANDLING
 - 6.5 X211-E3 TURBOMACHINERY
 - 6.6 ENGINEERING DRAWING LIST
 - 6.7 PRODUCT HANDBOOK
 - 6.8 REFERENCES
7. CONTROL SYSTEM
 - 7.1 INTRODUCTION
 - 7.2 ENGINE CONTROL SYSTEM
 - 7.3 TURBOMACHINERY CONTROL SYSTEM
 - 7.4 REACTOR CONTROL SYSTEM
 - 7.5 SAFETY SYSTEM
 - 7.6 OPERATIONAL CHARACTERISTICS

8
~~CONFIDENTIAL~~

~~CONFIDENTIAL~~

- 7.7 *PRODUCT HANDBOOK*
- 7.8 *REFERENCES*

PART D

8. TESTING

- 8.1 *INTRODUCTION*
- 8.2 *REACTOR TEST PROGRAMS*
- 8.3 *SHIELD TEST PROGRAM*
- 8.4 *CONTROL SYSTEM TEST PROGRAM*
- 8.5 *ENGINE TEST PROGRAMS*
- 8.6 *TEST INSTALLATIONS*
- 8.7 *TEST SUPPORT EQUIPMENT*
- 8.8 *AUXILIARY SUPPORT SYSTEMS*
- 8.9 *REACTOR DATA INSTRUMENTATION*
- 8.10 *END SHIELD DATA INSTRUMENTATION*
- 8.11 *SIDE SHIELD*
- 8.12 *NUCLEAR ENVIRONMENTAL DATA INSTRUMENTATION*
- 8.13 *USE OF CONTROL SYSTEM INSTRUMENTATION*
- 8.14 *DETAILS OF SENSOR INSTALLATION AND LEAD ROUTING*
- 8.15 *DATA RECORDING*
- 8.16 *PRODUCT HANDBOOK*
- 8.17 *REFERENCES*

9. MAINTENANCE

- 9.1 *INTRODUCTION*
- 9.2 *ENVIRONMENTAL RADIATION FIELD*
- 9.3 *MAINTENANCE OPERATIONS*
- 9.4 *SEPARATION OF THE ENGINE INTO MAJOR SECTIONS*
- 9.5 *PROCEDURES FOR HANDLING THE COMPRESSOR SECTION*
- 9.6 *PROCEDURES FOR HANDLING THE TURBINE SECTION*
- 9.7 *PROCEDURES FOR HANDLING THE REACTOR SECTION*
- 9.8 *ENGINE ACCESSORY HANDLING IN THE FET*
- 9.9 *DECONTAMINATION PROCEDURES*
- 9.10 *SPECIAL FIXTURES FOR REMOTE HANDLING OPERATIONS*
- 9.11 *PRODUCT HANDBOOK*
- 9.12 *REFERENCES*

10. OPERATIONAL HAZARDS

- 10.1 *INTRODUCTION*
- 10.2 *OPERATING PROCEDURES*
- 10.3 *FAILURE ANALYSIS*
- 10.4 *ANALYSIS OF UNCHECKED REACTOR EXCURSIONS AT STARTUP*
- 10.5 *NUCLEAR EXCURSIONS DURING OPERATION IN THE CONTROL SYSTEM
POWER RANGE*
- 10.6 *SECONDARY SCRAM SYSTEM*
- 10.7 *LOCAL MELTING DURING OPERATION AT HIGH POWER*
- 10.8 *MELTING FOLLOWING ENGINE SHUTDOWN*
- 10.9 *MECHANISMS FOR RELEASE OF FISSION PRODUCTS FROM FUEL ELEMENT
SURFACES*
- 10.10 *RADIOLOGICAL HAZARDS*
- 10.11 *REFERENCES*

~~CONFIDENTIAL~~

~~CONFIDENTIAL~~

FIGURES

	Page
4.1 - Cutaway view of XNJ140E-1 reactor	18
4.2 - Radial cross section of XNJ140E-1 reactor	19
4.3 - Longitudinal cross section of XNJ140E-1 reactor	20
4.4 - Reactor materials and representative design operating temperatures	21
4.5 - Regional composition and geometry of the XNJ140E-1 reactor	23
4.6 - Worth of equilibrium xenon as a function of nuclear power level, XNJ140E-1 reactor	36
4.7 - Calculated steady state temperature effect on reactivity, XNJ140E-1 reactor	37
4.8 - Calculated error in reactivity as a function of reactor period when neglecting photoneutrons	39
4.9 - XNJ140E-1 control rod worth relative to worth at full insertion	39
4.10 - Stable reactor period, XNJ140E-1 reactor	40
4.11 - Gross radial secondary heating distribution, XNJ140E-1 reactor	44
4.12 - Longitudinal secondary heating rate, XNJ140E-1 reactor	45
4.13 - Relative longitudinal secondary heating rate distribution in outer reflector, XNJ140E-1 reactor	46
4.14 - Relative longitudinal secondary heating rate distribution in inner reflector, shaft, core liner, and shaft tunnel	46
4.15 - Airflow distribution in the XNJ140E engine	49
4.16 - Cooling airflow paths and pressure stations, XNJ140E engine	50
4.17 - Airflow distribution in the XNJ140E-1 engine	53
4.18 - Net thrust and surface temperature influence coefficients for varying active core flow ratio	54
4.19 - Net thrust and surface temperature influence coefficients for varying number of fuel tubes	55
4.20 - Net thrust and surface temperature influence coefficients for varying fuel tube hydraulic diameter	56
4.21 - Net thrust and surface temperature influence coefficients for varying active core length	57
4.22 - Net thrust and surface temperature influence coefficients for varying temperature deviation factor	58
4.23 - Net thrust and surface temperature influence coefficients for varying relative reactor power	59
4.24 - Net thrust and surface temperature influence coefficients for varying integrated reactor power	60
4.25 - Net thrust and surface temperature influence coefficients for varying friction factor multiplier	61
4.26 - Net thrust and surface temperature influence coefficients for varying forward duct pressure ratio	62

*Each part of this volume contains its own list of figures.

~~CONFIDENTIAL~~

	Page
4. 27 - Net thrust and surface temperature influence coefficients for varying aft duct pressure ratio	63
4. 28 - Net thrust and surface temperature influence coefficients for varying turbine inlet temperature	64
4. 29 - Net thrust and surface temperature influence coefficients for varying fuel element power	65
4. 30 - Engine thrust as effected by fuel element cooling-air flow ratio	66
4. 31 - Required turbine inlet-air temperature for constant surface temperature.....	67
4. 32 - Optimum thrust with constant surface temperature, XNJ140E reactor ...	68
4. 33 - Required surface temperatures for constant thrust, XNJ140E reactor ...	69
4. 34 - Temperature and flow relationships, XNJ140E-1 reactor.....	70
4. 35 - Temperature and flow relationships, XNJ140E-1 reactor.....	71
4. 36 - Tube measurements for core definition studies	75
4. 37 - Coefficient of static friction of reactor materials in air and 75-psia nominal pressure	78
4. 38 - Layout map - fuel loading of the XNJ140E-1 reactor	80
4. 39 - Gross radial power profile for two control rod insertion lengths	81
4. 40 - Change in gross radial power resulting from fuel depletion and poison buildup after 55,000 megawatt hours operation, XNJ140E-1 reactor	81
4. 41 - XNJ140E-1 critical experiment assembly	82
4. 42 - Ratio of gross radial power in a homogeneous matrix to the power indicated by cell corrections	84
4. 43 - Ratio of steady state fission density at average design operating temperatures to that at room temperature (68°F).....	84
4. 44 - Correction factor curves to adjust the differences in inner and outer reflector compositions between the critical experiment and the design core	85
4. 45 - Airflow friction factors for fuel elements.....	87
4. 46 - XNJ140E-1 reactor thermal sizing study	88
4. 47 - XNJ140E-1 reactor thermal sizing study	88
4. 48 - Longitudinal temperature distribution, average channel	90
4. 49 - Radial temperature distribution at the longitudinal position of maximum temperature, XNJ140E-1 reactor	91
4. 50 - Gross radial power distribution for three rod-insertion depths in the XNJ140E-1 reactor	92
4. 51 - Relative longitudinal power distribution in the XNJ140E-1 reactor at three radial locations with control rods inserted 18 inches	92
4. 52 - Relative longitudinal power distribution in the XNJ140E-1 reactor at three radial locations with control rods inserted 10 inches	93
4. 53 - Relative longitudinal power distribution in the XNJ140E-1 reactor at three radial locations with control rods fully withdrawn	93
4. 54 - Radial variation of longitudinal maximum surface temperature in XNJ140E-1 fuel elements	94
4. 55 - Radial variation of exit air temperature from XNJ140E-1 fuel elements.	96
4. 56 - Temperature distribution of fuel elements in the XNJ140E-1 reactor ..	99
4. 57 - Maximum fuel element exit air temperature corresponding to a maximum surface temperature of 2500°F	102
4. 58 - Longitudinal power distributions at eight positions with control rods inserted to the 12.25 inch position (KEY-CE Data).....	106

	Page
4. 59 - Longitudinal power distributions at nine radial positions with control rods inserted to the 5 inch position	107
4. 60 - Longitudinal power distributions at four radial positions with control rods fully withdrawn (KEY-CE Data)	108
4. 61 - Longitudinal power distributions at five radial positions with control rods inserted to the 15 inch position as extrapolated from measurements made at the 12.25 inch position (KEY-CE Data)	109
4. 62 - Radial variation of longitudinal maximum surface temperature	110
4. 63 - Schematic of radial support system	111
4. 64 - Schematic of longitudinal support system	111
4. 65 - Construction of radial-support-system force diagram	113
4. 66 - Concept of "minimum" radial spring pressure	114
4. 67 - Three-tier mockup with 10 inch cavity after completion of 5 G shock load	115
4. 68 - Evaluation of stress concentration due to undersize elements	116
4. 69 - Force polygons for elements adjacent to undersize tubes	117
4. 70 - Method of calculating the deflection of the fuel element due to a linear gradient across the diameter	118
4. 71 - Camber forced by axial temperature gradient through core	119
4. 72 - Axial stresses in the fuel tubes	121
4. 73 - Maximum axial stress in fuel tubes	121
4. 74 - Maximum axial stress in the fuel tubes	122
4. 75 - Fuel element axial stress in hottest channel	123
4. 76 - Bending load and stress in fuel element	124
4. 77 - Hexagonal ring bending stress two side loading curved beam effect	125
4. 78 - Fuel element tangential stress evaluated at cruise flight condition along the average channel	126
4. 79 - Fuel element tangential stress in hottest channel	126
4. 80 - Fuel element tangential stress in hottest channel	127
4. 81 - Fuel element tangential stress in hottest channel	128
4. 82 - Tangential thermal stress in fuel element	130
4. 83 - Axial thermal stress in fuel element	131
4. 84 - Terminology for temperature distribution in the "equivalent" circular tube	131
4. 85 - Locations for tube thermal stresses, ANP program No. 602	132
4. 86 - Residual stress in the fuel tubes at room temperature	137
4. 87 - Stresses in outer-reflector, inner region tubes evaluated at cruise flight condition	138
4. 88 - Secondary heating rates in the outer-reflector	140
4. 89 - Space integrated secondary power in outer reflector	141
4. 90 - Outer reflector nodes used in FANTAN analysis	142
4. 91 - Reflector air-gap conductance	143
4. 92 - Effective conductivity of outer reflector region	144
4. 93 - Ratio of actual to effective conductivity of outer reflector tubes	145
4. 94 - Effect of contact resistance on conductivity of BeO	145
4. 95 - Radial temperature distribution in outer reflector	146
4. 96 - Effect of 0.001-inch air gap on radial temperature distribution in outer reflector	146
4. 97 - Outer reflector radial temperature distribution following locked rotor scram	147
4. 98 - Outer reflector longitudinal temperature profile following locked rotor scram	148

	Page
4.99 - Stress in inner reflector tubes	150
4.100 - Stress in inner reflector rods	150
4.101 - Inner reflector segment used in FANTAN analysis	151
4.102 - Effect of contact resistance on conductivity of Al ₂ O ₃ inner reflector tubes	152
4.103 - Ratio of actual to effective conductivity for Al ₂ O ₃ inner reflector tubes ..	153
4.104 - Radial temperature distribution in inner reflector	153
4.105 - Fueled zone transition piece	155
4.106 - Typical arrangement of transition pieces	156
4.107 - Transition piece ring loading	156
4.108 - Transition piece shear area	158
4.109 - Radial arch pieces	158
4.110 - Maximum thermal stress in radial arch due to circumferential temperature gradients	160
4.111 - Nodal layout of FANTAN analysis of radial arch region	162
4.112 - Circumferential temperature distribution in radial arch	163
4.113 - Circumferential temperature profile in radial arch	163
4.114 - Longitudinal temperature profile in radial arch	164
4.115 - Longitudinal temperature profile in radial arch	164
4.116 - Circumferential temperature profile in radial arch	165
4.117 - Longitudinal temperature profile in radial arch	165
4.118 - Core liner, XNJ140E-1	167
4.119 - Tangential stresses in core due to core-liner fit and radial-spring loading	168
4.120 - Sectors of forward reflector	171
4.121 - Aft-retainer sector, XNJ140E-1	174
4.122 - Aft-retainer assembly layout	175
4.123 - Aft-retainer assembly sector layout	176
4.124 - Stress magnification factor (theoretical) for maximum stress in a perforated plate	177
4.125 - Aft-retainer-plate loading analysis	178
4.126 - Aft-retainer assembly, center hub	181
4.127 - Insulation, aft face of aft-retainer assembly	183
4.128 - Longitudinal distribution of secondary heat generation in the aft- retainer assembly	186
4.129 - Radial distribution of secondary heat generation in aft-retainer assembly	186
4.130 - Thermal conductivity of Thermoflex insulation	187
4.131 - Radial temperature distribution in components of aft-retainer assembly .	188
4.132 - Temperature distribution surrounding the hottest tube of the aft-retainer assembly	189
4.133 - Parametric study of thermal performance, aft-retainer assembly	190
4.134 - Parametric study of pressure-temperature relationship in aft-retainer assembly	191
4.135 - Integration of radial support system spring rates	193
4.136 - Calculated deflection of core for various conditions of shear ties and radial spring constants	194
4.137 - Leaf spring assembly	195
4.138 - Reactor structural shell	196
4.139 - Spring retractor	198
4.140 - XNJ140E-1 control rod	198

~~CONFIDENTIAL~~

	Page
4.141 - Details of control rod, XNJ140E-1 reactor	199
4.142 - Control rod deflection stackup	201
4.143 - Comparison of operating and allowable stresses in control rod straps ...	204
4.144 - Thermal stresses in segment of control rod for case of no bond between matrix and clad, cruise flight condition	205
4.145 - Thermal stresses in segment of control rod for case of perfect bond between matrix and clad, cruise flight condition	206
4.146 - Control rod segment thermal bowing due to temperature differential between sides	207
4.147 - Results of parametric study of control rods with heating rate and airflow as parameters	207
4.148 - Variation of maximum surface temperature of control rod as rod is inserted	208
4.149 - Effect of rod insertion on maximum surface temperature of control rod..	209
4.150 - Effect of rod insertion on maximum surface temperature of guide tube...	210
4.151 - Effect of rod insertion on cooling-air discharge temperature	210
4.152 - Two extreme cases of eccentricity of a control rod within a guide tube...	211
4.153 - Effect of eccentricity of the control rod within the guide tube on control rod surface temperature	211
4.154 - Relative heat flow from radial arch to guide tube airflow leakage	212
4.155 - Effect of depth of control rod insertion on longitudinal temperature profiles along control rod channels	213
4.156 - Control rod surface and strap temperatures	213
4.157 - Thermal conductivities used in computer program number 330	216
4.158 - Thermal diffusivities used in computer program number 330	217
4.159 - Transient power generation following scram	218
4.160 - Transient power generation following scram	218
4.161 - Transient power generation following scram	219
4.162 - Fuel element average-channel maximum surface temperature following scram caused by rotor seizure	219
4.163 - Fuel element exit-air temperatures following scram caused by rotor seizure	220
4.164 - Fuel element surface temperature along average-channel following scram caused by rotor seizure	221
4.165 - Fuel element average-channel maximum surface temperature following scram caused by rotor seizure	221
4.166 - Fuel element exit-air temperature following scram caused by rotor seizure	222
4.167 - Fuel element average-channel maximum surface temperature following scram caused by rotor seizure (low airflows)	222
4.168 - Comparison of fuel element average-channel maximum surface temperature using laminar and turbulent flow correlations	223
4.169 - Fuel element average-channel maximum surface temperature following scram followed by engine coastdown	224
4.170 - Fuel element discharge air temperature following scram followed by engine coastdown	224
4.171 - Fuel element average-channel maximum surface temperature following scram caused by compressor stall	225
4.172 - Fuel element exit-air temperature following scram caused by compressor stall	225
4.173 - Fuel element average-channel maximum surface temperature following scram with low aftercooling airflow rates	227

~~CONFIDENTIAL~~

	Page
4.174 - Increase in fuel element average-channel maximum surface temperature in absence of aftercooling air	227
4.175 - Power decay curves following reactor scram after 100 hour operation ...	229
4.176 - Control rod transient temperature response for reactor scram without engine coastdown	229
4.177 - Afterheat generation rate as a fraction of operating power level versus time after shutdown for various periods of operating time	230

TABLES

	Page
4.1 - Summary of XNJ140E-1 Reactor Dimensions	25
4.2 - Standard Day Flight Conditions	30
4.3 - Hot Day Flight Conditions	31
4.4 - Cold Day Flight Conditions	32
4.5 - XNJ140E-1 Reactor Performance Parameters at Design Point	33
4.6 - Fuel Concentration and Distribution in the XNJ140E-1 Reactor	33
4.7 - Required Excess Reactivity for the XNJ140E-1 Reactor	34
4.8 - Excess Reactivity and Control Rod Worth in the XNJ140E-1 Reactor	34
4.9 - Temperature Reactivity Effects in the Clean XNJ140E-1 Reactor	37
4.10 - Effective Fraction of Delayed Neutrons in XNJ140E-1 Reactor	41
4.11 - XNJ140E-1 Reactor Energy Per Fission	41
4.12 - Secondary Heating Rates in XNJ140E-1 Reactor	42
4.13 - Fractional Energy Deposition in XNJ140E-1 Reactor	42
4.14 - Capture Gamma-Ray Heating in Control Rod Assembly	47
4.15 - After-Shutdown Power in XNJ140E-1 Reactor	47
4.16 - Static and Total Pressures and Flow Quantities for Cooling Airflow Paths	51
4.17 - Reactor Component Airflow Distribution and Exit-Air Temperatures	52
4.18 - Definition of Variables and Base Values for Unity Influence Coefficient	59
4.19 - Summary of Materials and Weights of XNJ140E-1 Reactor Components	73
4.20 - Coefficient of Friction Tests	76
4.21 - Fuel Element Aerothermal Design Parameters	86
4.22 - Thermal Characteristics of Average Fuel Element Flow Passage	89
4.23 - Final Fuel Element Geometry and Thermal Characteristics	90
4.24 - Contributions to Fuel Element and Exit-Air Temperature Deviations	98
4.25 - Maximum Fuel Element Temperature	99
4.26 - Temperature Deviations for Fabrication Tolerances	100
4.27 - Temperature Deviations for Fabrication Tolerances	101
4.28 - Reactor Aerothermal Characteristics for Standard-Day Flight Conditions, (S-18 Cycle)	103
4.29 - Reactor Aerothermal Characteristics for Hot-Day Flight Conditions, (S-18 Cycle)	104

*Each part of this volume contains its own list of tables.

~~CONFIDENTIAL~~

	Page
4.30 - Reactor Aerothermal Characteristics for Cold-Day Flight Conditions, (S-18 Cycle)	105
4.31 - Fuel Element Combined Operating Stresses and Maximum Combined Stresses at Room Temperature Following Shutdown from Design Point	134
4.32 - Fuel Element Combined Operating Stresses and Maximum Combined Stresses at Room Temperature Following Shutdown from Emergency Power Setting.....	134
4.33 - Fuel Element Combined Operating Stresses and Maximum Combined Stresses at Room Temperature Following Shutdown from Extended Ground Checkout.....	135
4.34 - Summary of Maximum Calculated Stresses for Outer Reflector Rods and Tubes and Allowable Strength at Indicated Temperature.....	139
4.35 - Summary of the Thermal Design Data and Criteria for the Outer Reflector.....	148
4.36 - Inner Reflector Aerothermal Design Criteria and Data	154
4.37 - Combined Stress in Radial Arches During Design Point Operation	161
4.38 - Radial Arch Thermal Design Data and Criteria.....	166
4.39 - Effects of Design Changes, Aft-Retainer Assembly	192
4.40 - Summary of Design Criteria of Radial Support System	194
4.41 - Summary of Mechanical Stresses In The Reactor Structural Shell	197
4.42 - Control Rods Design Data.....	202
4.43 - Structural Design Criteria for the Control Rod and Guide Tube.....	202
4.44 - Control Rod and Guide Tube Mechanical Design Results	203
4.45 - Steady-State Operating Parameters Used For Reactor Aftercooling Studies.....	216
4.46 - Pressure Drop Across Reactor During Aftercooling.....	226
4.47 - Temperature Rise In Reactor Components In Absence of Cooling-Air.....	228
4.48 - Specific Heat of Fuel Element Material.....	231

~~CONFIDENTIAL~~

4. REACTOR

4.1 INTRODUCTION

The XNJ140E-1 reactor consisted of (1) an annular cylindrical bundle of ceramic tubes which formed the active core, the outer reflector, the inner reflector, and the end reflectors, (2) control rods, (3) the longitudinal support structure, (4) the radial support structure, (5) the shaft tunnel, (6) the core liner, and (7) the enclosing structural shell. Figure 4.1 is an isometric cutaway view of the reactor. Figure 4.2 is a radial cross section of the reactor and Figure 4.3 is a longitudinal cross section. Reactor materials and representative calculated operating temperatures are shown in Figure 4.4.

The use of ceramic materials for the tube bundle components was a logical method of providing the desired high temperature capability; however, thermal stress considerations inherent in the use of ceramics necessitated small simple shapes, and a small hexagonal tube was chosen as the basic modular element of these components. The tubes were fitted together to form a bundle that was 62 inches in diameter and 33 inches long. A central void, 13.23 inches in diameter, accommodated the coupling shaft that joined the compressor and turbine.

The active core contained fuel tubes that were made of yttria-stabilized beryllia containing dispersed enriched urania. Each fuel element was a small hexagonal tube 0.249 inch across flats and 4.28 inches long with an inside diameter of 0.167 inch. The inside diameter was clad with a 0.003-inch-thick layer of yttria-stabilized zirconia.

There were approximately 25,000 airflow passages through the reactor and approximately 170,000 separate fuel elements in the active core. During engine test operation simulating the extended cruise-flight condition of the operational engine, the reactor fuel elements operated at a calculated peak temperature of approximately 2530°F.

An annular cylindrical central island located inside the active core was composed of (1) alumina tubes and bars with the same over-all dimensions as the fuel elements, (2) a metallic core liner, and (3) a metallic shaft tunnel. The alumina region served a three-fold function: (1) it acted as an inner reflector, (2) it provided thermal insulation for the metallic components in the central island, and (3) it acted as a gamma shield to reduce the secondary heating rate in the metallic components. The core liner acted as a structural arch permitting the inner reflector tubes to bridge the central void. The shaft tunnel was a structural component of the longitudinal support system and carried part of the longitudinal loads on the reactor from the aft-retainer assembly to the front shield. The shaft tunnel and core liner formed an annular duct that channeled cooling-air from the front shield to the rear shield. The shaft tunnel was supported in a manner that maintained concentricity with the core liner so that cooling-air flowing through the annular passage was not affected by deflections of the reactor under flight loads.

The outer reflector was an 8.5-inch-thick annular region of unfueled beryllium oxide tubes surrounding the active core. Control rods were located at 48 equally spaced places

~~CONFIDENTIAL~~

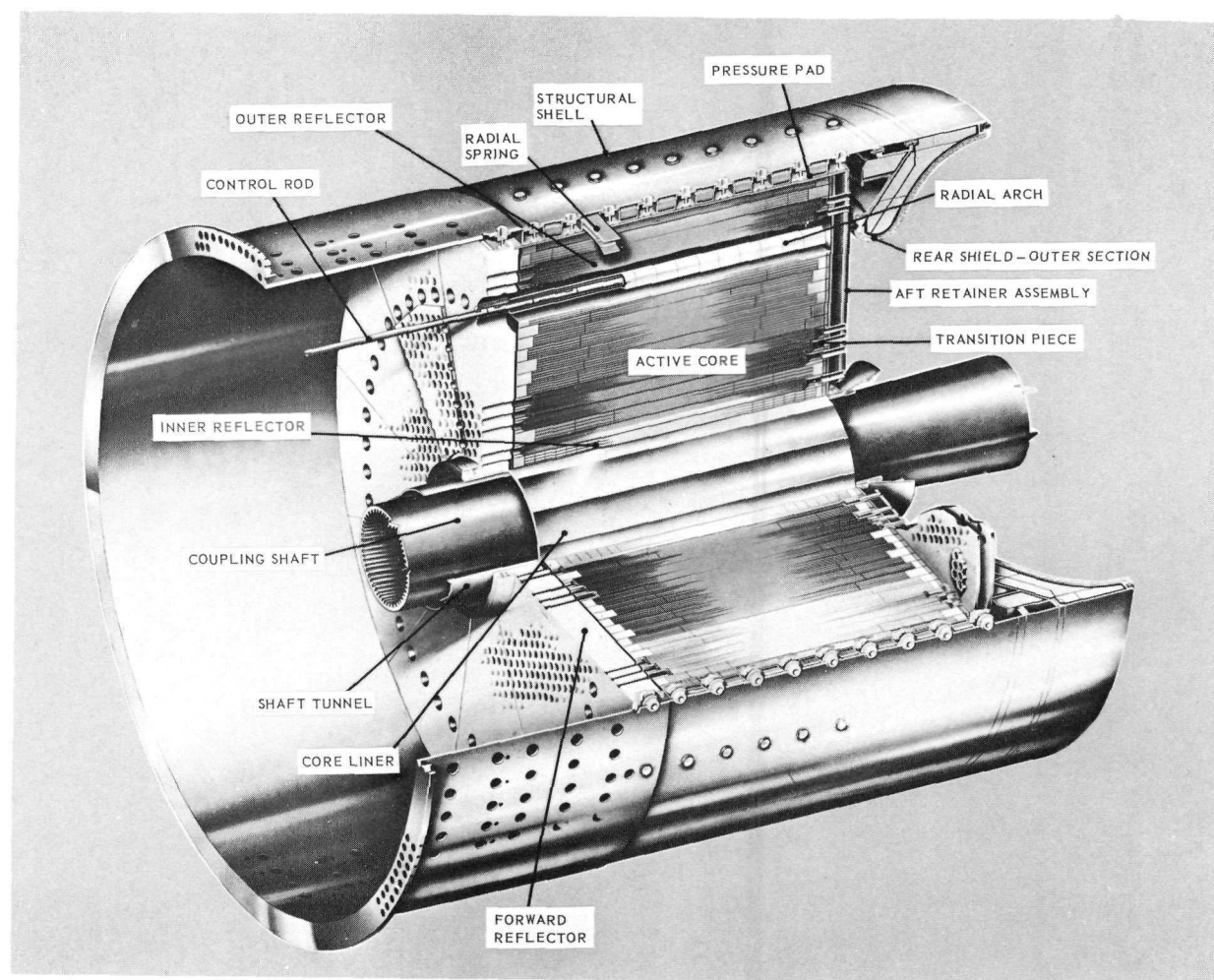
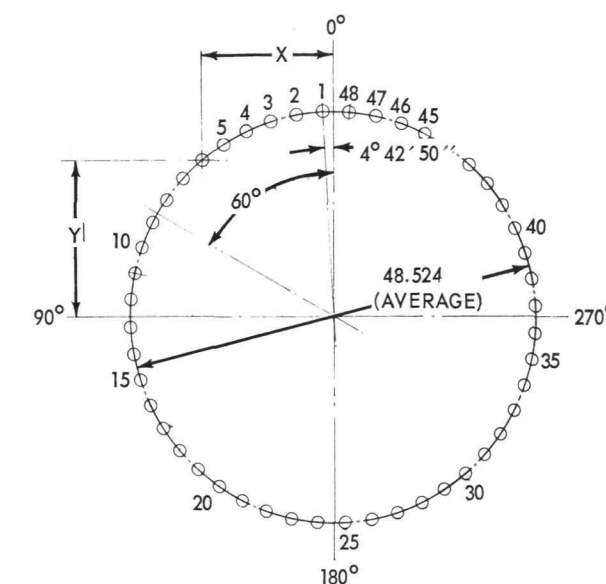
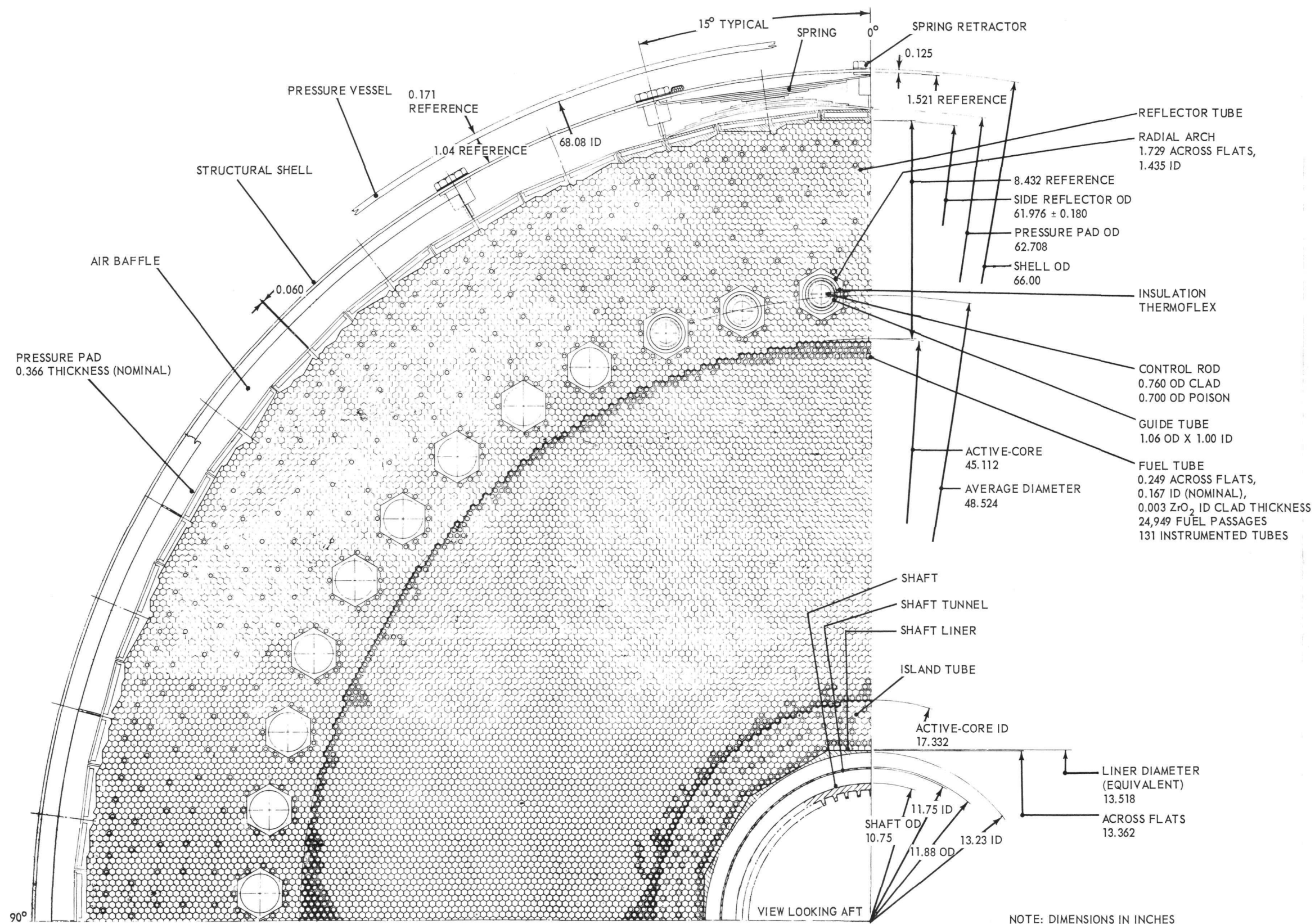


Fig. 4.1—Cutaway view of XNJ140E-1 reactor

CONFIDENTIAL

CONFIDENTIAL



CONTROL ROD LOCATION

C.R.	C.R.	X	Y
1	25	2.003	24.291
2	26	5.134	23.640
3	27	8.139	22.773
4	28	11.144	21.471
5	29	13.774	19.954
6	30	16.403	18.001
7	31	18.532	15.615
8	32	20.410	13.230
9	33	22.038	10.410
10	34	23.040	7.374
11	35	23.791	4.338
12	36	24.167	1.084
13	37	24.167	1.951
14	38	23.791	5.205
15	39	22.789	8.241
16	40	21.662	11.061
17	41	20.035	13.881
18	42	17.906	16.266
19	43	15.652	18.435
20	44	13.023	20.387
21	45	10.393	21.905
22	46	7.388	23.206
23	47	4.257	23.857
24	48	1.252	24.291

NOTE: DIMENSIONS IN INCHES

206R687

Fig. 4.2—Radial cross section of XNJ140E-1 reactor

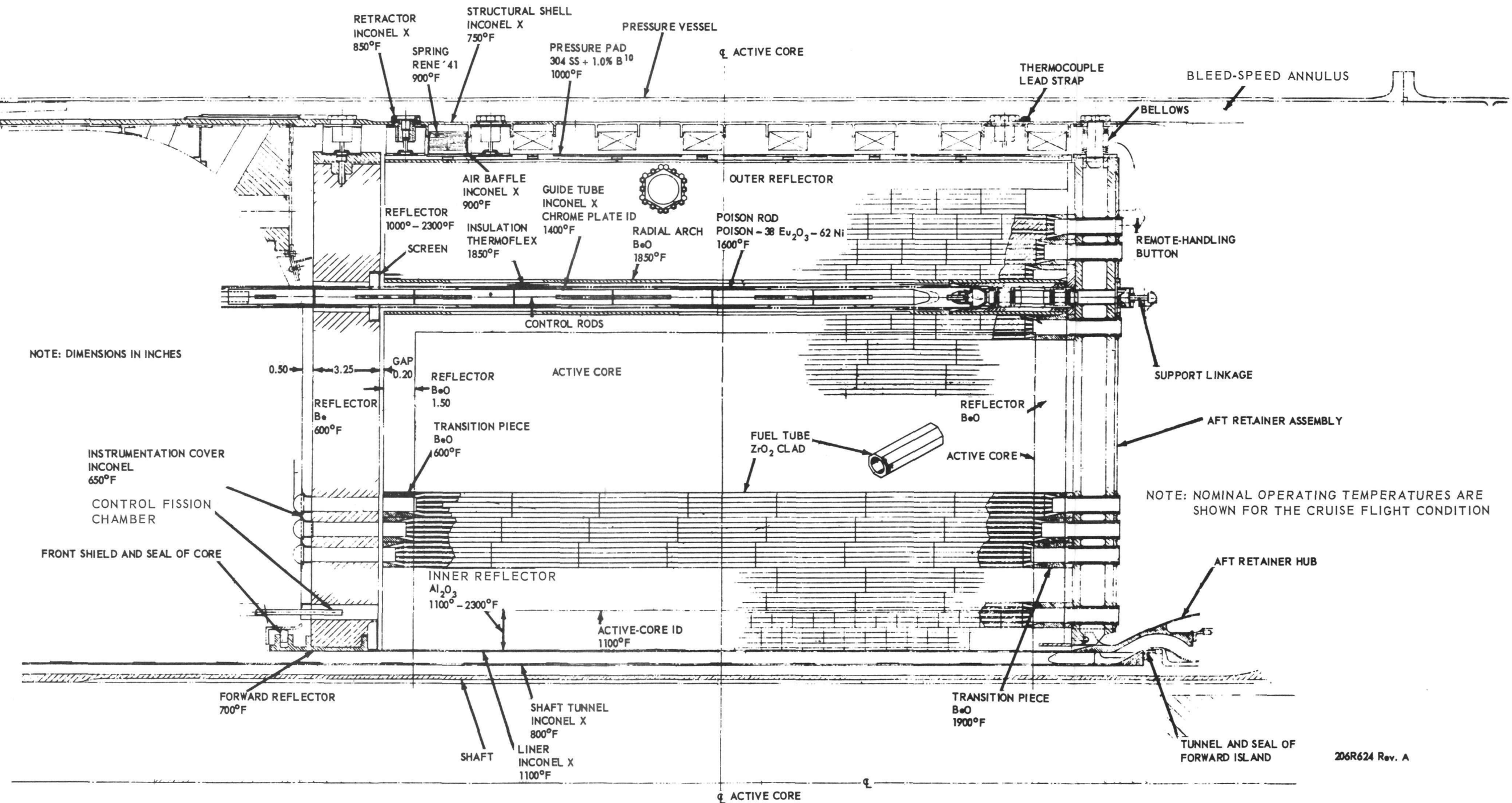


Fig. 4.4—Reactor materials and representative design operating temperatures (Dwg. 206R624 Rev. A)

CONFIDENTIAL

within the outer reflector, 1.75 inches from the boundary of the active core. The control rods contained Eu_2O_3 poisoning in a nickel matrix clad with 80Ni - 20Cr, and were withdrawn or inserted for reactivity control. Radial arches (ceramic hexagonal tubes 1.729 inches across flats, 0.741 inch long, and containing a cylindrical bore 1.435 inches in diameter) provided tunnels through the outer reflector for the control rod guide tubes.

The rear reflector was 1.5 inches thick, and was formed by the multiple beryllia fuel-tube transition pieces. Each transition piece received air from 19 fuel element channels and collected it into a single large-diameter channel. Transition pieces also were used at the forward end of the reactor between the front reflector sectors and the active core. These transition pieces permitted the use of large-diameter channels in the end structural components and facilitated the structural and aerodynamic design.

The front reflector was composed of 12 beryllium sectors 3.25 inches thick. Perforations in the sectors served as passages for the primary airflow. In addition to acting as a neutron reflector, the front reflector also acted as a structural component that restrained the tube bundle against forward motion. The forward beryllia fuel-tube transition pieces also acted as an additional 1.5-inch-thick neutron reflector.

The external structure of the reactor was composed of a radial support system and a longitudinal support system. The radial structure restrained the ceramic tube bundle in a compressed unit assembly and resisted lateral loads. The longitudinal structure resisted aerodynamic drag on the reactor and axial inertial loads.

The radial support structure was composed of the structural shell, leaf springs, and pressure pads. The structural shell surrounded the reactor and was cantilevered at its forward end from the flanged connection to the front shield. The leaf springs were loaded outwardly against the structural shell and inwardly through the pressure pads into the tube bundle. The pressure pads served to distribute each spring load over several outer reflector tubes. Secondary heat due to neutron reactions in the side shield was reduced by neutron absorption in the pressure pads resulting from the addition of 1 weight percent of B^{10} added to the pressure pad material.

The aft-retainer assembly was the main structural element of the longitudinal support system and resisted aft loads on the reactor. It was fabricated from twelve 30-degree sectors supported near the middle by the shaft tunnel, and near the outside by the rear shield outer section. Each sector consisted of parallel end-plates separated by tubes. The tubes acted as shear ties for the plates and also served as passages for primary-air discharged from the fuel elements. The assembly was cooled internally by a portion of the air flowing through the bleed-speed annulus.

The fuel element matrix and inner clad were formed simultaneously by a coextrusion process. After extrusion, the tubes were heated to approximately 1100°F for removal of moisture and organic binder materials, and then were fired at an approximate temperature of 2900°F to achieve final sintering to high density and final dimensions. The coefficients of thermal expansion of the stabilized-zirconia clad and the beryllia-yttria-uranium matrix were essentially the same (differing by less than 1 percent), and differential thermal expansion did not cause the clad to flake from the matrix. Moreover, since the clad and matrix were coextruded, intimate contact between the clad and the matrix also acted to assure a high degree of adherence.

The radial power distribution was flattened by varying the fuel concentration in annular regions of the active core, and resulted in radial power variations not exceeding 6 percent of the average over the core lifetime. The longitudinal power peak was shifted forward by the 4.75-inch thickness of Be at the forward end of the core, and the customary 2/1 chopped cosine longitudinal power profile did not occur. Figure 4.5 is the nuclear model used for gross nuclear calculations.

CONFIDENTIAL

CONFIDENTIAL

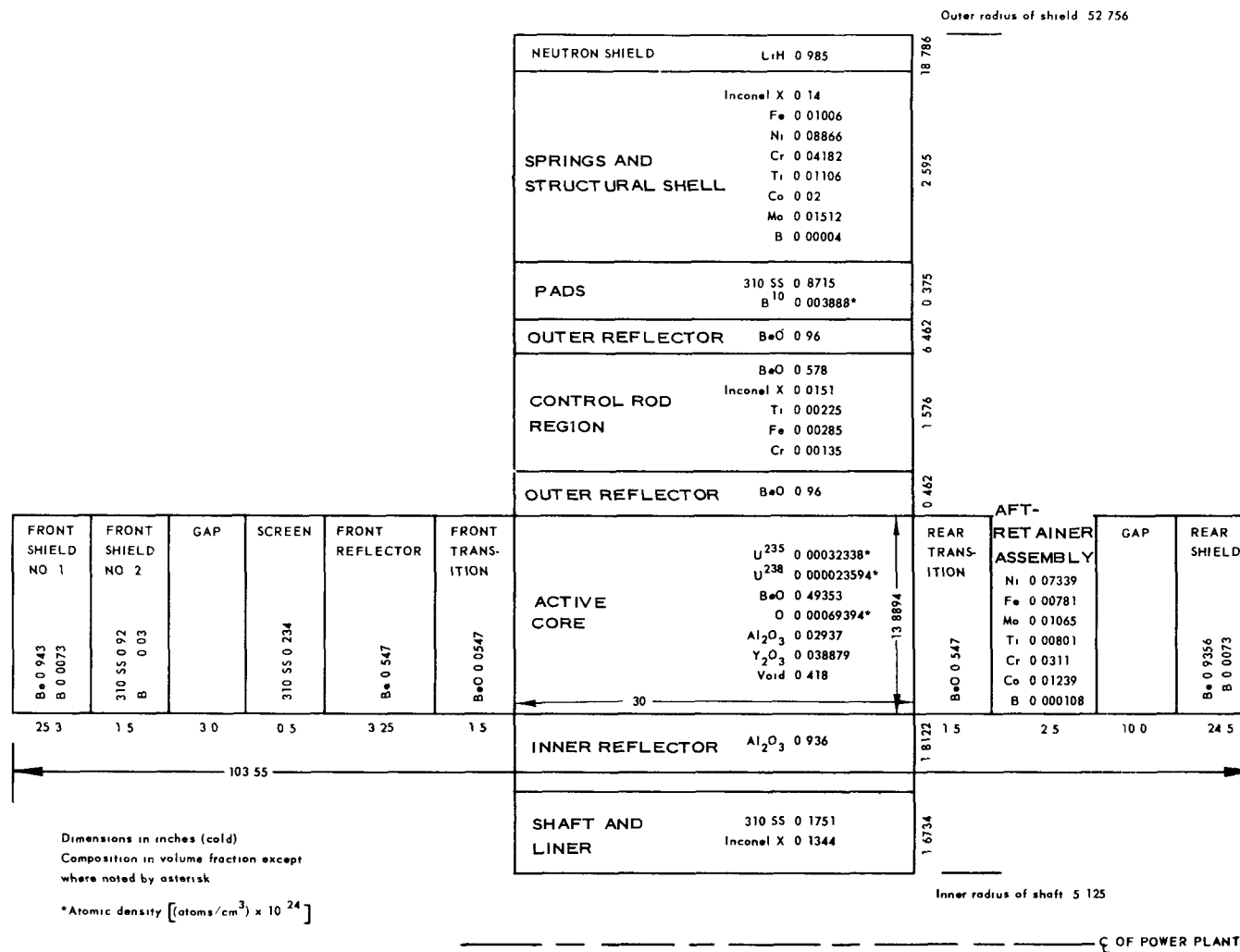


Fig. 4.5—Regional composition and geometry of the XNJ140E-1 reactor

~~CONFIDENTIAL~~

Approximately 90 percent of the compressor inlet airflow was delivered to the nuclear midsection of the engine. Of this air, approximately 84 percent was used for cooling the active core and 16 percent was used for cooling the end shields and nonfueled components of the reactor. All air passing into the nuclear midsection was mixed and delivered to the turbine at various points upstream from the exhaust duct.

The reactor pressure ratio of 0.857 was selected following evaluations of (1) the optimum over-all pressure ratio from compressor discharge to turbine inlet, and (2) estimates of pressure ratios across the forward and aft ducts, and the chemical combustor. Studies indicated that this value yielded near optimum engine performance for the over-all values of midsection pressure ratio and turbine inlet-air temperature.

The calculated fuel element average-channel maximum surface temperature was 2210°F at the design point. The corresponding fuel element maximum "hot spot" surface temperature was 2500°F. The temperature rise due to heat conduction through the fuel element was 30°F, and the maximum fuel element back-side surface temperature was 2530°F.

4.2 DESCRIPTION OF REACTOR COMPONENTS

A summary of XNJ140E-1 reactor dimensions is given in Table 4.1.

4.2.1 FUEL ELEMENTS

The active core was an annular cylindrical region 30 inches long, with a 45.1-inch outside diameter and a 17.2-inch inside diameter. There were 174,643 fuel elements (tubes) and 917 thermocouple insulator tubes within the active core. These were hexagonal tubes nominally 0.249 inch across flats, and 4.286 inches long with an inside diameter of 0.167 inch. A total of 24,949 cooling air channels and 131 passages to accommodate fuel element data instrumentation were formed by the holes in the individual tubes.

The fuel element body was composed of a BeO matrix containing a uniformly dispersed fuel additive that was a solid solution of enriched uranium oxide and yttrium oxide with a composition of 45 weight percent UO_2 and 55 weight percent Y_2O_3 . Seventeen different concentrations of the fuel additive were employed in 23 distinct radial regions in the core cross section to flatten the radial power distribution. The inside surfaces of the fuel elements were coated with 0.003-inch-thick zirconium oxide to minimize water vapor corrosion of the BeO matrix. The zirconium oxide was stabilized with 15 weight percent yttrium oxide. The composition of the thermocouple tubes was 99.5 weight percent BeO and 0.5 weight percent magnesium oxide. The MgO aided in the densification of the BeO.

4.2.2 OUTER REFLECTOR

The outer reflector was composed of approximately 511,000 unfueled BeO tubes and rods which formed an 8.5-inch-thick annulus around the active core over its entire length. The tubes were interspaced among the rods at specific locations to provide cooling channels which removed the heat generated in the reflector. The tubes and rods were nominally 0.247-inch-across-flats (compared to 0.249 inch for the fuel elements), and 1.426 inches long. The inside diameter of the tubes forming one continuous cooling channel were constant; however, the inside diameters of the tubes varied from channel to channel to accommodate local cooling requirements. The inside diameters ranged from 0.144 to 0.195 inch.

~~CONFIDENTIAL~~

TABLE 4.1
SUMMARY OF XNJ140E-1 REACTOR DIMENSIONS

	<u>Radial Dimensions, in.</u>
Shaft, OD	10.75
Tunnel, ID	11.75
Tunnel, OD	12.00
Liner, ID	13.23
Inner reflector, ID (equivalent)	13.518
Inner reflector thickness	1.859
Active core, ID	17.236
Active core, OD	45.075
Outer reflector thickness	8.378
Reflector, OD	61.976
Pressure pad assembly thickness (nominal) ^a	0.366
Pressure pad, OD	62.708
Spring gap thickness	1.553
Structural shell, ID	65.75
Structural shell thickness	0.125
Over-all diameter of structural shell (nominal)	66.00
	<u>Longitudinal Dimensions, in.</u>
Forward hardware (screen and instrumentation)	0.50
Front Be reflector	3.25
Expansion gap	0.20
Forward BeO reflector	1.50
Active core	30.00
Rear reflector	1.50
Aft-retainer assembly	2.50
Total reactor length (nominal)	39.45
	<u>Core Volume Fractions</u>
Fuel element matrix	0.5467
Fuel element cladding	0.0294
Data instrumentation	0.0046
Fuel element cooling channels	0.4014
Fuel element interstices	0.0179
	<u>Aerothermal And Nuclear Dimensions</u>
Dimensions across flats of tubes, in.	0.249
Hydraulic diameter, in.	0.167
Bore cladding thickness of ZrO ₂ , in.	0.003
Number of fuel element passages	24,949
Fuel element free-flow area, in. ²	545
Number of variations in fuel loading	23
Number of unique fuel concentrations	17
Maximum fuel concentration, wt % UO ₂	10
Minimum fuel concentration, wt % UO ₂	4.3
Average fuel concentration, wt % UO ₂	8.55

^aEquivalent solid thickness is 0.25-inch.

~~CONFIDENTIAL~~

4. 2. 3 INNER REFLECTOR

The inner reflector was composed of approximately 35,000 aluminum oxide tubes and rods that formed a 1.8-inch-thick annular region located between the inner diameter of the active core and the outside of the core liner. The tubes were nominally 0.249-inch-across-flats and 1.426 inches long. The inside diameters of the tubes forming one cooling channel were the same; however, the inside diameters of the tubes varied from channel to channel to accommodate local cooling requirements. The inside diameters ranged from 0.110 to 0.160 inch. Cooling channels formed by the tubes were dispersed throughout the inner reflector to extract the heat generated within a number of rods surrounding the channel.

4. 2. 4 TRANSITION PIECES

The transition pieces were BeO bodies that formed a 1.5-inch-thick reflector on each end of the active core. The external configuration of a transition piece was identical to the outer perimeter of a bundle of 19 fuel elements. One end of the transition piece contained 19 small holes that converged into a large diameter hole in the opposite end of the piece.

The transition pieces were oriented at each end of the core to form a manifold for air entering and leaving the fuel element passages. At the forward end of the core, the air entered the large hole and was distributed to 19 fuel element passages. At the aft end, the air from the same 19 passages was collected into the large hole before it passed through the aft-retainer assembly. This permitted the use of large diameter holes through the forward reflector and the aft-retainer assembly, and led to a better structural and aerodynamic design of these components, as well as reducing the cost.

Three lengths of transition pieces were used, thereby staggering the planes of separation of fuel tubes between the various bundles of 19 tubes. This prevented misalignment of the tubes that formed each flow passage, and maintained a shear plane across the diameter of the core.

4. 2. 5 RADIAL ARCHES

The radial arches were hexagonal BeO tubes that were 1.745 inches across flats and 0.741 inch long, and contained a bore 1.435 inches in diameter. A column of 41 arches formed an axial cavity through the outer reflector to accommodate a control rod and guide tube. Forty-eight such cavities were equally spaced around a circle conforming with the control rod pattern and located approximately 1.75 inches from the outside diameter of the active core.

4. 2. 6 CORE LINER

The core liner was a tubular structural member, with an inside diameter of 13.23 inches and a dodecagonal outside surface that was 13.362 inches across flats, located within the inner reflector, and passing through the center of the tube bundle. This metallic liner, fabricated from Inconel X, provided an axial hole through the center of the reactor assembly for the shaft tunnel and the turbomachinery coupling shaft. The core liner further served as a structural member that resisted the radial spring pressure transmitted through the tube bundle and the forward reflector.

4. 2. 7 SHAFT TUNNEL

The shaft tunnel was an Inconel X tube with an inside diameter of 11.75 inches and a wall thickness of 0.140 inch that extended from the front shield to the aft end of the reactor assembly. It was located between the core liner and the coupling shaft, and served as a structural component as well as part of the air ducting system. It transmitted part of the

~~CONFIDENTIAL~~

longitudinal loads on the reactor from the aft-retainer assembly through the central hub to the front shield. The annular duct formed by the inside diameter of the core liner and the outside diameter of the shaft tunnel channeled cooling-air to the rear shield. The tunnel was kept concentric with the liner so that the airflow in the annular passage was not affected by deflections of the reactor under flight loads.

4. 2. 8 FORWARD REFLECTOR

The forward reflector was a 3.25-inch-thick perforated circular plate of Be, with an outside diameter of 62 inches and an inside diameter of 13.46 inches. It was located immediately in front of the ceramic tube bundle, and was formed by 12 individual 30-degree sectors.

The functions of the forward reflector were: (1) to act as a neutron reflector, (2) to distribute the reactor inlet-air to the cooling channels within the tube bundle, and (3) to serve as a structure that restrained the tube bundle from forward movement.

Primary-air passed through circular holes penetrating the forward reflector. Thin-walled circular baffles were placed inside these passages to serve as thermal barriers protecting the forward reflector from adverse temperature gradients during transient conditions. The circular baffles also acted as forward locators for data instrumentation leads brought forward out of the tube bundle and routed radially outward over the front face of the forward reflector. An instrumentation cover, secured to a forward reflector sector, was used to hold the instrumentation leads in place. A semicircular bumper was mounted on the front face of the instrumentation cover over each cooling air passage to keep large foreign particles from completely blocking an air passage.

4. 2. 9 AFT-RETAINER ASSEMBLY

The aft-retainer assembly provided longitudinal support of the tube bundle against aerodynamic drag forces, friction, and aft acceleration loads. The structure was formed by 12 independent 30-degree sectors, which were simply supported at the inside radius by the shaft tunnel and near the perimeter by the rear shield outer section. The aft-retainer assembly was a sandwich-type tube sheet having two parallel plates separated by tubes that served the dual purpose of providing shear ties for the plates, and passages for the reactor discharge air. The structure was isolated from surrounding heat sources by (1) a zirconia spacer on the forward face, (2) an insulating liner consisting of a Thermoflex sandwich within the structural tubes, and (3) a Thermoflex blanket on the aft surface. Mean temperature of the structure was controlled by cooling air flowing radially inward around the tubes and between the plates. Each of the 12 sectors was a sealed, self-contained unit obtaining its cooling-air supply from the bleed-speed annulus and discharging it near the center.

Structural material of the aft-retainer assembly was Rene' 41, selected to obtain maximum high-temperature rupture strength. Tube ends were vacuum-furnace-brazed to each plate with PD61 alloy, a high-strength braze developed specifically for this application.

Longitudinal loading was reacted at the center by a central hub, supported longitudinally by the shaft tunnel. Outer reactions were transmitted to the rear shield outer section through free-swiveling linkages of ball-and-socket design. These linkages permitted limited relative displacement of the retainer plates and supporting structure without inducing further stresses. Each support point was located approximately in line with a guide tube and was cooled by discharge-air from the guide tubes, radial springs, and outer reflector.

~~CONFIDENTIAL~~

4. 2. 10 RADIAL SUPPORT STRUCTURE

Structural components of the radial support system included (1) a structural shell, (2) leaf springs and, (3) pressure pads. The leaf springs, located inside the structural shell between the internal ribs and keyed to both the structural shell and the pressure pads, were used to compress radially the tube bundle through the pressure pads and to provide shear ties for lateral support of the tube bundle. The structural shell, fabricated from Inconel X, supported the reactor and served to locate it within the pressure vessel. It was cantilevered from the triple flange connection at the forward end of the pressure vessel. The structural shell had a diameter of 66 inches and was 66 inches long. The forward portion of the shell was perforated to provide passage of compressor discharge-air into the bleed-speed annulus (after this air had passed through, and cooled the front shield outer section). The aft portion of the shell had internal circumferential ribs for orificing the cooling-air through the radial spring channels. The ribs also stiffened the shell and located the springs in the axial direction. The aft portion of the shell also was perforated to accommodate the spring retractors.

A system of 432 leaf springs mounted between the ribs on the inside of the structural shell was used to support the tube bundle. Each individual spring was formed by two semi-elliptical leaf springs 1.85 inches wide welded together to form an 11-leaf assembly. Each spring spanned a 15-degree arc of the bundle and had a spring rate of 300 pounds per inch. The tangential spring rate ranged between 11,100 and 17,200 pounds per inch.

Pressure pads were located in the outer periphery of the tube bundle and extended axially, in four sections, the full length of the bundle (33 inches). They covered a 7-1/2-degree arc of the bundle. The purpose of the pads was to distribute the concentrated loads from the radial springs uniformly around the bundle. The pads had a nonuniform cross section in order to maintain a flat outer surface while conforming to the shape of the tube bundle on the inner surface. They were made of 304 stainless steel with an addition of 1 percent enriched boron (92 weight percent B¹⁰). Borating the stainless steel served as thermal neutron shielding for the side shield. Fifteen 0.156-inch-diameter axial holes in each pad provided the necessary cooling-air channels. The cooling-air channels were located a uniform distance from the irregular inner surface of the pressure pads at approximately the area of maximum secondary heat generation. Accordingly, radial temperature gradients through the pressure pads were minimized.

4. 2. 11 CONTROL ROD ASSEMBLIES

The control rod and its thermally insulated guide tube comprised the control-rod assembly that was contained within the axial cavity through the reactor formed by the radial arches. The control rods were positioned within guide tubes which were surrounded by insulation material.

The neutron-absorbing material was 38 weight percent Eu₂O₃ in a nickel matrix. This mixture, in the form of 0.700-inch-diameter cylinders, was encased in modified 80 Ni - 20 Cr tubing with 0.030-inch-thick walls to form 4.8-inch-long segments. Five segments were joined together with Inconel X straps to form a 24-inch-long control rod.

The Inconel X straps provided both structural support and bearing surfaces. The rod was sectioned to allow small dimensional changes of the cladding and poison matrix, and to permit some degree of flexibility in the rod as it traversed the guide tube. The guide tube provided an uninterrupted path for the control rod travel and extended the full length of the fueled core. It was fabricated from Inconel X, and had an inside diameter of 1.00-inch and 0.030-inch walls. The inner bore was chromium plated to reduce the coefficient of friction.

~~CONFIDENTIAL~~

The guide tube was thermally insulated by 0.090-inch-thick Thermoflex RF2400 inserted in two halves between the guide tube and the radial arch. Inconel 702 foil, 0.010-inch-thick, covered the outer diameter of the molded insulation.

4.3 PERFORMANCE REQUIREMENTS

The XNJ140E-1 reactor was designed to meet the performance requirements shown in Table 4.2, standard-day flight conditions. Hot-day and cold-day flight conditions are shown in Tables 4.3 and 4.4, respectively. Based upon the design point flight condition d, Table 4.2, the reactor performance parameters shown in Table 4.5 were established as the basis of design. Aerothermal and structural parameters of the reactor design, generated on this basis, were then modified and adjusted as required to meet the general design criteria established by all flight conditions for standard-, hot-, and cold-day operations.

4.4 OVER-ALL REACTOR DESIGN

4.4.1 NUCLEAR DESIGN

The nuclear model of the reactor and the shield used in reactivity and power distribution analysis is shown in Figure 4.5. Regional composition and geometry are given, and the active core is represented as a single region of average composition. One-dimensional nuclear analyses included additional regions, such as borated Be shielding material, not shown on the principal coordinate axes. Table 4.6 gives the loading details of the active core, showing weight percent UO_2 , and the equivalent outer radius of each of the 23 discrete regions of 17 different fuel loadings.

4.4.1.1 Reactivity Requirements

Predicted reactivity changes for the reactor over its design life are summarized in Table 4.7. The tolerances shown for the reactivity decrements were estimated with a 99 percent confidence factor. As shown in Table 4.7, 5.2 percent $\Delta k/k$ excess reactivity was needed in the cold clean reactor to yield a 95 percent probability of meeting the operating requirements.

Table 4.8 gives the cold clean excess reactivity of the reactor as developed from critical experiment data with analytical corrections for known differences between the critical experiment and the XNJ140E-1 reactor. The tolerances given in Table 4.8 are quoted with 99 percent confidence. This table shows that a 95 percent probability existed that the cold clean excess reactivity of the XNJ140E-1 reactor would be between 5.2 and 6.6 percent $\Delta k/k$. The fuel inventory to provide the excess reactivity was 87.0 kilograms of U^{235} .

4.4.1.2 Factors Affecting Reactivity

Fuel Burnup and Long-Term Poisons - Table 4.7 shows a change in excess reactivity of -2.9 percent $\Delta k/k$ for fuel burnup and long-term poisons. The fuel burnup contribution included depletion of U^{235} and U^{238} , and buildup of U^{236} and Pu^{239} . The long-term poisons treated were (1) Sm^{149} , (2) Li^6 , which is an end product of neutron absorption in Be, and (3) slag, an artificial poison invented for analytical purposes.

Each isotope included in the slag representation had a thermal absorption cross section less than 10^3 barns and was the first isotope in its decay chain with a half-life greater

TABLE 4.2
OBJECTIVE-POWER-PLANT STANDARD-DAY FLIGHT PARAMETERS (S-18 CYCLE)

Flight Conditions	a	b	c	d	e	f	1	2A "q" Limit, No Power Limit	2B "q" Limit, Min. Power Limit	3 Sustain Flight at M_n 0.6, SL	5 Climb to Station, Mil
$T_{0,}$ °F	59	59	-13	-66	-66	23	59	59	59	59	-13
M_n	0	0	0.7	0.8	0.8	0.6	0	0.6	0.6	0.6	0.7
Altitude, ft	0	0	20,000	35,000	35,000	10,000	0	0	0	0	20,000
Power Setting	NC	Max	NC	NC	Mil	NC	Max	Mil	Mil	NC	Mil
% N	98	100	98	98	100	98	100	100	97.2	95	100
$W_{2,0,}$ lb/sec	412	426	280	173	176	361	426	493	462	435	286
$W_{3,2,}$ lb/sec	369	382	252	155	157	323	381	441	414	390	256
$P_{3,2,}$ psia	171	162	117	72.8	74.9	150	179	207	192	172	121
$T_{3,2,}$ °F	665	663	638	583	597	665	685	722	689	665	655
$T_{4,0,}$ °F	1,740	1,640	1,740	1,740	1,800	1,740	1,800	1,800	1,705	1,695	1,800
Q, mw	112		78.1	50.5	53.6	98.5	121	136	120	102	83.2
F_n , lb	21,600	34,160	12,050	8,120	8,570	14,830	35,310	19,250	16,420	13,320	12,840
Life, hr	20	5	20	885	20	50					
Torque, lb-ft	92,680	93,420	62,830	38,240	38,970	81,330	97,000	112,780	102,800	92,500	64,860

CONFIDENTIAL

CONFIDENTIAL

CONFIDENTIAL

CONFIDENTIAL

TABLE 4.3
OBJECTIVE-POWER-PLANT HOT-DAY FLIGHT PARAMETERS (S-18 CYCLE)

Flight Conditions	a Ground Checkout	b Chemical Take-off	c Climb To Station	d Cruise On Station	e Maneuver On Station	f Two-Engine Operation	1 Nuclear Take-off	2 Accelerate To "q" Limit	3 Sustain Flight At "q" Limit	4 Emergency Power Setting At M_n 0.43
T_O , °F	103	103	25	-30	-30	64	103	103	103	85
M_n	0	0	0.7	0.8	0.8	0.6	0	0.6	0.6	0.6
Altitude, ft	0	0	20,000	35,000	35,000	10,000	0	0	0	5,000
Power setting	NC	Max	NC	NC	Mil	NC	Max	Mil	NC	Emg
% N	98	100	98	98	100	98	100	100	98.5	103
$W_{a2.0}$, lb/sec	363	380	251	160	163	318	379	420	418	406
$W_{a3.2}$, lb/sec	324	340	225	143	146	285	338	387	375	364
$P_{3.2}$, psia	151	145	105	67.4	69.6	133	160	181	173	173
$T_{3.2}$, °F	706	709	681	636	653	705	729	764	747	778
$T_{4.0}$, °F	1,740	1,640	1,740	1,740	1,800	1,740	1,800	1,800	1,755	1,830
Q, mw	95.1		67.5	44.6	47.5	83.7	104	114	106	109
F_n , lb	17,060	26,760	9,720	6,830	7,260	11,480	29,910	14,400	13,320	14,580
Life, hr										5
Torque, lb-ft	81,340	84,080	56,780	36,080	37,130	71,590	86,850	97,880	92,500	94,550

TABLE 4.4
OBJECTIVE-POWER-PLANT COLD-DAY FLIGHT PARAMETERS (S-18 CYCLE)

Flight Conditions	a	b	c	d	e	f	1A	1B	1C	2	3
	Ground Checkout	Chemical Take-off	Climb To Station	Cruise On Station	Maneuver On Station	Two-Engine Operation	Nuclear Take-off	Nuclear Take-off, Nom. Power Limit	Nuclear Take-off, Max. Power Limit	Max. Acceleration To "q" Limit, Max. Power Limit	Sustain Flight At "q" Limit
T_0 , °F	-60	-60	-46	-85	-85	-15	-60	-60	-60	-60	-60
M_n	0	0	0.7	0.8	0.8	0.6	0	0	0	0.6	0.6
Altitude, ft	0	0	20,000	35,000	35,000	10,000	0	0	0	0	0
Power setting	NC	Max	NC	NC	Mil	NC	Max	Max	Max	Mil	NC
% N	96	96.6	98	98	100	98	91.6	93.7	96	92.8	90
$W_{a2,0}$, lb/sec	524	531	303	181	184	399	507	516	524	608	580
$W_{a3,2}$, lb/sec	470	475	272	161	165	357	454	467	470	546	520
$P_{3,2}$, psia	210	189	126	76	78.3	165	188	200	210	230	186
$T_{3,2}$, °F	496	472	592	553	565	620	456	480	496	505	440
$T_{4,0}$, °F	1,640	1,640	1,740	1,740	1,800	1,740	1,465	1,550	1,640	1,515	1,295
Q, mw	150		87.7	54.2	57.5	113	120	135	150	150	103
F_n , lb	32,800	48,740	14,200	8,920	9,420	18,140	40,300	46,000	50,900	25,000	13,320
Life, hr											
Torque, lb-ft	110,000	105,120	66,750	39,340	40,020	89,000	102,000	106,000	110,000	127,000	109,400

CONFIDENTIAL

CONFIDENTIAL

TABLE 4.5
XNJ140E-1 REACTOR PERFORMANCE
PARAMETERS AT DESIGN POINT

Reactor airflow rate, lb/sec	154.6
Fuel element airflow rate, lb/sec	129.9
Reactor inlet pressure, psia	69.2
Reactor pressure ratio	0.857
Reactor inlet temperature, °F	582
Turbine inlet temperature, °F	1740
Total reactor power, mw	50.4

TABLE 4.6
FUEL CONCENTRATION AND DISTRIBUTION
IN THE XNJ140E-1 REACTOR

Region	Fuel Conc. Wt % UO ₂	Inner Radius, cm	Outer Radius, cm
1	7.9	21.869	23.176
2	8.2	23.176	24.483
3	8.5	24.483	25.789
4	8.8	25.789	27.096
5	9.1	27.096	29.056
6	9.4	29.056	31.670
7	9.7	31.670	34.283
8	10.0	34.283	44.736
9	9.7	44.736	46.043
10	9.4	46.043	47.350
11	9.1	47.350	48.656
12	8.5	48.656	49.963
13	8.2	49.963	50.617
14	7.9	50.617	51.270
15	7.3	51.270	51.923
16	7.0	51.923	52.577
17	6.6	52.577	53.230
18	6.2	53.230	53.883
19	5.8	53.883	54.537
20	5.4	54.537	55.190
21	5.0	55.190	55.843
22	4.6	55.843	56.497
23	4.3	56.497	57.150

~~CONFIDENTIAL~~

TABLE 4.7
REQUIRED EXCESS REACTIVITY FOR THE XNJ140E-1 REACTOR

	Change In Reactivity, $\% \Delta k/k$
Equilibrium xenon at 50.4 mw	- 1.5 \pm 0.5
Fuel burnup and long-term poisons	- 2.9 \pm 1.0
Temperature effect	<u>0.0 \pm 0.6</u>
Total change	- 4.4 \pm 1.3
Margin for 95% confidence	<u>- 0.8</u>
	- 5.2
Required excess reactivity (95% confidence level)	<u>5.2% $\Delta k/k$</u>

TABLE 4.8
EXCESS REACTIVITY AVAILABLE AND CONTROL ROD WORTH
IN THE XNJ140E-1 REACTOR

Available Excess Reactivity	Reactivity, $\% \Delta k/k$
Excess reactivity of critical experiment (corrected for full core substitution of fuel tubes, aft retainer, etc.)	4.96 \pm 0.6
Corrections for differences between critical experiment and XNJ140E-1 design	<u>0.95 \pm 0.9</u>
	5.9 \pm 1.1
Excess reactivity available in the XNJ140E-1 reactor, 95% confidence factor	5.9 ^a \pm 0.7
XNJ140E-1 control rod worth, extrapolated from measurement	10.2

^aThis excess reactivity required 87.0 kilograms of U²³⁵.

~~CONFIDENTIAL~~

than 100 days. The total thermal cross section of slag was 50 barns per fission. Slag had an absorption resonance integral of 268 barns per fission, while the absorption resonance integral for a $1/v$ absorber having the same 2200 meters per second capture cross section was 100 barns per fission.

Concentrations of the various fuel and non-fuel isotopes were calculated by an isotopic history trace which treated the effect of neutron captures by using flux-integrated, 19 lethargy level cross sections. This isotopic trace closely approximated the analytic solution of a five-member linear decay chain, assuming that power and flux were constant over the time period being computed.

The procedure used to calculate the worth of fuel depletion, equilibrium xenon, and stable fission product poisons was as follows:

1. The neutron flux at 19 energy levels for each core region of discrete fuel loading was calculated by a 19-energy-group, radial, diffusion analysis of the clean, undepleted core.
2. These 19-level flux values were entered into the isotopic history trace calculation to compute the flux-integrated, 19-level cross sections of the pertinent isotopes. The concentrations of these isotopes were then calculated for each of the 23 core regions for an operating life of 55,000 megawatt-hours at approximately 50 megawatts.
3. The calculated concentrations for the fully depleted and poisoned core were entered in a three-energy-group diffusion calculation where the reactivity worths of Xe^{135} , fuel burnup, and stable poisons were determined.

This method of analysis gave negative reactivity worths of 1.1 percent $\Delta k/k$ for fuel depletion (U^{235} , U^{236} , U^{238} , and Pu^{239}), 0.6 percent $\Delta k/k$ for Sm^{149} , and 1.2 percent $\Delta k/k$ for the combined worth of slag and Li^6 . The total worth of -2.9 percent $\Delta k/k$ for these effects is shown in Table 4.7 under fuel burnup and long-term poisons. The calculated worth of equilibrium xenon at 50.4 megawatts was -1.3 percent $\Delta k/k$. Correcting this value by a factor of 1.15 from experiment correlation gave the worth of -1.5 percent $\Delta k/k$ shown in Table 4.7. The reactivity worth of peak xenon for any combination of circumstances in the design life showed an increase of no greater than 0.5 percent $\Delta k/k$, indicating that xenon buildup would not limit normal operation of the reactor. Calculations showed that non-uniform longitudinal fuel depletion and non-uniform longitudinal temperature had no significant effect on the reactivity worths of fuel depletion, Xe^{135} , and stable poisons.

The calculated reactivity worth of equilibrium xenon as a function of nuclear power level is shown in Figure 4.6.

Temperature - Analysis of the reactivity effects of core and reflector temperature variations of the XNJ140E-1 reactor considered three contributing factors: thermal base change, material expansion, and Doppler broadening.

The magnitude of the temperature effect on reactivity caused by the thermal base change was calculated using a multiregion, slowing-down analysis to generate three-group constants for use in a one-dimensional, diffusion-theory analysis.

From the homogenized composition of each region, the flux and the slowing-down density were computed at 19 lethargy levels. Three-group constants were then computed by flux weighting the appropriate parameters. These constants were used in the spatial solution of coupled diffusion equations for both the radial and the longitudinal dimensions. The resulting reflector savings were compared to those initially assumed in establishing the group constants. An iterative procedure was followed until the savings used to determine group constants were consistent with those determined in the spatial solutions of the

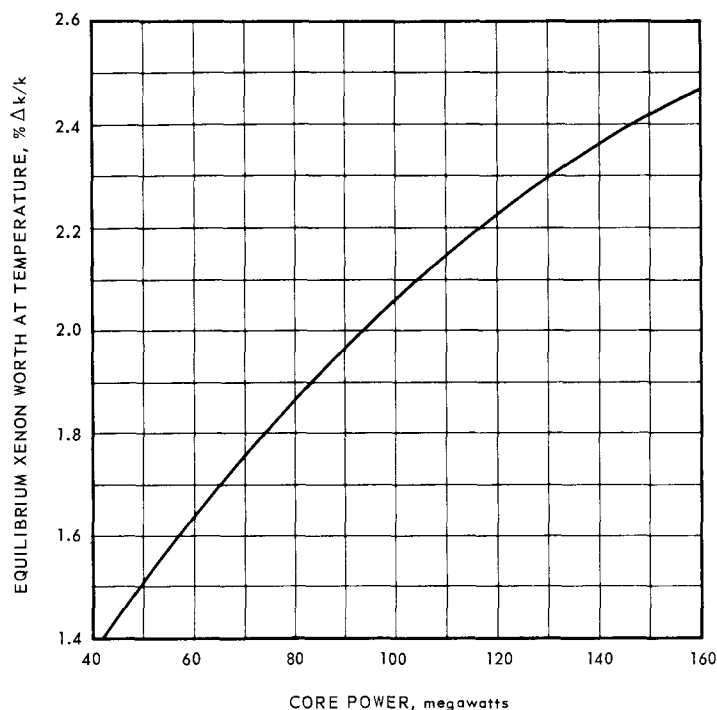
~~CONFIDENTIAL~~

Fig. 4.6—Worth of equilibrium xenon as a function of nuclear power level, XNJ140E-1 reactor

diffusion equations. Each thermal group was treated by assuming a Maxwellian distribution at the specified temperature. Calculations showed that the thermal base contribution was positive with increasing temperature, principally due to the fact that the poisoning effect of the control rod guide tubes (located in the reflector) decreased with increasing reflector temperature.

The effect of thermal expansion of reactor materials was calculated simply by considering only changes in density and reactor volume, neglecting any effects of reduced leakage due to shrinkage of clearance gaps. The geometric effect was calculated, using the same analytical methods as were used for the thermal base calculations, and shown to be a negative change with increasing temperature.

The effect on reactivity due to Doppler broadening was computed by a many-level, slowing-down, diffusion analysis using Doppler-broadened U^{235} and U^{238} cross sections over the energy range of available resonance parameters. The effect was a negative change with increasing core temperature. These effects are summarized in Table 4.9.

The analysis of the steady-state characteristics assumed that all components were at the same temperature as the core until the compressor discharge-air temperature was reached. Thereafter, the physical temperatures of the components were taken as the equilibrium temperature these components would assume at a power level which would produced the specified core discharge-air temperature. Neutron temperatures were assumed to be established by the moderator material within, or adjacent to, the component being analyzed. Thermal expansion effects were based upon physical temperatures. Thermal base and Doppler effects were based on effective neutron temperatures.

Figure 4.7 shows the variation in excess reactivity of the clean reactor with temperature, including the influence of fuel depletion, stable fission-product poisons, and Xe^{135} on the temperature-reactivity characteristics of the reactor. The calculated temperature

~~CONFIDENTIAL~~

TABLE 4.9
TEMPERATURE REACTIVITY EFFECTS IN THE
CLEAN XNJ140E-1 REACTOR

Core Average Temperature, °F	Reactivity Change, % $\Delta k/k$		
	Thermal Base Plus Expansion ^a	Doppler	Net
68	0	0	0
600	+ 0.50	-0.12	+0.38
1000	+ 0.37	-0.16	+0.21
2000	+ 0.16	-0.23	-0.07

^a-1.14% $\Delta k/k$ calculated for thermal expansion,
68°F to 2000°F.

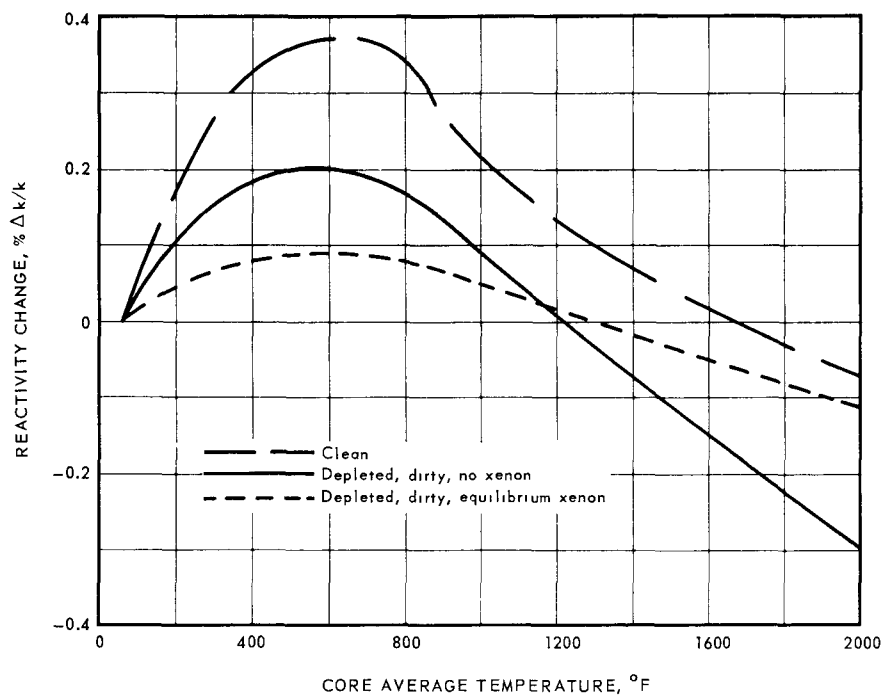


Fig. 4.7 - Calculated steady state temperature effect on reactivity,
XNJ140E-1 reactor

~~CONFIDENTIAL~~

coefficient of reactivity at design temperature was negative for both the clean and the dirty core.

Under the transient temperature conditions occurring during reactor startup, the interplay of the various temperature effects could produce a net change in excess reactivity different from that seen during steady state operation. The principal factor of this difference was the lag in temperature rise of the outer reflector compared to the core. The reflector might not reach operating temperature until several minutes after startup, resulting in a temperature effect on reactivity more negative than that of steady state.

Other Reactivity Factors Affecting Excess Reactivity - Data instrumentation planned for the engineering test programs included approximately 225 thermocouples in the core and aft-retainer assembly. The reactivity worth of the thermocouples, based on critical experiment measurements, was about -0.5 percent $\Delta k/k$. Be, when exposed to a neutron and a gamma-ray flux, undergoes reactions such as (n, α) , $(n, 2n)$, and (γ, n) . The (n, α) reaction has a threshold energy of about 1 Mev and leads to the production of Li^6 through beta decay of the He^6 intermediary. The negative effect of Li^6 on excess reactivity was treated in the allowance for long-term poisons, Table 4.7.

The positive effect of the $(n, 2n)$ reaction on excess reactivity was about 3 percent $\Delta k/k$. The analysis assumed that two neutrons were emitted per one absorbed. One of these neutrons degraded in energy by adjustment of the inelastic scattering cross section, and the other was emitted as a fission neutron.

The (γ, n) reaction in Be had a negligible effect on the reactivity of the reactor during nuclear operation. The significance of the reaction was limited to the effect it had on the kinetics and on after-shutdown heat generation in the core. The error in reactor period as a function of reactivity due to neglecting photoneutrons is shown in Figure 4.8 for three different operating times. Approximately three minutes after shutdown the photoneutron-induced heat generation in the core was equal to the heat generation from delayed neutrons; at 8 minutes after shutdown the photoneutron-induced heat generation was at least ten times as great as the delayed-neutron-induced heat generation.

4.4.1.3 Reactivity Effect of Control Rods

From critical experiment measurements, the best value of reactivity worth for the bank of 48 control rods at 24 inches (full) insertion was 9.6 percent $\Delta k/k$. When corrected to the XNJ140E-1 design, the worth was 10.2 percent $\Delta k/k$ for the fully inserted rod bank. Figure 4.9 shows the relative worth of the rod bank as a function of depth of insertion measured from the front face of the active core. The curve was established by a series of two-dimensional (R, Z) three-energy-group diffusion theory calculations. The minimum shutdown margin expected during normal operation was greater than 2 percent $\Delta k/k$.

4.4.1.4 Reactor Kinetics

The stable reactor period versus reactivity for a homogeneous, reflected XNJ140E-1 core at 68°F as calculated by the in-hour formula is shown in Figure 4.10. The effective delayed neutron fractions and the average neutron generation time are given in Table 4.10. The data in the table were obtained from a two-group, multi-region, diffusion calculation using the delayed-neutron-emission spectrum.

4.4.2 SECONDARY HEATING

An accurate knowledge of the magnitude and the distribution of secondary heating, i. e., the heat generated in non-fueled components of the reactor by neutron reactions and by the interaction of gamma rays passing through reactor components, was essential to the reactor design. The amount of heat generated and the site of its deposition were evaluated so that aerothermal designs could provide for the removal of this heat.

~~CONFIDENTIAL~~

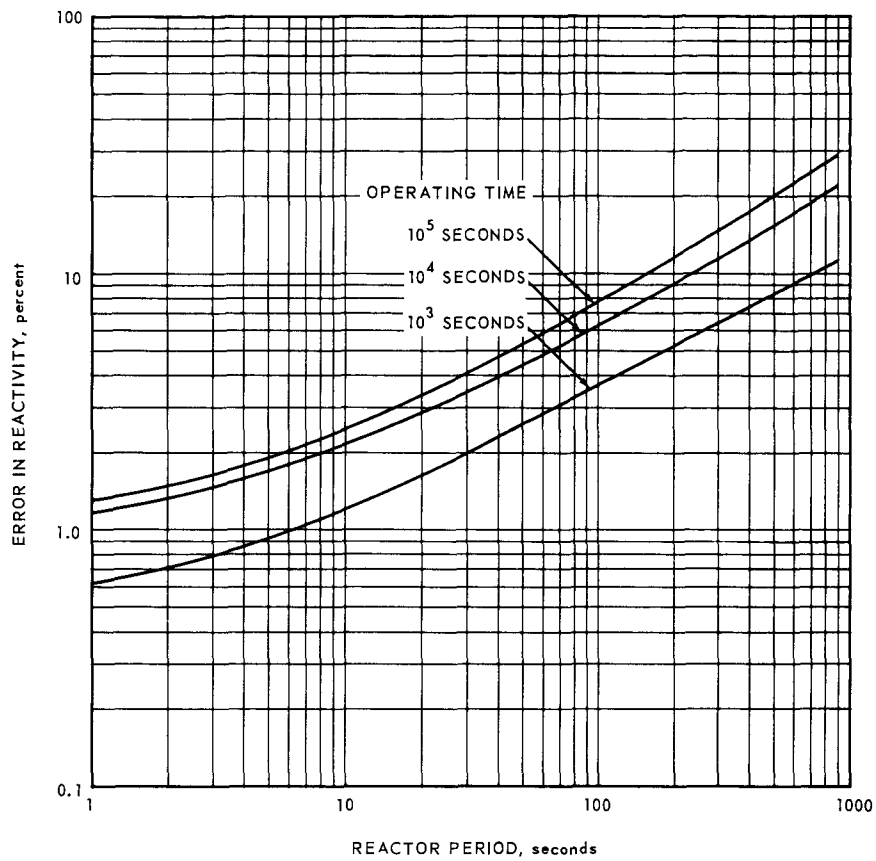


Fig. 4.8 – Calculated error in reactivity as a function of reactor period when neglecting photoneutrons

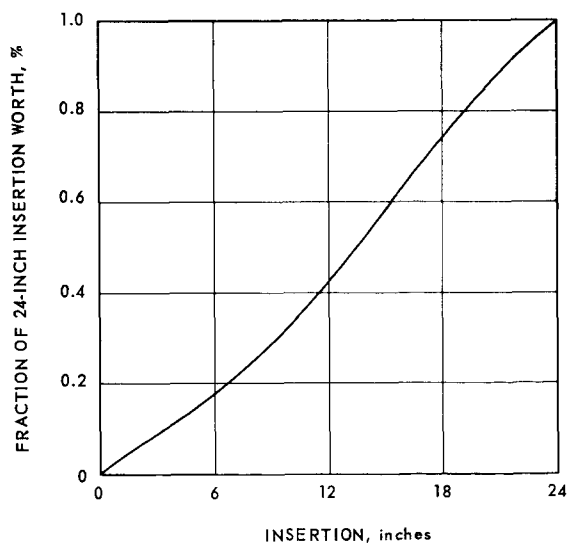


Fig. 4.9 – XNJ140E-1 control rod worth relative to worth at full insertion

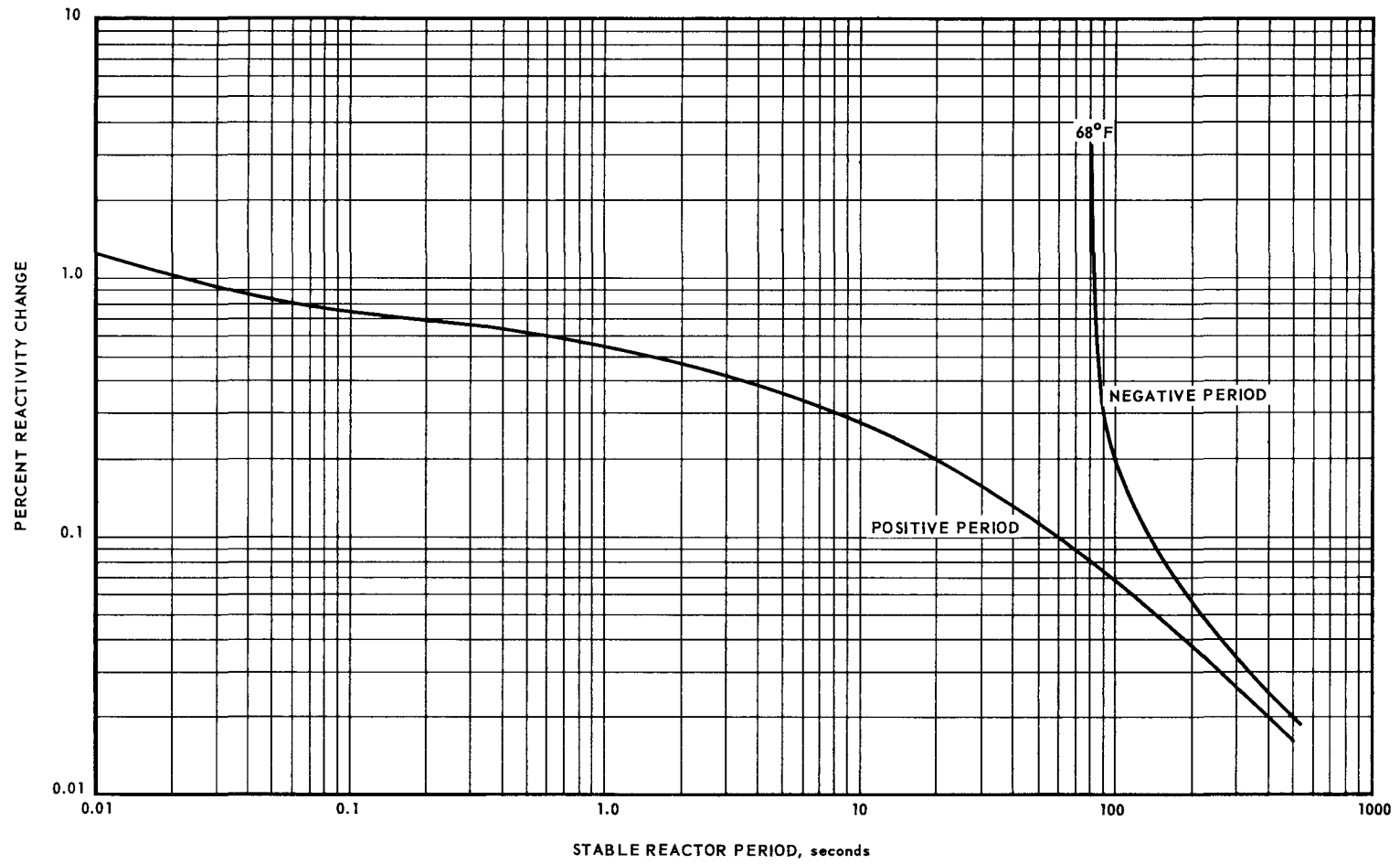


Fig. 4.10 – Stable reactor period, XNJ 140E-1 reactor

CONFIDENTIAL

CONFIDENTIAL

TABLE 4.10
EFFECTIVE FRACTION OF DELAYED NEUTRONS
IN XNJ140E-1 REACTOR

Actual Delay Fraction	Effective Delay Fraction	Decay Constant, sec ⁻¹
0.00023	0.00025	0.0126
0.00142	0.00149	0.0311
0.00126	0.00135	0.1134
0.00264	0.00280	0.3060
0.00080	0.00086	1.2530
0.00022	0.00023	3.3810
$\beta_{act} = 0.00657$	$\beta_{eff} = 0.00698$	
Average neutron generation time, ℓ , = 56.18 μ sec (68° F)		
= 42.78 μ sec (2000° F)		

Neutron heating calculations took into account the kinetic energy loss of the neutron in slowing down, and the heating caused by the (n, α) reaction in borated pressure pads.

Sources of gamma-ray heating in the core were (1) prompt fission gammas, (2) fission-product-decay gammas, and (3) non-fission gammas liberated in neutron capture reactions in the core. Another gamma source considered was the extra-core (n, γ) reaction which produced the gammas resulting from neutron captures in the reflectors and structural components.

Correlation of gamma-ray heating analyses with critical experiment measurements showed that the analytical methods used gave results both in the core and outside the core that were within the uncertainty limits of the experimental data. The data were estimated to be accurate within about ± 10 percent in the core and from ± 30 percent to ± 40 percent in the various extra-core components. Measurements of gamma-ray energy deposition were made with ionization chambers satisfying the Bragg-Gray conditions. Comparisons of calculated and experimental relative spatial distribution for foil neutron sensors showed that the calculated values for neutron activation were within the limits of measurement accuracy.

The reactor, during steady-state operation, produced 198.3 Mev available energy per fission from the combined primary and secondary sources summarized in Table 4.11. Average secondary-heating rates for the major components of the XNJ140E-1 reactor are presented in Table 4.12. A summary of the fractional energy deposition in the XNJ140E-1 reactor is given in Table 4.13. Not included in this summary was the energy from neutron-

TABLE 4.11
XNJ140E-1 REACTOR ENERGY PER FISSION

	Mev
Neutron Kinetic Energy Loss	4.9
Core Gamma Rays	
Prompt	7.8
Decay	6.2
Non-fission capture	2.6
Extra-Core Capture Gamma Rays	3.7
Beta	7.7
Fission Fragment	165.0
(n, α) Reaction in Boron	0.4
Total	198.3

~~CONFIDENTIAL~~

TABLE 4.12
SECONDARY HEATING RATES IN XNJ140E-1 REACTOR

Component	Weight, g	Nominal Average Heating Rates, w/g-mw		
		Neutron	Gamma	Total
Core	1.3×10^6	0.014	0.047	0.061
Forward Reflector				
Beryllium, 3.25 in.	8.3×10^4	0.006	0.008	0.014
Beryllium oxide, 1.150 in.	5.4×10^4	0.006	0.018	0.024
BeO Aft Reflector, 1.50 in.	5.4×10^4	0.005	0.0132	0.018
Rear Gate	6.0×10^4	-	0.010	0.010
Shaft	4.2×10^4	0.0008	0.020	0.023
Tunnel and Liner	6.1×10^4	0.0009	0.025	0.026
Al ₂ O ₃ Island, 1.8 in.	1.4×10^5	0.005	0.030	0.035
Be Shaft Stuffing				
Front	1.1×10^4	0.006	0.010	0.016
Rear	8.2×10^3	0.005	0.006	0.011
Radial Reflector	1.7×10^6	0.002	0.011	0.013
Pressure Pads (1% B ¹⁰), 0.25 in. nominal	1.7×10^5	0.018	0.0026	0.021
Springs	3.2×10^5	-	0.0030	0.0030
Pressure Shell, 0.125 in.	1.1×10^5	-	0.0015	0.0015
Absorber Rod	-	-	0.068	0.068

TABLE 4.13
FRACTIONAL ENERGY DEPOSITION IN XNJ140E-1 REACTOR

Region	Watts Deposited Per Watt Of Total Fission Energy ^a			
	Neutron	Total Gamma	Fission Fragment And Beta	Total
Core	0.0184	0.0614	0.8772	0.9570
Forward reflector and transition	0.00082	0.00168	-	0.0025
Aft transition, aft-retainer assembly	0.00027	0.00133	-	0.0016
Shaft, tunnel, liner, Be shaft inserts	0.00019	0.00261	-	0.0028
Inner reflector	0.00070	0.00420	-	0.0049
Outer reflector	0.00357	0.0187	-	0.0223
Pressure pads (n, α)	0.00310	0.00044	-	0.0035
Springs and shell	-	0.00081	-	0.0008
Reactor total	0.0270	0.0912	0.8772	0.9954
Estimated escape from reactor	0.0015	0.0031	-	0.0046

^aTotal fission energy does not include energy from neutron-induced reactions in the side shield or end shields.

~~CONFIDENTIAL~~

induced reactions in the side shield or end shields. Radial and longitudinal heating rate distributions in the reactor are shown in Figures 4.11 and 4.12, respectively.

4.4.2.1 Distribution of Secondary Heating in Reactor Components

The longitudinal relative heating rate distribution in the outer reflector is shown in Figure 4.13. This distribution also closely applied to the longitudinal relative heating rates in the control rod (excluding neutron absorption in the Eu_2O_3), the guide tube, and in the springs and support shell. Figure 4.14 shows the longitudinal relative heating rate distribution in the inner reflector, the shaft, core liner, and shaft tunnel. The radial heating rate distributions for the inner reflector and the outer reflector are shown in Figure 4.11. The radial heating rate in the pressure pads, primarily from the (n, α) reaction in boron, peaked at the inner side so that about 90 percent of the total secondary heat generation in the pads occurred in the first 0.1-inch thickness. The heating rate at the inner surface of the pads was about 0.12 watts per gram per megawatt of steady-state reactor power.

Secondary heating caused by gammas from two different sources occurred in the control rods. These sources were (1) gamma rays originating outside the control rod and (2) gamma rays that originated from neutron captures in the control rod. Beta ray heating also contributed to the control rod secondary heating. Table 4.14 shows the average fine radial gamma ray heating rates in the control rod assembly.

4.4.2.2 Reactor Afterheat

Heat generation in the major components of the XNJ140E-1 reactor after shutdown from nuclear operation is shown in Table 4.15. The fractional heat generation shown was based on the steady-state heat generation in each of the components.

The pressure pads were the only component in which heat generation decayed as fast as in the core. The difference in the rate of decay of heat generation between the core and the other components required that the relative distribution of cooling-air after shutdown be different from the distribution during operation, or, alternatively, that the cooling-air requirements be determined by the component material maximum temperatures.

4.4.2.3 Analytical Methods

Gamma Heating Analysis - Secondary heating caused by absorption of gamma rays was determined by using a Monte Carlo calculation which traced gamma histories from emission through Compton collision to photoelectric absorptions, pair production reactions, or escape from the reactor. The spatial distributions of the gamma sources (fissions and neutron captures) were determined by a one-dimensional, multi-energy, slowing-down diffusion analysis and by a two-dimensional, three-energy-group diffusion analysis.

The cross sections used to calculate the captures per fission for the structural members outside the core were 19 lethargy level cross sections obtained from digitalized cross sections at 3622 lethargy levels. This lethargy lattice was fine enough to give a good representation of the cross sections by straight line segments, even in the resonance region. The calculated ratio of capture-per-fission when using the refined 19 level cross sections was up to 50 percent higher than when the ratio was calculated using the original 19 level cross sections.

Neutron Heating Analysis - Secondary heating caused by neutron slowing down and capture processes was determined with the aid of a one-dimensional, eighteen-energy-group, slowing-down diffusion analysis, and a two-dimensional, three-energy-group diffusion analysis.

The kinetic energy per cubic centimeter of homogenized material deposited by neutron slowing down was calculated at several radial and longitudinal points in the core and

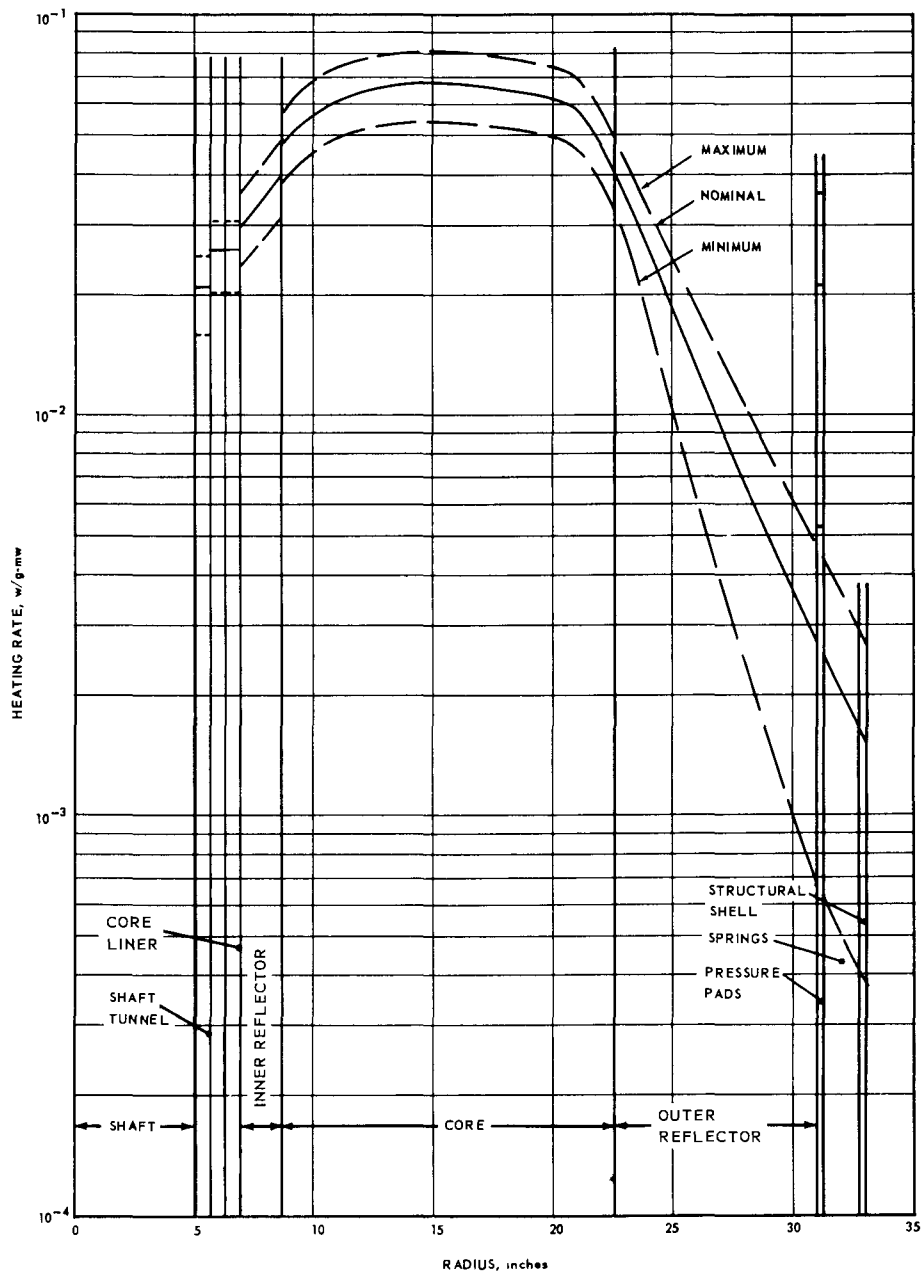
~~CONFIDENTIAL~~

Fig. 4.11 - Gross radial secondary heating distribution, XNJ140E-1 reactor

~~CONFIDENTIAL~~

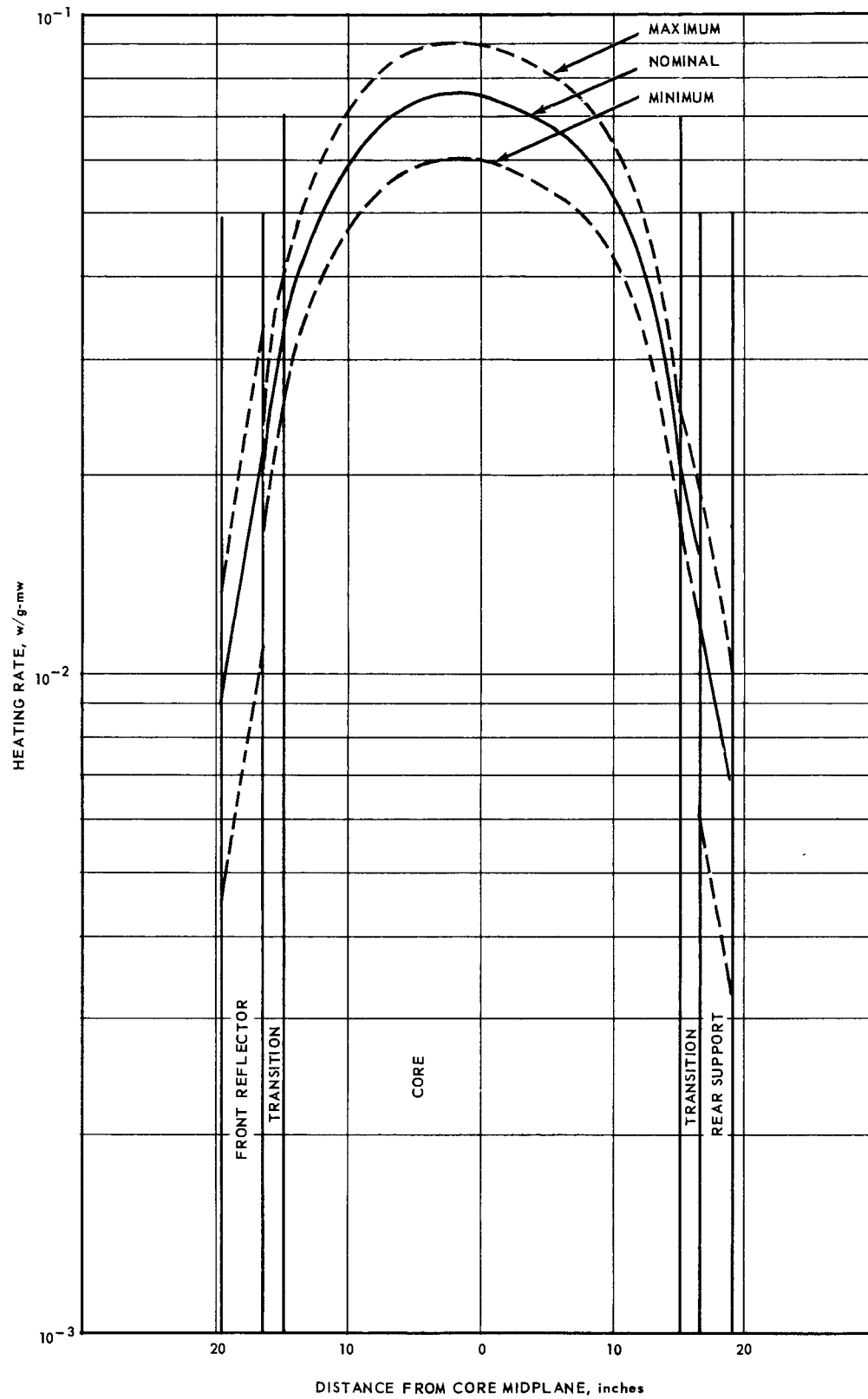


Fig. 4.12—Longitudinal secondary heating rate, XNJ140E-1 reactor

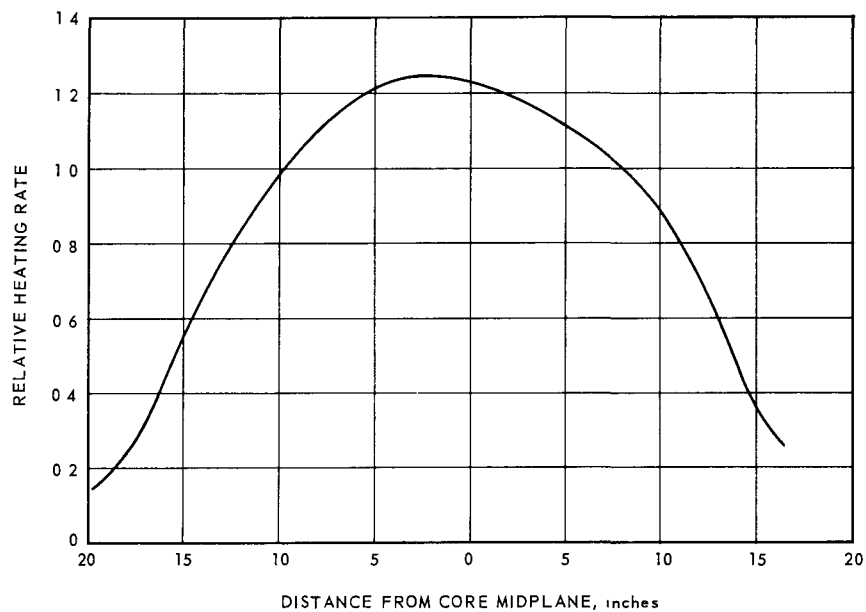
~~CONFIDENTIAL~~

Fig. 4 13—Relative longitudinal secondary heating rate distribution in outer reflector, XNJ 140E-1 reactor

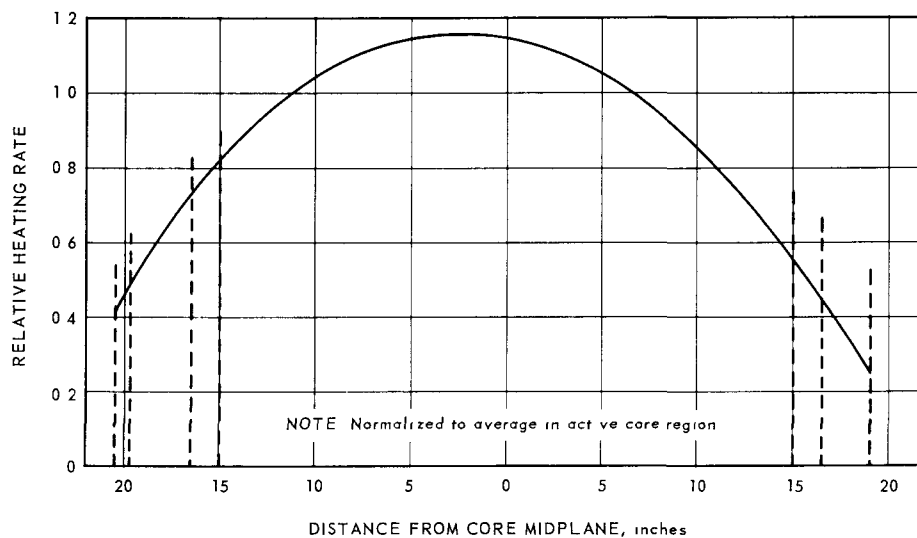


Fig. 4 14—Relative longitudinal secondary heating rate distribution in inner reflector, shaft, core liner, and shaft tunnel

~~CONFIDENTIAL~~

TABLE 4.14
CAPTURE GAMMA-RAY HEATING IN CONTROL ROD ASSEMBLY

Region And Material	Outer Radius, in.	Relative Heating Rate
Matrix ($\text{Eu}_2\text{O}_3\text{-Ni}$)	0.350	1.0
Cladding, Nichrome	0.380	0.846
Bearings and air, Inconel X	0.500	0.513
Guide tube, Inconel X	0.530	0.410
Insulation and air, Thermoflex	0.625	0.333
Hexagonal arch, BeO	0.784	0.249

TABLE 4.15
AFTER-SHUTDOWN POWER IN XNJ140E-1 REACTOR

Component	Fraction Of Component Heating At Steady State								
	Time (t) After Shutdown, sec								
	0	1	5	10	50	10^2	10^3	10^4	10^5
Active core (includes fission)	1.0	0.290	0.173	0.123	0.0459	0.0344	0.0176	0.00970	0.00516
Be front reflector	1.0	0.547	0.368	0.308	0.214	1.162	0.0855	0.0427	0.0256
BeO front reflector	1.0	0.572	0.387	0.323	0.226	0.169	0.0887	0.0484	0.0242
Rear reflector	1.0	0.577	0.392	0.330	0.237	0.175	0.0928	0.0515	0.0268
Rear grid plate	1.0	0.685	0.463	0.407	0.296	0.222	0.111	0.0556	0.0370
Shaft	1.0	0.629	0.426	0.361	0.268	0.204	0.102	0.0556	0.0278
Liner	1.0	0.667	0.454	0.388	0.285	0.218	0.109	0.0606	0.0303
Inner reflector	1.0	0.605	0.410	0.345	0.248	0.188	0.0976	0.0524	0.0286
Outer reflector	1.0	0.592	0.398	0.335	0.238	0.182	0.0932	0.0511	0.0268
Pads	1.0	0.297	0.177	0.126	0.0516	0.0387	0.0194	0.00968	0.00548

~~CONFIDENTIAL~~

the reflector. The method used was to sum, at the desired point, the product of the scattering probability (Σ_s) times the average energy loss per collision over the 18 lethargy levels. The absolute heating rate was then calculated by normalizing the energy deposition to the total core power and converting to a heating rate in watts-per-gram per megawatt of reactor power.

The heating caused by (n, α) captures in the borated pressure pads was calculated by determining the number of neutron captures in boron per fission and then converting to watts-per-gram per megawatt of reactor power.

4.4.3 AEROTHERMAL DESIGN

4.4.3.1 Distribution of Cooling-Air

Preliminary investigations of fission heating and secondary heating in reactor components as envisioned during the Advanced Configuration Study indicated that about 6 to 7 percent of the reactor inlet-air would be required for reactor component cooling purposes.^{1*} Soon thereafter, component cooling-air requirements for the XNJ140E engine were established at 8.6 percent with the assumption that estimated nominal heating rates would be realized.

As XNJ140E-1 reactor component design progressed through the early stages and as new estimates of heating rates were received it became apparent that the allotted component cooling-air flow should be revised upward with a corresponding decrease in fuel element cooling-air flow.

The upward revision of component cooling-air flow was associated with "best" predictions of total deposition and distribution of secondary heat within nonfueled reactor components. An inherent difficulty was caused by the fact that precise predictions of component heating were difficult. Hence, it had become the practice to quote the best estimate as a nominal heat rate and then to estimate upper and lower limits assuming the probability was low that heating rates would be greater than the quoted maximum heating rate, or lower than the quoted minimum heating rate. It was the further practice to relate these rates by heating rate factors in such a manner that maximum was nominal times the factor, and minimum was nominal divided by the factor.

Design philosophy was based on the assumption that revisions in the best estimate or nominal heating rate normally occurring during the finalization of a design, and particularly as improved measurements were completed in initial critical experimental mock-ups, would lead to uncertainty estimates falling between the original maximum and minimum heating rates. Hence, it was felt that, early in the design activity, coolant passages should be sized such that, if the true heating rate equaled the original maximum, the available pressure drop would permit enough coolant flow to maintain component design temperatures. If the latest available best estimate, or nominal times the latest heating rate factor, was significantly less than the original maximum, flow restrictors or orifices could be included in the final assembly and sized to allow the coolant flow needed to maintain component design temperatures.

Because an uncertainty in the predictions would still exist at the time of final design, surface temperatures of components would be monitored during the engineering test program using the fully assembled engine. Cooling-air orificing could then be adjusted to give the desired cooling-air flow rates and distributions.

This design approach would result in minimum temperature penalties in the adjusted reactor assembly compared to the performance penalty that would result if the coolant passages had been redesigned to utilize the total available pressure drop without orifices. The film temperature differentials were small compared to the air temperature rises.

*Superscripts refer to the reference lists that appear at the end of each section.

~~CONFIDENTIAL~~

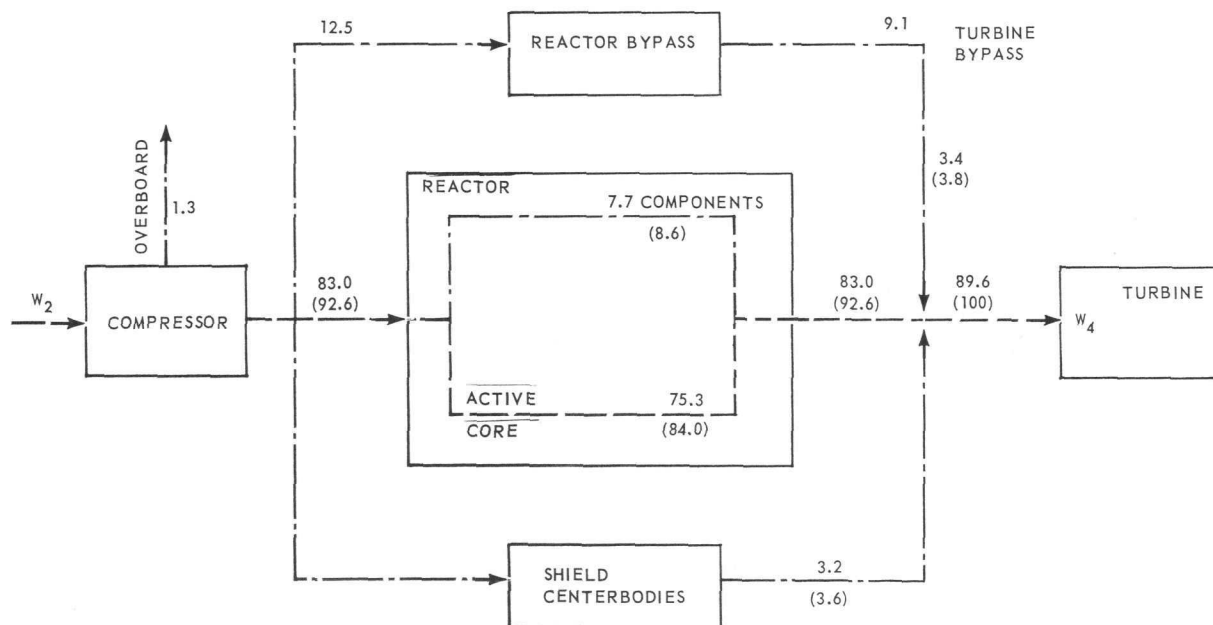
Component cooling-air requirements discussed in the following paragraphs were based on nominal heating rates.

Use of the terms maximum, nominal, and minimum in the rest of this chapter is based upon the above definitions, i. e., as pertaining to prediction uncertainties rather than distributions.

Reference to maximum coolant flows, or coolant flows associated with maximum coolant rates, are not to be interpreted as flow requirements for the purpose of summarizing total flow requirements of the components. Rather, it should be considered as the flow requirement for that component based on uncertainty estimates that existed early in the iterative design process.

Because the predictions of distribution of heating were more uncertain than the predictions of total secondary heating, it was expected that the total coolant flow would approximate that flow associated with nominal heat rates, even though some flow redistribution between the components would be required.

Airflow Distribution in the XNJ140E Engine - A simplified schematic of the cooling-air flow distribution within the XNJ140E engine is shown in Figure 4.15. As shown therein, W_2 is compressor inlet-air flow and $W_{a4.0}$ is turbine inlet-air flow. Eighty-four percent of the turbine airflow rate passed through the active core, and 8.6 percent of the turbine airflow rate was used for secondary component cooling purposes. Figure 4.16 is a more detailed diagram showing all flow paths within the engine. Letter designations of the flow paths, cooling-air quantities expressed as a percentage of $W_{a2.0}$ flow, and pressures at various stations are shown in Table 4.16. Table 4.17 shows reactor component cooling-air quantities expressed as a percentage of $W_{a4.0}$ flow and exit-air temperatures are shown for flight condition d (standard-day cruise flight condition).



1. Numbers enclosed in parentheses are flows expressed as a percentage of W_4
2. Numbers not enclosed in parentheses are flows expressed as a percentage of W_2

Fig. 4.15 - Airflow distribution in the XNJ140E engine

CONFIDENTIAL

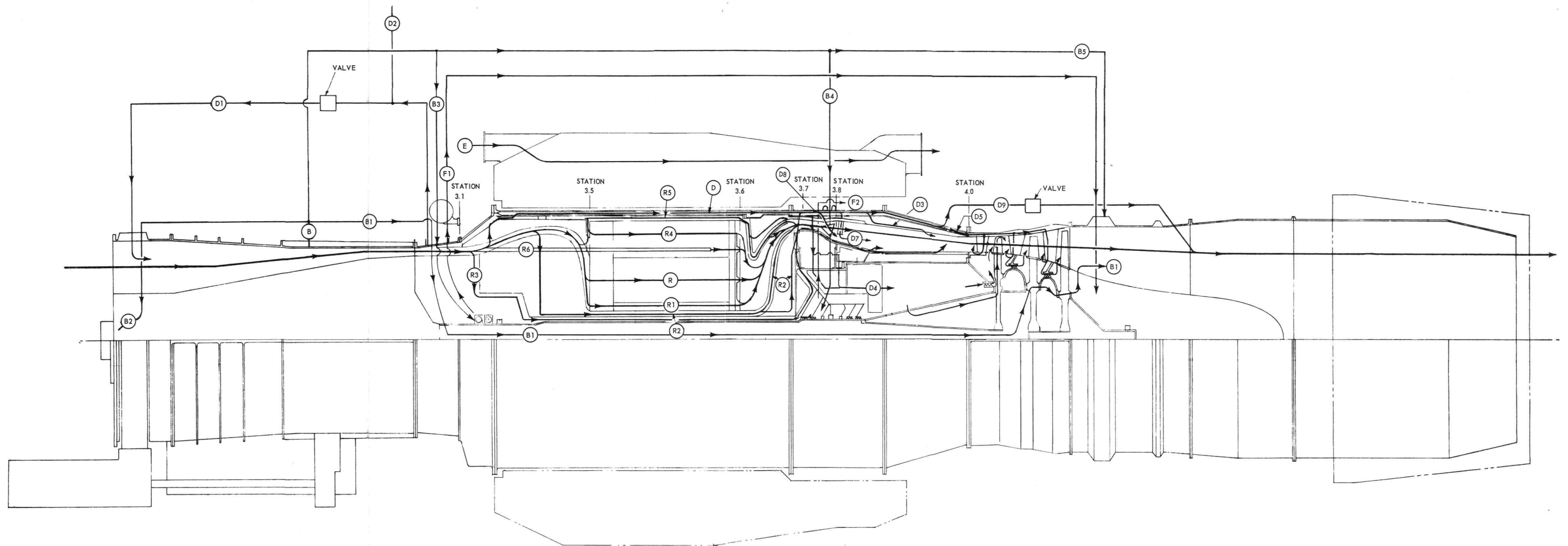


Fig. 4.16 - Cooling airflow paths and pressure stations, XNJ140E engine

CONFIDENTIAL

TABLE 4. 16

NOTES:

- ^a Condition 1: Objective power plant, cruise flight condition.
- ^b Condition 2: Objective power plant, maximum sea-level acceleration. This condition is more severe than any ACT test condition.
- ^c Pressures are given in psia.
- ^d Varies as function of control rod position.
- ^e At retainer plate discharge.
- ^f Upstream of 10 strut fairings.
- ^g Flow path "D" is origin of D1 through D9.
- ^h Intermittent.
- ⁱ This value is for the cooled turbine. For XNJ140E-1, D4 = 1 percent.
- ^j Maximum steady-state bleed-speed control above 90 percent N.

CONFIDENTIAL

TABLE 4.17

REACTOR COMPONENT AIRFLOW DISTRIBUTION AND EXIT-AIR TEMPERATURES

Component	Flow Path Designation	Airflow, lb/sec		Airflow, % $W_{a4.0}$		Exit-Air Temperature, °F
		XNJ140E	XNJ140E-1	XNJ140E	XNJ140E-1	XNJ140E
Fuel elements	R	129.9	123.9	84.0	80.1	1896
Inner reflector	R ₁	1.38	1.39	.89	.9	1240
Outer reflector	R ₄	7.08	6.19	4.58	4.0	1120
Pressure pads		a	1.55	a	1.3	740
Radial springs	R ₅	2.07	2.01	1.34	1.0	740
Control rods						
Guide tubes	R ₆	2.77	2.32	1.79	1.5	1050
Aft-retainer assembly	R ₈	a	2.01	a	1.3	1025
Sub-total		143.2	139.4	92.6	90.1	
Shield central islands and other reactor bypass		11.4	15.2	7.4	9.9	

^aPressure pads and aft-retainer assembly were cooled by a portion of outer reflector coolant-air.

Note: 1. This table is for flight condition d and is based upon nominal heating rates within unfueled components. Temperatures are based upon no heat transfer from active core components.

2. For XNJ140E, $W_{a4.0}/W_2 = 0.896$. For XNJ140E-1, $W_{a4.0} = W_2 = 0.891$.

3. Fuel element power equals 96 percent of total reactor power.

Airflow Distribution in the XNJ140E-1 Engine - Final predictions of airflow distribution in the XNJ140E-1 engine are shown in Figure 4.17. About 80 percent of the turbine airflow passed through the active core; an additional 10 percent was utilized for component cooling. The component coolant flows were based upon the assumptions of nominal heating rates within the components and orificed flow passages.

The 1.4-percentage-point increase in component coolant flow relative to the XNJ140E component cooling flow was caused primarily by the flow requirement of the aft-retainer assembly. This component was cooled with reactor bypass air rather than with radial-spring cooling-air as in the XNJ140E engine. The 4-percentage-point decrease in fuel element cooling-air flow was caused in part by the new flow requirements for the aft-retainer assembly. In addition, engine and shield cooling requirements were increased relative to the XNJ140E requirements. A detailed discussion of XNJ140E-1 reactor component coolant requirements is given in reference 2. Table 4.17 gives a comparison of individual component flows and exit-air temperatures for both the XNJ140E and the XNJ140E-1 engine.

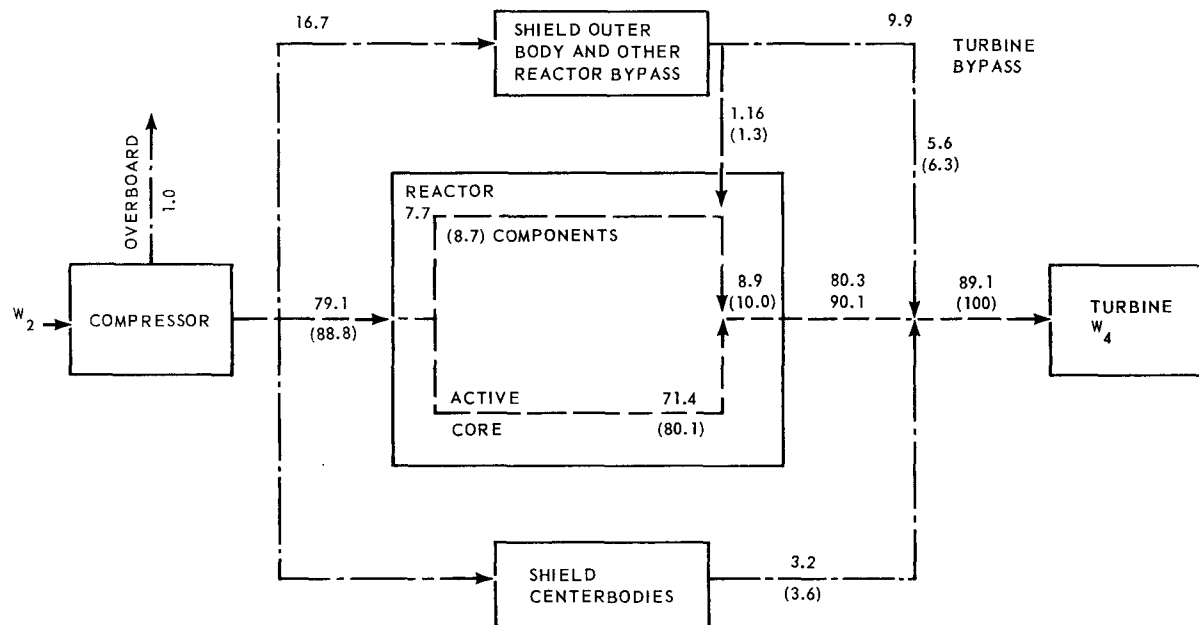
4.4.3.2 Influence of Reactor Design Parameters on Engine Thrust and Fuel Element Surface Temperature

The influence coefficients shown in Figures 4.18 through 4.29 were developed as an aid in estimating the first-order effects of varying one or several reactor parameters. These analyses assumed that, as one parameter was varied, the secondary effects of the change were negligible. For instance, with a change in aft-duct configuration and pressure ratio, no accounting was made of the possibility that the core discharge-air pressure drop might vary as the aft-duct configuration changed. Definitions of the variables used, and base values for which their influence coefficients were 1.0, are given in Table 4.18.

The coefficients given were based upon the S-18 engine cycle and flight condition d, cruise-on-station. The fuel element average-channel maximum surface temperature had a base value of 2210°F. The net thrust base value was 8526 pounds. Engine speed was held constant at 4900 rpm (98 percent N, corresponding to the normal continuous power setting).

CONFIDENTIAL

CONFIDENTIAL



1. Numbers enclosed in parentheses are flows expressed as a percentage of W₄
2. Numbers not enclosed in parentheses are flows expressed as a percentage of W₂

Fig. 4.17 – Airflow distribution in the XNJ140E-1 engine

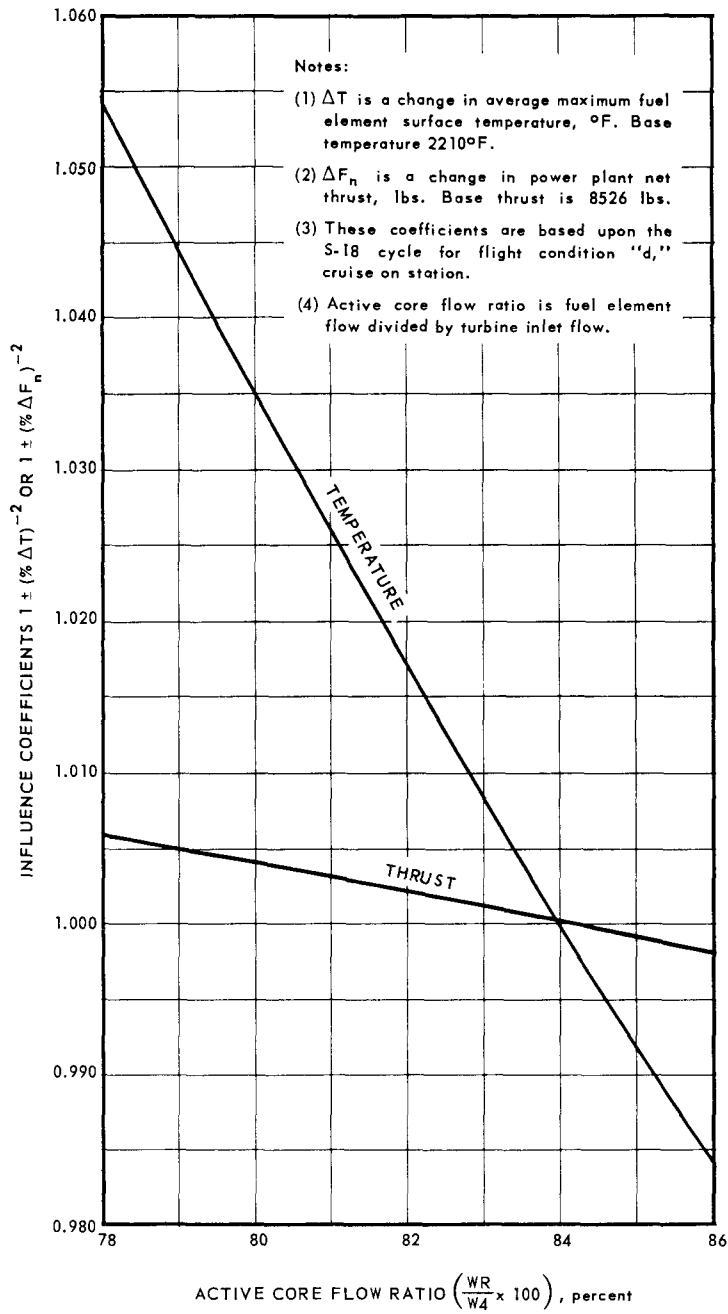
~~CONFIDENTIAL~~

Fig. 4.18—Net thrust and surface temperature influence coefficients for varying active core flow ratio

~~CONFIDENTIAL~~

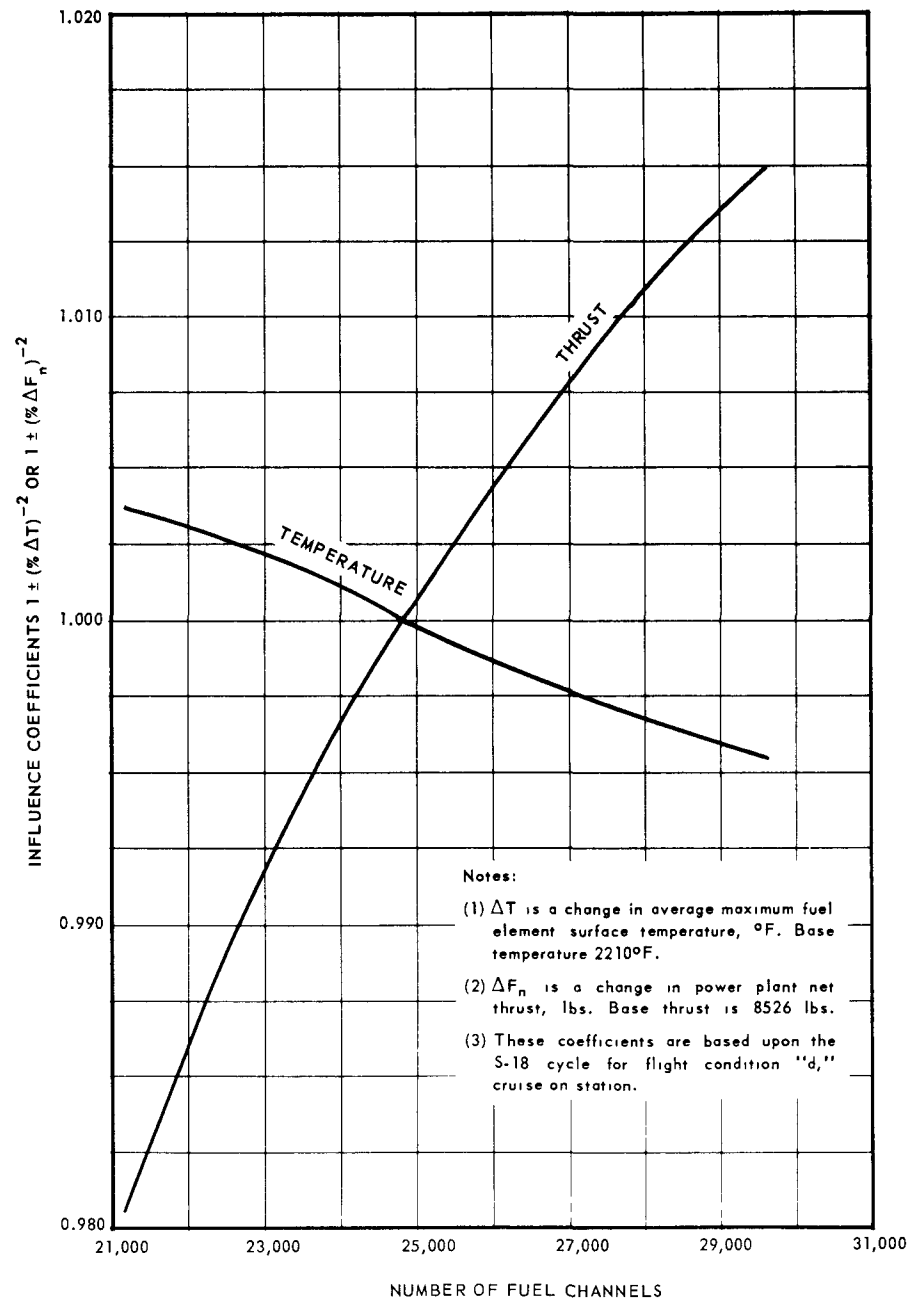


Fig. 4.19 - Net thrust and surface temperature influence coefficients for varying number of fuel channels

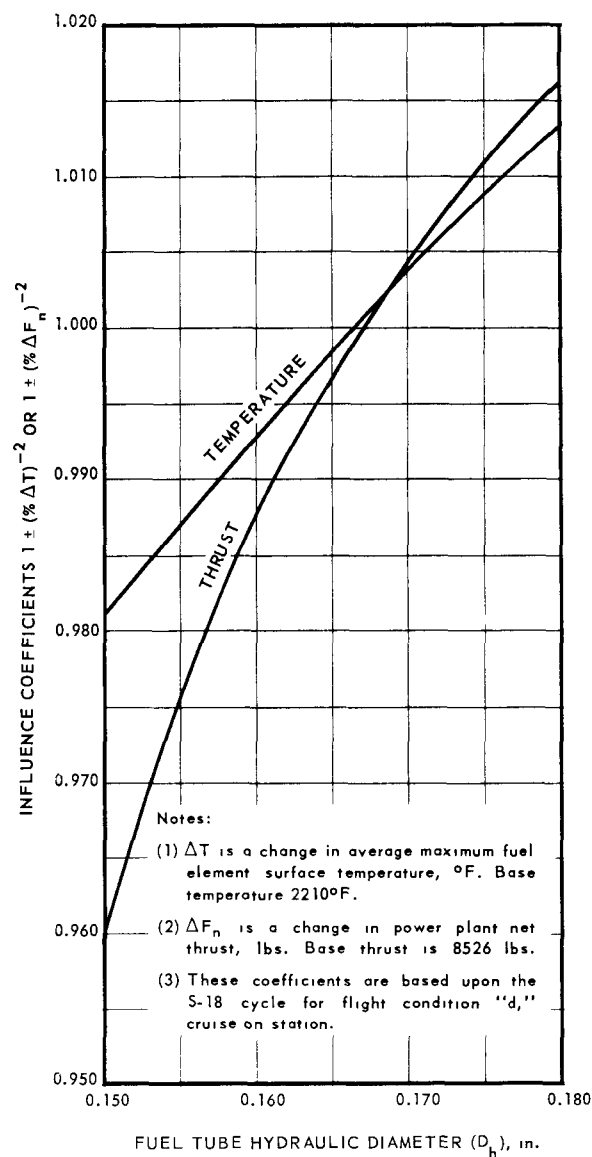
~~CONFIDENTIAL~~

Fig. 4.20—Net thrust and surface temperature influence coefficients for varying fuel tube hydraulic diameter

~~CONFIDENTIAL~~

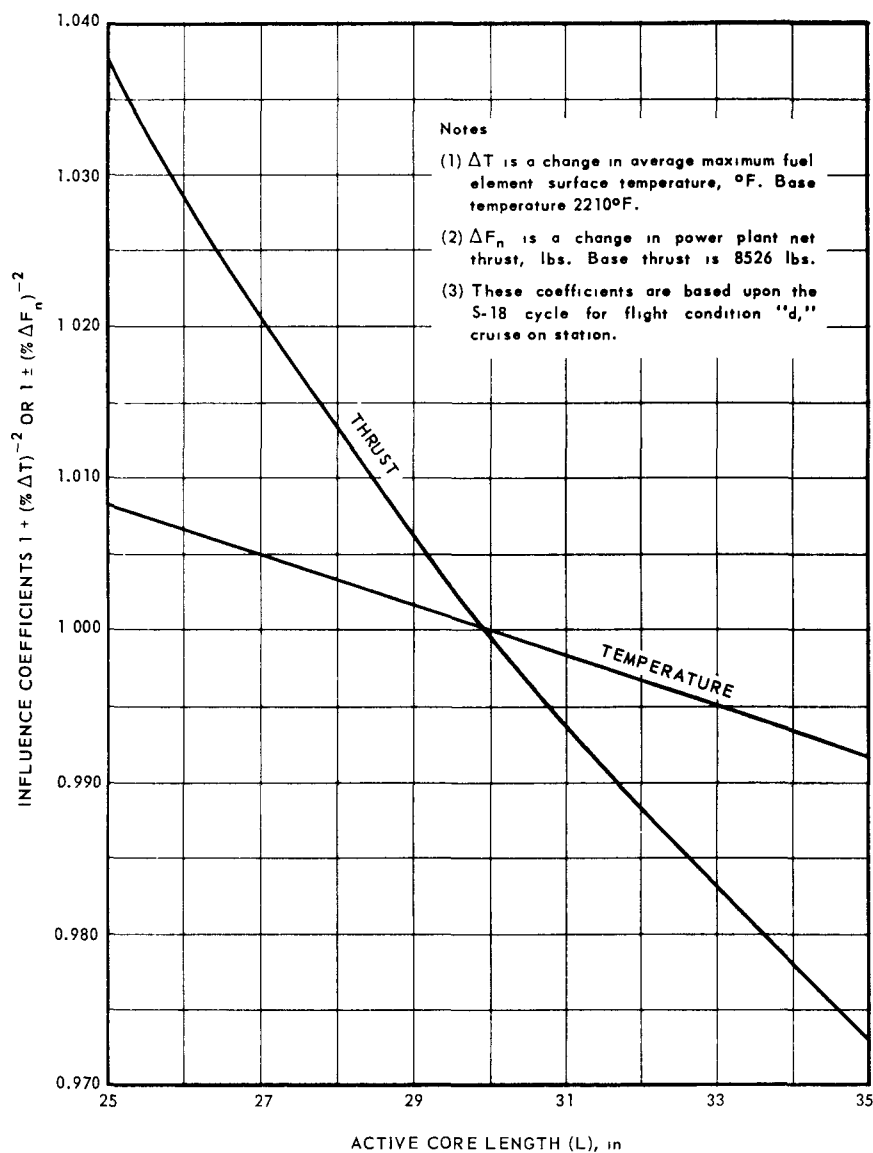


Fig. 4.21—Net thrust and surface temperature influence coefficients for varying active core length

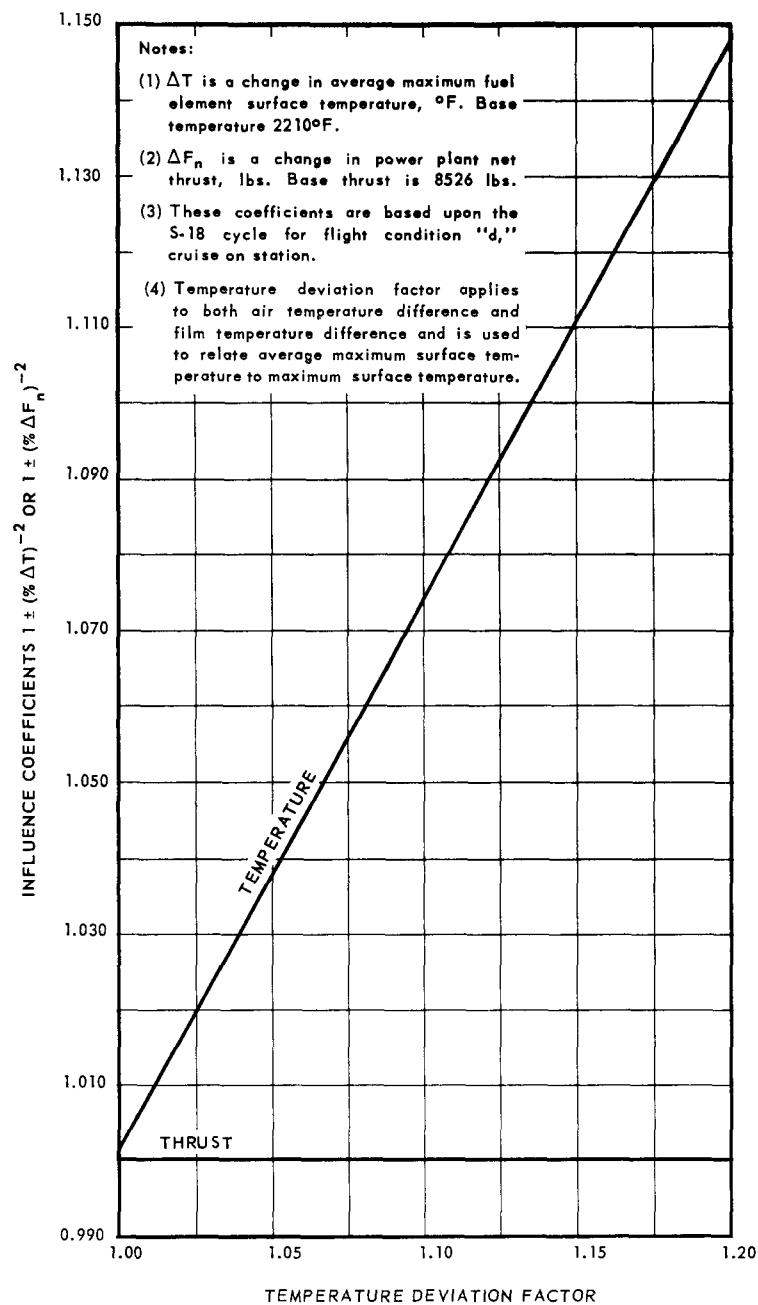
~~CONFIDENTIAL~~

Fig. 4.22—Net thrust and surface temperature influence coefficients for varying temperature deviation factor

~~CONFIDENTIAL~~

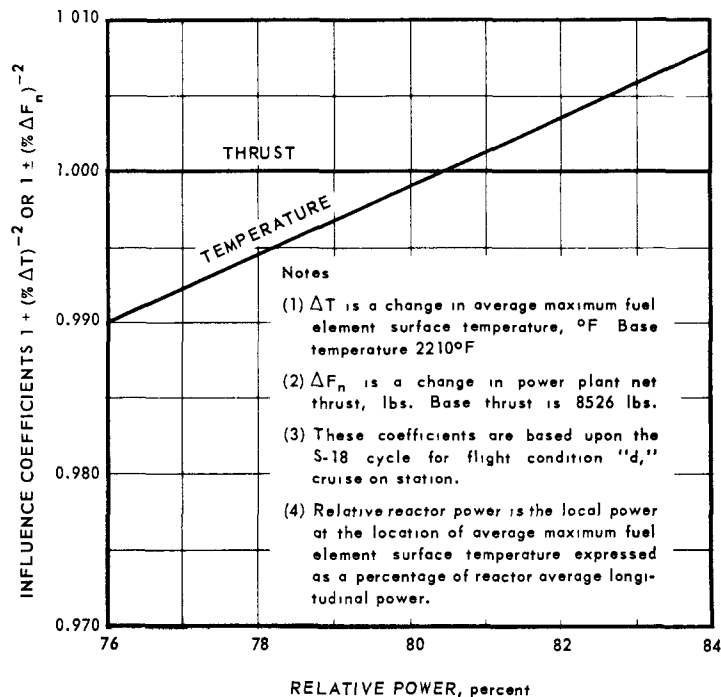


Fig. 4.23—Net thrust and surface temperature influence coefficients for varying relative reactor power

TABLE 4.18
DEFINITION OF VARIABLES AND BASE VALUES FOR UNITY
INFLUENCE COEFFICIENT

Figure No.	Variable	Base Value
4.18	Active core flow ratio ($W_R/W_{a4.0} \times 100$), %	84
4.19	Number of fuel channels	24,881
4.20	Fuel tube hydraulic diameter, in.	0.167
4.21	Active core length, in.	30.0
4.22	Temperature deviation factor	1.0
4.23	Relative power, %	80.4
4.24	Integrated power, %	93.3
4.25	Fuel tube friction factor multiplier	1.15
4.26	Forward duct pressure ratio, $P_{3.5}/P_{3.0}$	0.953
4.27	Aft duct pressure ratio, $P_{4.0}/P_{3.6}$	0.916
4.28	Turbine inlet-air temperature, T_{a4}	1740
4.29	Fuel element power, %	96

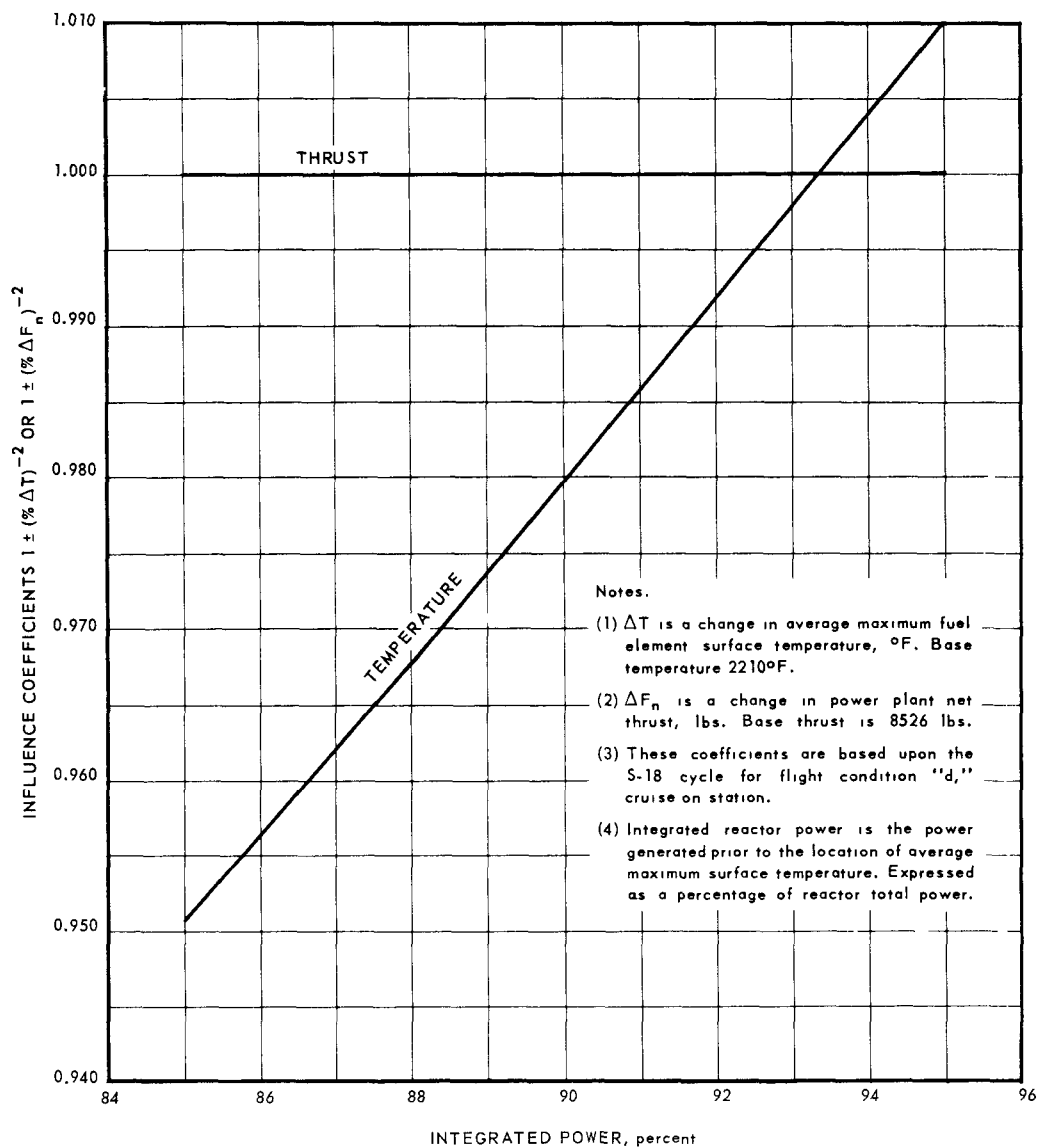
~~CONFIDENTIAL~~

Fig. 4.24—Net thrust and surface temperature influence coefficients for varying integrated reactor power

~~CONFIDENTIAL~~

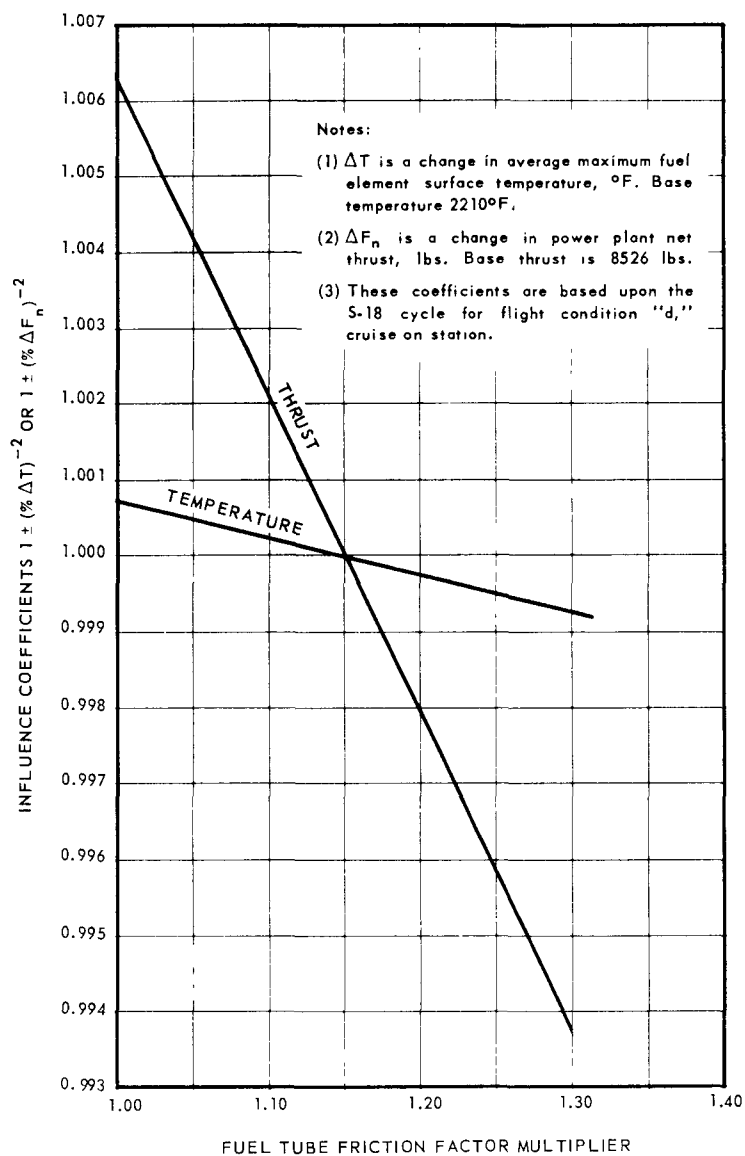


Fig. 4.25—Net thrust and surface temperature influence coefficients for varying friction factor multiplier

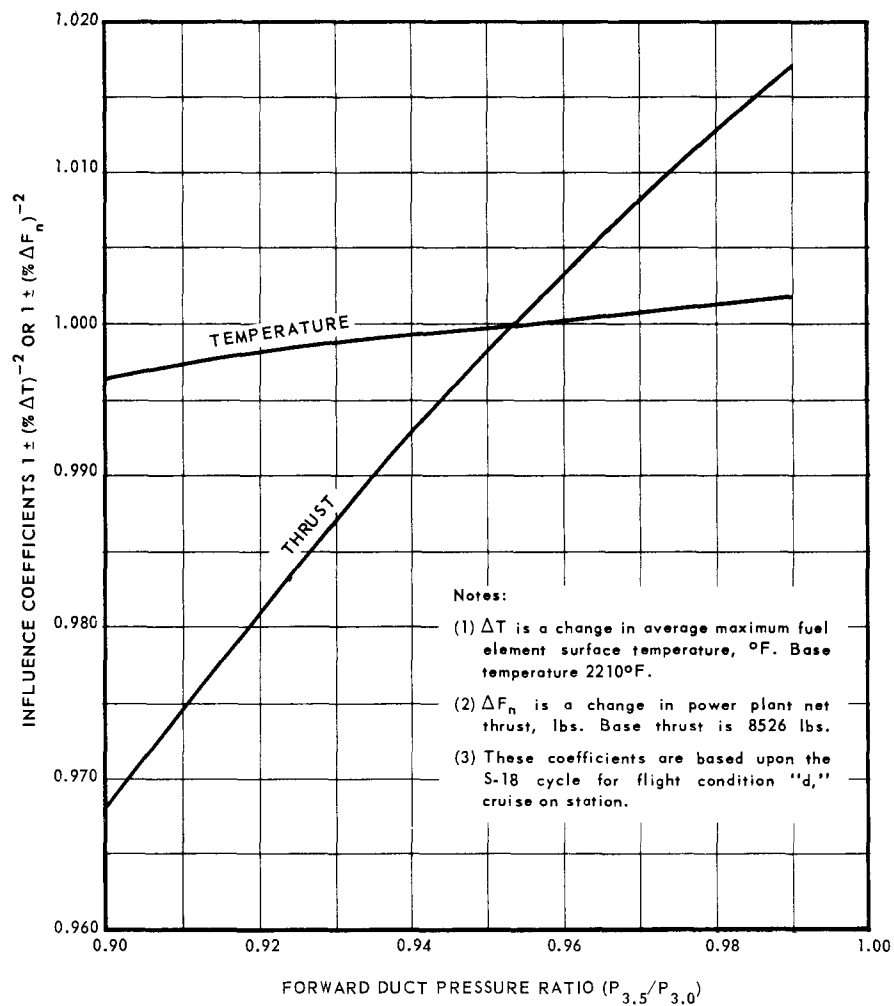
~~CONFIDENTIAL~~

Fig. 4.26—Net thrust and surface temperature influence coefficients for varying forward duct pressure ratio

~~CONFIDENTIAL~~

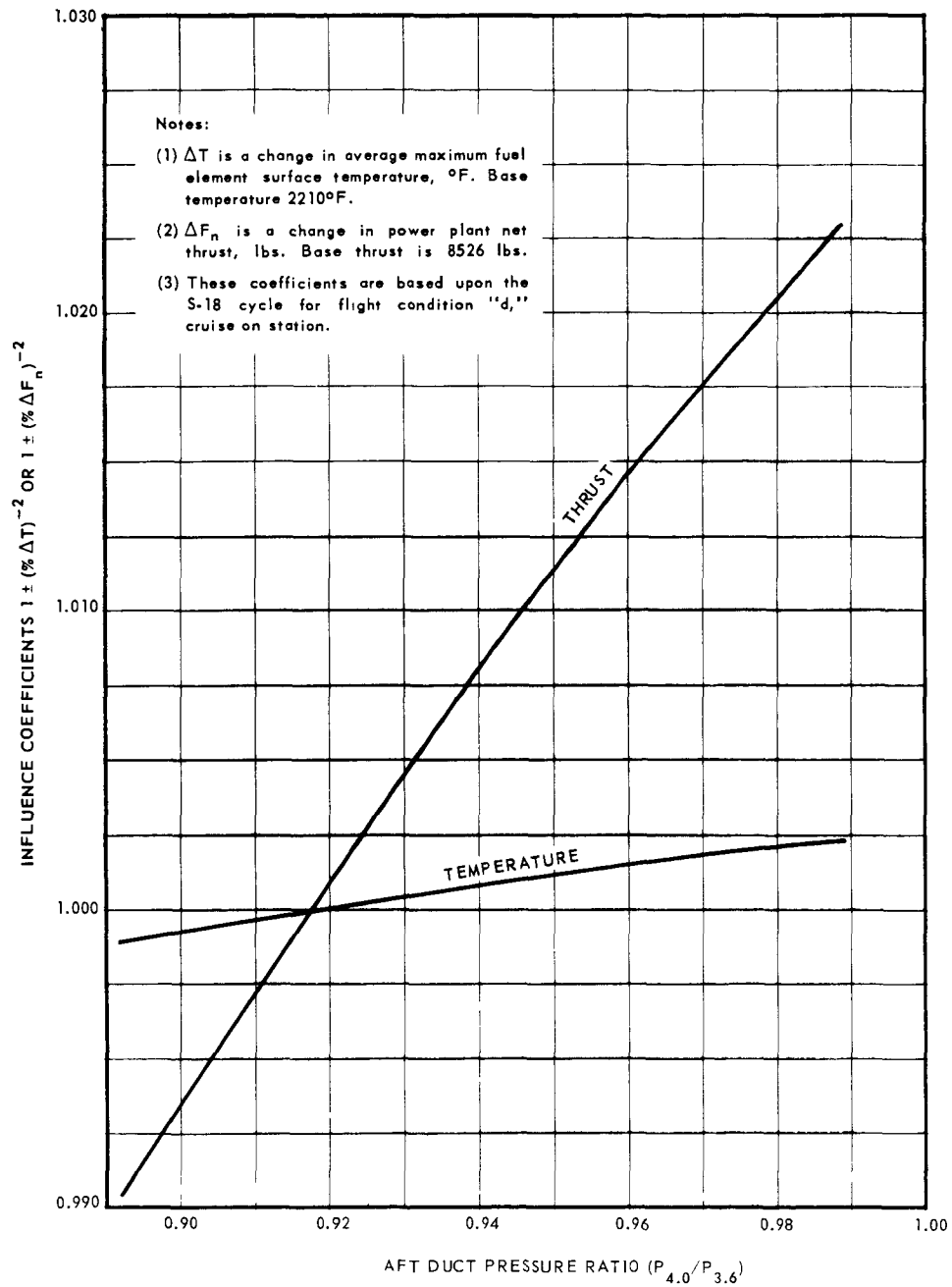


Fig. 4.27 - Net thrust and surface temperature influence coefficients for varying aft duct pressure ratio

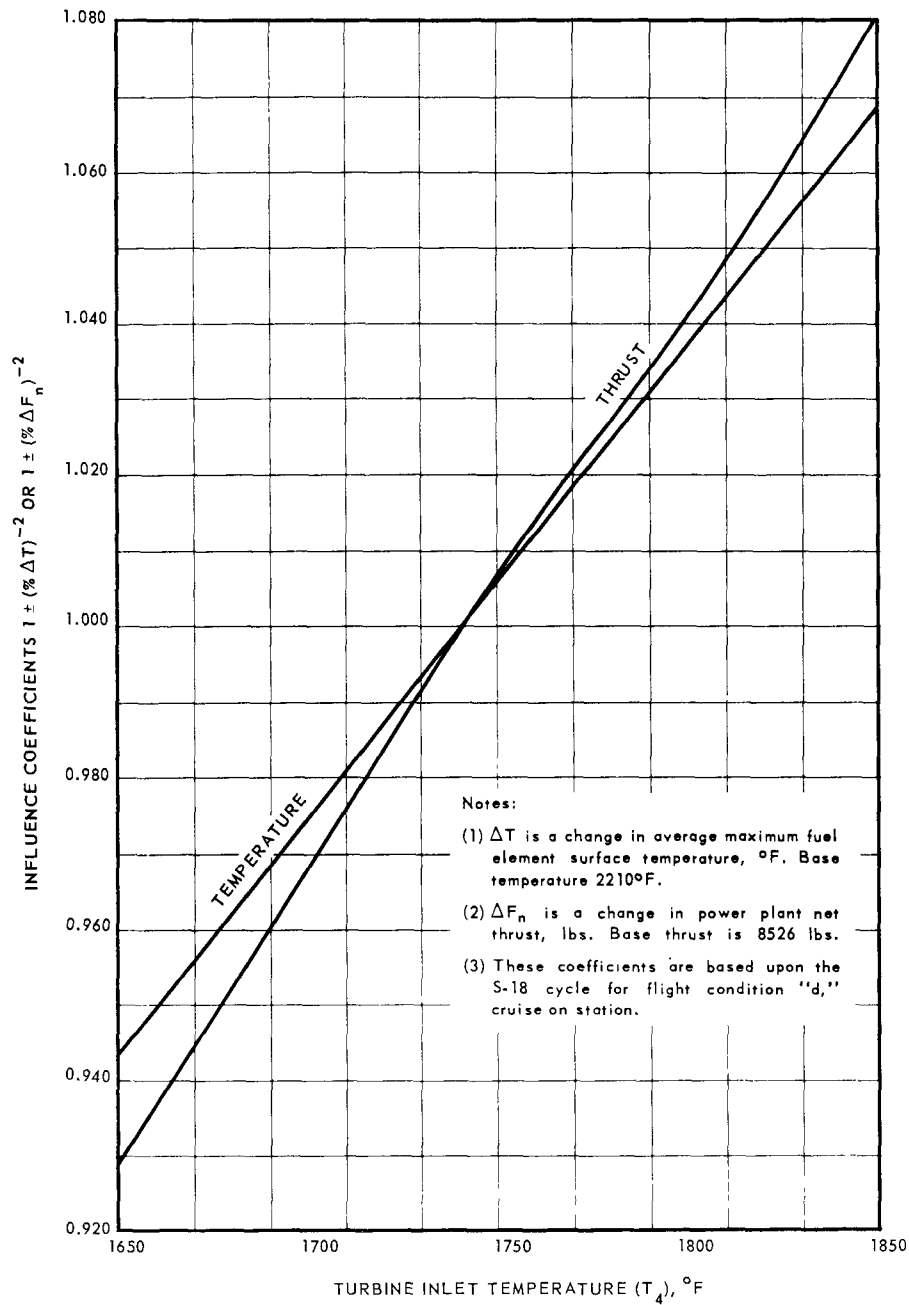
~~CONFIDENTIAL~~

Fig. 4.28—Net thrust and surface temperature influence coefficients for varying turbine inlet temperature

~~CONFIDENTIAL~~

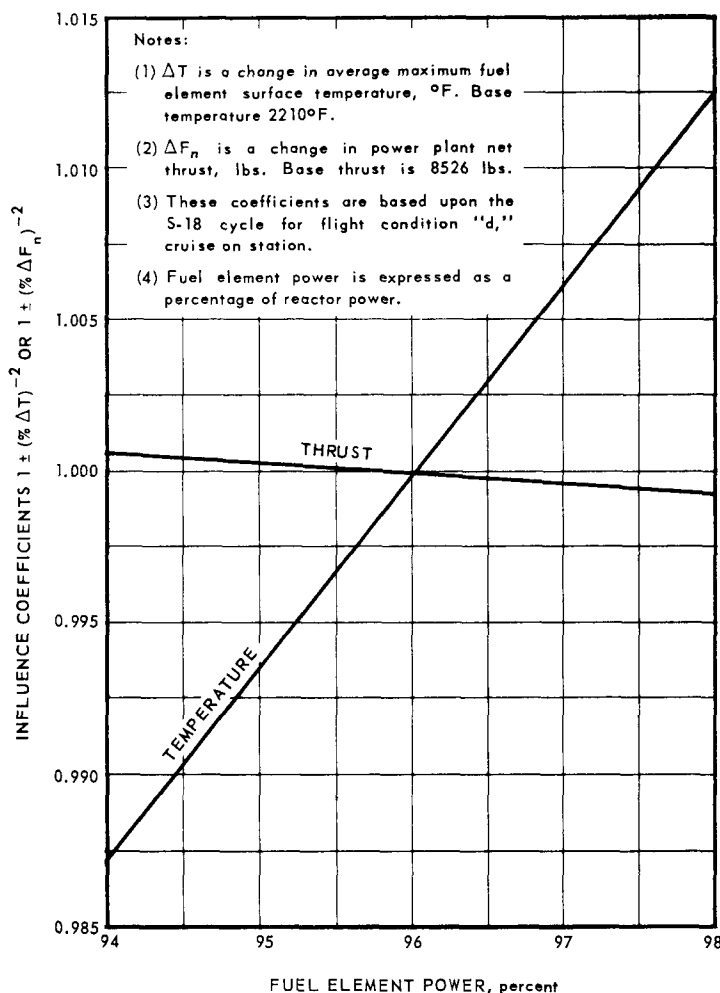


Fig. 4.29—Net thrust and surface temperature influence coefficients for varying fuel element power

Although data shown in Figures 4.18 through 4.29 are valid over the ranges shown, extrapolation beyond these ranges is not desirable. Combinations of trends from two or more curves were sufficiently accurate for preliminary studies of design perturbations.

As an example of the use of these curves, it is seen that the effect on thrust and wall temperature caused by a reduction in hydraulic diameter from the base value of 0.167 inch to 0.150 inch may be found by use of Figure 4.19. The net thrust influence coefficient is 0.960 and the surface temperature influence coefficient is 0.981. These coefficients indicate that the hydraulic diameter variation will decrease the base thrust of 8526 pounds by 4 percent (to 8186 pounds), and will decrease the base surface temperature of 2210°F by 1.9 percent (to 2168°F).

Effects of Variations in Fuel Element Cooling-Air Flow Rate - Table 4.17 shows that the fuel element cooling-air flow rate, W_R , expressed as a percentage of turbine flow, $W_{a4.0}$ was 84.0 for the XNJ140E engine and 80.1 for the XNJ140E-1 engine. Figures 4.30 and 4.31 have been developed to show the effects of these flow variations upon thrust and/or fuel element maximum surface temperature. For a constant surface temperature of 2500°F , Figure 4.30 indicates about 4 percent loss in thrust for the above identified decrease in flow rate from 84.0 to 80.1. This loss applied to XNJ140E engine operation assuming that

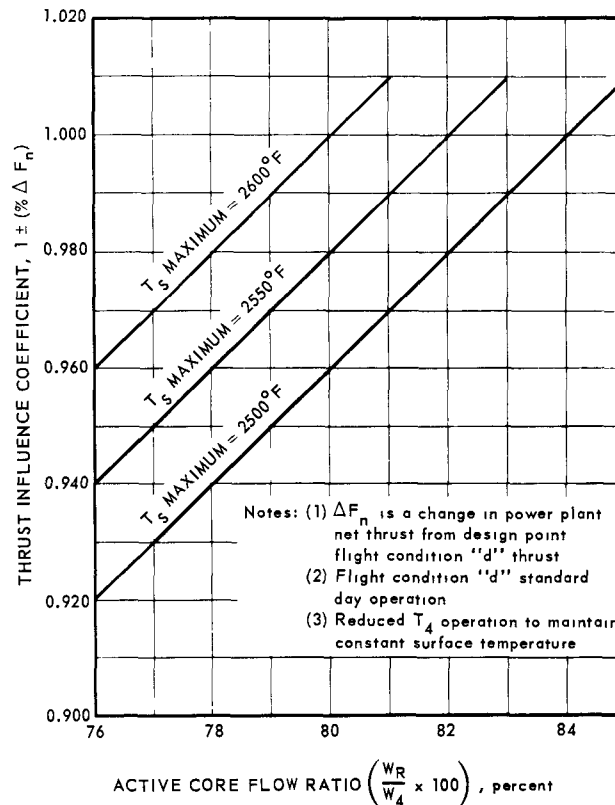
~~CONFIDENTIAL~~

Fig. 4.30—Engine thrust as effected by fuel element cooling-air flow ratio

turbine inlet-air temperature was reduced to 1685°F to offset the increase in fuel element maximum surface temperature resulting from the decreased fuel element cooling-air flow. The required turbine inlet-air temperature with constant fuel element maximum surface temperature and varying core flow ratio are shown in Figure 4.31 for three different operating conditions.

Optimum Thrust - Figure 4.32 shows attainable relative thrust with various combinations of fuel element hydraulic diameter, core flow ratio, turbine inlet-air temperature and core pressure ratio. The XNJ140E reactor (0.167 inch D_h , 0.84 $W_R/W_{a4,0}$, 0.857 $P_{3.6}/P_{3.5}$) is shown as the base thrust level of 1.0. For 0.84 $W_R/W_{a4,0}$, 0.85 $P_{3.6}/P_{3.5}$, and 1760°F T_4 , thrust could be increased about 0.5 percent by lowering the fuel element hydraulic diameter to 0.160 inch and maintaining fuel element maximum surface temperature at 2500°F.

Reduction of Maximum Surface Temperature - Figure 4.33 indicates that the fuel element maximum surface temperatures could be reduced only 10°F below 2500°F for the conditions of 0.84 $W_R/W_{a4,0}$, 0.84 $P_{3.6}/P_{3.5}$, and 1760°F T_4 if the hydraulic diameter were reduced from 0.167 inch to 0.155 inch.

In summary, the reactor design parameters resulted in very nearly maximum thrust and minimum attainable fuel element maximum surface temperature.

4.4.3.3 Generalized Equations for Reactor Pressure Ratio and Fuel Element Surface Temperature

Analytical expressions were developed for predicting reactor pressure ratio and fuel element surface temperatures for various operating conditions, and for various assumed

~~CONFIDENTIAL~~

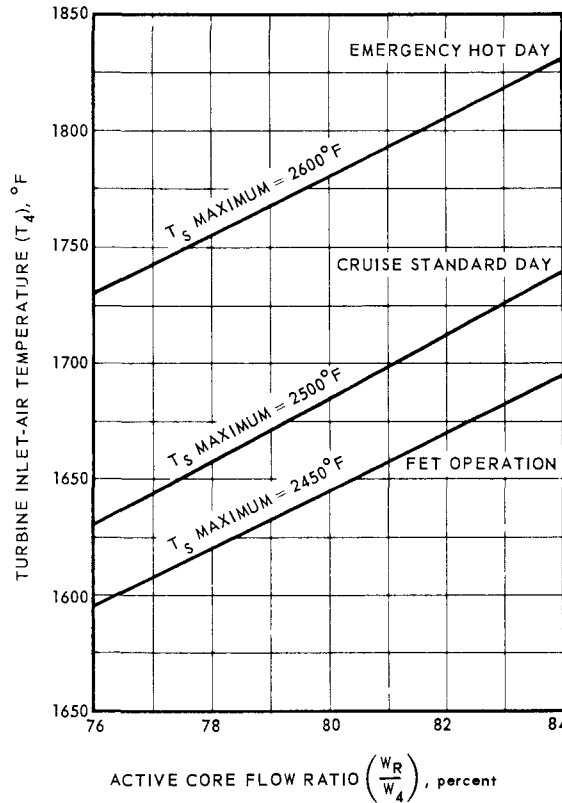


Fig. 4.31 – Required turbine inlet-air temperature for constant surface temperature

fuel element configurations. These expressions were valuable both as means of making quick estimates, and as sub-routines in engine performance decks for parametric studies. The results of one such study were presented as the influence coefficients discussed in the preceding section, 4.4.3.2.

Fuel Element Average-Channel Maximum Surface Temperature - With utilization of basic heat transfer relationships together with reactor power profile characteristics, the following equation was obtained for the fuel element average-channel maximum surface temperature (all temperatures are total temperatures):

$$T_S = T_3 + (T_{3.6} - T_3) (.994A) \left[B + 136.5 \frac{C W_R^{0.2} D_h^{0.8}}{L N^{0.2}} \right] \quad (1)$$

wherein the following symbol definitions apply:

- T_S = Average-channel maximum surface temperature, $^{\circ}\text{R}$
- T_3 = Compressor discharge-air temperature ($T_{3.5}$), $^{\circ}\text{R}$
- $T_{3.6}$ = Fuel element discharge-air temperature, $^{\circ}\text{R}$
- A = Temperature deviation factor for hot-spot predictions
- B = Integrated power at 0.90 core fractional length, percent
- C = Relative power at 0.90 core fractional length, percent
- D_h = Fuel element hydraulic diameter, inch
- N = Number of fuel channels in active core
- W_R = Fuel element cooling-air flow rate, pounds per second
- L = Active core length, inches

~~CONFIDENTIAL~~

- Notes: (1) These curves are based upon the following values:
 Core free flow area, $A_{ff} = 545 \text{ in.}^2$
 Maximum surface temperature $T_{s \text{ max}} = 2500^\circ\text{F}$
 Flow ratio, $W_4/W_2 = 0.896$
 (2) Pressure ratio shown is $P_{t3.6}/P_{t3.5}$
 (3) T_4 is turbine inlet-air temperature, $^\circ\text{F}$

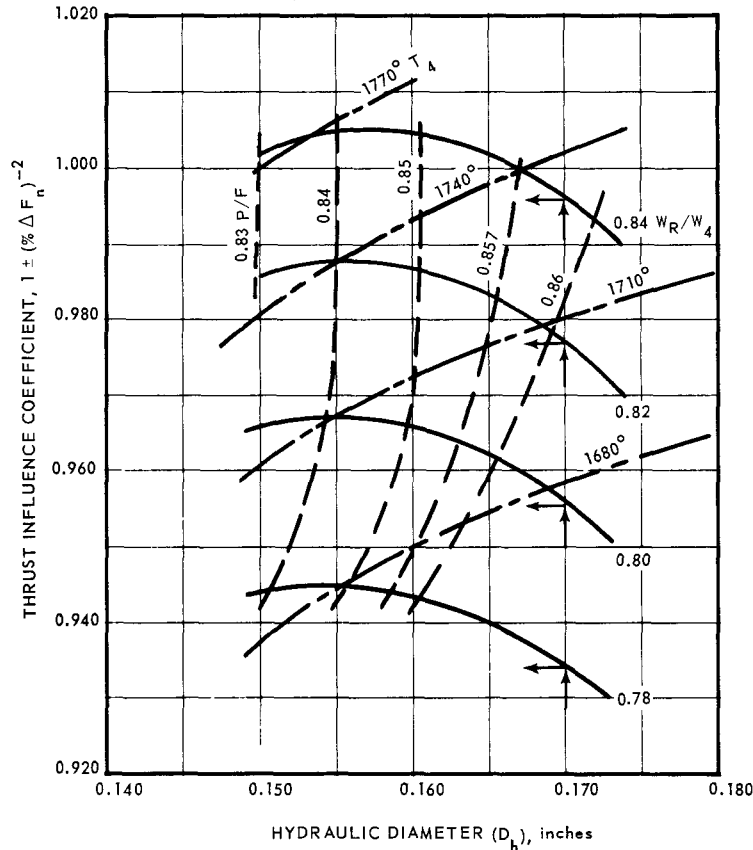


Fig. 4.32—Optimum thrust with constant surface temperature, XNJ140E reactor

When determining the average-channel maximum surface temperature, the temperature deviation factor "A" was 1.0. If maximum surface temperature, $T_{S_{\text{max}}}$, was desired, an "A" value of 1.175 was used.

When the final design values for the several symbols were used, equation (1) reduced to these expressions:

$$T_S = T_3 + (T_{3.6} - T_3)(0.927) \left[1 + 0.1242 W_R^{0.2} \right] \quad (2a)$$

$$T_S = T_3 + (T_4 - T_3) \frac{0.89}{W_R/W_{a4.0}} \left[1 + 0.1242 W_R^{0.2} \right] \quad (2b)$$

based on the following constants

- A = 1.0
- B = 0.933
- C = 0.804
- $D_h = 0.167 \text{ inch}$
- N = 24,881
- L = 30 inches

~~CONFIDENTIAL~~

- Notes: (1) These curves are based upon the following values:
 Core fuel flow area = 545 in.²
 Flow ratio $W_4/W_2 = 0.896$
 Turbomachinery speed, % = 98
 (2) Pressure ratio shown is $P_{3.6}/P_{3.5}$
 (3) T_4 is turbine inlet temperature, °F
 (4) Thrust is constant

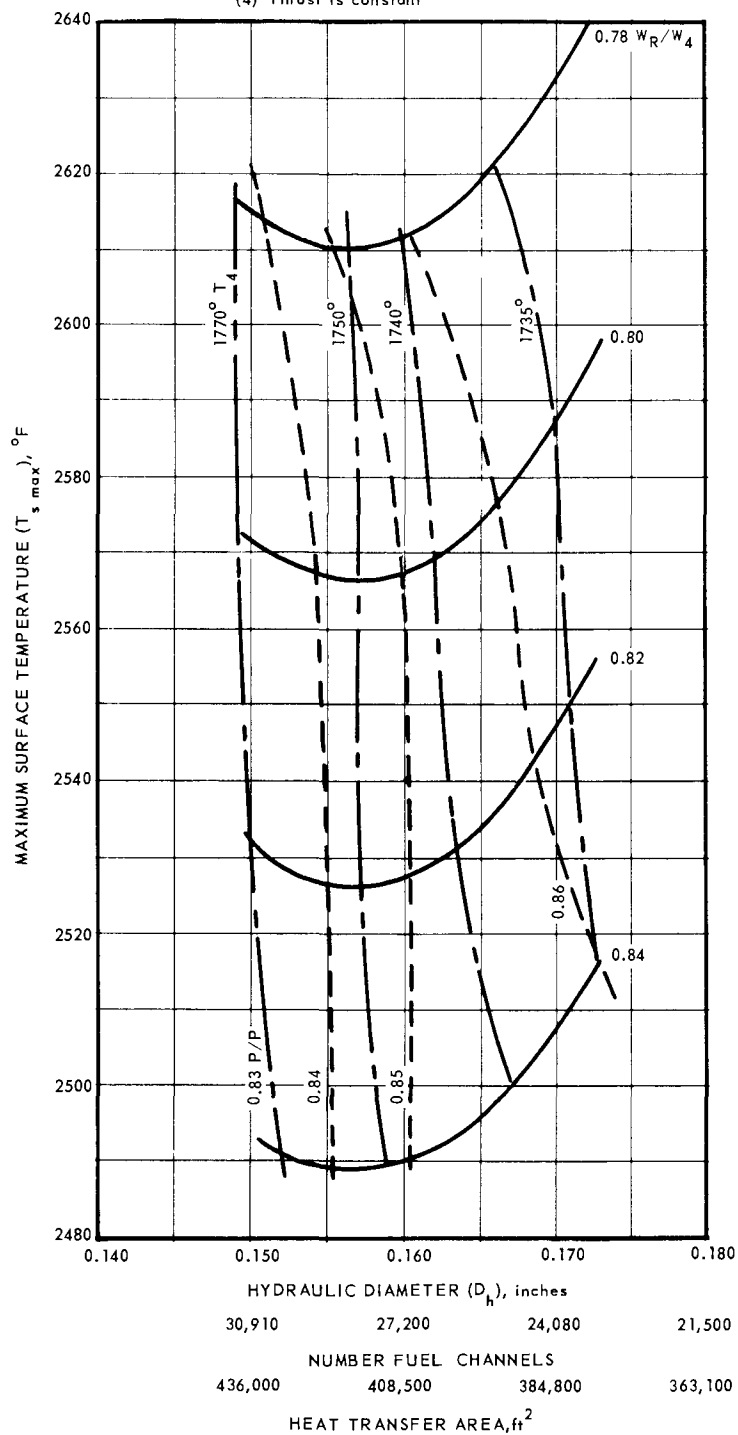


Fig. 4.33 – Required surface temperatures for constant thrust, XNJ140E reactor

~~CONFIDENTIAL~~

To determine the fuel element maximum surface temperature, with $A = 1.175$, equation (2b) reduced to

$$T_{s_{\max}} = T_3 + (T_4 - T_3) \frac{1.047}{W_R/W_{a4.0}} \left[1 + 0.1242 W_R^{0.2} \right] \quad (3)$$

Figures 4.34 and 4.35 are graphical representations of equation (2b) for the XNJ140E-1 reactor.

The above expressions were based on the assumption that the fuel element average-channel maximum surface temperature occurred at the same fractional core distance, namely $0.90 X/L$, regardless of the magnitude of fuel element cooling-air flow ratio ($W_R/W_{a4.0}$), turbine inlet-air temperature, and compressor discharge-air temperature. The percentage of total reactor heat generation delivered to the fuel elements was assumed to be 96 percent in all cases.

Reactor Core Pressure Ratio - Using the compressible flow equation (4) as a basis for pressure ratio determination, and with the aid of several simplifying assumptions, an expression for the reactor core pressure ratio was obtained.

$$dp/p = -KM^2/2 \left(\frac{dT}{T} + 4f \frac{dX}{D} \right) \quad (4)$$

where p represents pressure, $K = c_p/c_v$, M is Mach number, T is temperature $^{\circ}F$, f is friction factor multiplier, X is passage length and D is passage hydraulic diameter.

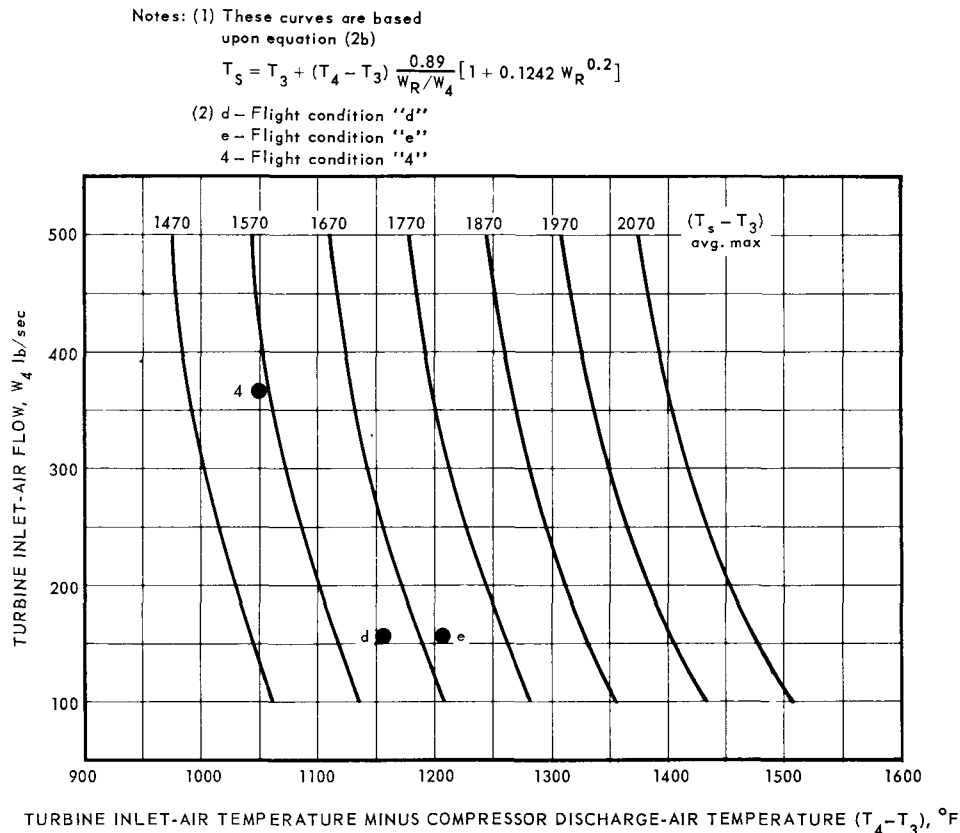


Fig. 4.34—Temperature and flow relationships, XNJ140E-1 reactor

~~CONFIDENTIAL~~

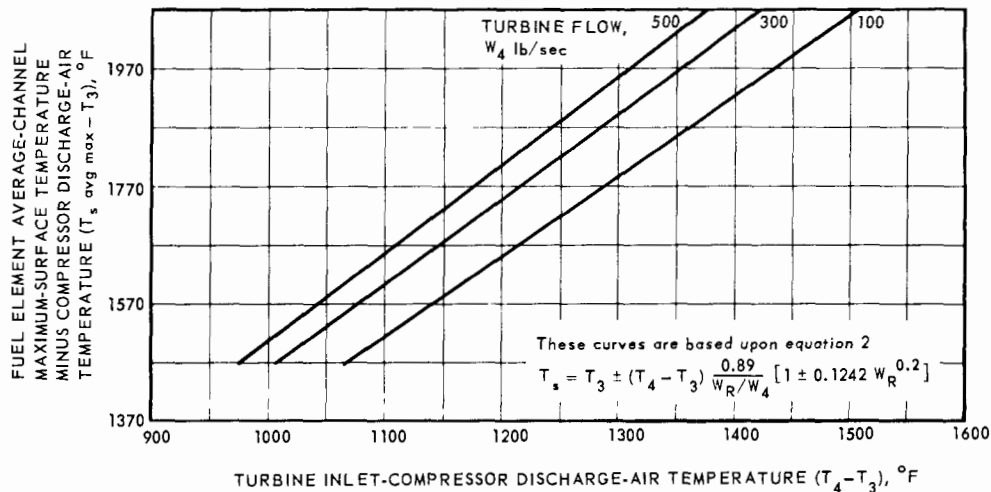


Fig. 4.35—Temperature and flow relationships, XNJ140E-1 reactor

Based on the assumptions that

- Mach number was based upon average values of pressure and temperature along the flow path.
- $\ln (T_{3.6}/T_3) = \text{Constant} \times \ln (T_4/T_3)$
- $T_3 + T_{3.6} = \text{Constant} \times (T_3 + T_4)$
- $f = (1.15) (0.046) Re^{-0.2}$

then, the core pressure ratio, from plenum to plenum, was as follows:

$$\frac{P_{3.6}}{P_{3.5}} = \sqrt{\frac{P_{3.5}^2 - \frac{0.948 W_R^2 (T_3 + T_4)}{(D_h^2 N)^2} \left[\ln \frac{T_4}{T_3} + 0.01385 \frac{N^{0.2} (T_3 + T_4)^{0.136}}{D_h^{0.8} W_R^{0.2}} \right]}{P_{3.5}}} \quad (5)$$

where $P_{3.5}$ and $P_{3.6}$ were forward and aft plenum total pressures, respectively, and other symbols are as defined previously.

Substituting the design point values of

$$\begin{aligned} D_h &= 0.167 \text{ inch} \\ N &= 24,881 \text{ (channels)} \\ W_R/W_{a4.0} &= 0.84 \end{aligned}$$

equation (5) reduces to

$$\frac{P_{3.6}}{P_{3.5}} = \sqrt{\frac{P_{3.5}^2 - 2.885 \times 10^{-5} W_{a4.0}^2 (T_3 + T_4) \left[\ln \frac{T_4}{T_3} + 4.53 \frac{(T_3 + T_4)^{0.136}}{W_{a4.0}^{0.2}} \right]}{P_{3.5}}} \quad (6)$$

These equations for pressure ratio yielded solutions which were accurate for turbulent flow conditions within about ± 0.5 percent. However, at high pressure ratio levels the error in pressure loss was considerable and use of the equation was limited to pressure ratios less than 0.92 when 5 percent accuracy in predicting pressure loss was desired.

~~CONFIDENTIAL~~

Pressure Ratio and Surface Temperature Calculations for Off-Design Operating Conditions - Cycle program decks were based in part upon the reactor-shield assembly design point pressure drop and fuel element surface temperature relationships. Surface temperatures for off-design conditions were determined in the program deck by use of equation (3), above. Pressure ratio calculations for off-design conditions were determined by the following expression:

$$A^3 + A^2 + AM + N = 0$$

$$\text{where } A = \frac{P_{3.6}}{P_{3.5}}$$

$$M = \left[\frac{W_3 \phi \sqrt{T_3}}{P_{3.5}} \right]^2 \left[a \frac{T_{3.6}}{T_{3.0}} + b \right] - 1$$

$$N = \left[\frac{W_3 \phi \sqrt{T_3}}{P_{3.5}} \right]^2 \left[c \frac{T_{3.6}}{T_{3.0}} + d \right] - 1$$

$$\phi = -0.015 + 1.52 (W_3)^{-0.08}$$

$$a = 0.1823 \times 10^{-4}$$

$$b = -0.0350 \times 10^{-4}$$

$$c = 0.2181 \times 10^{-4}$$

$$d = 0.1565 \times 10^{-4}$$

The same accuracy and limitations applied to this equation as for equation (6) above.

4.4.3.4 Utilization of X211-E3 Turbomachinery

During the last quarter of 1960 attention was focused upon means for increasing power plant performance by utilizing the X211-E3 turbomachinery in the S-23A cycle. References 3, 4, and 5 present details of reactor sizing and performance estimates for the modified engine. The S-23A cycle is discussed in section 3.4.3.4.

4.4.4 MECHANICAL DESIGN

Radial and longitudinal cross sections of the XNJ140E-1 reactor were shown in Figures 4.2 and 4.3, respectively. Figure 4.4 showed nomenclature, materials, and operating temperatures of the various reactor components. Design parameters and significant geometric data were shown in Tables 4.5 and 4.1, respectively. Materials and weights are summarized in Table 4.19. The center of gravity of the reactor assembly was located 43.172 inches aft of the front face of the structural shell front flange. The center of gravity of the reactor section, consisting of the reactor assembly and the rear-shield outer section, was located 45.3 inches aft of the front face of the structural shell front flange.

4.4.4.1 Core Definition

The objective of the core definition program was to define the radial and longitudinal dimensional configuration of the tube bundle for various reactor operating conditions. These data were required for design of the longitudinal and radial support systems, the resolution of component alignment between the reactor and the front shield, and aerothermal and nuclear analyses of the reactor. The displacements analyzed by the core definition studies were those produced by manufacturing tolerance stackups, thermal expansions, and mechanical deflections of the loaded tube bundle due to aerodynamic and inertial effects.

The radial dimensional configuration of the reactor was complex in that it consisted of closely packed hexagonal elements. Each element was capable of slipping relative to the surrounding tubes, depending upon the load distributions throughout the bundle. In order

~~CONFIDENTIAL~~

TABLE 4.19
SUMMARY OF MATERIALS AND WEIGHTS OF
XNJ140E-1 REACTOR COMPONENTS

Region	Component	Materials	Quantity	Weight, lb
Inner structure	Tunnel and hub	Inconel X	1	82
	Liner	Inconel X	1	83
Inner reflector	Tubes	Al ₂ O ₃	9,702	497
	Rods	Al ₂ O ₃	22,806	
	Partial rods	Al ₂ O ₃	2,772	
Active core	Fuel tubes	BeO + fuel	176,643	3,011
	Instrumentation tubes	BeO	917	20
	Thermocouples	Pt/Pt-Rh	4,000	20
Outer reflector	Rods	BeO	457,900	4,001
	Tubes	BeO	29,085	
	Partial rods	BeO	24,192	
	Arches	BeO	1,968	173
	Guide tubes	Inconel X	48	54
	Poison tips	Eu ₂ O ₃ , Ni, Cr	48	236
Outer structure	Pressure pads	304 SS + B	48	589
	Springs	Rene' 41	432	842
	Shell and hardware	Inconel X	1	865
	Spring retractors	Inconel X	432	128
	Baffles	Inconel X	216	35
Forward reflector	Transition pieces	BeO	2,306	244
	Reflector structure	Be	12	445
	Outer structure	Inconel	36	31
	Instrumentation cover	Stainless steel	24	32
Aft reflector	Transition pieces	BeO	2,306	244
Aft-retainer assembly	Retainer plates	Rene' 41	12	752
Data instrumentation				300
Total weight				12,424

to determine the dimensions across the bundle the problem was separated into two parts: (1) the determination of the dimensional stackup for tubes whose corners were coincident throughout the entire bundle, and (2) determination of the effects of displacements due to various causes on the over-all dimensions of the assembly. These displacements could be caused by oversizing the core liner, oversizing or undersizing the tubes in specified areas, and nonuniform temperature distributions within the bundle.

The variation of the tube dimensional characteristics (dimension across flats, camber, twist, etc.) prevented contact between all adjacent surfaces of the tubes. This resulted in a stackup somewhat larger than would have occurred if all elements had been perfect hexagons of identical size. Due to these dimensional characteristics, variable void areas were expected to be interspersed between adjacent surfaces throughout the assembly. The problem of predicting the stackup was a problem of defining the extent of these void areas and their distribution in the tube bundle.

~~CONFIDENTIAL~~

Method of Analysis - Since the physical characteristics of the tubular elements were controllable during the manufacturing process, it was advantageous to define a relationship between the tube characteristics and the stackup dimensions. This relationship enabled the prediction of the stackup dimension for a given set of tubes, and also indicated the dimensional control limits required during the manufacturing processes to give a specified assembly stackup.

Due to the complexity of a purely mathematical analysis of the problem, a semiempirical attack was chosen wherein several types of tube assemblies were constructed and measured. Tubes of varying characteristics were used in the assemblies to determine the correlations between the tube characteristics and the assembly dimensions.

Statistical methods were used in the analysis of the experimental data since the measurements followed statistical distributions. For each set of data, the mean and standard deviations of the stackup measurements were calculated or determined using normal probability coordinate paper. Similarly these statistical parameters were determined for each characteristic of a sample group of tubes used in each assembly. The characteristics measured were: (1) dimension across flats, (2) camber, (3) twist, (4) corner angle, and (5) surface finish (in some cases).

Using statistical methods of addition, the distribution of measurements across n tubes was assumed to be described by:

$$\mu_n = n\mu_F + (n-1)\mu_G \quad (1)$$

$$\sigma_n^2 = n\sigma_F^2 + (n-1)\sigma_G^2 \quad (2)$$

where:

- μ_n = population mean of measurements across n tubes
- μ_F = population mean of across-flats measurement distribution of tubes used
- μ_G = population mean interstitial gap between tubes
- σ_n^2 = population variance of measurements across n tubes
- σ_F^2 = population variance of across-flats measurement distribution
- σ_G^2 = population variance of interstitial gap between tubes

The values of μ_F and σ_F were found from the individual tube inspections which were assumed to equal the population parameters. The parameters μ_G and σ_G were more difficult to evaluate and they could not be determined directly. By measuring experimental setups, it was possible to determine X_G for the particular assembly of tubes by:

$$X_G = \frac{X_n - nX_F}{n-1} \quad (3)$$

where

- X_G = sample mean interstitial gap between tubes
- X_n = sample mean measurement across n tubes
- X_F = sample mean across-flats measurement of tubes

By testing several assemblies and determining the relation of X_G and S_G (sample variance) it was possible, when using equations (1) and (2), to define the stackup of any assembly when given the tube parameters and assuming that the sample characteristics equaled the population characteristics (this required that the quantity of samples be large).

The characteristics of the tubes were derived from extensive measurements of the parameters shown in Figure 4.36. Tubes used in these measurements were taken from each typical population.

~~CONFIDENTIAL~~

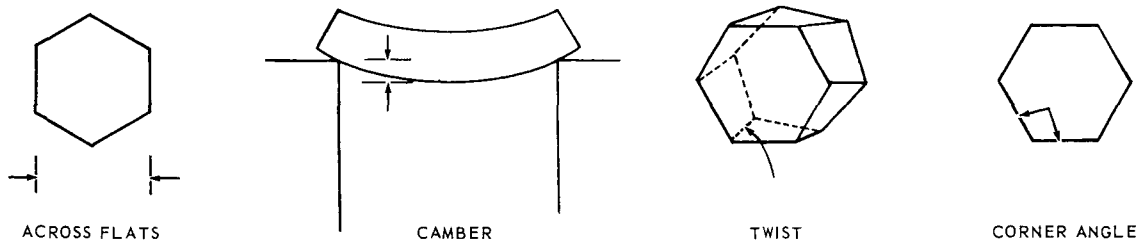


Figure 4.36 - Tube measurements for core definition studies

An analysis of the test data was performed using statistical methods to determine the correlation between the tube characteristics and the over-all dimensional characteristics of the assembly. Specifically, the analysis determined the statistical distribution parameters for the interstitial gap as a function of the distribution parameters of the characteristics.

An equation of the following form was assumed for the correlation of the experimental data:

$$\mu_G = a_0 + a_1 \sigma_F + a_2 \sigma_F^2 + a_3 \sigma_F P \quad (4)$$

where:

a_0, a_1, a_2, a_3 = unknown constants

P = average radial pressure, psi

Data from the various tests were used in the analysis for the coefficients of the assumed equation, equation (4). The analysis produced the following values of the coefficients:

$$a_0 = -0.0013649671$$

$$a_1 = 6.1052021$$

$$a_2 = -1789.7309$$

$$a_3 = -0.025283227$$

Therefore:

$$\mu_G = -0.0013649671 + 6.1052021 \sigma_F - 1789.7309 \sigma_F^2 - 0.025283227 \sigma_F P \quad (5)$$

A critical problem in the reactor design was the alignment of control rod passages in the reactor with those in the front shield. One of the factors was the tolerance stackup across the tube bundle between the core liner and the radial arches which provided the cavities for the control rods. Seventy tubes, flat-to-flat, lay between these two components.

Since production-caliber ceramic tubes were not available, μ_F and σ_F were estimated from past experience in production of ground tubes as 0.2493 inch and 0.00037 inch, respectively. Substitution into equation (5) yielded a value of the mean interstitial gap, μ_G , of 0.000509 inch. The analysis then predicted that, for an average assembly of tubes of characteristics as indicated, the mean of the distribution of the stackup across 70 tubes would be 17.486 inches with a standard deviation of 0.0274 inch. Assuming a normal distribution function, 95 percent of the measurements were expected within the region 17.486 ± 0.054 inch and 99.7 percent were expected within 17.486 ± 0.082 inch.

Another design problem dependent upon the core definition program was the determination of the nominal core liner oversizing for a required contact area between the liner and the inner reflector to prevent arching of the tube bundle around the liner. The aver-

~~CONFIDENTIAL~~

age number of tubes displaced by the liner, flat-to-flat, from the reactor centerline was 26-1/2. By similar analyses the mean measurement and standard deviation across this number of tubes were 6.619 inches and 0.0167 inch, respectively. Neglecting thermal expansion effects, and assuming a liner with a mean radial dimension of 6.619 inches, the expected area of contact was 50 percent (half the measurements from the theoretical axial centerline of the liner to the tubes were expected to be greater than the mean, and half smaller). By the same rationalization, with the liner size increased to 6.636 inches, the expected contact area was 84.1 percent. The nominal liner dimensions were calculated for a minimum of 75 percent contact during reactor operation. This calculation required analysis of the longitudinal expansion profiles of the liner and tube bundle, assuming tangential contact between the tubes. Due to the longitudinal temperature profiles, the total contact area was determined by dividing the length into regions, calculating the average contact area of each region and summing all the regions to obtain the total contact area.

4.4.4.2 High-Temperature Frictional Studies

Coefficients of friction were determined at various temperatures for four different combinations of reactor materials. The materials and test conditions are given in Table 4.20.

Test Procedure - For each combination of materials, ten different determinations were made using a different set of specimens in each determination. The BeO-on-BeO measurements then were repeated using the same ten sets of specimens.

In measuring the friction, the specimens were heated in an electric furnace. The load required to give a surface pressure of 75 psi was applied with weights. A steady, increasing pull was exerted by a gear motor driving a screw. The screw was connected to the moving specimen through a strain ring and a coil spring. A strip chart recorder recorded the pull on the movable specimen. As the coil spring was stretched, the pull on the specimen increased until the force to overcome static friction was reached. At that time the specimen moved suddenly, momentarily decreasing the pull. This sudden drop in force was noted on the recording chart and the value of the force was read from the chart.

Seven such determinations were made in succession at each temperature. After the seven readings at a particular temperature were taken, the temperature was increased to the next value and the process repeated. When the readings at the maximum tempera-

TABLE 4.20

COEFFICIENT OF FRICTION TESTS

Materials Combinations	Temperature Range, °F
Beryllium oxide on beryllium oxide (2 runs)	70-2350
Type 304 stainless steel plus 1 w/o boron on beryllium oxide	70-1400
Fueled BeO ^a on fueled BeO	70-2350
Aluminum oxide on aluminum oxide	70-2350
Note: The maximum contact pressure for all tests was 75 psi which corresponded to the maximum radial pressure expected within the XNJ140E-1 reactor.	

^aStabilized BeO containing 6 wt % UO₂.

~~CONFIDENTIAL~~

ture had been taken, the temperature was reduced, with measurements being taken at selected points on the decreasing part of the temperature cycle.

Test Results - The average coefficients of friction for the four combinations measured during the increasing temperature part of the test are shown in Figure 4.37a. The values for the decreasing temperature part of the test (the Al_2O_3 -on- Al_2O_3 curves are the average of six tests only) are shown in Figure 4.37b. The 1-sigma limit for the maximum spread in the data was approximately 28 percent.

In order to determine whether the differences between the increasing temperature curves and the decreasing temperature curves were repeatable, the BeO-on-BeO measurements were repeated using the same specimens. The fact that the results showed the same general pattern for the rerun indicated that the difference between the increasing and decreasing temperature experiments was a function of the time-temperature sequence used in the tests.

The first reading of the seven values obtained at each condition was called the initial breakaway friction because it was the static friction resulting from the specimen having been under pressure for the time required to increase the temperature to the level for the next test. It was noted that in the higher temperature (900° to 1800°F) region, the breakaway friction was consistently higher than the average of the succeeding six values. In some cases the initial value was as much as 25 percent greater than the average of the remaining values. In the lower temperature region, the breakaway friction was consistently lower, although in most cases the differences were quite small.

4.5 FUEL ELEMENT COMPONENT DESIGN DATA

4.5.1 NUCLEAR DESIGN

Radial power flattening in the reactor core was accomplished by using fuel elements of 17 different fuel concentrations placed in 23 annular regions in the active core. This design was expected to result in the maximum fuel-channel power being about 6 percent higher than the average during any occasion in the design lifetime. The size and composition of the fuel elements provided excess reactivity of about 5.9 percent $\Delta k/k$ as compared to the sum of expected reactivity decrements and the margin for uncertainty of about 5.2 percent $\Delta k/k$.

The fuel element nuclear design was based upon reactivity measurements and U^{235} activation data taken in a mockup critical experiment with theoretically derived corrections for known differences, including temperature, between the critical experiment and the reactor design. Activation measurements were made within a 60-degree sector of the KEYCE. The KEY sector was loaded with fueled BeO tubes in contrast to the enriched uranium foil and unfueled BeO shapes used in the rest of the core.

The fuel element nuclear design specifications reported below were integrated into the aerothermal design of the reactor and were in sufficient detail to have been translated into production orders.

A cross section of the XNJ140E-1 core with the regional variation of fuel concentrations similar to that required to flatten the gross radial power is shown in Figure 4.38. The final fuel concentration specifications for the fuel elements and the inner and outer radii of the equivalent annular regions of the active core were given previously in Table 4.6.

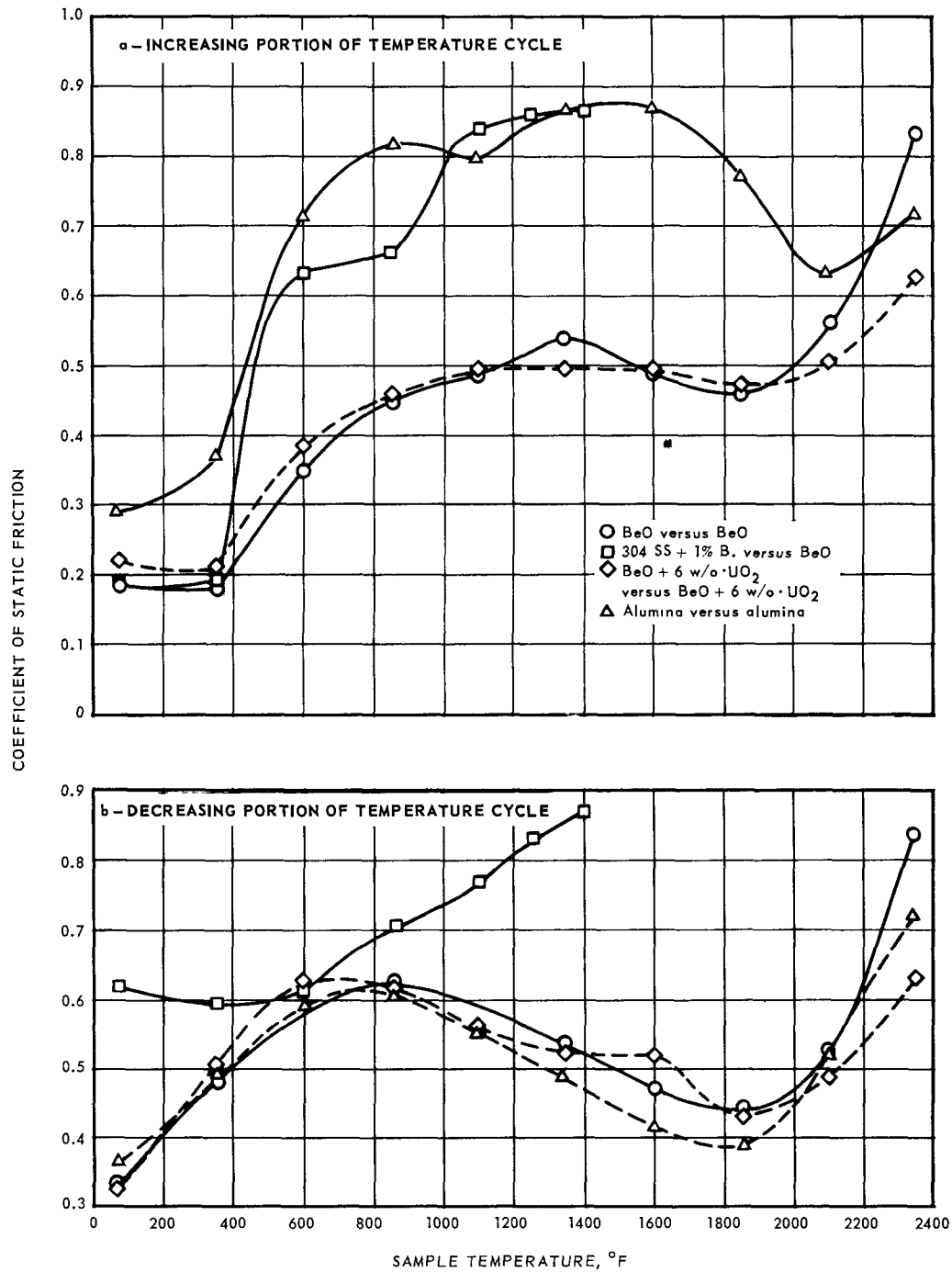
~~CONFIDENTIAL~~

Fig. 4.37 - Coefficient of static friction of reactor materials in air and 75-psi nominal pressure

~~CONFIDENTIAL~~

The adjustment of power throughout operating life to produce minimum fuel element temperatures required a number of nuclear and aerothermal iterations. It was desired to limit the maximum power in the outer fuel channels for the rods-withdrawn condition to the same maximum power that occurred in the inner fuel channels for the rods-inserted, hot, clean condition. Control rod insertion to 15 inches in the hot, clean condition resulted in a perturbation of the longitudinal power profile that was pronounced in the outer fuel channels but was relatively unnoticed in the fuel channels near the inner reflector.

As the rods were withdrawn the integrated power in the outer channel increased and the longitudinal power perturbation was reduced. When the rods reached the position corresponding to the hot, dirty condition (0-inch insertion), the longitudinal power profile was similar to that in the inner fuel channels. At this time the maximum fuel element surface temperatures occurred in the outer fuel channels. To minimize the effect of longitudinal power perturbation on the fuel element maximum surface temperature, fuel content was adjusted radially so that the total (integrated) power along the length of any fuel channel did not exceed a calculated maximum value in any radial position at any time in the core lifetime. The maximum perturbation in radial power resulting from this design was approximately 6 percent greater than the core average. Figure 4.39 shows gross radial profiles for the fuel concentrations specified in Table 4.6 and Figure 4.38.

4.5.1.1 Reactivity Requirements

To meet operational requirements, it was necessary to establish a fuel-matrix volume fraction and a core diameter that provided sufficient excess reactivity and, at the same time, resulted in fuel element dimensions which maintained fuel element temperatures within design limits. For a fixed maximum fuel concentration and specified performance objectives, core diameter was the only parameter that could be varied to adjust installed reactivity. Varying core diameter changed the distance across flats of the fuel element, the total number of tubes in the core, or both. Consequently, if the core diameter were fixed and a reactivity adjustment became necessary, it could be accomplished only by a change that would also affect engine performance, e.g., a change in the fuel element inside diameter, D_h . The required excess reactivity not only determined fuel element dimensions but also influenced fuel distribution because of the effect on control rod insertion depth.

Control of the reactor by axial movement of control rods located in the outer reflector resulted in a perturbation of the longitudinal power profile which was nonuniform as a function of radial position. When the control rod bank was inserted to 15 inches, the longitudinal power near the inner reflector showed only a slight perturbation from the zero insertion profile, although the rod bank influence was strong near the outer reflector. As the rod bank was withdrawn the longitudinal power shape in the outer channels approached that near the inner channels. The effect of control rod movement was to change the average power in a fuel element channel, and the power change was greatest in the channels near the outer reflector. Consequently, the gross radial power curve was a function of the excess reactivity held by the rod bank and this reactivity varied over core lifetime, due to rod movement, to compensate for fuel depletion and fission-product poison buildup.

The total rod bank worth did not affect significantly the gross radial power. Increasing the total bank worth would have confined the longitudinal power perturbation to a shorter length. Since the maximum fuel element surface temperature early in life occurred in the central region of the core where longitudinal perturbations were small, and occurred late in life in the outer core region after the rods were withdrawn, the design was relatively insensitive to total rod bank worth.

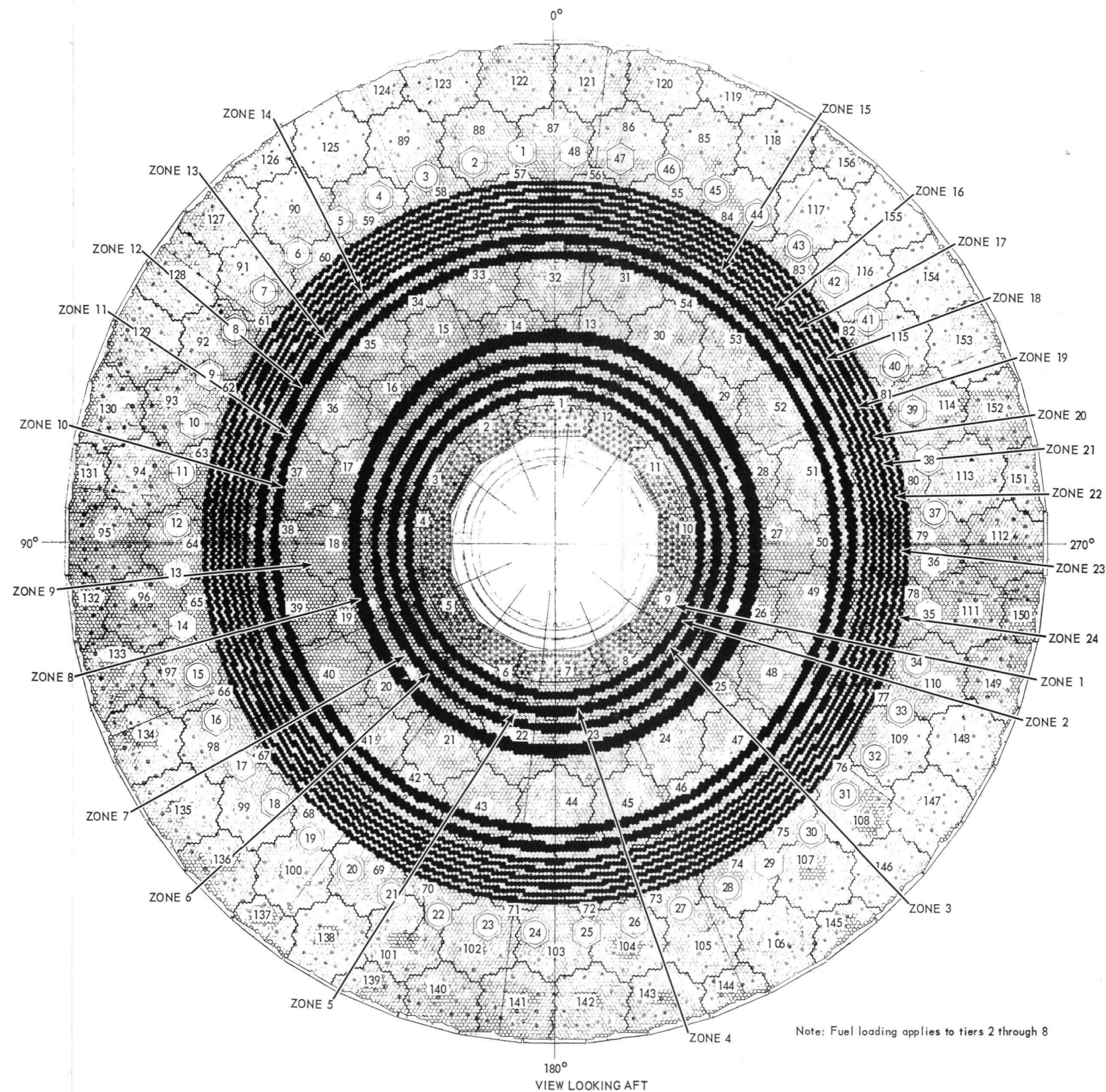
~~CONFIDENTIAL~~

Fig. 4.38—Layout map—fuel loading of the XNJ140E-1 reactor

~~CONFIDENTIAL~~

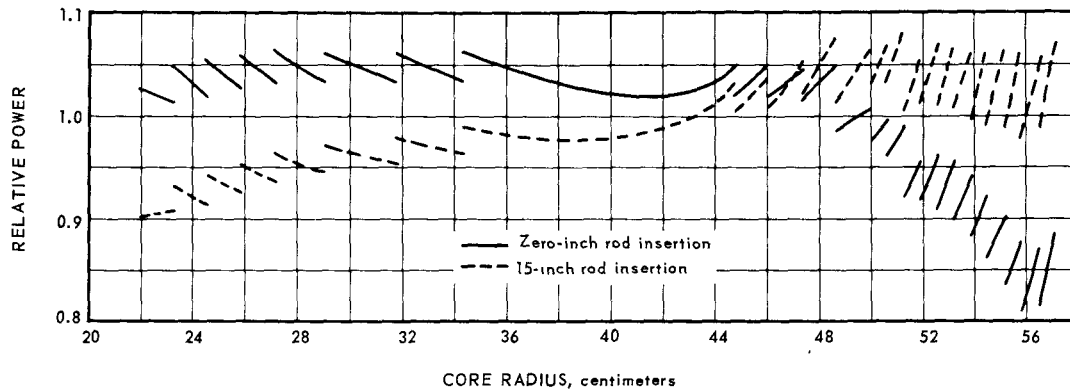


Fig. 4.39 - Gross radial power profile for two control rod insertion lengths

In order to achieve the desired gross radial power flattening, the fuel concentrations were varied across the core. The lowest fuel concentrations were those near the outer reflector. To obtain nearly uniform power distribution during core lifetime, those regions with the lowest fuel concentrations would have undergone the highest percentage loss in fuel content with an attendant drop in power as operating time increased. Also, the difference in neutron energy spectra in the various radial regions produced a nonuniform fission-product poison concentration that affected the radial power profile. The combination of these effects is shown in Figure 4.40.

4.5.1.2 Critical Experiment

The objectives of the critical experiment power mapping and reactivity measurement program were to predict the fuel loading and zonal distribution that would meet the performance requirements. The measurements were designed to determine: (1) the change in longitudinal power profile and changes in gross radial power with control rod move-

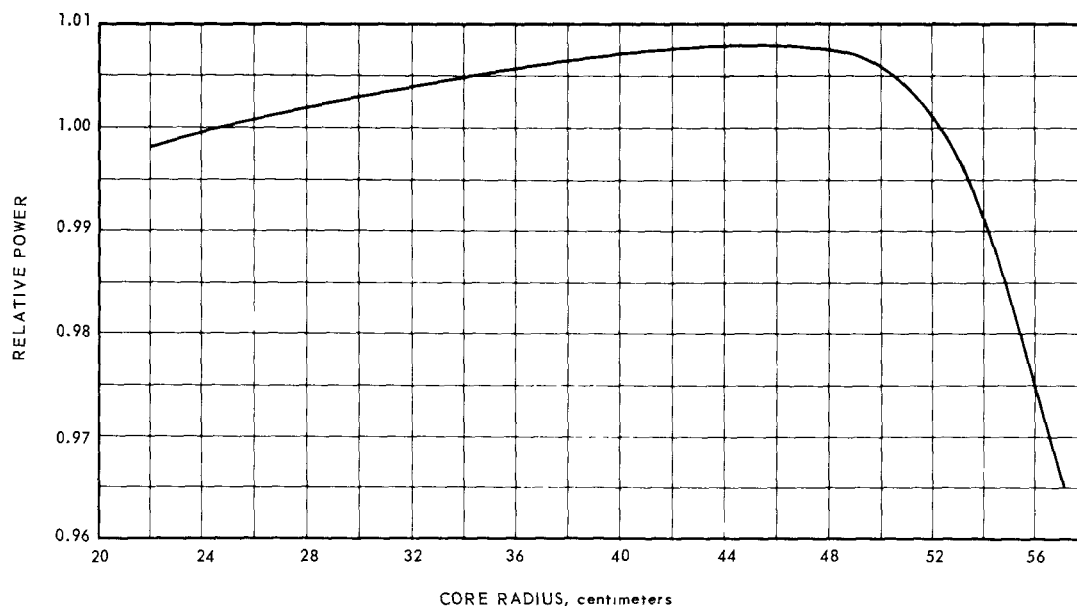


Fig. 4.40 - Change in gross radial power resulting from fuel depletion and poison buildup after 55,000 megawatt hours operation, XNJ140E-1 reactor

CONFIDENTIAL

ment, (2) the magnitude of circumferential power scalloping due to control rods, (3) the power-peaking influence of the inner and outer reflectors, and (4) the distribution of fission density resulting from a radial variation of fuel concentration.

Mockup Description - The XNJ140E-1 critical experiment, Figure 4.41, consisted of a gross mockup containing slabs and tubes of BeO and metallic uranium foil with an insert (KEY sector) in which the reactor design was closely approximated. The features of the KEY sector were:

1. Fueled BeO tubes were used.
2. Nine europium oxide control rod mockups were used in the sector.
3. Pressure pads, pressure vessel, aft-retainer assembly, side shield, and control rod guide tubes, made of design materials, were used.

The KEY sector and its testing are described in reference 6.

Measurements were made by irradiating small (0.9 inch x 0.035 inch diameter) calibrated uranium dioxide-nichrome wire segments. The fission-product beta activity was counted and adjusted to activity-per-unit mass of U^{235} . Three types of measurements were taken: (1) fine longitudinal, using 17 or more wire segments; (2) gross longitudinal, using 6 segments; and (3) single point measurements, 1 segment, each, placed at planes 5.75 inches and 14.5 inches from the front reflector-active core interface. Measurements were made with the rod bank at 12.25, 10.75, 5.0, and 0 inches rod insertion.

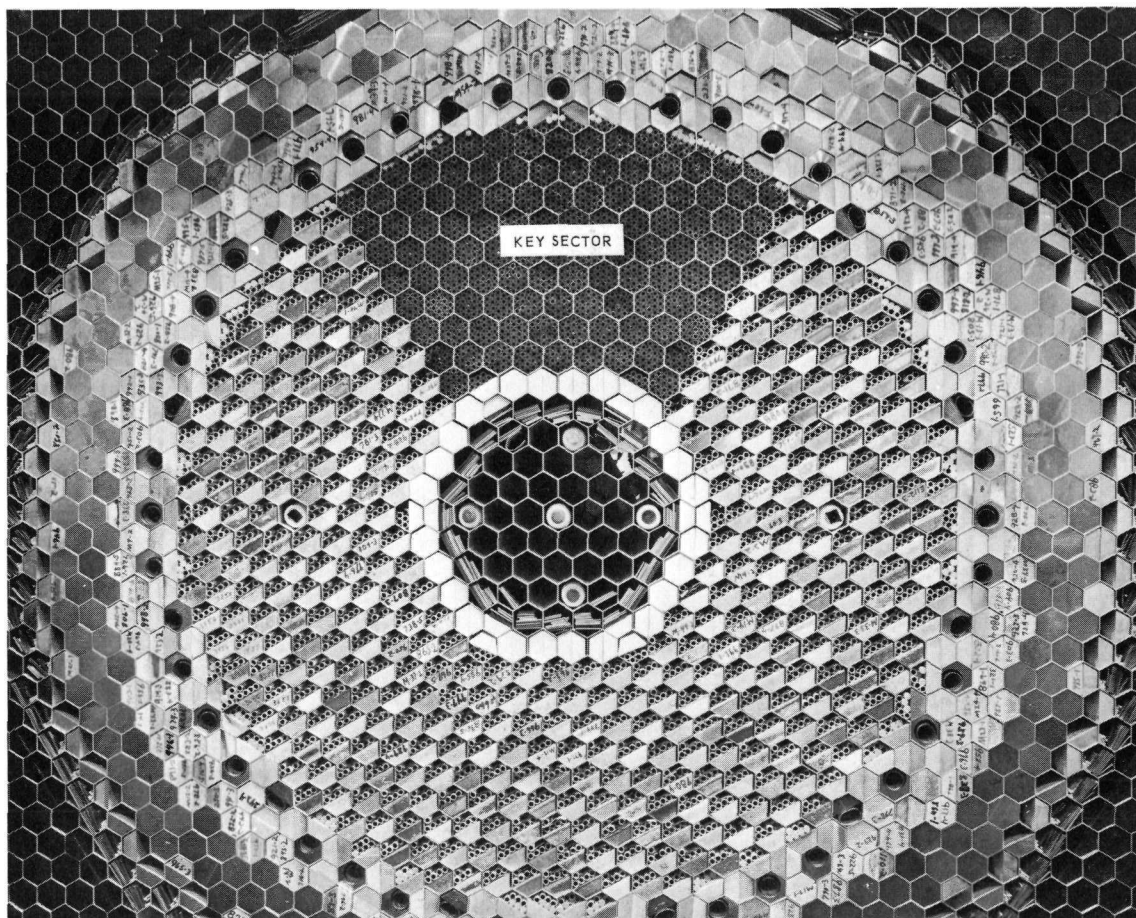


Fig. 4.41 - XNJ140E-1 critical experiment assembly (C23623)

CONFIDENTIAL

2

Measurement Precision - After the majority of the power measurement data was accumulated, the data were analyzed statistically and showed, for single point measurements, a precision of ± 11 percent for a 95 percent confidence interval. Two methods were used to determine the measurement precision. The first method was based on the concept of using the range as an estimate of the standard deviation, and the second method utilized a least-squares fit to a fine longitudinal power map, using the goodness-of-fit of the measured points to the generated curve as an estimate of the scatter of the single point measurements.

When the measurements program was terminated, a study of power-mapping precision was conducted. This study concluded that the measurement of the integrated power in a fuel channel containing 16 wire segments had a fractional standard deviation of 2.5 percent for a 95-percent confidence interval. The precision for single point measurements was 8 percent for a 95-percent confidence interval.

Supporting Analysis - The translation of fission flux curves measured in the critical experiment to power distributions which would exist in the core required a number of adjustments. It was necessary to correct for differences in material between the design and the experiment, for differences in temperature, and for self-shielding in the wire segment. Changing regional fuel concentrations to adjust power resulted in a change in the shape of the radial fission flux curve due to changes in the attenuation characteristics of the various core regions.

Starting with a configuration in which the power distribution was known (the critical experiment), analytical methods were used to predict changes in the power distribution resulting from changes in core and reflector composition, dimensions, and temperature. The fission flux curve obtained from the modified power distribution was multiplied by the ratio of experimental-fission-flux/analytical-fission-flux for the given configuration (the critical experiment) to produce the revised curve corresponding to the modified configuration (the design reactor). A machine program (one-dimensional three-energy-group diffusion analysis) was modified so that the calculated power distribution could be multiplied or divided by three input curves expressed as a function of radius. These input curves were the experimental fission flux curve, the analytical fission flux curve, and a correction factor curve to account for self-shielding in the wire segments and the non-uniform effect of fuel depletion and long-term accumulation of fission product poisoning.

The need for specifying a wire segment self-shielding correction arose from the change in the neutron flux spectrum across the core resulting in the measured beta activity of the wire not accurately reflecting the power generation in a homogeneous medium. Cell corrections at three lethargy levels were obtained using transport theory. These cell corrections were used to determine U^{235} activation across the core in a multi-energy-group diffusion analysis. Figure 4.42 compares the U^{235} activation calculated with and without the application of cell corrections. The ratio of these curves was the self-shielding correction curve.

Figure 4.43 illustrates the change in gross radial power resulting from a temperature change from 68° to 2000°F (average fuel element temperature during steady-state operation at 50.4 megawatts). These calculations were based on a three-energy-group diffusion analysis. Maxwellian-averaged cross sections were used in the thermal group with the neutron temperature equivalent to the physical temperatures of the materials. An 18-energy-group diffusion analysis using the same recipe for the thermal group gave generally the same results. Figure 4.44 shows the effect of material differences, including material substitution, impurities, BeO density, and guide tube thickness, between the design outer reflector and the mockup reflector. The difference in inner reflector composition also was included in this curve. This analysis was based on a three-energy-group diffusion calculation.

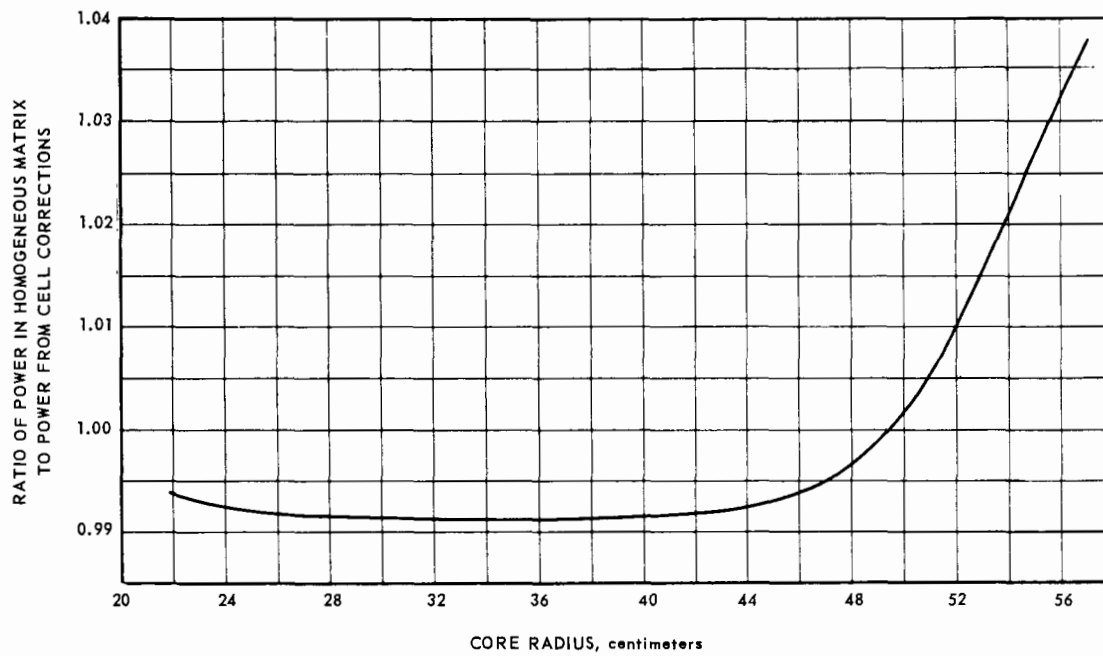
~~CONFIDENTIAL~~

Fig. 4.42 - Ratio of gross radial power in a homogeneous matrix to the power indicated by cell corrections

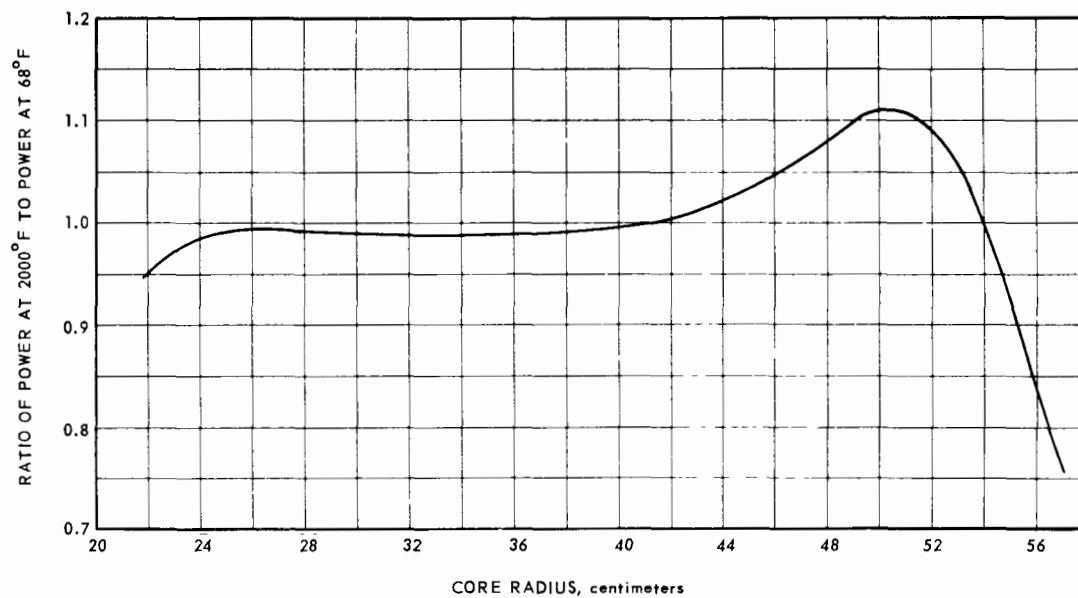


Fig. 4.43 - Ratio of steady state fission density at average design operating temperature to that at room temperature (68°F)

~~CONFIDENTIAL~~

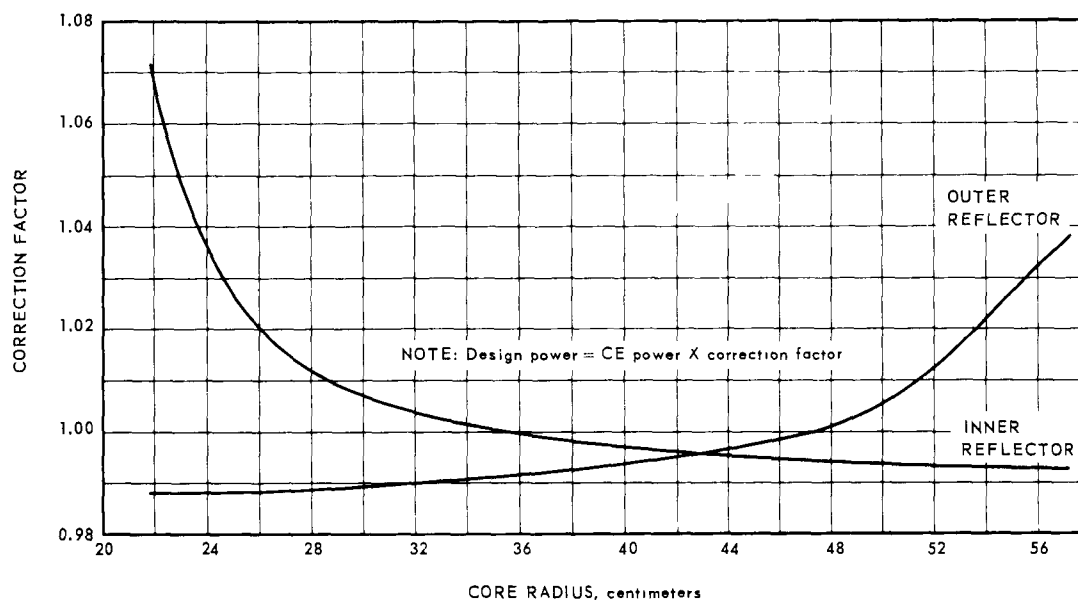


Fig. 4.44 - Correction factor curves to adjust the differences in inner and outer reflector compositions between the critical experiment and the design core

The change in gross radial power which resulted from fuel depletion and fission product buildup for 55,000 megawatt-hours operation was shown in Figure 4.40. The comparison was based on a three-energy-group diffusion analysis in which the regional concentrations of fuel and poisons were determined from the flux spectrum calculated by an 18-energy-group radial diffusion analysis.

4.5.1.3 Choice of Reflector Control Configuration

The XNJ140E-1 reactor configuration utilized reflector control geometry; i.e., control rods were located in the outer reflector. Radial power flattening was accomplished with variable fuel concentrations. The maximum fuel concentration was 10 percent UO_2 by weight. These design features were based on parallel studies of reflector-control geometry and core-control geometry (control rods in the active core region). Temperature flattening studies were performed comparing the variable-fuel-loading method with the variable-hydraulic-diameter method. In both of the above methods, the fuel loading, or hydraulic diameter, was held constant within a single channel and varied with the radial position of the channel. The results and a discussion of these studies are contained in reference 7.

4.5.2 AEROTHERMAL DESIGN OF FUEL ELEMENTS

The aerothermal design parameters listed in Table 4.21 were used in the identification of fuel element geometry and thermal characteristics of the fuel element average-channel shown in Table 4.22. The average-channel was defined as a channel that produced average power and handled average cooling-air flow.

The longitudinal and radial power distributions listed in Table 4.21 were used for the identification of the reactor geometry from which the corrected longitudinal and radial power distributions were calculated.

The heat transfer correlation shown in Table 4.21 was based on data presented in reference 8. Reference 9 discusses the form of the heat transfer equation; and data in reference 10 support the correlation.

~~CONFIDENTIAL~~

TABLE 4. 21

FUEL ELEMENT AEROTHERMAL DESIGN PARAMETERS

Configuration	
Length of active core, in.	30
Length of forward reflector, in.	4
Length of aft reflector, in.	1.5
Aft retainer thickness, in.	1.0
Holes for passage of fuel element cooling-air through forward reflector, aft reflector, and aft-retainer assembly	Same number and diameter as for fuel elements
Nuclear	
Longitudinal power distribution	Chopped cosine curve symmetrical about reactor midplane with a maximum-to-minimum ratio of 2
Radial power distribution	Uniform
Thermal	
Heat transfer coefficient (Smooth tube; subscripts b and f refer to bulk and film temperature, respectively) $T_f = (T_s + T_b)/2$	$\frac{hD}{k_f} = 0.0205 \left(\frac{DG}{\mu_f} \right)^{0.8} \left(\frac{T_b}{T_f} \right)^{0.8} \left(\frac{C_p \mu_f}{k_f} \right)^{0.4}$
Friction factor	$f = 1.15 \times 0.046 (N_{Re})^{-0.2}$ ($f = 1.15 \times f_{\text{smooth tube}}$)
Inlet loss coefficient (based on fuel dynamic head at reflector inlet), $\Delta P/q$	0.36
Exit loss coefficient (based on fuel dynamic head at fuel tube exit), $\Delta P/q$	0.40
Average-channel maximum surface temperature, $^{\circ}\text{F}$	2210

Properties of air are given in reference 11, and properties of the various reactor materials are given in reference 12.

The friction factor multiplier used for aerothermal calculations was 1.15, and originated as a result of cold airflow tests using Al_2O_3 -lined ceramic tubes 4.25 inches long with a 0.283-inch cylindrical bore. A description of these tests and detailed test data are given in reference 13. Later tests with 12-tube channels and two different diameters yielded results shown in Figure 4.45. For all tests the friction factor results were consistent with predicted values based upon relative roughness measurements of the tubes.

Two curves are shown in Figure 4.45 which were based upon Pigott's cold flow data for small diameter tubes. At a Reynolds number of 20,000 (the average Reynolds number for the XNJ140E-1 active core at the design point), the friction factor curve for a 0.167-inch hydraulic diameter tube indicates a friction factor about 1.3 times the calculated friction factor obtained using the equation $f = (1.15)(0.046) \text{Re}^{-0.2}$. Tests were scheduled for verification of friction factors for 0.167-inch-diameter tubes but were not completed.

If the 0.167 D_h curve of Figure 4.45 rather than the adjusted curve of McAdam's data (Figure 4.45) had proved to be valid, the effect on engine thrust would have been a 1.2-

~~CONFIDENTIAL~~

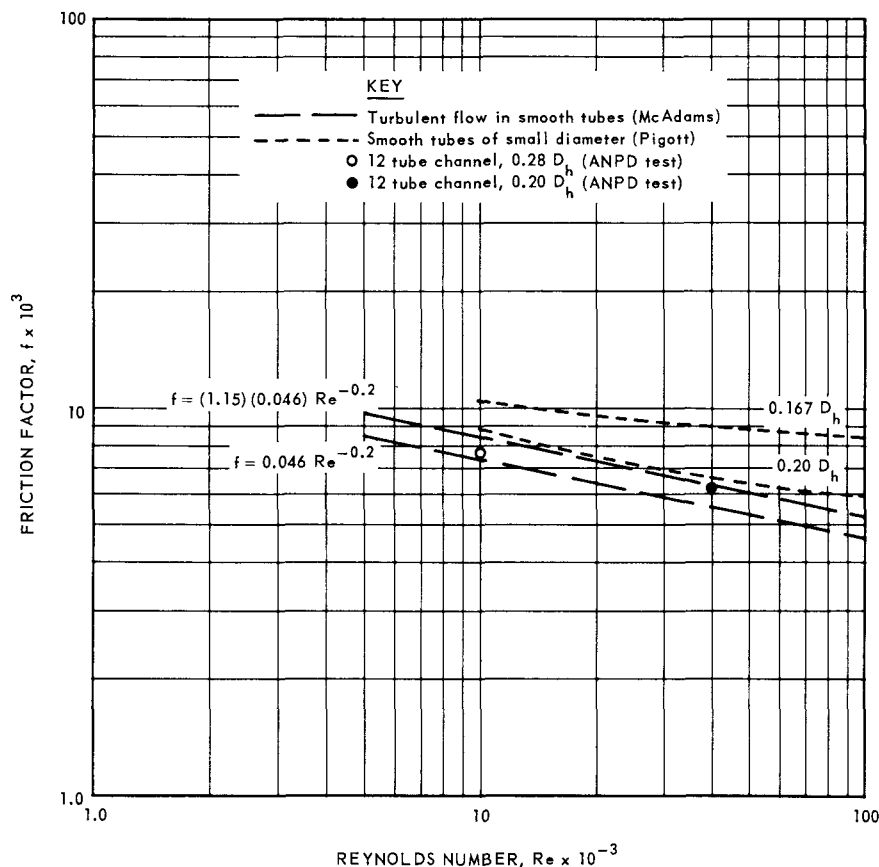


Fig. 4.45—Airflow friction factors for fuel elements

percent decrease. However, the basis used for calculating Reynolds number provided a compensating effect since bulk fluid properties rather than film fluid properties were used. If film fluid properties had been used, a less conservative (but probably more realistic) core pressure loss prediction would have resulted. Calculated pressure losses based on film fluid properties would be 10 to 15 percent less than calculated pressure losses based on bulk fluid properties, and would lead to a calculated gain in engine thrust of about 1.5 percent.

Test results discussed in references 14 and 15 indicated that friction factors for airflow with heat addition were lower than those for isothermal flow conditions.

4.5.2.1 Fuel Element Sizing

The design requirements imposed on the XNJ140E-1 reactor and the parameters listed in Table 4.21 established the fuel element hydraulic diameters and free flow area.

Figure 4.46 depicts average-channel maximum surface temperature as a function of fuel element free flow area, with reactor pressure ratio and fuel element hydraulic diameter as parameters. The average-channel maximum surface temperature of 2210°F and reactor pressure ratio of 0.857 dictated a fuel element free flow area of 545 square inches and a hydraulic diameter of 0.167 inch.

For a reactor pressure ratio of 0.857, the variations of fuel element free flow area with hydraulic diameter and the resulting effects on surface temperature are shown in Figure 4.47. For example, a specified free flow area of 486 square inches, together

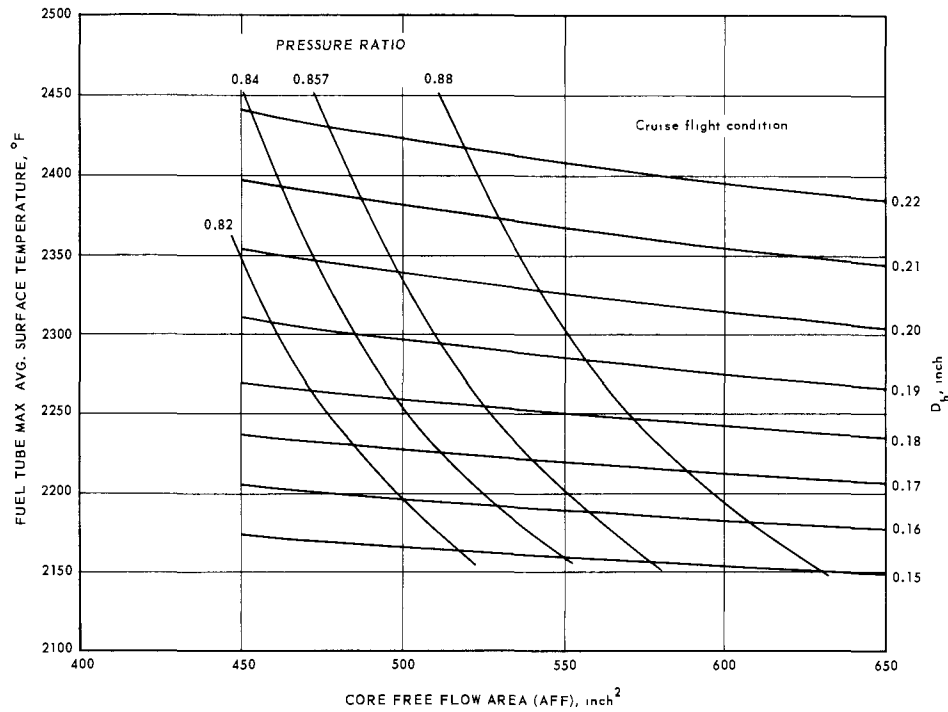
~~CONFIDENTIAL~~

Fig. 4.46 - XNJ140E-1 reactor thermal sizing study

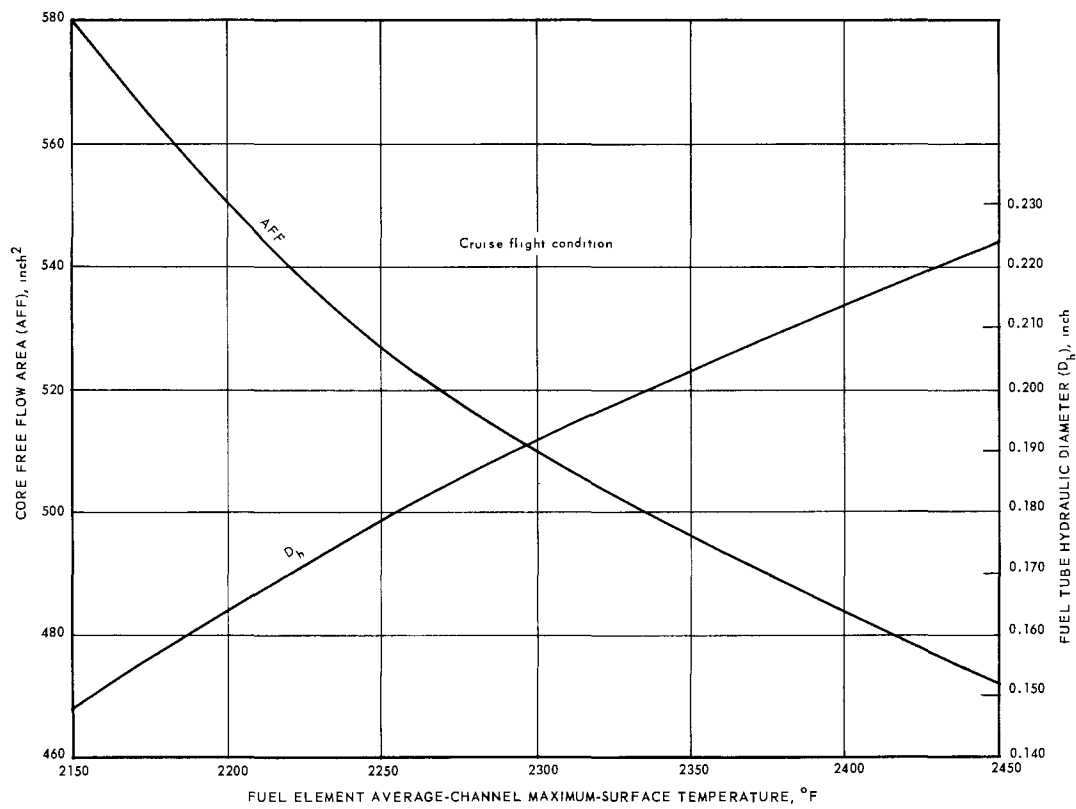


Fig. 4.47 - XNJ140E-1 reactor thermal sizing study

~~CONFIDENTIAL~~

with a reactor pressure ratio of 0.857, required a hydraulic diameter of 0.211 inch and the resulting average-channel maximum surface temperature was 2390°F.

Based on a free flow area and hydraulic diameter of 545 square inches and 0.167 inch, respectively, a listing of the thermal characteristics of the average fuel element flow passage was shown previously in Table 4.22. The longitudinal temperature profile through the length of the reactor shown in Figure 4.48 was calculated for the average-channel with a maximum surface temperature of 2210°F.

Figure 4.49 shows the temperature distribution in a radial cross section of the reactor at the position of maximum temperature in the longitudinal direction. Fuel element temperatures shown in this figure indicate the gross effect of control rod movement. Since the control rods were located in the outer reflector, the power, and consequently the temperatures, was highest near the core-inner reflector interface when the control rods were fully inserted early in core life. A second curve shows temperatures for the other extreme position of the control rods, the completely withdrawn rod bank position that occurred at the end of core life. The average of these two curves was 2210°F, the design average-channel maximum surface temperature.

Identification of fueled volume fractions for the active core, together with coating assumptions and the flow passage dimensions, established the final fuel element geometry and thermal characteristics shown in Table 4.23.

TABLE 4.22
THERMAL CHARACTERISTICS OF AVERAGE
FUEL ELEMENT FLOW PASSAGE

Temperatures, °F	
Inlet air to forward reflector	582
Exit air from aft-retainer assembly	1,896
Fuel surface - average maximum	2,210
Configuration	
Area for airflow, in. ²	545
Hydraulic diameter, in.	0.167
Length, in.	36.5
Forward reflector	4
Fuel elements	30
Aft reflector	1.5
Aft-retainer assembly	1.0
Number of passages	24,881
Heat transfer area, ft ²	2,720
Mass Velocity, lb/sec-ft ²	34.3
Heat Flux, Average, Btu/hr-ft ²	64,700
Total Pressure, psia	
Reactor inlet-air	69.2
Reactor exit-air	59.3
Total Pressure Loss, psi	
Entrance loss	9.93
Friction and heat addition	0.25
Exit loss	8.95
Reynolds Number	
Fuel element inlet-air	0.73
Fuel element exit-air	2.37 × 10 ⁴
Mach Number	
Fuel element inlet-air	1.44 × 10 ⁴
Fuel element exit-air	0.121
Dynamic Head	
Fuel element inlet-air, psi	0.214
Fuel element exit-air, psi	0.69
	1.79

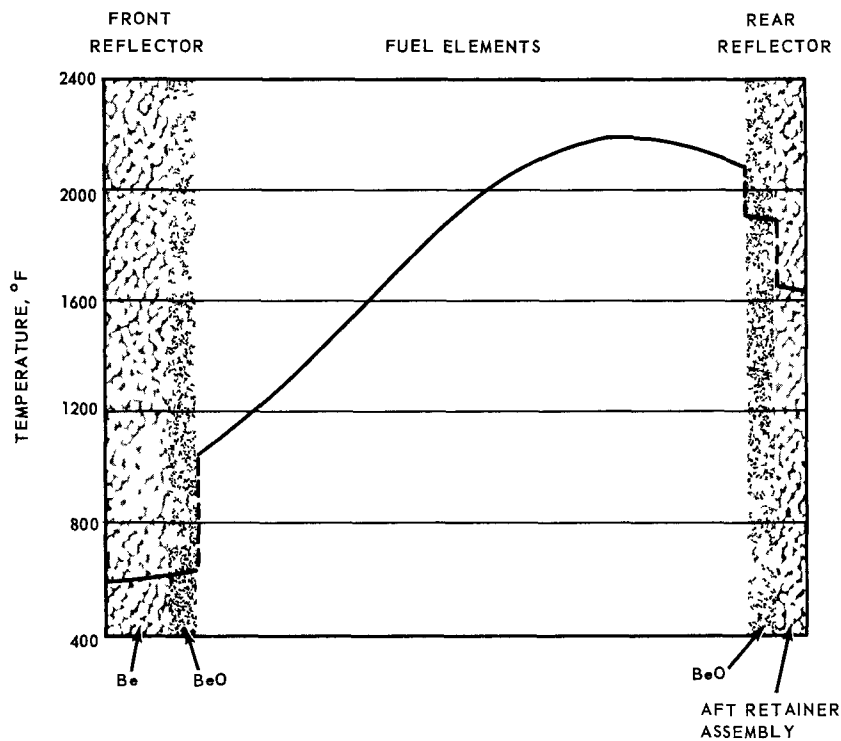
~~CONFIDENTIAL~~

Fig. 4.48 – Longitudinal temperature distribution, average channel

TABLE 4.23

**FINAL FUEL ELEMENT GEOMETRY AND
THERMAL CHARACTERISTICS**

Fuel Element Dimensions, in.	
Hydraulic diameter	0.167
Width across flats	0.249
Coating thickness	0.003
Fueled matrix, inner diameter	0.173
Core Dimensions, in.	
Inner diameter	17.22
Outer diameter	45
Length	30
Volumetric Heating, Btu/sec-in. ³	
Average	2.04
Average-channel maximum	2.49
Average Internal Temperature Rise, °F	
Coating	12
Matrix	13

~~CONFIDENTIAL~~

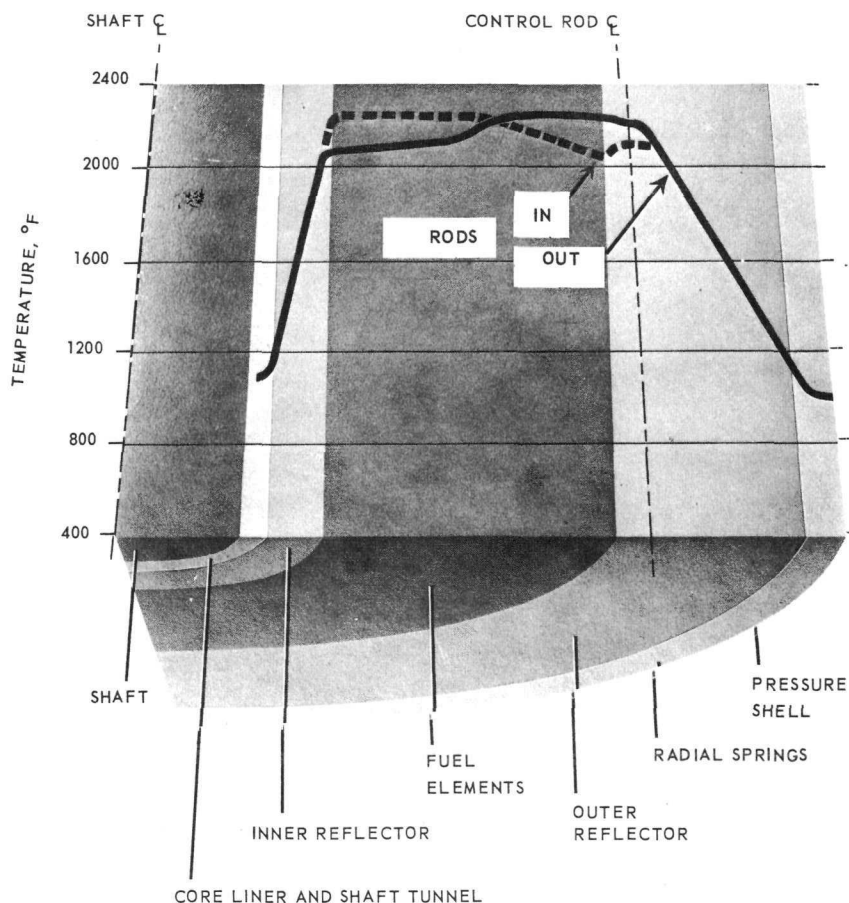


Fig. 4.49—Radial temperature distribution at the longitudinal position of maximum temperature, XNJ140E-1 reactor

4.5.2.2 Aerothermal Characteristics of the Active Core

Aerothermal calculations were based on the radial power profile shown in Figure 4.50, and the longitudinal power profiles of Figures 4.51, 4.52, and 4.53. Radial temperature distributions in the active core are shown in Figure 4.54 in greater detail than was shown in Figure 4.49. The two curves in Figure 4.49 showing temperature distributions for control rods fully inserted and fully withdrawn are repeated in Figure 4.54 and show the effect of radial fuel distribution. A third curve for an intermediate rod insertion of 10 inches was added. The calculated radial power shifts, due to control rod movement, resulted in a fuel element maximum surface temperature of about 2290°F, 80 degrees higher than the average-channel maximum temperature of 2210°F, and represented the maximum value for an average-channel within any radial region.

Since fuel loading was varied in discrete regions as previously shown in Table 4.6, power gradients occurred across regions of constant fuel loading. The fuel loadings of Table 4.6 were consistent with the gross radial power distributions of Figure 4.50. Power gradient effects on surface temperature were twofold: (1) the regional local temperatures deviated about 40°F from regional average temperatures, and (2) because of the power gradient across a single tube, a further deviation from average temperature was encountered. With a power gradient of ± 5 percent across a single fuel element, and assuming that all the heat generated at a point passes radially inward to the air stream, the deviation from channel average temperature would be about $\pm 25^\circ\text{F}$. Previous analyses

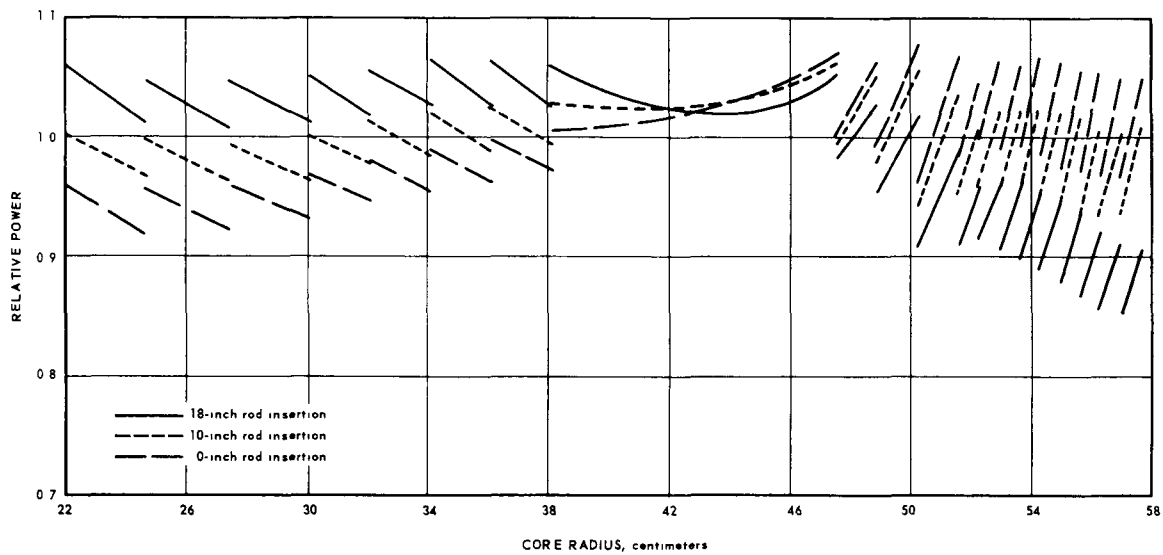
~~CONFIDENTIAL~~

Fig. 4.50 - Gross radial power distribution for three rod-insertion depths in the XNJ140E-1 reactor

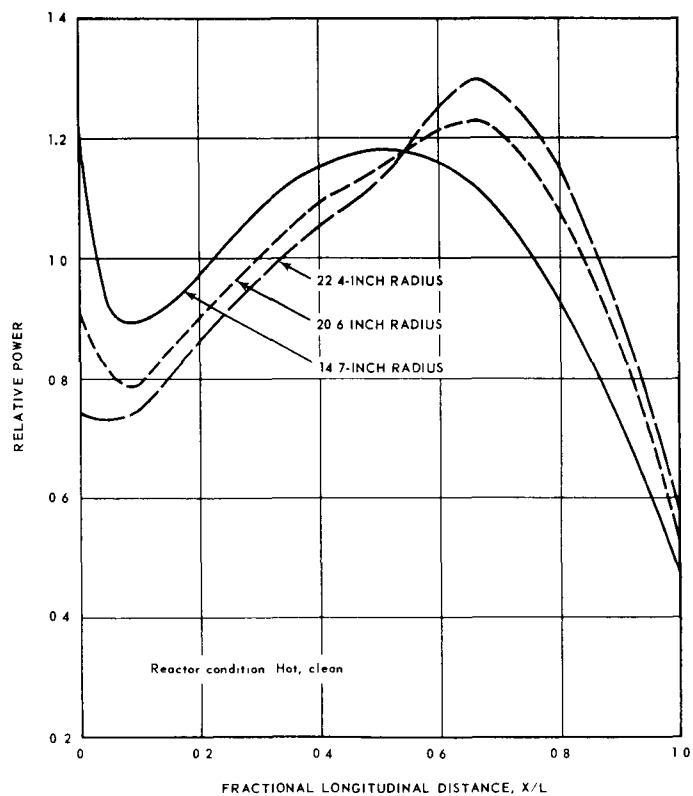


Fig. 4.51 - Relative longitudinal power distribution in the XNJ140E-1 reactor at three radial locations with control rods inserted 18 inches

~~CONFIDENTIAL~~

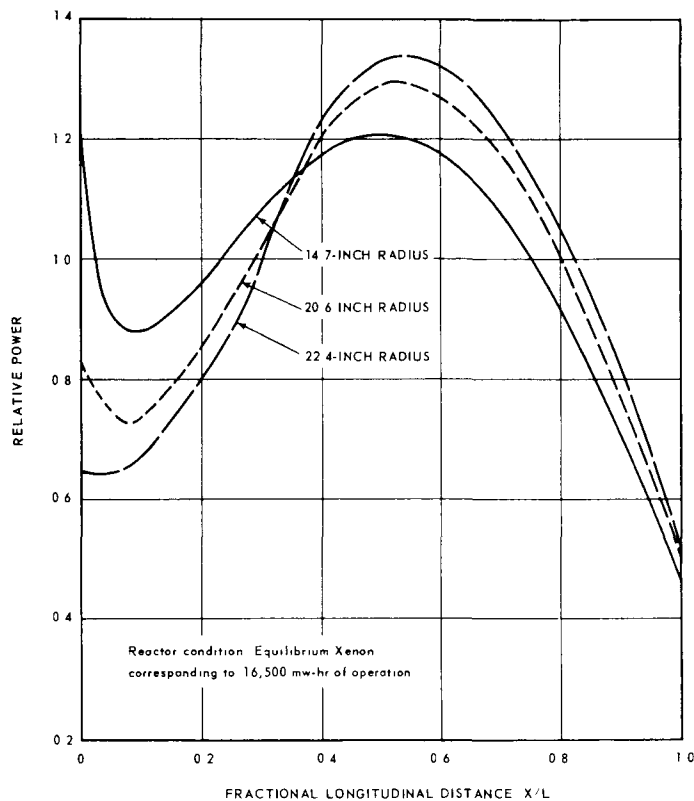
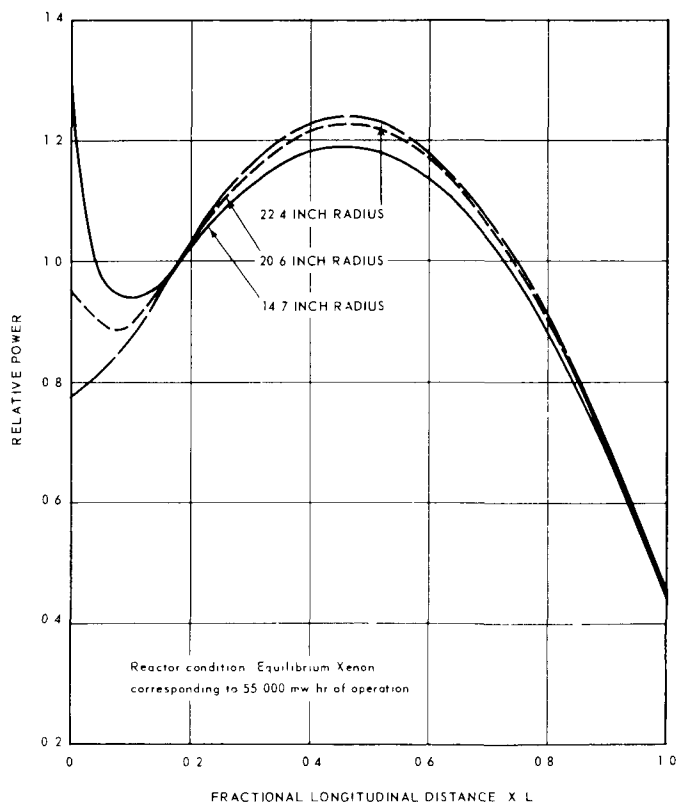


Fig. 4.52 - Relative longitudinal power distribution in the XNJ140E-1 reactor at three radial locations with control rods inserted 10 inches

Fig. 4.53 - Relative longitudinal power distribution in the XNJ140E-1 reactor at three radial locations with control rods fully withdrawn



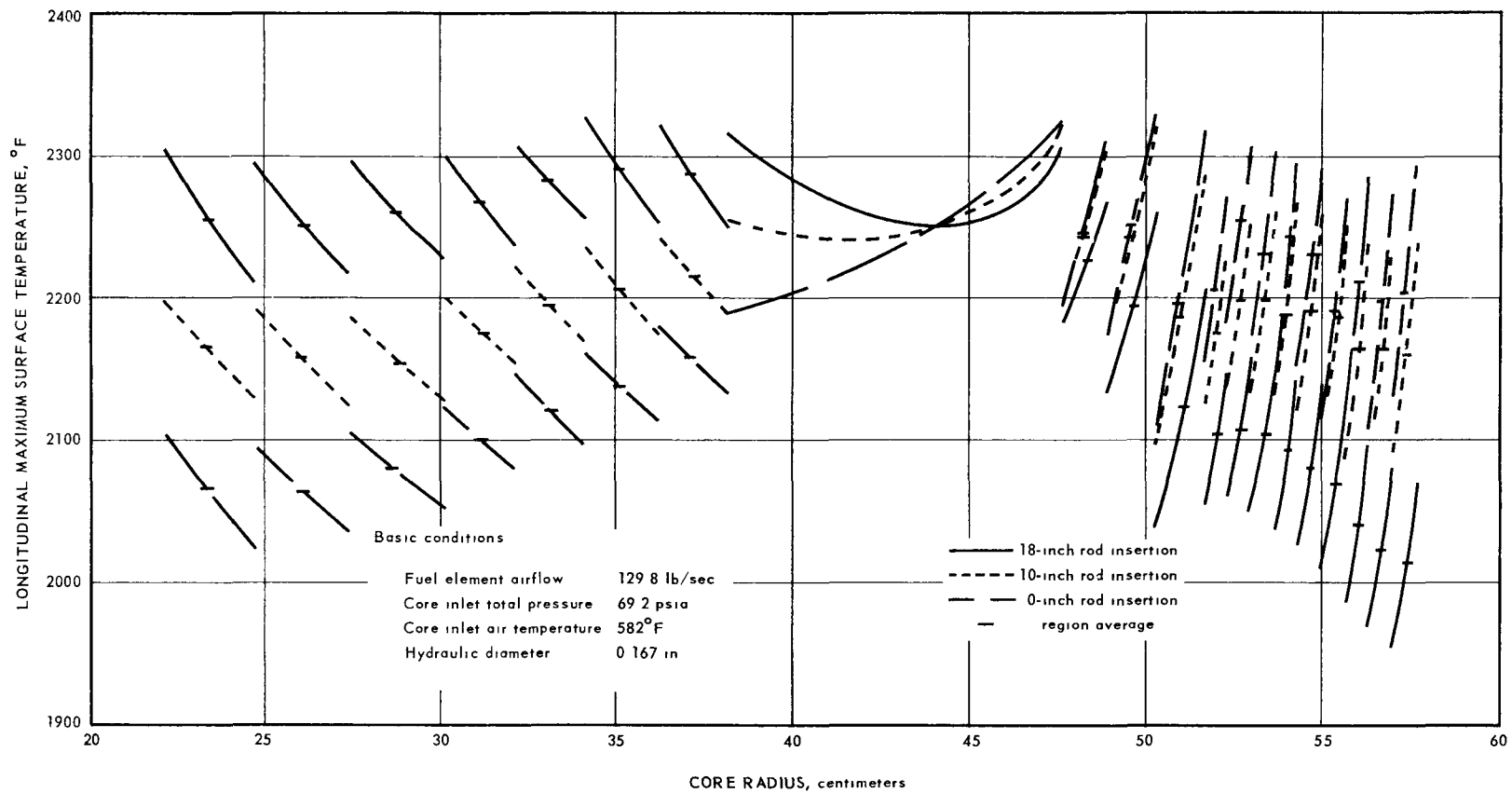


Fig. 4.54—Radial variation of longitudinal maximum surface temperature in XNJ140E-1 fuel elements

indicated that circumferential heat transfer by conduction would relax this deviation to about one-third of the unrelaxed (25°F) deviation. Fuel tube temperature relaxation, both within tubes and between adjacent tubes, is discussed in reference 16.

The concept of temperature flattening is best illustrated by the curves in Figure 4.54. Withdrawal of control rods to compensate for nuclear poisons produced temperature swings. At the beginning of core life, the temperatures were highest in the inner regions of the core, and at the end of core life, the temperatures were highest in the outer regions of the core. A pivotal zone, approximately at 45 centimeters radius, existed in which the temperatures remained essentially constant throughout reactor life. The aim of temperature flattening was to equalize the maximum temperatures at the two extremes of rod position while maintaining the rest of the core as near to these temperatures as possible.¹⁷

Radial distribution of temperature of the cooling-air issuing from the active core is shown in Figure 4.55. These data reflect the same general design characteristics as Figure 4.54.

All of the fuel element flow passage calculations reported herein, including the configuration studies of reference 7, were performed with ANP computer programs 443 and 439. Program 443 (Off Design) was used to determine flow passage surface temperatures and pressure losses for the conditions of compressible flow with heat addition. A description of the Off Design Program is contained in reference 18. Program 439 (Isothermalize) incorporated the Off Design Program as a subroutine and permitted rapid identification of power level, air temperature rise, and mass velocity for a given channel when the pressure loss and maximum surface temperature and longitudinal power profile were specified.

4.5.2.3 Fuel Element Temperature Deviations

Reactor design in its conceptual phase was based upon various mechanical, thermal, and nuclear design assumptions. In this phase, as well as in later final design stages, variations between design assumptions (or expectations) and calculated values were inevitable. In the interest of increasing both reliability and the level of engine performance, variations between design assumptions and calculated values were estimated as accurately as possible. For example, excessive fuel temperatures throughout extended regions of the core were not permissible from a reliability standpoint, whereas extended regions of low fuel temperature penalized the thermal performance level. Thorough selection and accurate analysis of those engineering characteristics which affect fuel element temperature were required to achieve simultaneously both high reliability and high performance levels.

A study was performed which included: (1) definition of those reactor characteristics contributing to hot spots within fuel elements, (2) analysis of those characteristics to determine the magnitudes of their effects, and (3) combination and realistic grouping of the various characteristics and their associated temperature deviations. Several of the temperature deviations used in the study were estimated and were not supported by final calculations. The method used was to establish a reference temperature and then add the various significant temperature deviations.

The following definitions were used in the study.

Fuel Element Average-Channel Maximum Surface Temperature - The maximum temperature occurring on the surface of an average fuel element channel. The average fuel element had nominal dimensions, nominal cooling-air flow rate, and average radial fission power density.

CONFIDENTIAL

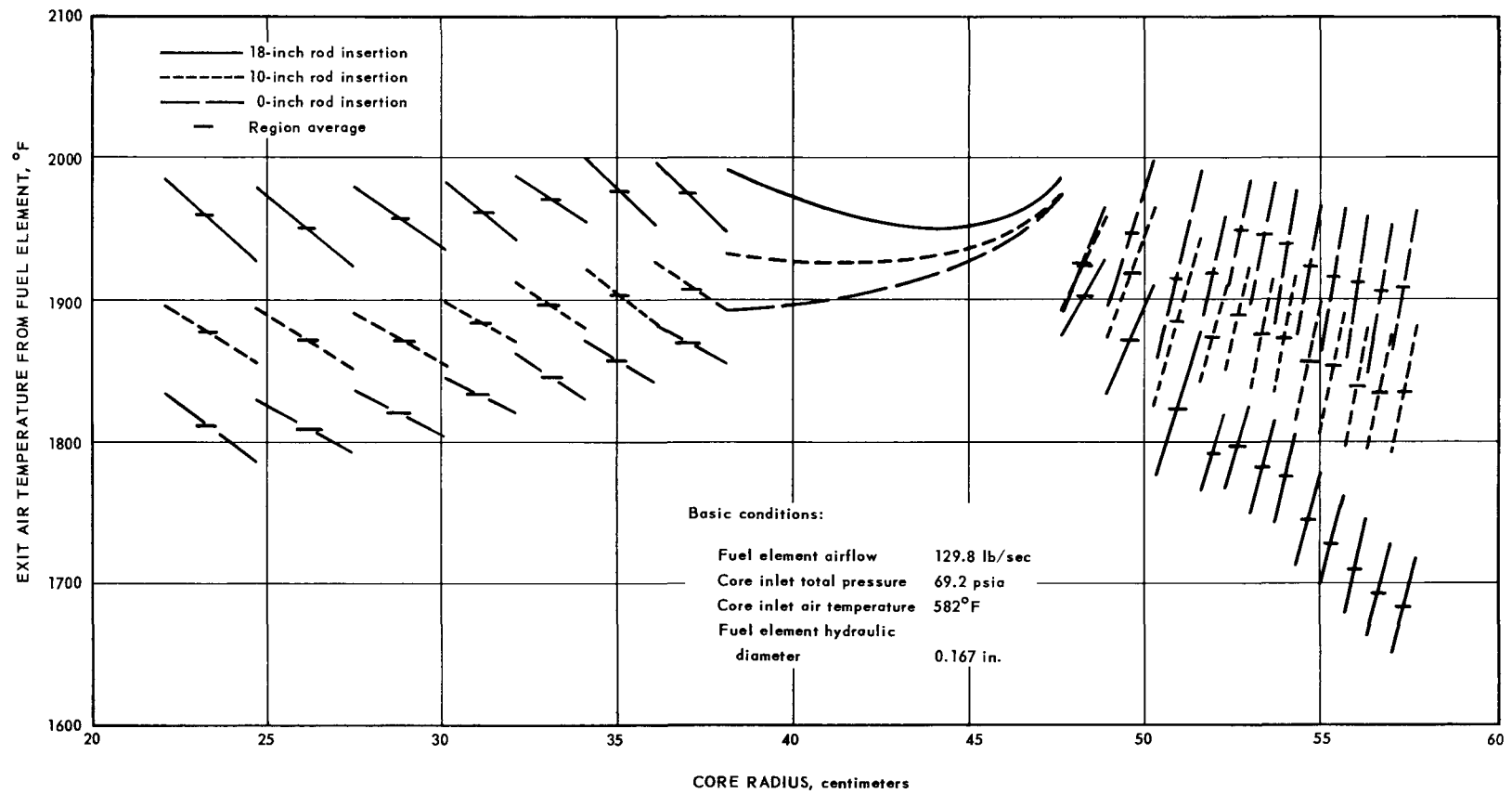


Fig. 4.55 – Radial variation of exit air temperature from XNJ140E-1 fuel elements

CONFIDENTIAL

Reference Surface Temperature - The fuel element average-channel maximum surface temperature that would exist if the longitudinal power profile were a 2/1 chopped cosine distribution and similar to that shown in Figure 4.48.

Region Average Surface Temperature - The average of the various surface temperatures within a regional zone of constant fuel loading. This value varied with varying radii and fractional reactor lengths, but was considered in this study to occur at the reference temperature location of $0.9 X/L$. The region average temperature used in this study was the highest region average temperature shown in Figure 4.54, i.e., 2290°F at a 35-centimeter core radius.

Local Deviation From Region Average - Figure 4.54 shows the typical temperature deviations from the regional average value within a particular region of constant fuel loading. This deviation varied depending upon fuel loading and fuel region location. At a 35-centimeter radius the local deviation from region average was 40°F .

Calculated Maximum Surface Temperature - The calculated maximum surface temperature was equal to the average-channel maximum surface temperature plus the built-in temperature deviation of 80°F between average-channel maximum surface temperature and region average temperature plus 40°F local deviation from the region average value. The calculated maximum surface temperature, therefore, was 2330°F .

Estimates were made for the significant probable deviations of fuel surface temperature due to design features and fabrication tolerances. In addition to these reasonably well defined areas, there were several contributions to temperature deviations for which the magnitudes and likelihood of occurrence were uncertain. These general areas were as follows:

1. It was estimated that the actual radial power profile might be 5 percent higher than the assumed power profile. It further was estimated that the resulting temperature deviation would relax to 50 percent of the estimated value. A 60°F increase in surface temperature was assigned to this effect.
2. The longitudinal power profile was subject to uncertainties. A 5 percent increase in local power caused approximately 20°F wall temperature deviation.
3. It was believed that the thermal conductivity of fuel element material might vary as much as ± 10 percent from values used in the calculations. A temperature deviation of 3°F was assumed.
4. Fabrication specifications for fuel tubes permitted acceptance of out-of-round channels. If the major axis of one such tube was normal to that of the following tube, flow maldistribution between channels would occur. An allowance of 6°F was made for the effect of decreased mass flow caused by this flow disturbance.
5. Uncertainties were assumed to be ± 0.0005 inch in the on-flats dimension and hydraulic diameter measurements. A 15°F temperature deviation was estimated.
6. It was assumed that fore and aft plenum effects and control rod effects upon radial airflow distribution were known, and that adjustments would be made to prevent flow maldistribution. However, an allowance of ± 2 percent flow measurement uncertainty was provided for conservatism. The corresponding temperature deviation was 20°F .
7. Uncertainties in the accuracy of evaluating heat transfer film coefficients and friction factor multipliers also existed. It was felt that the assigned values were conservative and temperature deviations would not result from these sources.
8. Three temperature drops were added to the surface temperature when values of fuel element internal temperatures were desired. Allowances of 12°F drop through the clad and 13°F drop through the fuel matrix were realistic. A 5°F temperature rise was used to account for the increased heat flux in the region of external corners.
9. A grouping of the individual surface temperature deviations and the associated reactor exit-air temperature deviations are given in Table 4.24. The four major group-

~~CONFIDENTIAL~~

TABLE 4. 24

CONTRIBUTIONS TO FUEL ELEMENT AND EXIT-AIR TEMPERATURE DEVIATIONS

		Temperature Deviation, °F	
		Fuel Element	Exit-Air
Power Distribution			
Reference-to-region average temperature deviation		80	70
Local deviation from region average		40	30
Fabrication Tolerances			
Hydraulic diameter	-0.001 in.	20	15
Flats dimension	+0.001 in.	15	10
Eccentricity	0.0025 in.	10	0
Fuel loading	+3.7% of value	40	30
Coating thickness	-0.001 in.	15	10
Measurement Uncertainties			
Radial power		60	50
Longitudinal power		20	0
Thermal conductivity		3	0
Channel axis misalignment		6	4
Tube dimension measurement		15	10
Flow measurement		20	15
Configuration			
Cladding		12	0
Fuel element		13	0
Hexagonal shape (outer corners)		5	0

ings are power distribution, fabrication tolerances, measurement uncertainties, and configuration. A significant aspect of the study was the statistical use of a root mean square summation of the measurement uncertainty contributions. Inherent assumptions were that the uncertainties involved had normal curve distribution, and were statistically independent.

Table 4. 25 shows a summary of the fuel element surface temperature allowances for built-in deviations, and added allowances for other variables that were used to predict the hot channel maximum temperature. The reference temperature was 2210°F and the built-in deviation total was 120°F. Therefore, the maximum calculated surface temperature was 2330°F and represented the maximum predicted surface temperature, assuming that power and airflow were correctly matched. Addition of the fabrication tolerance and measurement uncertainty allowances yielded an estimated maximum surface temperature of 2500°F. Since the temperature rise through the fuel element was 30°F, the highest temperature in the fuel material was predicted to be 2530°F. No relaxation in the radial direction was assumed in the 40°F local deviation from region average temperature.

Consideration of the longitudinal temperature distributions, the built-in radial temperature deviations, and the statistical temperature deviations resulting from tolerances and measurement uncertainties indicated that a small part of the core would operate at temperatures approaching 2500°F. These temperatures are shown in Figure 4.56, in which the percentage of the active core surface at any given temperature is plotted against that temperature. The average surface temperature is 2000°F.

~~CONFIDENTIAL~~

TABLE 4.25
MAXIMUM FUEL ELEMENT TEMPERATURE

	Temperature, °F
Average Maximum Surface Temperature (reference)	2210
Plus Built-in Temperature Deviations	120
Maximum Calculated Surface Temperature	2330
Plus Allowances	
Fabrication tolerance	100
Measurement uncertainty	70
Total	170
Maximum Estimated Surface Temperature	2500
Plus Internal Temperature Rise	30
Maximum Fuel Element Temperature	2530

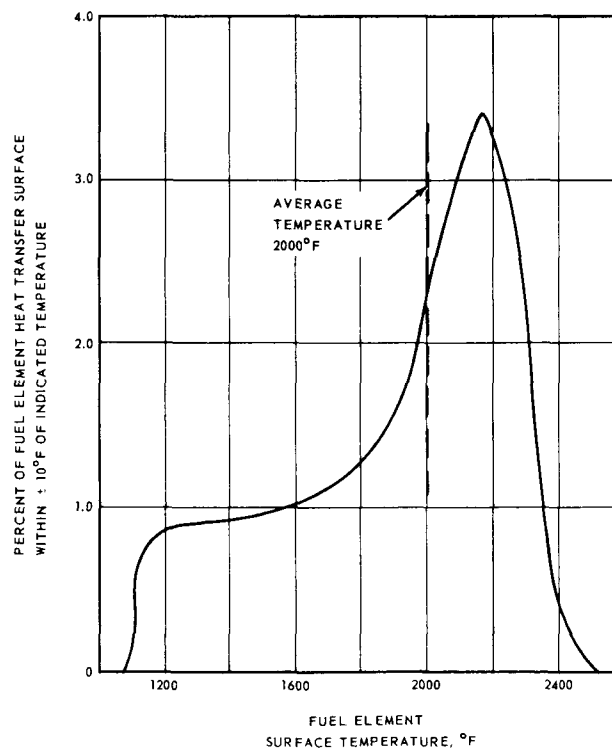


Fig. 4.56—Temperature distribution of fuel elements in the XNJ140E-1 reactor

~~CONFIDENTIAL~~

Additional calculations for estimating temperature deviations caused by fabrication generally substantiated the initial prediction of 100°F shown in Table 4. 25. One calculation consisted of using a statistical treatment for combining the effects of various tolerances upon fuel element surface temperature and was based upon selecting fuel elements having hydraulic diameters within ± 0.001 -inch tolerance. The 3-sigma temperature deviation for this fabrication tolerance allowance was estimated to be 77°F. Individual deviations for the calculation are given in Table 4. 26. If a fuel element hydraulic diameter tolerance of ± 0.0025 -inch had been used, the 3-sigma temperature deviation for fabrication tolerances would have been approximately 95°F.

TABLE 4. 26
TEMPERATURE DEVIATIONS FOR FABRICATION TOLERANCES^a

Source Of Deviation	$\Delta T_{\text{air}}, ^\circ\text{F}$		$\Delta T_{\text{film}}, ^\circ\text{F}$		$\Delta T_{\text{surface}}, ^\circ\text{F}$
	Power $3\sigma/\sqrt{5}$	Flow $3\sigma/\sqrt{7}$	$\frac{Q}{hA} \times W^{0.8}$ 3σ	$W^{-0.8}$ $3\sigma/\sqrt{7}$	
Hydraulic Diameter					
- 1 mil	4	8	3	3	18
Hexagonal Flats					
+ 1 mil	7		8		15
Fuel Loading					
Density + 1. 65%	9		10		19
UO ₂ + 3%	16		18		34
U ²³⁵ + 0. 21%	2		2		4
Coating Thickness					
- 1 mil	7		8		15
Eccentricity					15
Total: $\Sigma \Delta T$					124
<hr/>					
Statistical Deviation, $3\sigma = \sqrt{\Sigma (\Delta T)^2}$			51°F		
Corrected 3 Sigma Temperature Deviation =					
1. 5 ^b x 51.			77°F		

^aSelection by hydraulic diameter.

^bTruncated distribution curve correction factor - 1. 5.

Assumptions used in the preparation of Table 4. 26 were as follows:

1. Variations in each of the five listed characteristics causing temperature deviations would closely approximate a normal distribution curve. This assumption was substantiated in a study of the fuel elements fabricated for ETR99 CR20 test cartridge. Histograms for these measurements are shown in reference 19.
2. Variations in the fuel element characteristics were statistically independent.
3. The Central Limits Theorem was applicable.
4. Calculated or estimated temperature deviations were 3-sigma deviations. The calculated temperature was exceeded in only 1. 3 elements per thousand in the highest temperature tier.

~~CONFIDENTIAL~~

5. The air temperature deviation caused by a variation in power from nominal power was the statistical average for the five tubes preceding the hot spot in a particular channel ($\Delta T = 3\sigma/\sqrt{5}$).
6. The air temperature deviation caused by a variation in airflow was the statistical average for a total of seven tubes in a channel ($\Delta T = 3\sigma/\sqrt{7}$).
7. The film temperature deviation at the hot spot caused by local power variation was equal to the 3-sigma deviation caused by the variation local power.
8. The film temperature deviation at the hot spot caused by flow variation was equal to the statistical average deviation for the whole channel ($\Delta T = 3\sigma/\sqrt{7}$).

Another calculation consisted of selecting tubes on a basis of individual fuel loadings. A tolerance of ± 1 percent in fuel loading was assumed, and tube acceptance was assumed to be based upon ± 0.0025 -inch tolerance in hydraulic diameter. A statistical treatment to determine the effects of fabrication tolerances upon temperature deviation with this fuel tube acceptance method resulted in an estimate of a 45°F 3-sigma temperature deviation. Individual deviations for this calculation are given in Table 4. 27.

TABLE 4. 27
TEMPERATURE DEVIATIONS FOR FABRICATION TOLERANCES^a

Source Of Deviation	$\Delta T_{\text{air}}, ^{\circ}\text{F}$		$\Delta T_{\text{film}}, ^{\circ}\text{F}$		$\Delta T_{\text{surface}}, ^{\circ}\text{F}$
	$3\sigma/\sqrt{5}$	$3\sigma/\sqrt{7}$	3σ	$3\sigma/\sqrt{7}$	
Hydraulic Diameter					
- 2.5 mils		20	-6	+6	20
Power, + 1%	6		9		15
Eccentricity					
2.5 mils					15
Total: $\Sigma \Delta T$					50
Statistical Deviation: $3\sigma = \sqrt{\Sigma (\Delta T)^2} \dots \dots \dots 29^{\circ}\text{F}$					
3 Sigma Deviation x 1.5					
Truncation Correction			44 ⁰ F		

^aSelection by fuel loading.

Using the statistically determined temperature deviations for fabrication tolerances shown in Tables 4. 26 and 4. 27 when estimating maximum surface temperature yielded a maximum surface temperature lower than 2500°F . In addition, temperature relaxation of hot spots caused by fabrication tolerances was not included in these tabulations. Accordingly, the estimated maximum surface temperature of 2500°F was believed to be conservative, possibly by as much as 70°F .

A parametric study of the reactor maximum exit-air temperatures from the fuel elements, corresponding to the maximum surface temperature of 2500°F is shown in Figure 4. 57. Surface temperatures and exit-air temperatures are plotted as a function of channel power and airflow ratios. The fuel element surface temperature and corresponding exit-air temperature may be obtained from Figure 4. 57 for any combination of power and airflow deviations. Maximum exit-air temperatures are shown for any combination of power and airflow deviations which would yield a maximum surface temperature of 2500°F . The

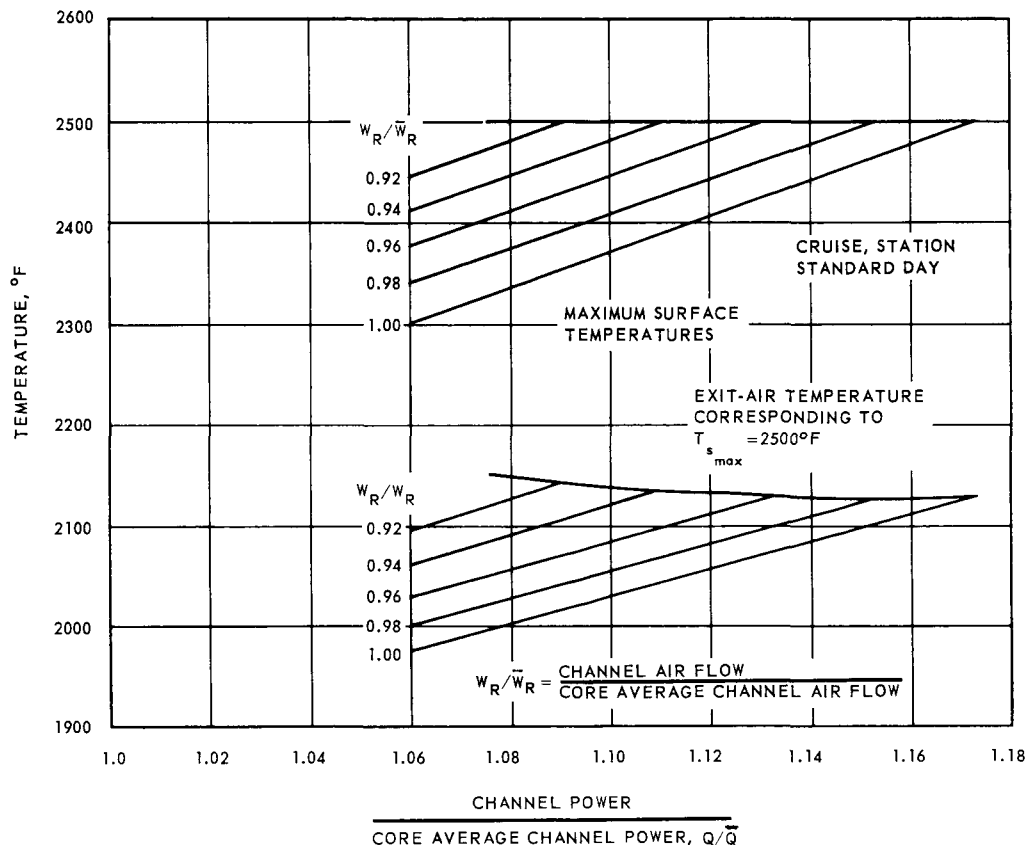
~~CONFIDENTIAL~~

Fig. 4.57 – Maximum fuel element exit air temperature corresponding to a maximum surface temperature of 2500°F

maximum exit-air temperature varied less than 20°F for any combination of power and airflow deviations shown, and did not exceed 2150°F .

4.5.2.4 Aerothermal Characteristics of Off-Design Points

Reactor aerothermal characteristics for standard-day flight conditions are shown in Table 4.28. Comparable data for the hot-day and cold-day flight conditions are shown in Tables 4.29 and 4.30, respectively. Flight condition No. 1, nuclear take-off, and No. 3, sustained sea-level flight at Mach 0.6 (structural limit of the Convair NX2 airframe) were added for evaluation of reactor performance. These data represented the average-channel thermal characteristics.

4.5.2.5 Effects of Critical Experiment Data on Radial Temperature Distribution

The XNJ140E-1 reactor nuclear mockup installed in the KEY matrix facility, was used to provide gross nuclear characteristics as well as the fine details of power distribution. A description of the nuclear mockup is contained in reference 20.

Longitudinal power distributions, obtained from the nuclear mockup, are shown in Figures 4.58, 4.59, and 4.60, for rod insertions of 12.25 inches, 5.0 inches, and 0 inch, respectively. Because of reactivity limitations, no data were available for the 15-inch rod insertion. However, by extrapolating the available data, estimates of power distributions for the 15-inch rod insertion were obtained, and are shown in Figure 4.61.

Comparing these figures with the analytically determined power distributions of Figures 4.51, 4.52, and 4.53, power distributions near the control rods obtained from experi-

~~CONFIDENTIAL~~

TABLE 4.28

REACTOR AEROTHERMAL CHARACTERISTICS FOR
STANDARD-DAY FLIGHT CONDITIONS, (S-18 CYCLE)

Flight Condition	a	b	c	d	e	f	1	3
Mach No.	0	0	0.55	0.8	0.8	0.6	0	0.6
Altitude, ft	0	0	10,000 - 35,000 (20,000)	35,000	35,000	10,000	0	0
Power Setting	NC	MAX	NC	NC	MIL	NC	MAX	NC
W_a (fuel elements), lb/sec	310.0	320.9	211.7	129.9	131.9	271.3	320.0	327.6
Pressures								
$P_{T3.5}$, psia	162.7	152.2	111.5	69.2	71.7	142.7	170.4	162.4
$P_{T3.6}$, psia	141.6	139.2	96.2	59.3	61.6	123.9	148.4	139.4
$P_{T3.6}/P_{T3.5}$	0.870	0.914	0.863	0.857	0.858	0.868	0.871	0.857
$P_{T3.5}-P_{S3.6}$	25.4	15.3	18.2	11.8	12.0	22.6	26.5	28.0
Temperatures								
$T_{3.5}$, °F	665	663	638	582	597	665	685	665
$T_{3.6}$, °F	1,886	675	1,889	1,896	1,962	1,886	1,951	1,835
T_S (max avg), °F	2,258	680	2,230	2,210	2,289	2,243	2,340	2,199
T_S (max), °F	2,530	680	2,511	2,500	2,593	2,518	2,624	2,459
Flow Conditions in Fuel Elements ^a								
Inlet Mach No.	0.13	0.14	0.13	0.12	0.12	0.13	0.13	0.14
Exit Mach No.	0.21	0.15	0.21	0.21	0.21	0.21	0.21	0.23
Inlet q, psi	1.81	2.07	1.20	0.69	0.70	1.58	1.87	2.02
Exit q, psi	4.24	2.24	2.91	1.79	1.81	3.71	4.43	4.70
Inlet Reynolds No.	53,700	55,660	37,280	23,700	23,800	47,000	54,800	56,760
Exit Reynolds No.	34,390	55,260	23,480	14,400	14,380	30,110	34,970	36,800

^aStatic pressure, Mach number, q, and Reynolds numbers are calculated on basis of fuel element flow area.

CONFIDENTIAL

CONFIDENTIAL

TABLE 4. 29

**REACTOR AEROTHERMAL CHARACTERISTICS FOR
HOT-DAY FLIGHT CONDITIONS, (S-18 CYCLE)**

Flight Condition	a	b	c	d	e	f	1	3	4
Mach No.	0	0	0.7	0.8	0.8	0.6	0	0.6	0.6
Altitude, ft	0	0	20,000	35,000	35,000	10,000	0	0	5,000
Power Setting	NC	MAX	NC	NC	MIL	NC	MAX	NC	EMERGENCY
W_a (fuel elements), lb/sec c	272.2	285.6	189.0	120.1	122.6	239.4	283.9	315.0	305.8
Pressures									
$P_{T3.5}$, psia	143.4	135.9	99.9	64.3	66.5	126.4	152.1	163.7	164.1
$P_{T3.6}$, psia	124.4	123.5	86.0	55.0	56.8	109.3	132.2	141.6	142.6
$P_{T3.6}/P_{T3.5}$	0.868	0.909	0.861	0.855	0.854	0.865	0.869	0.865	0.869
$P_{T3.5}-P_{S3.6}$	22.8	14.5	16.6	11.0	11.4	20.4	23.9	26.6	25.9
Temperatures									
$T_{3.5}$, °F	706	709	681	636	653	705	729	747	778
$T_{3.6}$, °F	1,880	723	1,884	1,889	1,955	1,881	1,946	1,892	1,973
T_S (max avg), °F	2,222	729	2,202	2,183	2,267	2,212	2,305	2,241	2,332
T_S (max), °F	2,487	729	2,469	2,459	2,549	2,476	2,578	2,497	2,601
Flow Conditions In Fuel Elements^a									
Inlet Mach No.	0.13	0.15	0.13	0.12	0.12	0.13	0.13	0.13	0.13
Exit Mach No.	0.21	0.16	0.21	0.21	0.21	0.21	0.21	0.22	0.21
Inlet q, psi	1.64	1.92	1.11	0.67	0.68	1.44	1.71	1.99	1.92
Exit q, psi	3.70	2.08	2.59	1.64	1.70	3.26	3.90	4.38	4.24
Inlet Reynolds No.	46,030	48,220	32,440	21,180	21,400	40,510	47,400	52,060	49,690
Exit Reynolds No.	30,230	47,840	20,980	13,320	13,390	26,590	31,050	34,880	33,210

^aStatic pressure, Mach number, q, and Reynolds numbers are calculated on basis of fuel element flow area.

CONFIDENTIAL

CONFIDENTIAL

TABLE 4.30
REACTOR AEROTHERMAL CHARACTERISTICS FOR
COLD-DAY FLIGHT CONDITIONS, (S-18 CYCLE)

Flight Condition	a	b	c	d	e	f	1	3
Mach No.	0	0	0.7	0.8	0.8	0.6	0	0.6
Altitude, ft	0	0	20,000	35,000	35,000	10,000	0	0
Power Setting	NC	MAX	NC	NC	MIL	NC	MAX	NC
W_a (fuel elements), lb/sec	394.8	399.0	228.5	135.2	138.6	300.0	392.3	436.8
Pressures								
$P_{T3.5}$, psi	200.8	178.4	120.3	72.9	75.1	157.3	190.5	172.9
$P_{T3.6}$, psi	176.0	165.0	104.2	62.8	64.5	136.9	165.6	142.5
$P_{T3.6}/P_{T3.5}$	0.876	0.925	0.866	0.862	0.860	0.870	0.869	0.824
$P_{T3.5}-P_{S3.6}$	30.3	15.8	19.3	12.0	12.5	24.6	30.4	37.4
Temperatures								
$T_{3.5}$, °F	496	472	592	553	565	620	480	440
$T_{3.6}$, °F	1,794	487	1,895	1,900	1,966	1,891	1,694	1,411
T_S (max avg), °F	2,227	493	2,258	2,226	2,306	2,275	2,100	1,752
T_S (max), °F	2,509	493	2,550	2,523	2,618	2,560	2,361	1,952
Flow Conditions In Fuel Elements ^a								
Inlet Mach No.	0.12	0.14	0.12	0.12	0.12	0.13	0.13	0.15
Exit Mach No.	0.21	0.15	0.21	0.21	0.21	0.21	0.22	0.27
Inlet q, psi	2.01	2.27	1.24	0.69	0.71	1.68	2.06	2.72
Exit q, psi	5.31	2.44	3.14	1.83	1.92	4.11	5.33	6.67
Inlet Reynolds No.	76,470	78,660	41,430	25,170	25,590	53,420	76,880	88,240
Exit Reynolds No.	44,870	77,790	25,310	14,970	15,100	33,250	45,750	55,300

^aStatic pressure, Mach number, q, and Reynolds numbers are calculated on basis of fuel element flow area.

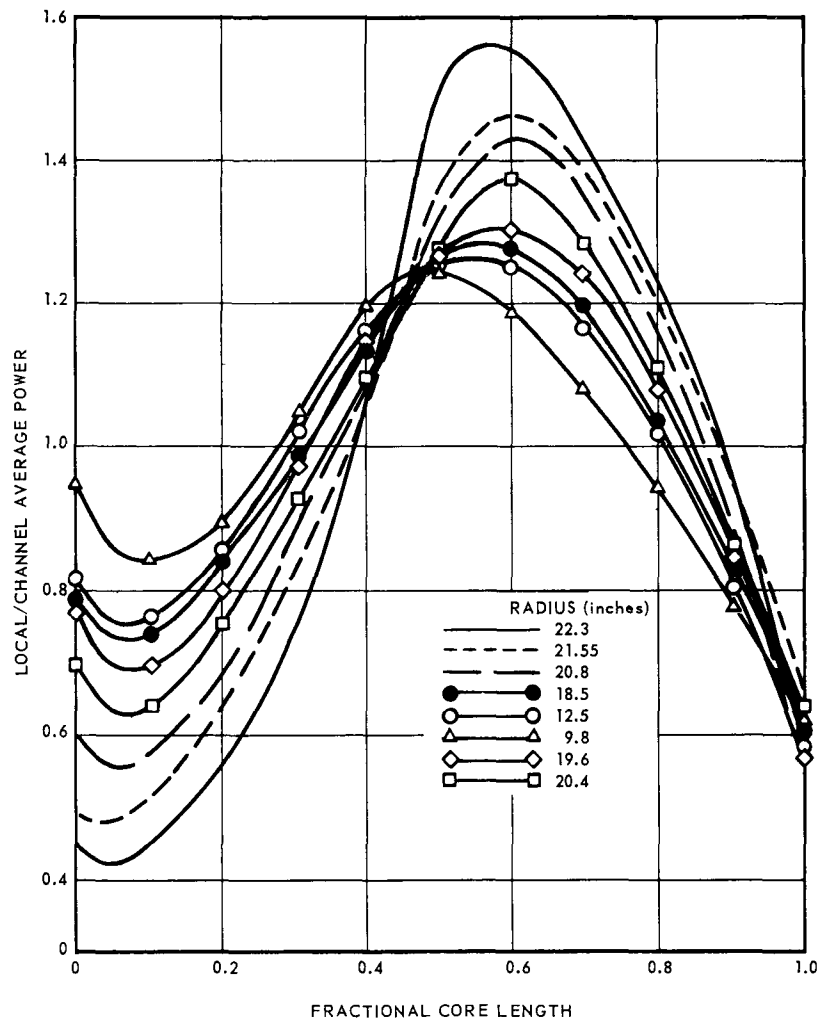
~~CONFIDENTIAL~~

Fig. 4.58—Longitudinal power distributions at eight positions with control rods inserted to the 12.25 inch position (KEY-CE Data)

~~CONFIDENTIAL~~

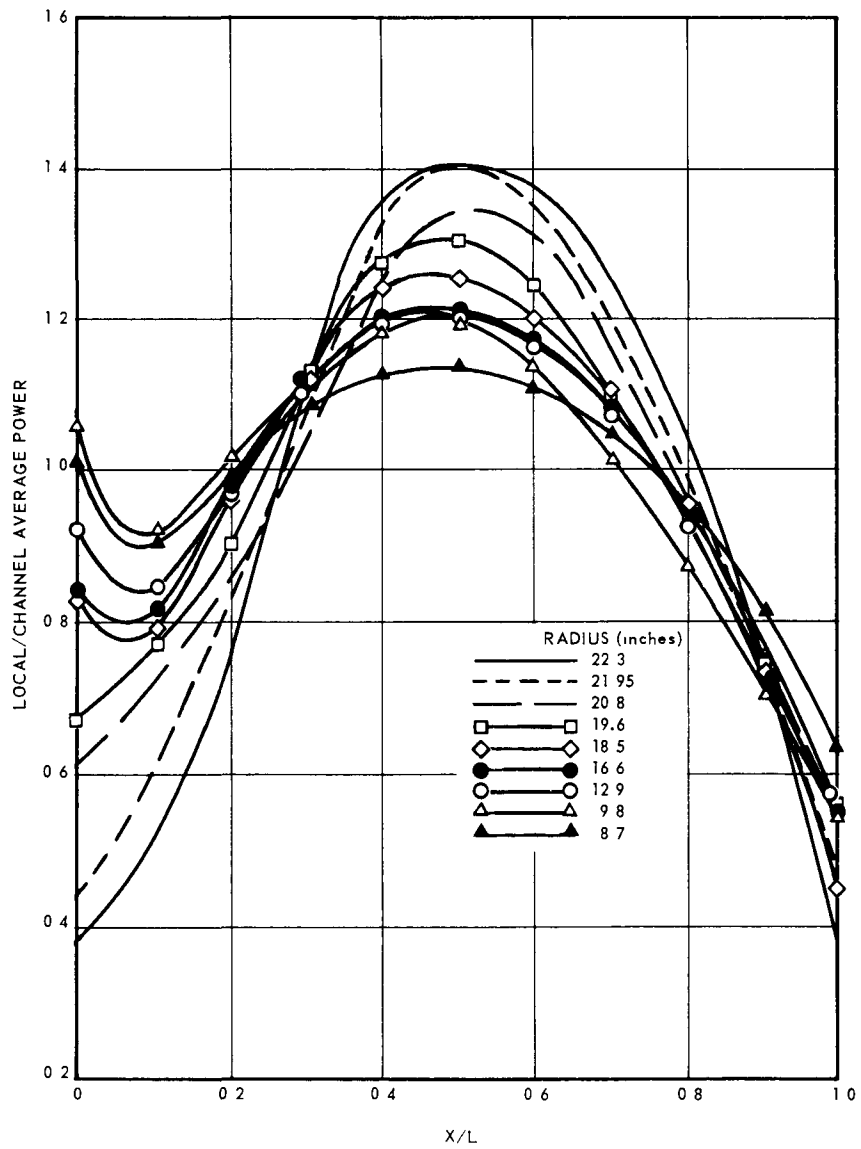


Fig. 4.59—Longitudinal power distributions at nine radial positions with control rods inserted to the 5 inch position

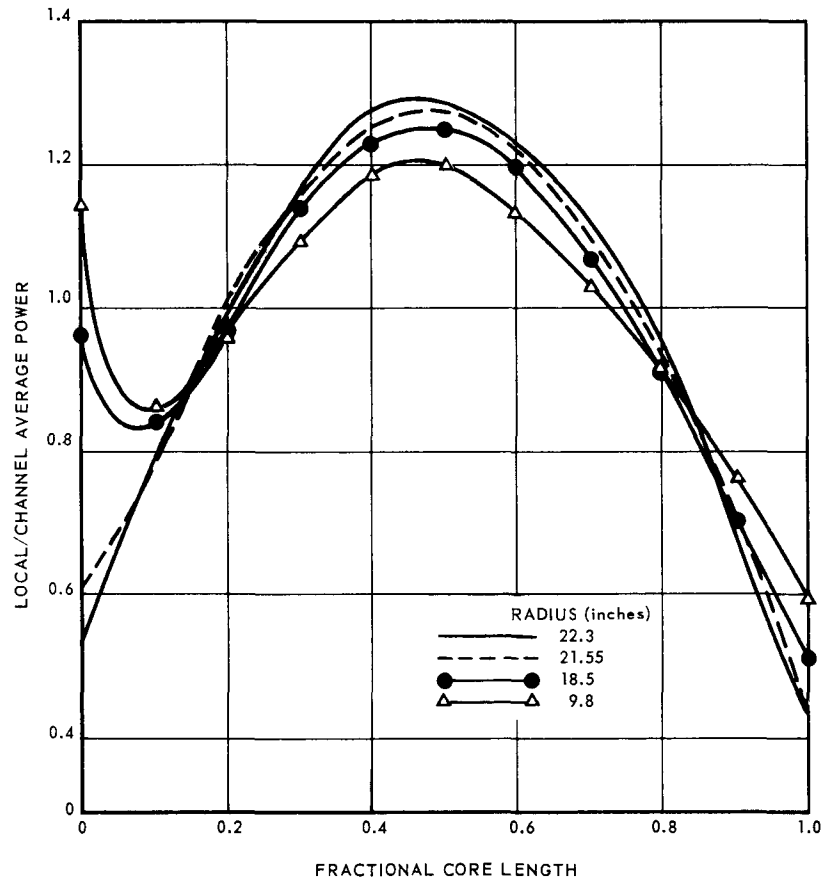
~~CONFIDENTIAL~~

Fig. 4.60—Longitudinal power distributions at four radial positions with control rods fully withdrawn (KEY-CE Data)

mental data peaked further aft and at a higher maximum value. Near the center of the core, the differences were negligible. At the fully withdrawn rod position, the differences were negligible at all radial positions.

Based on the experimental results of the nuclear mockup, and a series of nuclear and thermodynamic iterations, the radial power distribution previously shown in Figure 4.39 was identified as being most nearly optimum. The fuel loading schedule, which yields the radial power distributions of Figure 4.39, was shown in Table 4.6.

Radial variations of longitudinal maximum temperature distributions, corresponding to the radial power distributions of Figure 4.39, are shown in Figure 4.62 for the design point. The peak temperature, 2340°F, occurred at a core radius of 35 centimeters during 15-inch rod insertion. The pivotal zone (zone at which surface temperature remained essentially constant, regardless of rod insertion) occurred at about 48 centimeters radius. The surface temperature in this zone was approximately 2300°F.

The data of Figure 4.62 reflected the temperature relaxation afforded by conduction within each fuel element, but did not include the effect of heat conduction between fuel elements. An additional relaxation of 10°F in the maximum surface temperature due to conduction between the fuel elements was predicted.

Additional nuclear and thermodynamic design iterations aimed at further decreasing the calculated maximum temperature of 2340°F were not warranted.

~~CONFIDENTIAL~~

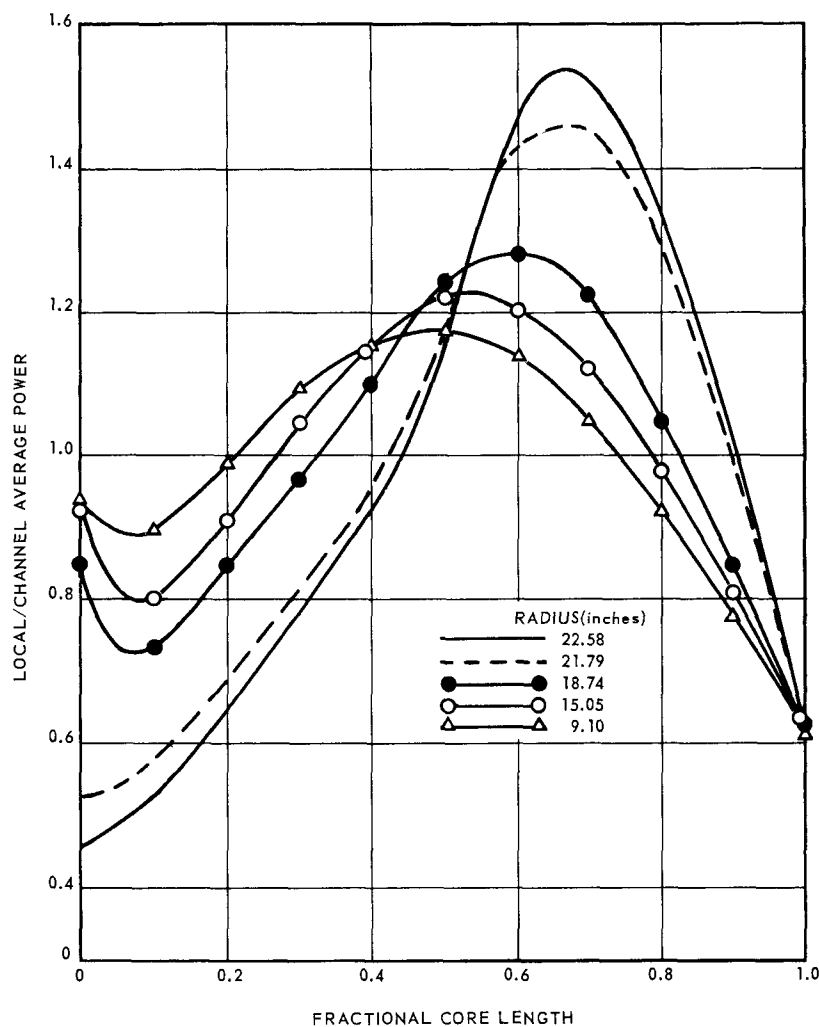


Fig. 4.61--Longitudinal power distributions at five radial positions with control rods inserted to the 15 inch position as extrapolated from measurements made at the 12.25 inch position (KEY-CE Data)

4.5.3 MECHANICAL DESIGN OF FUEL ELEMENTS

4.5.3.1 Design Criteria

The small hexagonal ceramic tubes used as the basic elements of the core were assembled in the shape of a large circular cylinder. This cylindrical shape was maintained throughout all operating conditions and aerodynamic and inertial loading by the radial and longitudinal support systems. The principal components of each system are illustrated schematically in Figures 4.63 and 4.64.

Radial Support System - The design philosophy of the radial support system depended on maintaining sufficient radial pressure through the tube bundle to insure that it behaved as a rigid body under inertial loads. Therefore, to prevent separation of the tubes within the bundle, the radial springs supplied sufficient compressive loading to suppress tensile stresses across the interfaces of the tubes, based on an inertial limit load of 4 G's.

Radial spring loading alone could have been used to maintain stability of the tube bundle, but the deflection of the tube bundle relative to the shell would have been excessive. To minimize this deflection, the tube bundle was supported by shear distribution at the per-

CONFIDENTIAL

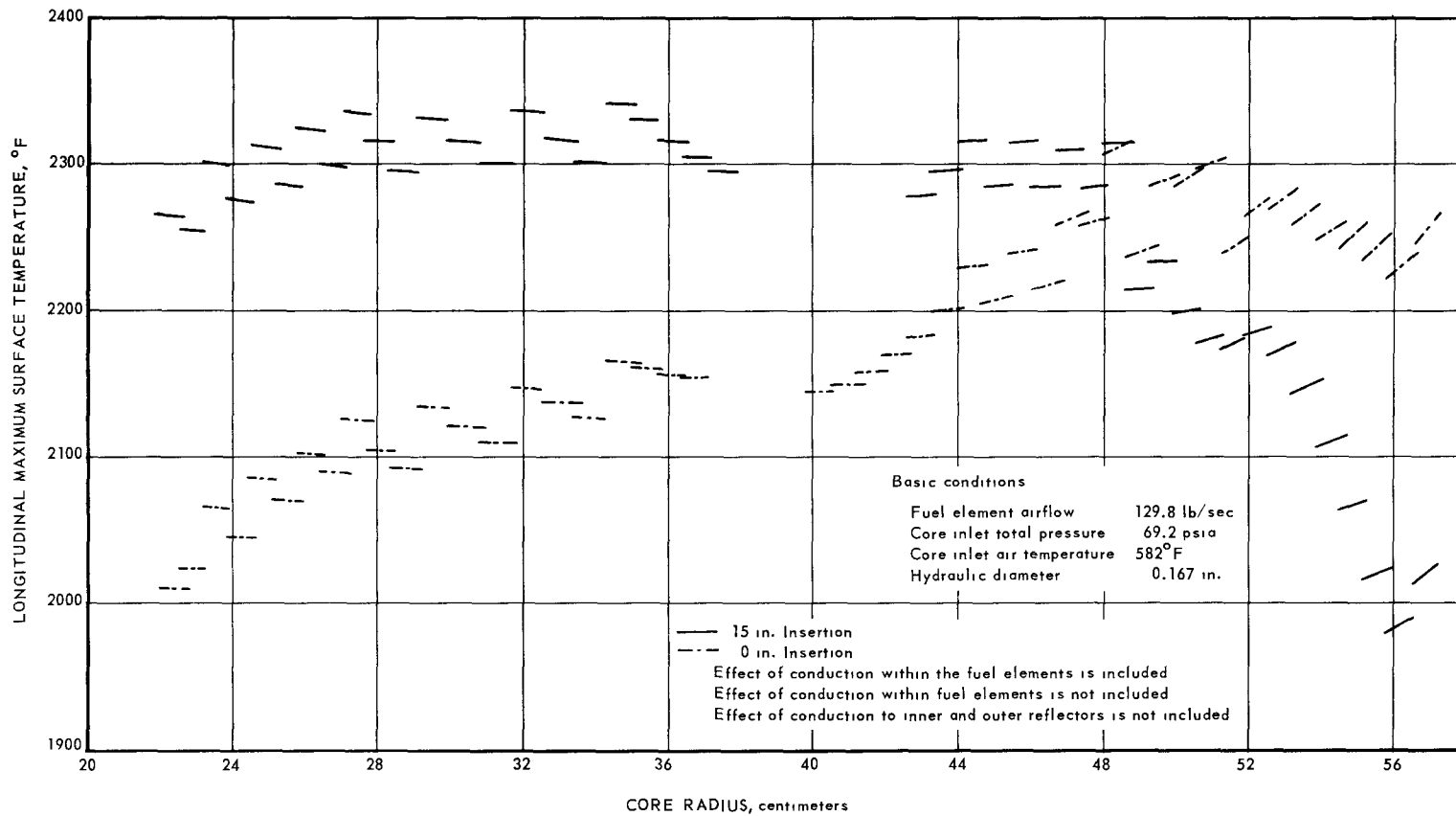


Fig. 4.62—Radial variation of longitudinal maximum surface temperature

CONFIDENTIAL

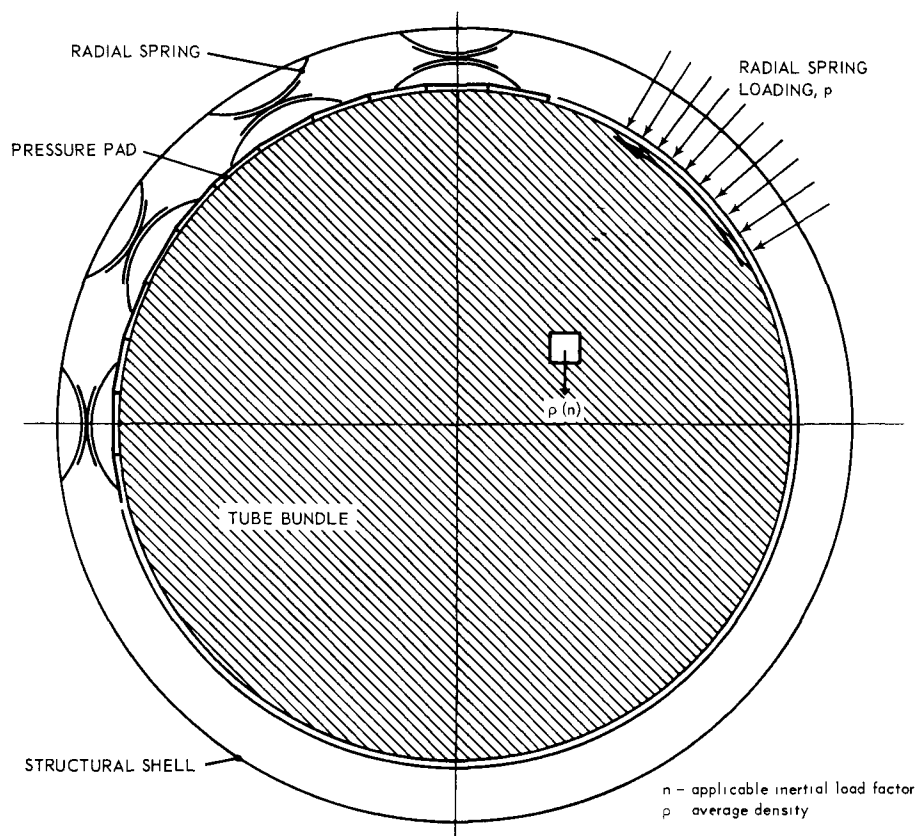


Fig. 4.63 - Schematic of radial support system

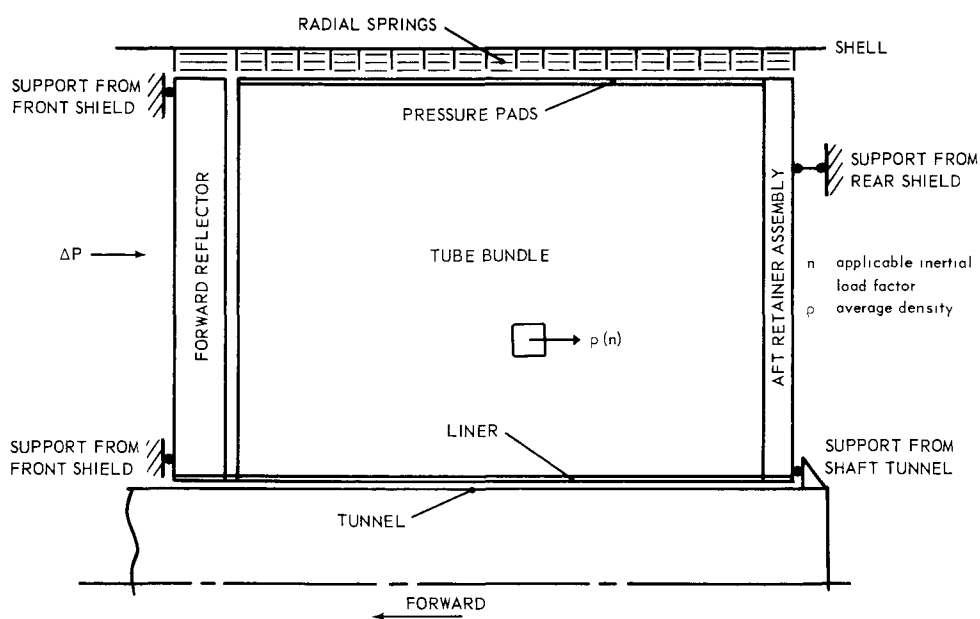


Fig. 4.64 - Schematic of longitudinal support system

~~CONFIDENTIAL~~

imeter. Radial leaf springs resisted tangential loads and supported the core in the structural shell by supplying a shear reaction through the springs. The stiffness of the springs under tangential loading was much greater than under radial loading, and virtually the entire support was furnished by the shear. In addition to minimizing the relative deflections between the core and shell, this method of support kept the radial spring loading nearly constant around the perimeter of the core under inertial loading.

Determination of Minimum Required Radial Pressure - Examining a radial cross section of the tube bundle under an inertial load, and assuming the bundle to be rigid, the tube bundle was visualized as a beam of variable depth, loaded by (1) body forces proportional to the depth and resisted by the shear reactions and (2) the consequent moment which moved the effective shear reaction away from the bundle. Figure 4.65 shows the construction of the force diagrams.

In a beam of this type, two tensile stresses were evaluated: (1) the normal flexural tensile stresses due to bending and (2) the induced diagonal tensile stresses resulting from shear and direct flexural stresses. The maximum flexural tensile stress occurred at the bottom of the vertical diameter and was equal to twice the product of the radius, the apparent density, and the limit inertial factors. The maximum diagonal tensile stress occurred at the ends of the diameter normal to the direction of inertial loading and was equal to the product of the radius, the apparent density and the limit inertial factor. Calculations of these stresses are shown in Figure 4.65. To completely suppress tube separation, the minimum radial compressive pressure equaled the flexural tensile stress (the greater of the two stresses). This minimum radial pressure caused the maximum compressive stress to equal twice the tension or $4R\rho n$.

The integrity of the tube bundle could be maintained with limited separation of the tubes along half of the critical diameter by applying an initial radial pressure of $R\rho n$. This was equal to one-half of the value of σ_t shown in Figure 4.65. The reduction in radial pressure was accomplished by balancing the moment about the vertical diameter with internal eccentric compression. Separation of the tubes under this condition was limited to the compressive strain along the top half of the critical diameter. Since the maximum compressive stress along the diameter with the eccentric compression remained $4R\rho n$, the compressive strain and tube separation was insignificant. Figure 4.66 shows calculations of the minimum radial pressure.

Since the tube bundle integrity could be maintained with the minimum radial pressure, the applied radial pressure was specified as $R\rho n$ so that the tube bundle would not be subjected to the larger pressure required to completely suppress separation.

A three-tier mockup which approximated a full-scale cross section of the reactor was fabricated specifically to investigate the interactions of (1) tube bundle components, (2) radial force devices, and (3) radial structure under various conditions of vibration, G loads, and longitudinal loads.

Test results confirmed that the use of mechanical shear ties definitely contributed to the retention and centering of the tube bundle within the structural shell. Test results also confirmed that the tube bundle integrity could be maintained under inertial loads as high as 5 G's. The mockup was shocked as high as 5 G's with a 10-inch cavity to simulate melting conditions. Figure 4.67 is a photograph of the mockup after this test was completed, and shows no appreciable changes in the core geometry.

Radial Pressure Distribution Within Tube Bundle - The minimum radial pressure was 12 psi, the product of the radius, the apparent density, and the ratio of the imposed acceleration divided by the acceleration of gravity as developed above. This minimum

~~CONFIDENTIAL~~

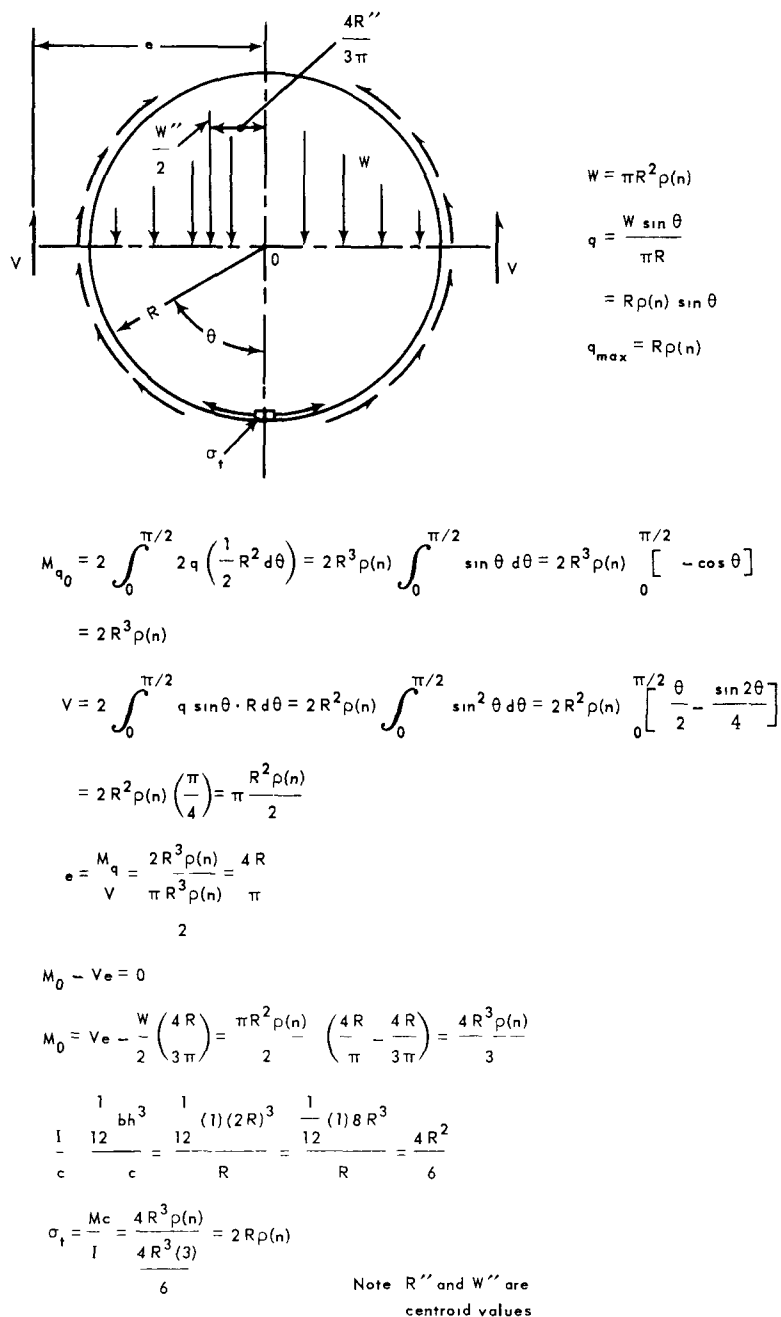


Fig. 4.65 - Construction of radial-support-system force diagram

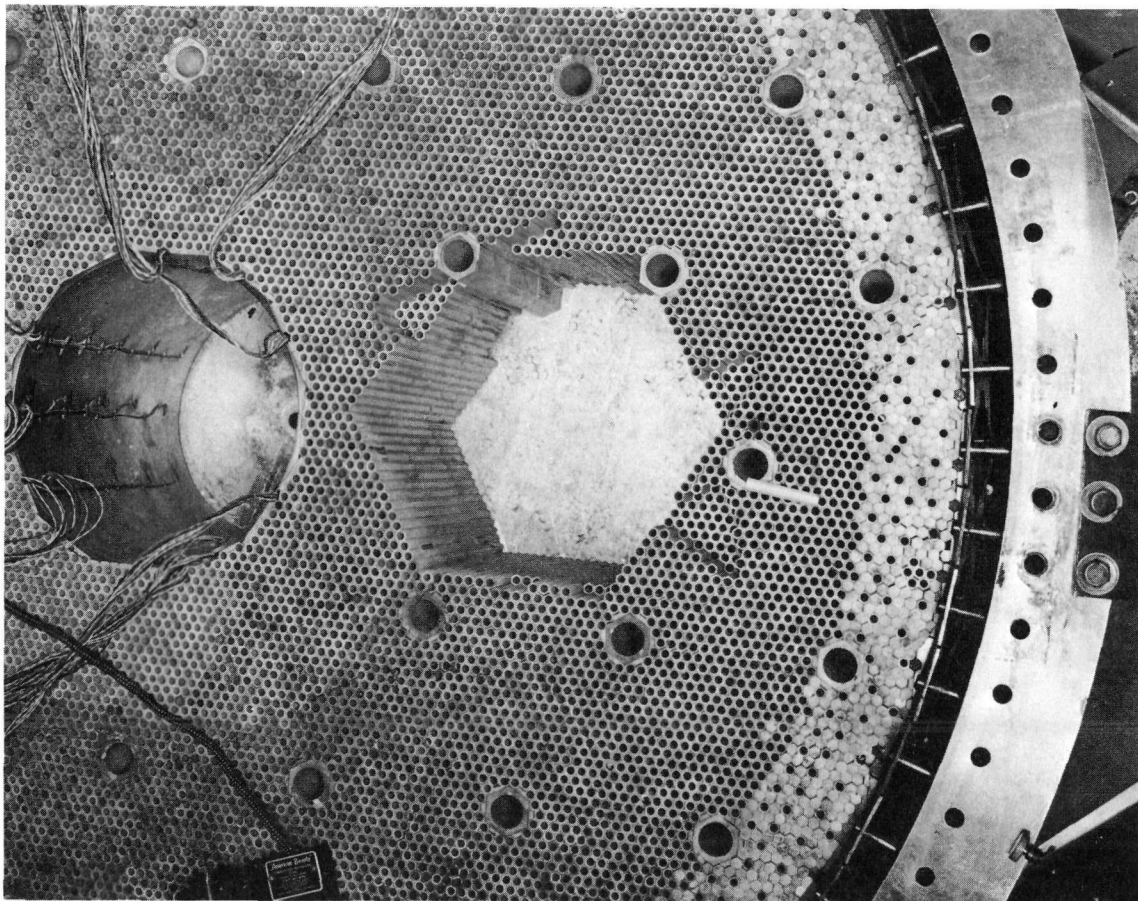


Fig. 4.67 - Three-tier mockup with 10 inch cavity after completion of 5 G shock load (C-23461)

edge of the hole is a function of the hole size relative to the size of the disc. By choosing a reasonable limit for this ratio, the stress (or pressure) concentration factor could be evaluated. Figure 4.68 shows an evaluation of this factor.

Considerations of local stability of the individual tubes, neglecting friction, showed that a single undersize tube could produce an adjacent pressure equal to twice the average pressure. From the same considerations, a pair of undersize tubes could produce an adjacent local pressure of three times the average pressure. Figure 4.69 illustrates these force polygons.

A pressure concentration factor of 3 was chosen on the basis of available experimental and analytical evidence. The maximum local pressure in the radial direction within the core was taken as 75 psi (the assumed maximum average radial pressure of 25 psi multiplied by a factor of 3 to account for the local pressure concentration factor).

A shift in the distribution of internal pressure was required to enable the bundle to act as a solid in distributing reactions to the structural shell. Figure 4.66 shows that the maximum compression incident to this shift occurred in the tangential direction, and was equal to four times the minimum pressure required to insure bundle stability. The maximum local pressure in the tangential direction within the tube bundle was 144 psi (the minimum average radial pressure of 12 psi multiplied by a factor of 4 to account for the pressure distribution resulting from inertial loading and a factor of 3 to account for the local pressure concentration factor).

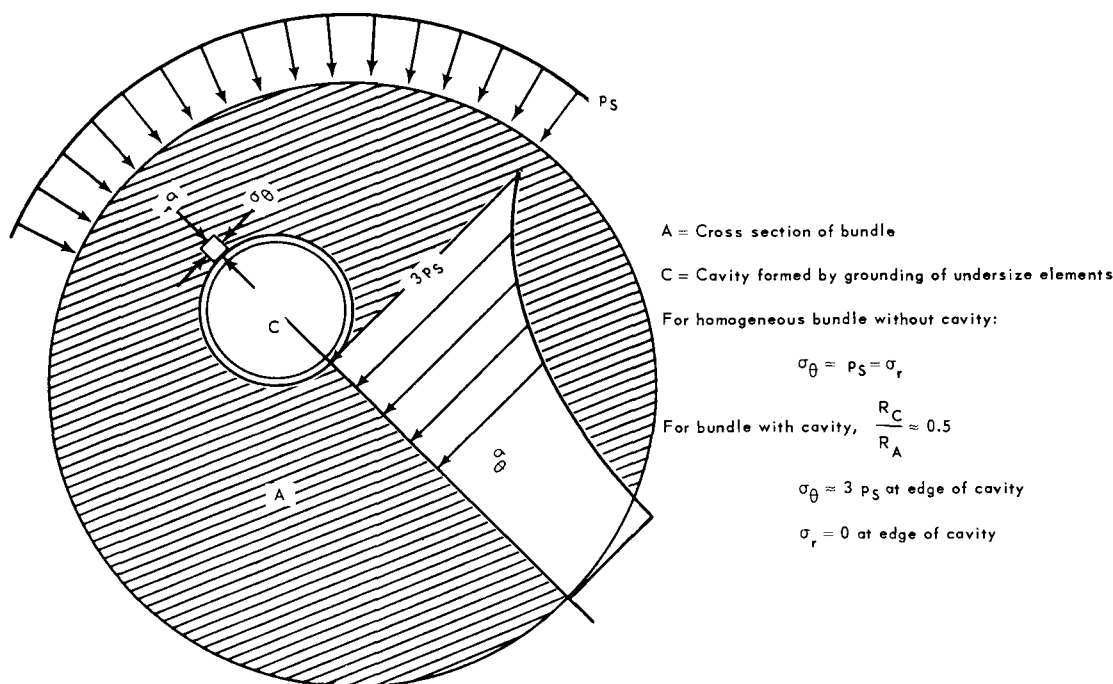
~~CONFIDENTIAL~~

Fig. 4.68 – Evaluation of stress concentration due to undersize elements

For either radial or tangential pressures, the average pressure was considered to be long-time loading. Maximum pressures were considered as short-time loading.

Longitudinal Support System - Axial restraint of the tube bundle was provided by aft-retainer plates and the forward reflector. The tube bundle was restrained but not pre-loaded by these components. Adequate clearance space was provided to permit the tube bundle and the metallic structure to expand independently as dictated by individual temperatures and material properties. Since the aerodynamic load was the principal load, the tube bundle normally was pressed against the aft-retainer assembly with a gap at the forward end. Frictional resistance to motion in the axial direction prevented dynamic loading.

Examination of the axial loading criteria showed that they were nearly as complex as the radial loading criteria. The complexities were introduced by the radial pressure and the consequent friction between elements that was developed in resisting and distributing axial loads. The friction enabled the bundle to perform as a load-carrying member and also introduced additional (to the aerodynamic forces) loads from the relative thermal displacements of the structural shell, shaft tunnel, core liner, and support structures. Axial loads were introduced into the core bundle by the effect of cooling-air pressure drop through the core, by friction through the pads caused by relative displacements between the shells and bundle, by friction from the core liner due to relative motion between liner and bundle, and by load bearing from the aft-retainer plates. Inertial loading also produced body forces within the bundle.

It was assumed that friction forces and body forces could be exerted in either direction, but that loads due to airflow pressure drop always were directed aft and that reactions from the aft-retainer plates always were directed forward. The load on individual tubes was friction limited, and excessive loads would spread the area of the reaction so that the friction limit would not be exceeded.

~~CONFIDENTIAL~~

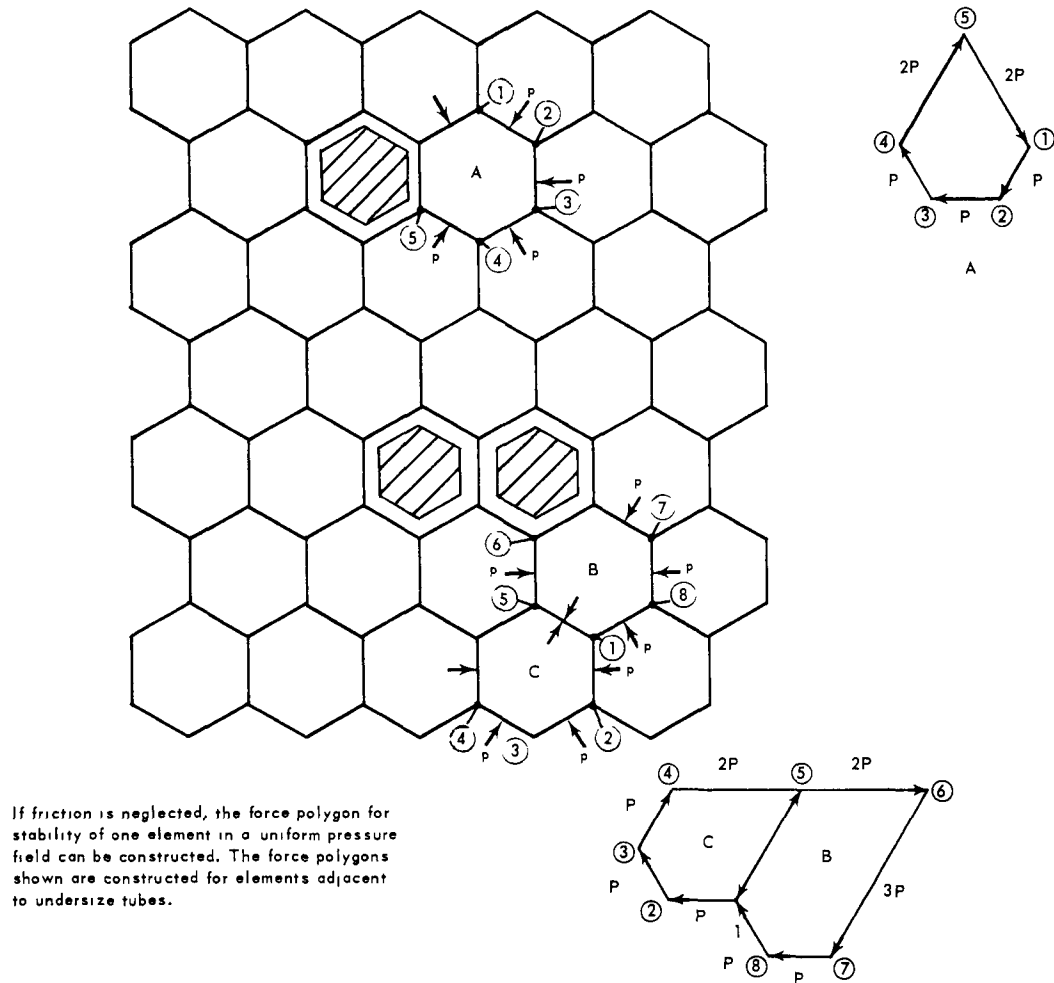


Fig. 4.69 – Force polygons for elements adjacent to undersize tubes

4.5.3.2 Mechanical Stresses in Fuel Element

The major mechanical loadings on the fuel elements were due to the radial pressure produced by the springs of the radial support system. The induced beam loading resulted from a fuel tube acting as a simple beam supported at each end with a concentrated load applied between the ends and tending to restrain or force deflections. These deflections could be caused by the manufacturing tolerances for camber and external surface dimensions, thermal camber, and core barrelling. The loading condition produced bending stresses in the axial direction. Ring loading resulted from the pressure concentrations acting on opposite faces of the hex tube. This loading condition also produced tangential bending stresses normal to the tube axis.

Tensile stresses were of primary concern in ceramic materials since the compressive strength was much greater than the tensile strength.

Method of Analysis - Thermal camber was the bowing in an element due to a linear temperature gradient across the diameter of the fuel tube. As shown in reference 21, the radius of curvature of a uniform bar of rectangular section that has one face at a uniform

~~CONFIDENTIAL~~

temperature T , the opposite face at a uniform temperature $T + \Delta T$, and a linear temperature gradient between these faces is as follows:

$$R = \frac{d}{\Delta T \alpha}$$

where d is the distance between the hot and cold faces. The method of computing this deflection is given in Figure 4.70.

The temperature distribution parallel to the core axis was not linear but varied as shown previously in Figure 4.48. As a result of radial expansions caused by this longitudinal temperature profile, the outer surface of the core bundle during nuclear operation assumed a curved shape similar to a barrel. This action was called core barreling.

In order to calculate the deflection of the tubes, the expansion of the tube bundle and the ability of the spring pressure to force the tubes into the barrel shape were evaluated. It was assumed that the maximum deflection occurred in the radial plane of the maximum longitudinal temperature. If each tube in this plane had been allowed to expand freely, it would take its own barrel shape. The problem lay in determining the shape of the individual tubes, and examining the effect of the available load on this shape.

Assuming the tubes fitted together as shown in Figure 4.71a, the gap, Δ , existing between the ends of adjacent tubes was given by the formula

$$\Delta = \alpha \left[T_m - \frac{1}{Z} (T_F + T_A) \right] w$$

where α was the instantaneous coefficient of thermal expansion, T is the temperature; the subscripts m , F , and A represented the middle, forward, and the aft ends of the tubes, respectively; w was the across-flats dimension, and Z was the total span.

Applying a load to the outer tube of a stack of barreled tubes, the tube would bend until it was in contact with the next tube, Figure 4.71b. The two tubes would then bend together as a composite beam ($I_n = 2I$ where I is the moment of inertia of one tube) until they contacted the third tube, Figure 4.71c. The three tubes would then act together until they

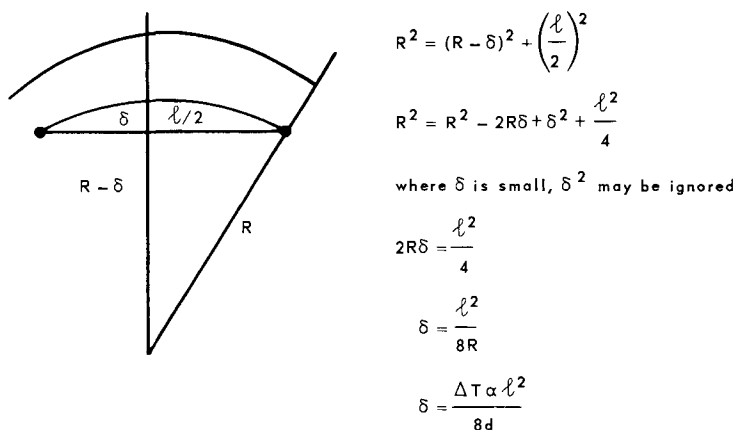


Fig. 4.70 – Method of calculating the deflection of the fuel element due to a linear gradient across the diameter

~~CONFIDENTIAL~~

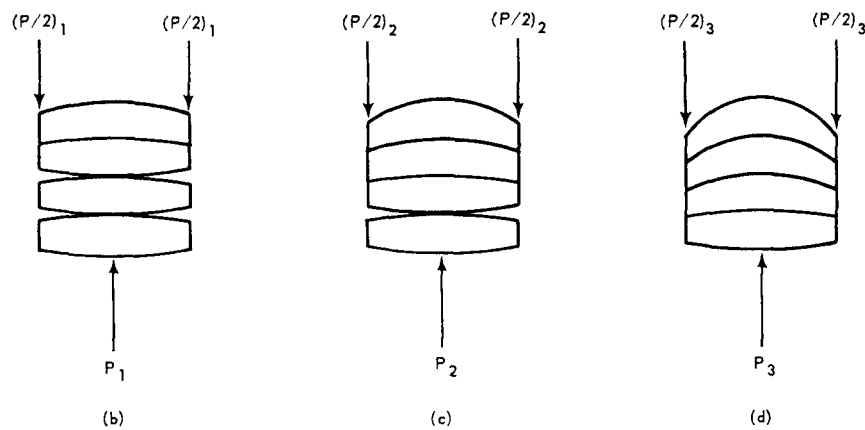
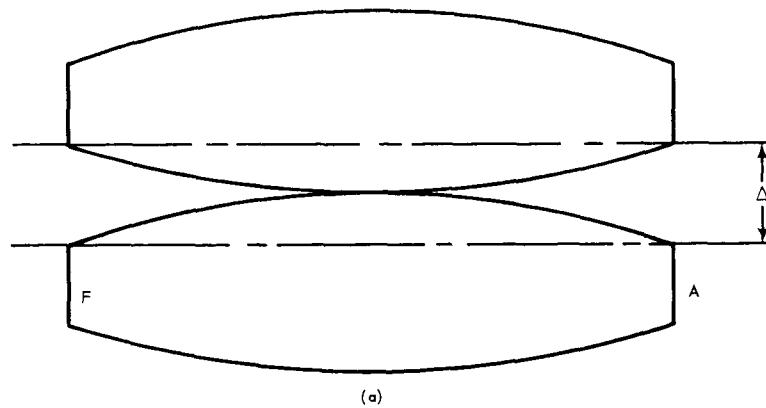


Fig. 4.71 – Camber forced by axial temperature gradient through core

contacted the fourth tube, Figure 4.71d. The process would continue until the total load causing the accumulated deflection was equal to the available load. Evaluating the loading,

$$\Delta_1 = \frac{P_1 l^3}{48EI}$$

$$\Delta_z = \frac{P_z l^3}{48E(zI)}$$

$$\Delta_n = \frac{P_n l^3}{48E(nI)}$$

$$P_n = \frac{48E(nI) \Delta_n}{l^3}$$

$$\sum P_n = \frac{48EI}{l^3} \sum n \Delta_n$$

Assuming Δ_n to be constant within the tubes considered,

$$\sum P_n = \frac{48EI \Delta_n}{l^3} \sum n$$

~~CONFIDENTIAL~~

Letting P_b be the available load, the number of tubes deflected, i , was determined as follows:

$$P_b = \sum_{n=1}^n P_n = \frac{48EI\Delta}{l^3} \sum_{n=1}^n n$$

$$\frac{P_b l^3}{48EI\Delta} = \sum_{n=1}^i n$$

The deflection of the first tube was $i\Delta_n$, and was equal to

$$i\Delta_n = \frac{Pl^3}{48EI}$$

The concentrated load necessary to completely force or restrain each individual deflection was computed from the familiar formula $P = 48EI\delta/l^3$. Inasmuch as it is possible for more than one individual deflection to occur in the same direction, the total load required to completely force or restrain the total deflection was calculated from the individual loads by superposition.

As previously shown, the maximum local pressure within the tube bundle was 144 psi in the tangential direction, and 75 psi in the radial direction. The load available to act as a concentrated load when restraining deflections in either direction was the corresponding pressure multiplied by the projected area of the fuel tube. For convenience, the projected area of the tube was chosen as the across-flats dimension multiplied by the length. Therefore, the maximum available concentrated load was 177 pounds in the tangential direction, and 92 pounds in the radial direction. If the available load in each direction was equal to or greater than the total load required to completely restrain or force deflections in the same direction, the stress was dependent on the deflection, and was computed by equating the deflection of the fuel tube to the deflection of a simple beam.

$$\delta = \frac{Pl^3}{48EI}, \text{ or } P = \frac{48EI\delta}{l^3}$$

$$m = \frac{Pl}{4}$$

$$\alpha = \frac{mc}{I} = \frac{Plc}{4I} = \frac{12E\delta c}{l^2}$$

However, if the maximum available load was less than the total load required to completely restrain or force the deflections in the same direction, the stress was dependent on the available load and was computed as follows:

$$m = \frac{Pl}{4}$$

$$\sigma = \frac{mc}{I} = \frac{Plc}{4I}$$

Since the available concentrated load was greater than the total load required to completely restrain or force the deflections of the fuel tubes, axial stresses were computed from the appropriate formulae. Plots of the calculated axial elastic stresses through the core are shown for three flight conditions, standard-day-cruise, emergency-power-setting, and ground-check-out in Figures 4.72, 4.73, 4.74, and 4.75.

~~CONFIDENTIAL~~

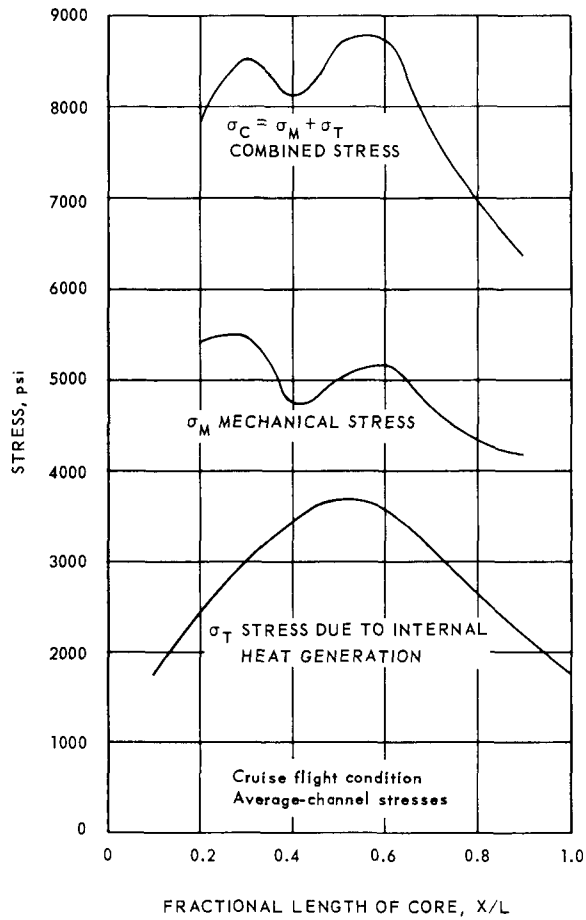
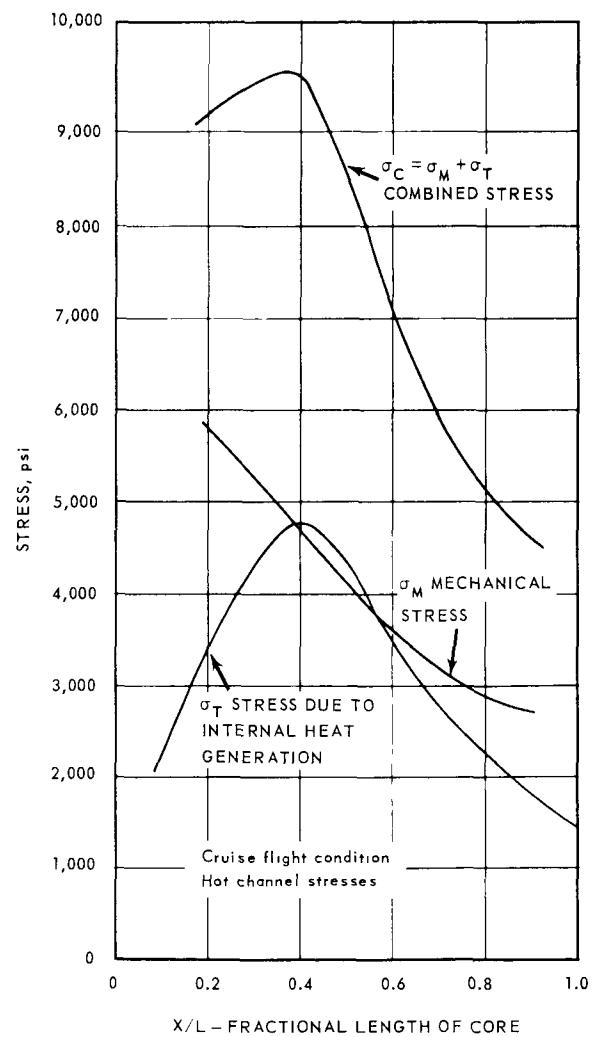


Fig. 4.72 – Axial stresses in the fuel tubes

Fig. 4.73 – Maximum axial stress in fuel tubes



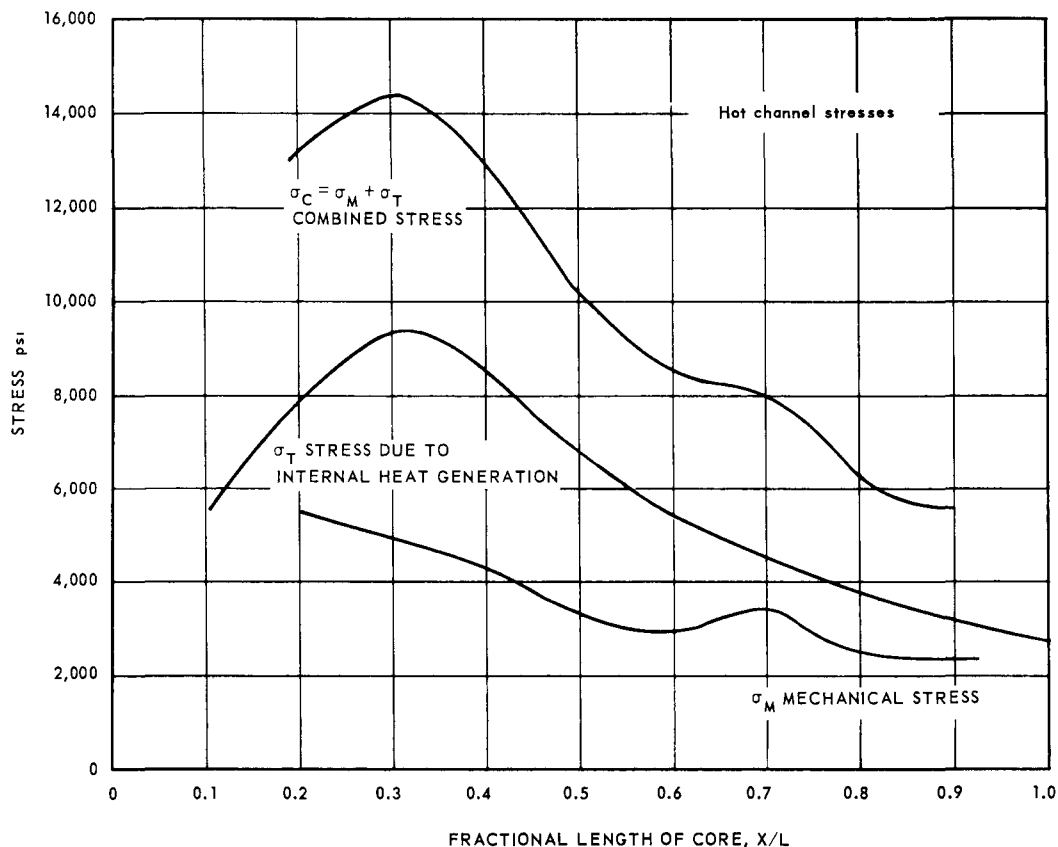
~~CONFIDENTIAL~~

Fig. 4.74 – Maximum axial stress in the fuel tubes, emergency flight condition

The maximum pressure concentrations acting on opposite faces of the tubes were evaluated to compute the ring bending stresses. The maximum concentrated loads used for ring loading calculations were computed by subtracting the concentrated load necessary to force or restrain the deflections from the total available load, and using the remainder as a uniformly distributed load. The concentrated load was assumed to act over a 1-inch length of the tube and was added to the uniformly distributed load to produce the maximum pressure concentration acting on opposite faces of the tube. (Other investigations of the effects of shear distribution of the load in the tube, and the reduction of stress under concentrated loading when the tube was loaded as a beam tended to confirm the assumption of the 1-inch load length.) Formulae for this loading are shown in Figure 4.76. Loads were computed for both the radial and tangential directions of the core, and the larger value was used for design purposes.

The ring bending stress then was computed, considering the tube as a ring of variable cross section, by the ASIST program for computer solution. The ASIST program was based on the principle of consistent deformations. Figure 4.77 shows the ratio of ring bending stress as a function of D/W calculated by this computer program.²²

Plots of the elastic tangential tensile stresses through the core for three flight conditions, standard-day-cruise, emergency-power-setting, and ground-check-out are shown in Figures 4.78, 4.79, 4.80, and 4.81.

~~CONFIDENTIAL~~

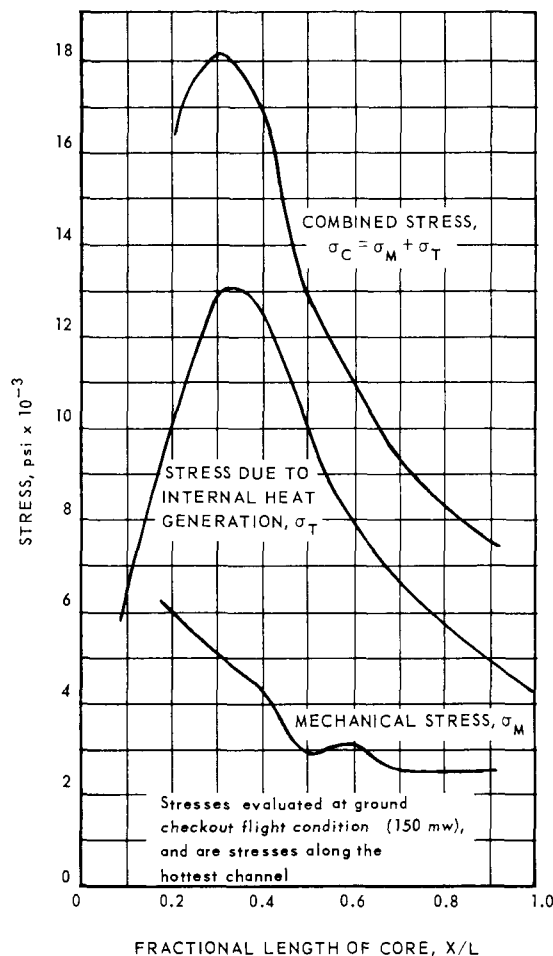


Fig. 4.75—Fuel element axial stress in hottest channel during ground checkout

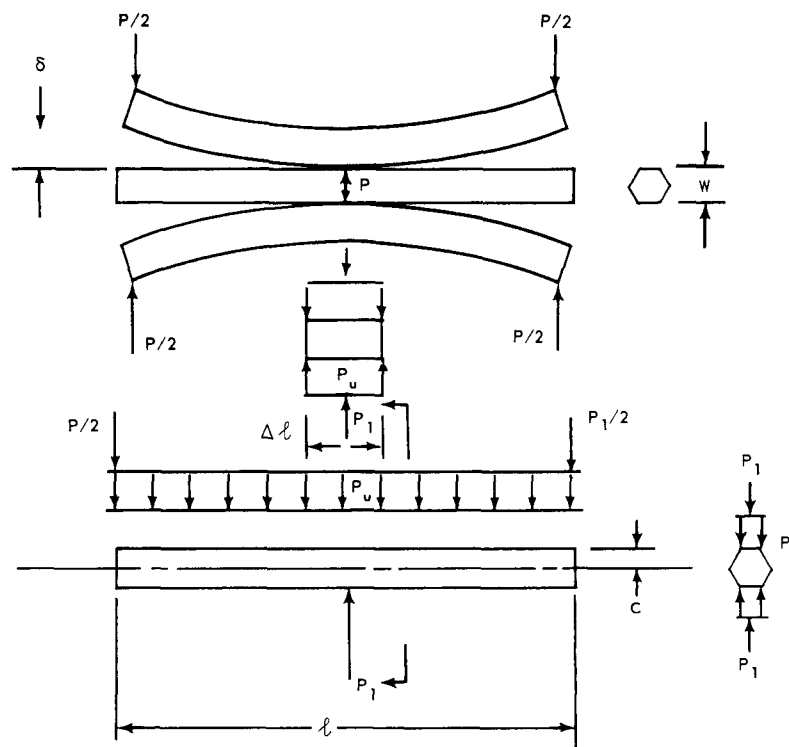
4.5.3.3 Thermal Stress in Fuel Elements

The fuel tube geometry represented a highly complex three-dimensional problem in thermoelasticity for which no completely rigorous analytical treatment was available. The differential equations of thermoelasticity are linear, and permit using the principle of superposition in the solution of thermoelastic problems. In the case of the XNJ140E-1 fuel element, the basic problem was divided into several component problems in order to simplify the analysis.

Examination of the problem indicated three significant sources of thermal stresses. These were as follows:

1. Radial temperature gradients.
2. Longitudinal (along the tube axis) temperature gradients.
3. Circumferential temperature scalloping.

Thermal stresses due to the radial temperature gradient were the primary thermal stresses in the fuel tubes. The approach used in the analysis of the thermal stresses due to the radial temperature gradients was first to solve the problem for an equivalent circular tube and then modify the solution with suitable correction factors to obtain the solution for the actual tube with hexagonal outer boundary. Correction factors were obtained

~~CONFIDENTIAL~~

δ = TOLERANCE OR THERMAL DEFLECTION

$$P_1 = \frac{48 E I \delta}{\ell^3}$$

$$\sigma = \frac{12 E \delta C}{\ell^2} \text{ (OUTER FIBRE)}$$

$$= \frac{12 E \delta D_h}{2 \ell^2} \text{ (BORE)}$$

$$P_u = \frac{P - P_1}{\ell}$$

$$P_C = P_1 + P_u (\Delta \ell)$$

Fig. 4.76—Bending load and stress in fuel element

~~CONFIDENTIAL~~

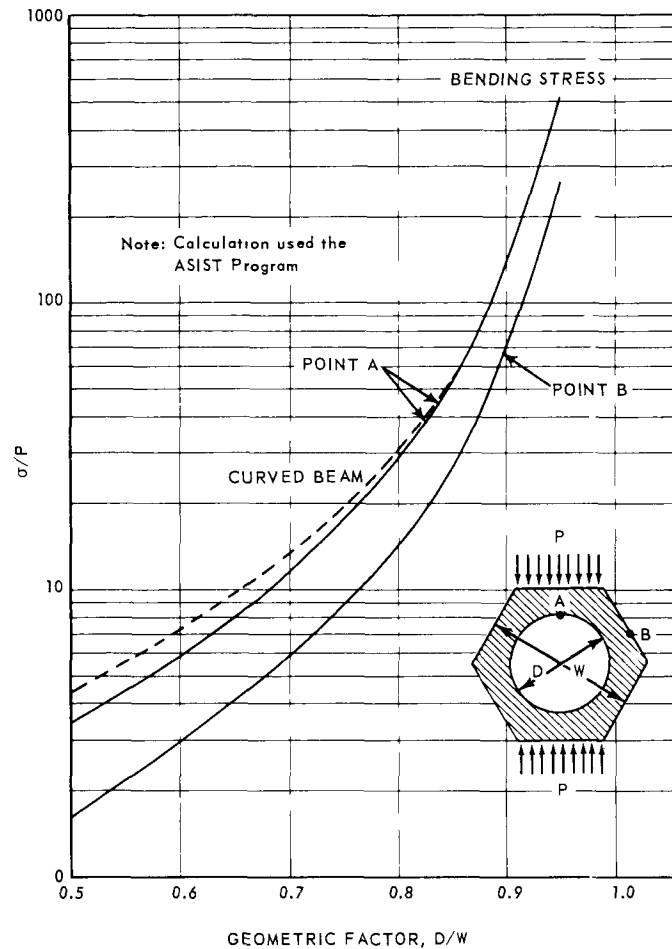


Fig. 4.77 — Hexagonal ring bending stress two side loading curved beam effect

from a finite difference IBM 704 computer solution of the thermoelastic equations. The computer program²³ solved the plane-stress and the plane-strain thermoelastic problem (both with internal heat generation) for any arbitrarily shaped two-dimensional region. Because of its generality, and also because of the large number of mesh points required in the solution of the hexagonal tube geometry, the most economical way to utilize this program was to conduct a parametric study to determine correction factors which could be used in conjunction with the equivalent circular tube solution. The correction factors were then expressed as functions of the parameter, W/D_i , where W is the across-flats dimension of the hexagonal tube and D_i is the inner diameter of the tube.

Since the solution included the case of plane-strain (infinite length tube), end correction factors were applied in order to obtain the maximum stresses at the ends of the tube. No exact solution was available for the end stresses in hexagonal tubes, and an approximate solution, based on the solution for a thin-walled circular tube, was developed.

Thermal stresses due to axial temperature gradients were negligible. Reference 24 shows that these stresses are proportional to the second derivative of the temperature with respect to the axial coordinate (d^2T/dx^2). Under reactor operating conditions the value of d^2T/dx^2 was always so small that the resulting stresses were neglected.

Stresses due to circumferential temperature scalloping could be caused by both internal and external reasons. Within an individual tube, the effects of the hexagonal outer

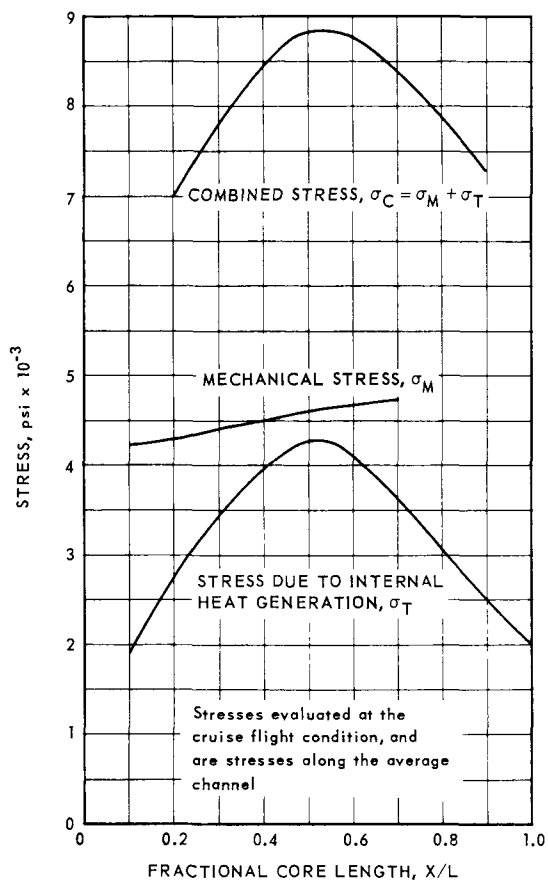
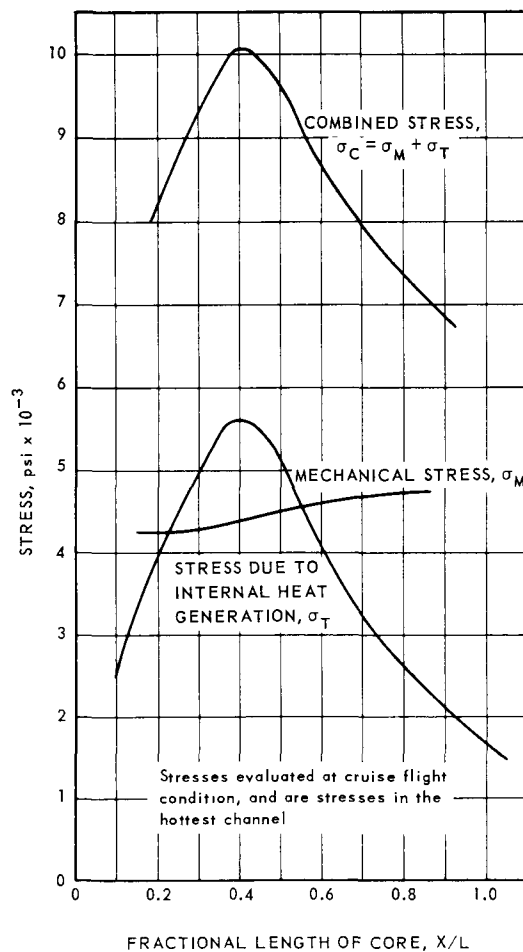
~~CONFIDENTIAL~~

Fig. 4.78 – Fuel element tangential stress in average channel

Fig. 4.79 – Fuel element tangential stress in hottest channel

~~CONFIDENTIAL~~

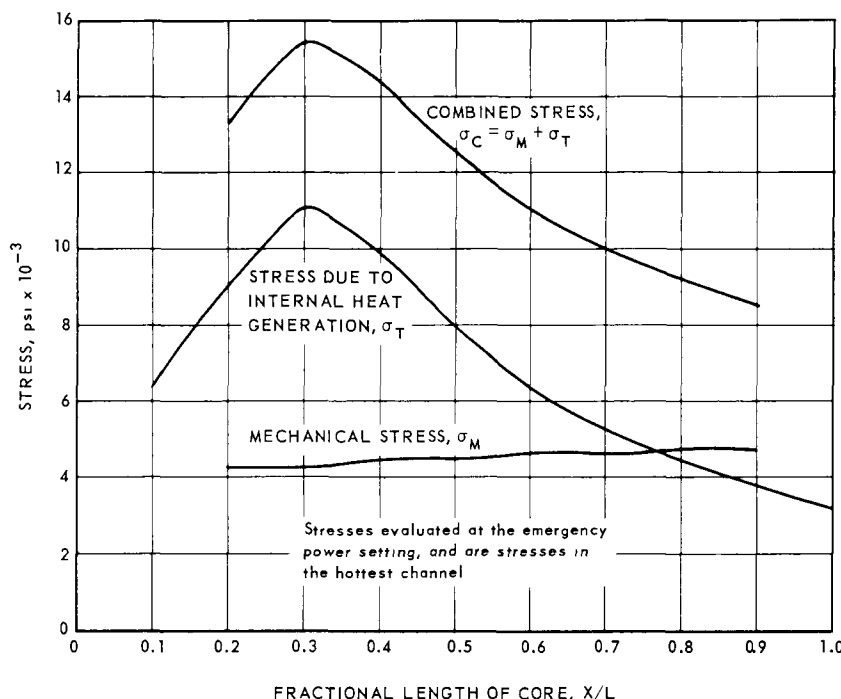


Fig. 4.80 - Fuel element tangential stress in hottest channel

surface of the tube and the lack of homogeneity of material properties were considered. The effect of the hexagonal outer surface was discussed as a radial temperature gradient. Thermal stresses induced by the lack of homogeneity of materials were negligible. Asymmetry of reactor configuration, neutron flux distribution, and temperature distributions were considered as external sources of thermal stresses. The most probable effects of asymmetry external to an individual tube were to produce linear temperature gradients across the diameter of the tube. These gradients would cause the tube to bow if it were not for external restraint. Stresses resulting from this external restraint were considered mechanical stresses as discussed previously.

Method of Analysis - The assumptions made in thermal stress analyses were the usual assumptions made in applying elasticity theory, together with the assumptions of a Maxwell-type model for representing creep behavior.

Assumptions concerned with the use of the circular tube analogy were as follows:

1. Plane sections remained plane.
2. The principle of superposition was applicable.
3. The materials obeyed Hooke's law on a short-time basis.
4. The materials obeyed a creep law in which the strain rate was proportional to the stress (Maxwell-type body).
5. Temperature variation within the body did not produce significant variations in material properties.
6. End correction factors derived for a thin circular cylinder were valid when used in conjunction with the infinite length solution for a hexagonal tube to obtain end stresses in a hexagonal tube of finite length.

Symbols used in the analysis are as follows:

Matrix inner radius, a	inch
Outer radius of an equivalent annulus, b	inch

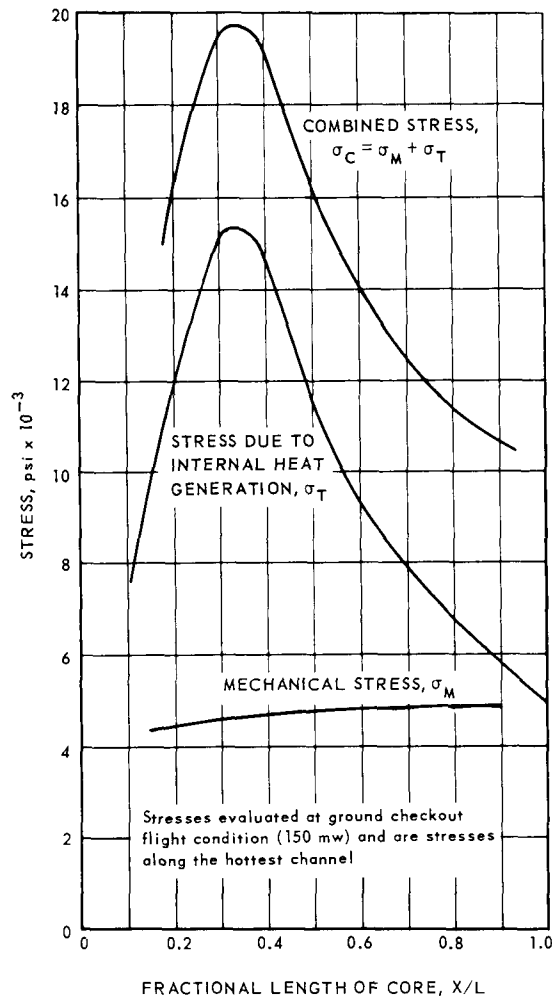
~~CONFIDENTIAL~~

Fig. 4.81—Fuel element tangential stress in hottest channel

Subscript referring to the clad, c

Modulus of elasticity, E

Conductivity, k

Subscript referring to the matrix, m

Subscript referring to the tube inner diameter, i

Internal heat generation rate, q'''

Time, t

Temperature, T

Across flats dimension of a hexagon, w

Axial coordinate, z

Coefficient of thermal expansion, α

Clad thickness, ϵ

Angular coordinate, θ

Poisson's ratio, ν

Stress, σ

psi

Btu per inch per second per $^{\circ}\text{F}$

Btu per cubic inch per second

second

$^{\circ}\text{F}$

inch

inch

inches per inch per $^{\circ}\text{F}$

inch

radians

psi

The general approach used in the calculation of the thermal stresses due to radial temperature gradients was to use hexagonal tube correction factors in conjunction with the equivalent circular tube solution. The hexagonal tube correction factors were ex-

~~CONFIDENTIAL~~

pressed as functions of the geometric parameter, W/D_i . Figures 4.82 and 4.83 show plots of nondimensionalized stress for the hexagonal tube and an equivalent annulus as a function of W/D_i . Stresses calculated in this manner represented an infinite length solution, and were stresses existing in sections remote from the ends of the tube.

ANP Computer Program No. 602 - An IBM 704 computer program, ANP Program No. 602, Clad Tube Stress Calculations was developed for the thermal stress calculations. The program considered the effect of the cladding material on thermal stresses.

Temperature profile calculations were based on an equivalent circular tube, equations for which are available in published literature.²⁵ These equations are repeated below, using nomenclature defined above and in Figures 4.84 and 4.85.

In the matrix

$$\begin{aligned}\Delta T_m &= (T_{mavg} - T_a) \\ &= \frac{q_m'''}{8k_m} \left[a^2 - 3b^2 + \frac{2b^4 \ln \frac{b^2}{a^2}}{b^2 - a^2} \right]\end{aligned}$$

and

$$T_b - T_a = \frac{q_m'''}{4k_m} \left[a^2 - b^2 + b^2 \ln \frac{b^2}{a^2} \right]$$

In the clad

$$\begin{aligned}\Delta T_c &= T_{cavg} - T_i \\ &= \frac{q_c'''}{8k_c} \left[\frac{(a - \epsilon)^2}{a^2} - 3 + \frac{4a^2 \ln \left(\frac{a}{a - \epsilon} \right)}{2a\epsilon - \epsilon^2} \right] a^2 \\ &\quad + \frac{q_m''' (b^2 - a^2)}{4k_c} \left[\frac{2a^2 \ln \left(\frac{a}{a - \epsilon} \right)}{2a\epsilon - \epsilon^2} - 1 \right]\end{aligned}$$

and

$$\begin{aligned}T_a - T_i &= \frac{q_c''' a^2}{4k_c} \left[2 \ln \left(\frac{a}{a - \epsilon} \right) - \frac{2a\epsilon - \epsilon^2}{a^2} \right] \\ &\quad + \left[\frac{q_m''' (b^2 - a^2)}{2k_c} \left(\ln \frac{a}{a - \epsilon} \right) \right]\end{aligned}$$

Thermal stress formulae for the case of a long tube (plane-strain) subject to an axisymmetric radial temperature profile also are readily available in the literature.²⁶

Thermal stresses induced by the differential thermal expansion between the clad and the matrix were calculated by allowing independent free thermal expansions of the clad and the matrix. Surface tractions (at the clad-matrix interface) required to restore continuity at the clad-matrix interface then were determined, based on thick cylinder equations.²⁷ The resulting stresses then were calculated and superimposed on the thermal stresses due to radial temperature gradients in each of the components.

Calculating stresses as indicated above, and including hexagonal tube and end correction factors, yielded the following equations for the stresses at points A, B, and O. (These were the points of the maximum tensile and compressive stresses in the tube at the operating condition.)

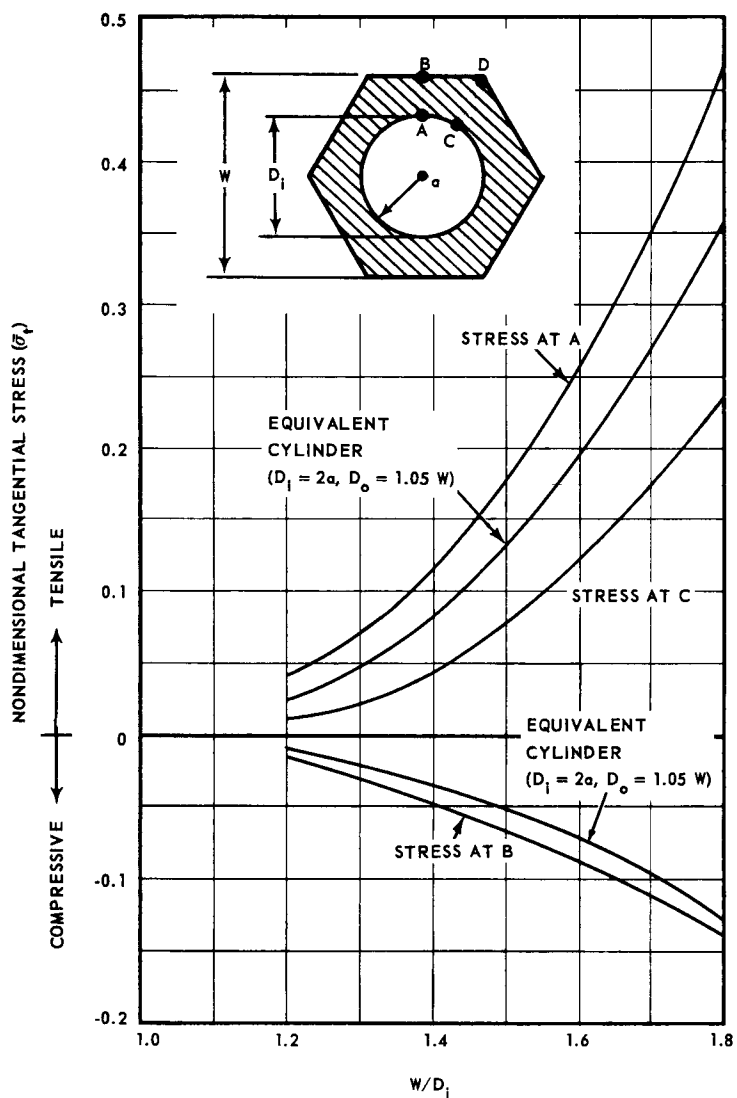
~~CONFIDENTIAL~~

Fig. 4.82—Tangential thermal stress in fuel element

~~CONFIDENTIAL~~

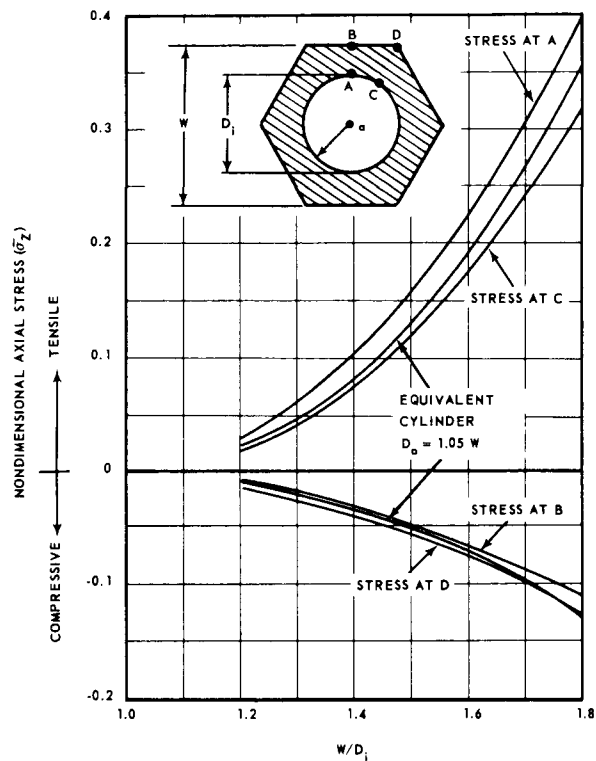


Fig. 4.83 – Axial thermal stress in fuel element

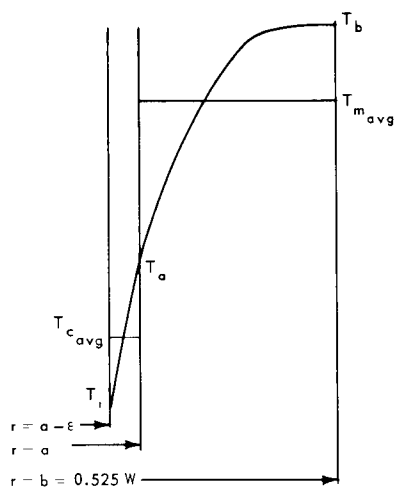


Fig. 4.84 – Terminology for temperature distribution in the "equivalent" circular tube

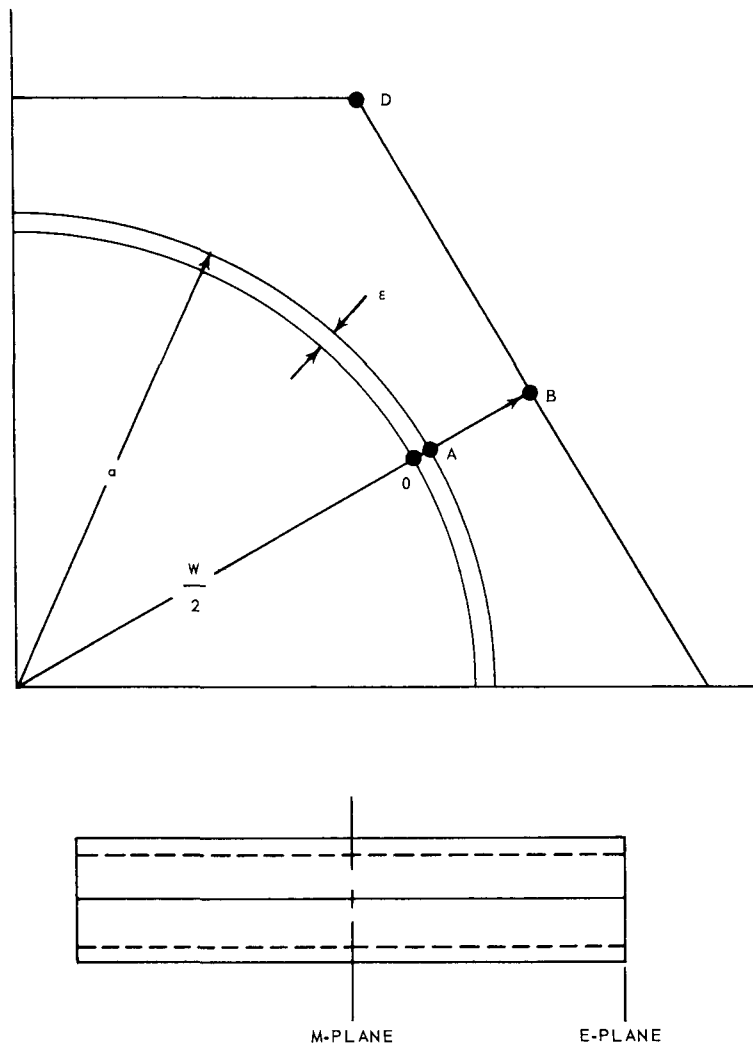
~~CONFIDENTIAL~~

Fig. 4.85—Locations for tube thermal stresses, ANP program No. 602

Stress in the clad at point O

$$\sigma_{\theta c} = e_i H_i \left[\left(\frac{E_c \alpha_c^*}{1 - \nu_c} \right) \Delta T_c - L_{ci} P_2 \right] - L_{ci} P_1$$

Stress in the matrix at point A

$$\sigma_{\theta m} = e_A H_A \left[\left(\frac{E_m \alpha_m^*}{1 - \nu_m} \right) \Delta T_m + L_{ma} P_2 \right] + L_{ma} P_1$$

Stress in the matrix at point B

$$\sigma_{\theta m} = e_B H_B \left(\frac{E_m \alpha_m}{1 - \nu_m} \right) \{ \Delta T_m - (T_b - T_a) \} + L_{mb} P_2 + L_{mb} P_1$$

~~CONFIDENTIAL~~

The following definitions apply to three equations given above:

e = appropriate end correction factor ($e = 1.0$ for points remote from the tube ends)

H = appropriate geometric correction factor for hexagonal tube geometry

$$P_1 = \frac{a}{k_m + k_c} [(1 + \nu_c) \alpha_c^{**} - (1 - \nu_m) \alpha_m^{**}] (T_i + \Delta T_c)$$

$$P_2 = \frac{-a}{k_m + k_c} [(1 + \nu_m) (\alpha_m^*) (T_{m_{avg}} + T_{c_{ave}})]$$

$$k_m = \frac{a(1 + \nu_m)}{E_m} [(1 - \nu_m) L_{ma} + \nu_m]$$

$$k_c = \frac{a(1 + \nu_c)}{E_c} [(1 - \nu_c) L_{ca} - \nu_c]$$

$$L_{ca} = \frac{2a^2 - 2a\epsilon + \epsilon^2}{2a\epsilon - \epsilon^2}$$

$$L_{ci} = \frac{2(a - \epsilon)^2}{2a\epsilon - \epsilon^2}$$

$$L_{mb} = \frac{2a^2}{b^2 - a^2}$$

$$L_{ma} = 1 + L_{mb}$$

and superscripts * and ** indicate instantaneous and mean values of the parameter, respectively.

The numerical values for H were obtained from Figures 4.82 and 4.83 as follows:

$$H = \frac{\bar{\sigma} (W/D_i) \text{ for the hexagonal tube}}{\bar{\sigma} (W/D_i) \text{ for the equivalent annulus}}$$

The maximum tangential and axial elastic thermal stresses as a function of the fractional distance through the core were shown previously in Figures 4.72 through 4.75, and Figures 4.78 through 4.81.

Combined Total Stresses and Allowable Stresses - Tensile stresses in the ceramic materials were of greater importance because the compressive strength was much greater than the tensile strength. Therefore, stress combinations were directed toward determining the maximum tensile stresses. The total stresses at a point were obtained by combining the thermal and mechanical stresses using the principle of superposition. These combinations were made for (1) the initial elastic tensile stresses that occurred during operation, and (2) the residual stresses that occurred at room temperature after reactor shutdown from nuclear operation. These combined stresses were the values plotted in Figures 4.72 through 4.75, and Figures 4.78 through 4.81.

A design criterion established for the fuel elements required that the ultimate stress (1.5 times the limit stress) be compared to the minimum modulus of rupture (average modulus of rupture minus three standard deviations). These comparisons, together with the resultant margins-of-safety, are shown in Tables 4.31, 4.32, and 4.33 for conditions following engine shutdown from standard-day-cruise, emergency-power-setting, and ground-checkout, respectively.

The validity of the above methods in calculating safe operating stress levels was demonstrated by a series of in-pile tests and a factorial experiment conducted in support of the reactor design program.²⁸

~~CONFIDENTIAL~~

TABLE 4.31

**FUEL ELEMENT COMBINED OPERATING STRESSES AND MAXIMUM COMBINED STRESSES
AT ROOM TEMPERATURE FOLLOWING SHUTDOWN FROM DESIGN POINT**

		Average Channel					Hot Channel				
	STA	T, °F	σ, psi	3σ/2, psi	MR, psi	MS	T, °F	σ, psi	3σ/2, psi	MR, psi	MS
Operating	0										
	3	1,173			32,600		1,278			33,800	
	6	1,411	7,829	11,744	35,200	1.99	1,559	9,189	13,784	36,300	1.63
	9	1,613	8,494	12,741	36,600	1.87	1,797	9,491	14,237	36,900	1.59
	12	1,792	8,383	12,575	36,900	1.93	2,008	10,045	15,068	35,700	1.36
	15	1,942	8,811	13,217	36,400	1.75	2,184	9,661	14,492	33,100	1.28
	18	2,067	8,778	13,167	35,200	1.67	2,331	8,656	12,984	30,000	1.31
	21	2,146	8,338	12,507	34,000	1.71	2,425	7,946	11,919	27,100	1.27
	24	2,196	7,840	11,760	33,000	1.80	2,483	7,371	11,057	25,200	1.27
	27	2,211	7,282	10,923	32,600	1.98	2,501	6,880	10,320	24,600	1.38
	30	2,189			33,000		2,475			25,500	
Residual	X		6,893	10,340	12,800	0.238		7,972	11,958	12,800	0.0704

STA = Longitudinal distance from leading edge of the active core, in.

T = Temperature at the longitudinal position

σ = Combined stress at the longitudinal position

MR = Average modulus of rupture minus a 3 standard deviation at the temperature indicated

MS = Margin of safety = $\frac{MR}{1.5\sigma} - 1$

X = Maximum combined stress at room temperature after shutdown, psi at 70°F

TABLE 4.32

**FUEL ELEMENT COMBINED OPERATING STRESSES AND MAXIMUM COMBINED STRESSES
AT ROOM TEMPERATURE FOLLOWING SHUTDOWN FROM EMERGENCY POWER SETTING**

		Average Channel					Hot Channel				
	STA	T, °F	σ, psi	3σ/2, psi	MR, psi	MS	T, °F	σ, psi	3σ/2, psi	MR, psi	MS
Operating	0										
	3	1,381			34,900		1,485			35,800	
	6	1,617	10,935	16,403	36,600	1.231	1,762	13,316	19,974	37,000	0.852
	9	1,814	12,113	18,170	36,900	1.03	1,993	15,410	23,115	34,700	0.501
	12	1,985	13,145	19,718	36,000	0.825	2,194	14,332	21,498	33,000	0.535
	15	2,124	12,900	19,350	34,100	0.762	2,357	12,489	18,734	29,200	0.558
	18	2,237	11,528	17,292	32,000	0.85	2,490	10,950	16,425	24,900	0.515
	21	2,299	10,643	15,965	30,500	0.91	2,562	10,011	15,017	22,400	0.491
	24	2,332	9,799	14,699	29,800	1.02	2,601	9,180	13,770	20,700	0.503
	27	2,330	9,009	13,514	29,800	1.2	2,599	8,478	12,717	20,700	0.627
	30	2,292			30,700		2,554			22,400	
Residual	X		5,936	8,904	12,800	0.437		10,425	15,638	12,800	-0.1815

STA = Longitudinal distance from leading edge of the active core, in.

T = Temperature at the longitudinal position

σ = Combined stress at the longitudinal position

MR = Average modulus of rupture minus a 3 standard deviation at the temperature indicated

MS = Margin of safety = $\frac{MR}{1.5\sigma} - 1$

X = Maximum combined stress at room temperature after shutdown, psi at 70°F

~~CONFIDENTIAL~~

TABLE 4.33

FUEL ELEMENT COMBINED OPERATING STRESSES AND MAXIMUM COMBINED STRESSES
AT ROOM TEMPERATURE FOLLOWING SHUTDOWN FROM EXTENDED GROUND CHECKOUT

	Average Channel						Hot Channel				
	STA	T, °F	σ , psi	$3\sigma/2$, psi	MR, psi	MS	T, °F	σ , psi	$3\sigma/2$, psi	MR, psi	MS
Operating 0											
↓	3	1,230			33,200		1,350			34,550	
	6	1,501	12,764	19,146	35,950	0.878	1,665	16,175	24,263	36,800	0.517
	9	1,717	14,408	21,612	36,900	0.707	1,916	19,575	29,363	36,500	0.243
	12	1,897	16,421	24,632	36,600	0.486	2,125	19,205	28,808	34,200	0.187
	15	2,038	16,593	24,890	35,400	0.422	2,289	16,341	24,512	30,800	0.256
	18	2,149	14,960	22,440	33,750	0.504	2,418	13,915	20,873	27,200	0.303
	21	2,204	13,586	20,379	32,800	0.609	2,482	12,600	18,900	25,200	0.333
	24	2,227	12,547	18,821	32,200	0.711	2,509	11,578	17,367	24,200	0.335
	27	2,213	11,441	17,162	32,500	0.894	2,493	10,637	15,956	24,800	0.554
	30	2,161			33,500		2,432			26,900	
Residual X			7,101	10,652	12,800	0.202		16,280	24,420	12,800	-0.4758

STA = Longitudinal distance from leading edge of the active core, in.

T = Temperature at the longitudinal position

σ = Combined stress at the longitudinal position

MR = Average modulus of rupture minus a 3 standard deviation at the temperature indicated

MS = Margin of safety = $\frac{MR}{1.5\sigma} - 1$

X = Maximum combined stress at room temperature after shutdown, psi at 70°F

These tests were oriented towards evaluating the residual tensile stresses in fuel elements at room temperature after operating for sufficient times at elevated temperatures to permit partial or complete relaxation of the initial elastic operating stresses. Residual stresses were computed as discussed above.

The factorial experiment was a statistical experiment designed to study the resistance of zirconia-clad tubes to thermal stress. The three variables, heat flux, temperature, and time, were chosen to produce no cracking at the least severe conditions, increased cracking at more severe conditions, and cracking in almost all of the tubes at the worst conditions. Five tubes were tested at each of 27 different combinations of the three variables. The outer fiber tensile residual stresses were calculated for each of the 27 different conditions. Initial elastic operating tensile stresses also were calculated, but were well below the residual stresses when relaxation was nearly complete.

These tests indicated that cracking did not occur when the calculated residual stress was less than the minimum modulus of rupture. It was also apparent that the tubes remained functional even if a crack did develop. Cracks were detectable only by sensitive inspection methods, using zyglo, statiflex, and ultrasonic techniques.

Results of an extended series of in-pile tests (MTR, ETR, ORR, LITR, and HTRE No. 2) also confirmed that tubes did not crack when the calculated stresses were below the minimum modulus of rupture. These tubes also maintained their functional ability even if minute cracks developed.

4.5.3.4 Stress Relaxation and Residual Stresses

The fuel element matrix crept under moderate stress levels at high temperature, approximately 2000°F and above. This creep affected fuel element stresses both during

~~CONFIDENTIAL~~

operation at elevated temperature, and following shutdown when the reactor had cooled to room temperature.

During operation at elevated temperatures, thermal stresses relaxed due to local plastic deformation, and led to a condition in which the fuel element contained thermal strains and low stresses following relaxation. When the fuel element later was cooled to room temperature, the plastic strain that had occurred at elevated temperature reappeared as elastic strain and introduced residual stresses (at room temperature). If creep had significantly relieved the operating stresses, the corresponding residual stresses could exceed the operating stresses by factors as high as the ratio of the modulus of elasticity at room temperature to the modulus of elasticity at the operating temperature.

In calculations of residual thermal stresses, it was assumed that the materials obeyed a creep law in which the strain rate is proportional to the stress (Maxwell-type body). The assumption of a Maxwell-type model, $\dot{\epsilon} = K_0 \sigma_0$ defining the creep behavior of the material concerned, implied that the elastic stresses at any given time, t , were $\sigma = \sigma_0 e^{-\beta t}$ where β was a materials constant associated with K_0 , and σ_0 was the calculated initial elastic stress. The residual stress which existed upon return to room temperature was

$$\sigma_{\text{Res}} = \frac{E_{\text{RT}}}{E_{\text{HT}}} \sigma_0 (e^{-\beta t} - 1).$$

Mechanical stresses also were affected by creep. During operation, the axial bending stresses relaxed until, assuming complete relaxation, the individual tubes were stress-free and bowed to fit the shape of the core. Ring-bending stresses caused by pressure concentrations acting on opposite faces of the tubes were relieved. In fact, plastic deformation resulted in a compressive stress as a result of the tube assuming a more favorable geometry for pressure distribution. The deformation proceeded until the surrounding elements were forced to assume their share of the load, and the loading pattern changed from that of a two-sided load to that of a six-sided load. Under this condition, further deformation was unlikely. Compressive stresses induced by a uniform six-sided loading, with average radial pressure of 25 psi, were approximately 75 psi. At this stress level, compressive creep was negligible except at very high temperatures. (At 2600°F, the amount of creep observed in 1000-hour testing was very small.) Since most of the reactor operated at temperatures well below those at which any significant creep occurred, compressive creep was not considered a design problem.

The thermal and mechanical stresses existing in the fuel elements at room temperature following shutdown from nuclear operation equivalent to the extended standard-day cruise flight condition are shown in Figure 4.86. Stresses following shutdown from other flight conditions are shown in reference 28. Residual thermal stresses did not occur in the cooler regions of the reactor because the creep rate was appreciably lower at the lower temperatures.

4.6 OUTER REFLECTOR COMPONENT DESIGN DATA

4.6.1 MECHANICAL DESIGN

The outer reflector consisted of hexagonal-shaped beryllia rods which formed an 8.5-inch-thick circular ring around the active core over its entire length. Interspaced between the rods at specific locations were hexagonal-shaped beryllia tubes which formed cooling channels to remove secondary heat. In addition to its function as a neutron reflector, the

~~CONFIDENTIAL~~

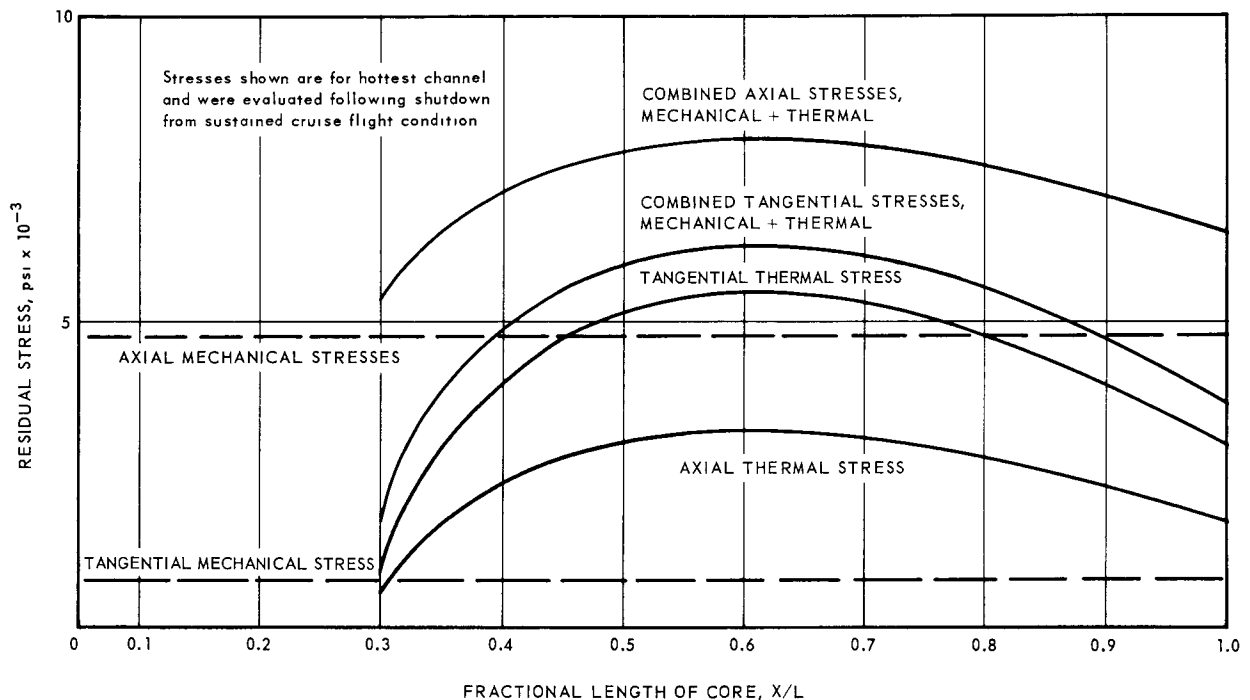


Fig. 4.86—Residual stress in the fuel tubes at room temperature

outer reflector also served as a thermal shield between the active core and the radial support system.

During steady-state operation at the design point, the temperature in the outer reflector increased in the longitudinal direction from 800°F at the forward end to 2200°F near the aft end. Radially, in the plane of the maximum longitudinal temperature, the temperature decreased almost linearly from 2200°F at the reflector core interface to 1000°F at the outside surface of the reflector. Following reactor shutdown, the reactor core cooled rapidly because of the large surface-to-volume ratio, while the outer reflector remained hot longer because of the smaller amount of cooling surface. Analysis of differential expansions indicated the possibility of a 0.150-inch radial gap between the active core and the reflector during certain operating conditions. The outer reflector pieces were undersized by 0.002 inch across flats relative to the fuel elements to allow for this difference in thermal expansion and insure that radial spring pressure was transmitted through the tube bundle to maintain structural integrity at all times.

4.6.1.1 Mechanical and Thermal Stresses

Mechanical loadings on the outer reflector elements, tubes and rods were the same as those imposed on the fuel elements. Beam loading resulted from the reflector elements acting as simple beams supported at each end with a concentrated load, resulting from the radial pressure, applied near the center and restraining, or forcing deflections. Thermal camber was much greater in the outer reflector elements than in the fuel elements because of the larger radial temperature gradient across the outer reflector.

If the outer reflector elements had been the same length as the fuel elements, sufficient radial pressure was available to force complete deflection. The resulting tensile bending stress would have exceeded the allowable stress. Therefore, the elements were shortened to 1.426 inches in length so that the available force would not restrain or force

~~CONFIDENTIAL~~

complete camber deflection. The stress then was independent of camber and was limited to the available load.

Stress in the outer reflector was computed by the following formula:

$$\sigma = \frac{1.155 W^2 l^2 p}{8I}$$

where

W = distance across flats, in.

l = length, in.

p = radial pressure including appropriate magnification factors, psi

I = moment of inertia, in.⁴

Maximum longitudinal tensile stresses were 12,700 and 16,500 psi for the rods and tubes, respectively.

The tubes also were subjected to ring loading which resulted from pressure concentrations tending to crush the tubular elements. These stresses were calculated by methods similar to those used in fuel element stress analysis.

Further tangential and axial thermal stresses were induced in the tubes by the temperature gradients resulting from conducting internally generated secondary heat to the convective heat transfer boundary.

Each of the individual stresses was computed. They then were combined by the principle of superposition. A survey of stresses in the outer reflector tubes along the length of the active core is shown in Figure 4.87.

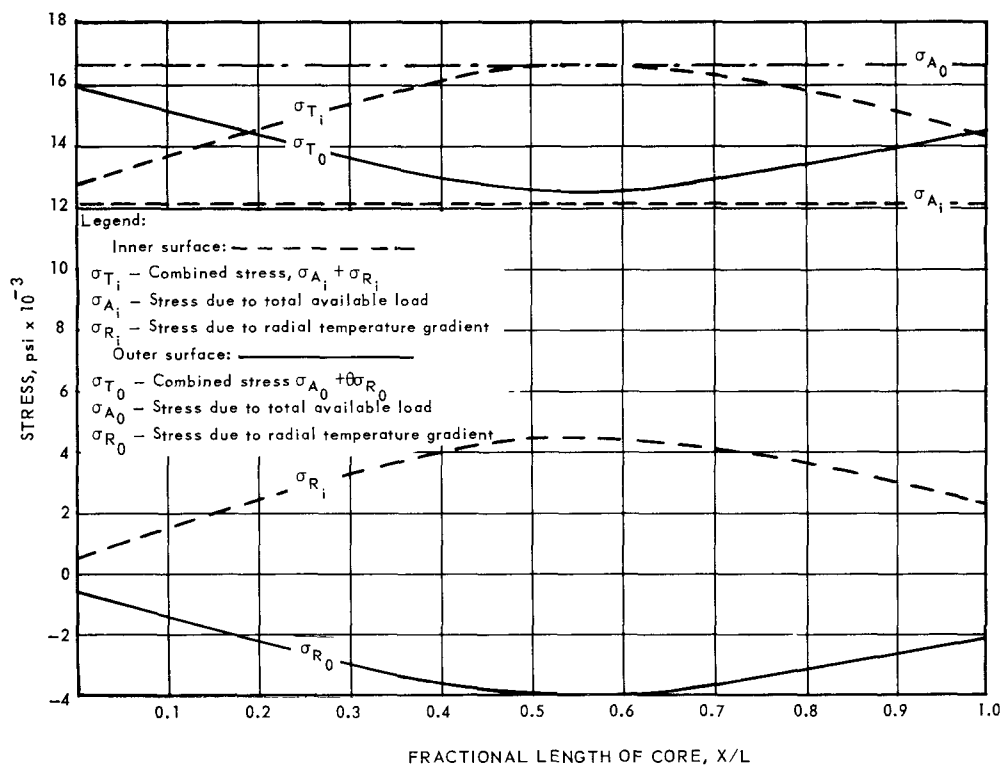


Fig. 4.87—Stresses in outer-reflector tubes, inner region evaluated at cruise flight condition

~~CONFIDENTIAL~~

A brief summary of the maximum stresses and the allowable material properties is tabulated in Table 4.34. The allowable material properties were based on a statistical treatment of experimental modulus of rupture data, and were the average minus three standard deviations. The comparison of the maximum calculated stress to the two-thirds strength value shows that the design was safe and that a reasonable margin of safety existed.

TABLE 4.34

SUMMARY OF MAXIMUM CALCULATED STRESSES FOR OUTER REFLECTOR RODS AND TUBES AND ALLOWABLE STRENGTH AT INDICATED TEMPERATURE

Item	Maximum Calculated Stresses, psi	Temperature, °F	Allowable Strength, psi	2/3 Allowable Strength, psi
Rod	12,700	2,060	24,500	16,300
Tube	16,500	1,890	28,000	18,700

4.6.2 AEROTHERMAL DESIGN

4.6.2.1 Design Requirements

The following temperature limitations and objectives were used to establish the radial temperature profile in the outer reflector:

1. Thermoflex insulation used in the radial arch had a short-time temperature limitation of 2000°F, and a 1000-hour limit of 1900°F.
2. The pressure pad maximum inner-surface temperature was limited to 1250°F.
3. All radial temperature gradients across the radial arch were minimized.

Secondary heating rates are reported in reference 29. Figure 4.11 showed the gross radial secondary heating rate distribution through the reactor. Figure 4.88 gives a detailed plot of the secondary heating rate distribution through the outer reflector. Figure 4.89 presents a space-integrated secondary power generated in the outer reflector.

All component thermal design was based on providing adequate cooling capabilities for the maximum secondary heating rate at the most severe operating condition. The outer-reflector cooling configuration was based on considerations of long-time, standard-day cruise temperature limitations. This configuration was then checked at the most severe short-time case (hot day, emergency power setting) to insure satisfactory performance within all temperature limitations. Perfect thermal contact between reflector tubes was assumed to prevail in the establishment of the cooling configurations, although other possibilities were analyzed.

At the time of contract termination, heating rates were not well defined. The uncertainty varied from 20 percent near the active core to 75 percent at the reactor structural shell. However, it was anticipated that more accurate predictions would be available before test operation, thereby allowing insertion of orifices in cooling channels to reduce the flow of cooling air as required to yield consistency with design objectives.

4.6.2.2 Characteristics of System

In order to meet design objectives and minimize secondary cooling-air flow requirements, cooling channels were distributed evenly throughout the reflector. The most economical way to cool the reflector, from the standpoint of minimum airflow, would have been to remove all heat at the point of generation; however, practical limitations on hole size and number required some compromises.

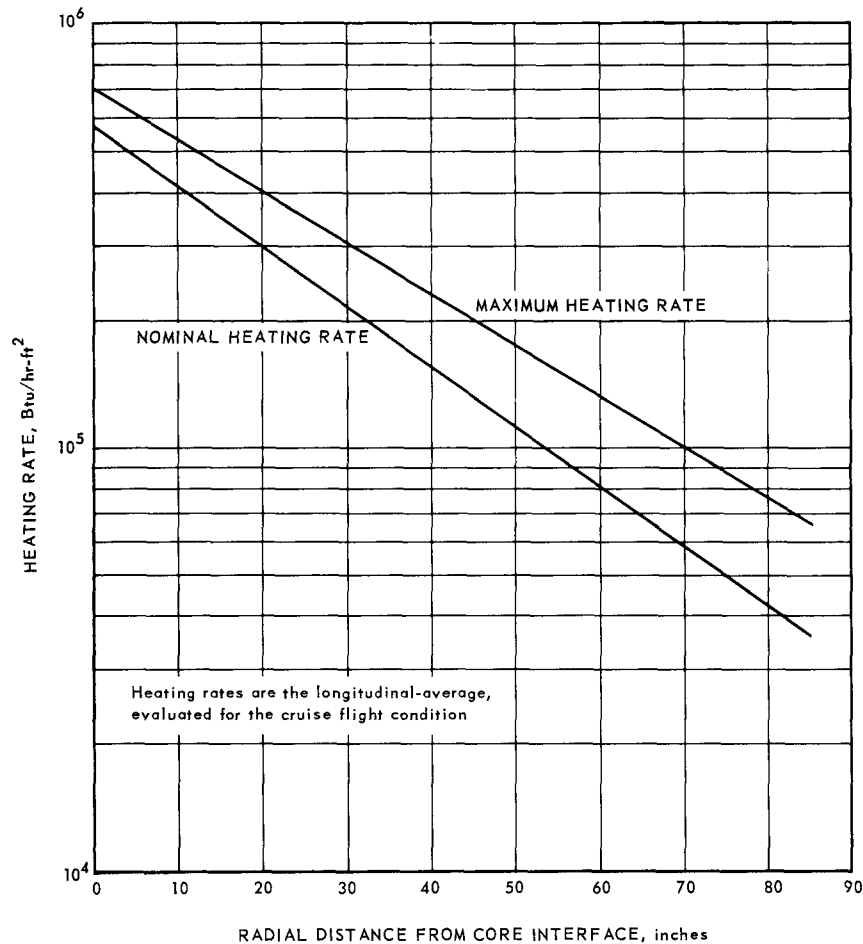
~~CONFIDENTIAL~~

Fig. 4.88 – Secondary heating rates in the outer-reflector

The cooling channel configuration in the outer reflector region, extending from a reactor radial distance of 25.5 to 31 inches, consisted of:

1. Six hundred and forty-two tubes with coolant channels of 0.144-inch hydraulic diameter with 19 solid rods surrounding each cooling channel, located in a triangular array in the radial region extending from 25.5 to 29.0 inches.
2. Four-hundred and thirty-eight tubes with coolant channels of 0.158-inch hydraulic diameter, uniformly spaced on a radial distance of approximately 30 inches.

The total cooling-air in the reflector region between 25.5- and 30-inch radii was 3.32 percent $W_{a4.0}$ for the maximum secondary heating rate. For nominal heating rates, with orificed coolant channels, the flow was estimated to reduce to 2.0 percent $W_{a4.0}$.

The major uncertainty in the thermal design of the outer reflector, other than the secondary heating rate uncertainty, was the magnitude of the surface contact resistance among the 511,000 reflector tubes and rods. The contact coefficient further could vary throughout the reactor lifetime. The design, therefore, was based on the conservative assumption of perfect thermal contact between tubes. This condition led to the maximum radial conductive heat flow from the outer diameter of the core to the outer diameter of the outer reflector. Variations in local temperatures were small, and limited by judicious distribution of cooling channels to minimize the effect of uncertainties in surface contact resistance. This precaution resulted in an airflow penalty of approximately 0.8 percent $W_{a4.0}$.

~~CONFIDENTIAL~~

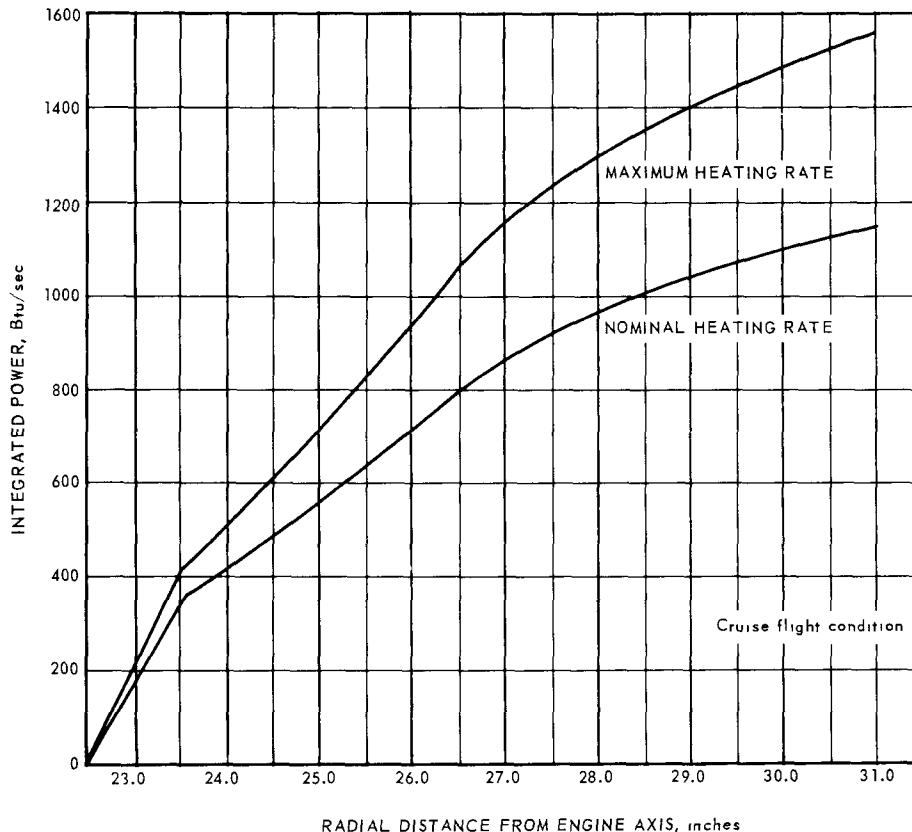


Fig. 4.89 - Space integrated secondary power in outer reflector

4.6.2.3 Assumptions and Methods of Analysis

The following assumptions were used in the aerothermal design of the outer reflector:

1. Imperfect surface contact was represented by use of an over-all thermal conductivity equivalent to the thermal conductivity of BeO tubes and rods separated by a 0.001-inch air gap.
2. Using this equivalent over-all thermal conductivity, perfect surface contact resistance was assumed.
3. Friction factor for airflow equaled 1.15 times smooth-tube friction factor.
4. Inlet loss coefficient for airflow was 0.36. Exit loss coefficient was 0.4.
5. Properties of BeO presented in reference 12 were used.

Digital computer programs used in analyzing the outer reflector were:

1. Transient Heat Transfer Program (228) THTA
2. Flow and Temperature Analysis Program (542) FANTAN
3. Modified Off-Design Program (443)

Figure 4.90 shows the nodal layout for a FANTAN analysis of an outer reflector segment. The purpose of the FANTAN mockup was to determine gross radial and longitudinal temperature gradients in the outer reflector. It was not used for detailed temperature analysis of the radial arch. Due to the computer capacity limitations, the reflector was divided into two separate longitudinal sections with the exit-air of the first section introduced as the inlet-air of the second section. This segmentation had the effect of thermally insulating the front half of the reactor from the rear half. The separation, however, did not affect steady-state temperatures.

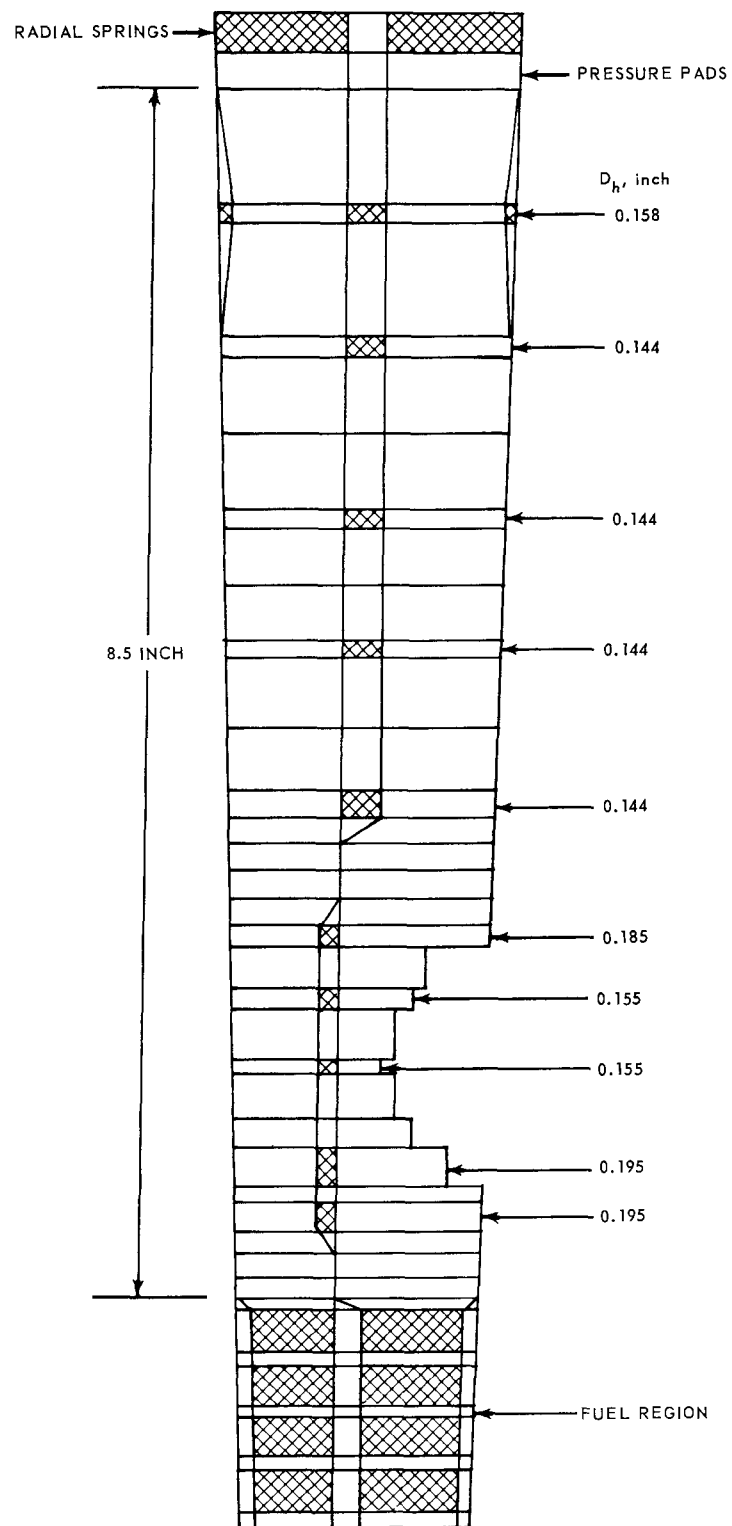
~~CONFIDENTIAL~~

Fig. 4.90 – Outer reflector nodes used in FANTAN analysis

~~CONFIDENTIAL~~

Contact resistance was expressed as an equivalent thickness of air gap between two tubes. Heat was transferred across the air gap by conduction and by radiation. The air gap conductance was defined as:

$$h_c = h_k + h_r = \frac{Q}{A \times \Delta T}$$

where: h_c = air gap conductance
 h_k = conductance by conduction
 h_r = conductance by radiation
 Q/A = heat flux across the air gap
 ΔT = temperature drop across the air gap

Figure 4.91 shows the air gap conductance as a function of mean temperature across the gap for various gap thicknesses. As shown therein, the conductance for a 0.001-inch air gap varied between 300 and 750 Btu per hour per square foot per °F. This range of air gap conductance was similar to conductances shown in unclassified literature (for reasonable air gap thicknesses), and was used in the outer-reflector aerothermal design.

Due to limitations of the FANTAN computer program, contact coefficients could not be used explicitly. The effective conductivity of BeO was defined as including the effect of contact resistance, and was equal to:

$$k_{\text{eff}} = \frac{k}{1 + \frac{k}{W h_c}}$$

where: k = actual BeO conductivity
 W = tube flats dimension
 h_c = air gap conductance

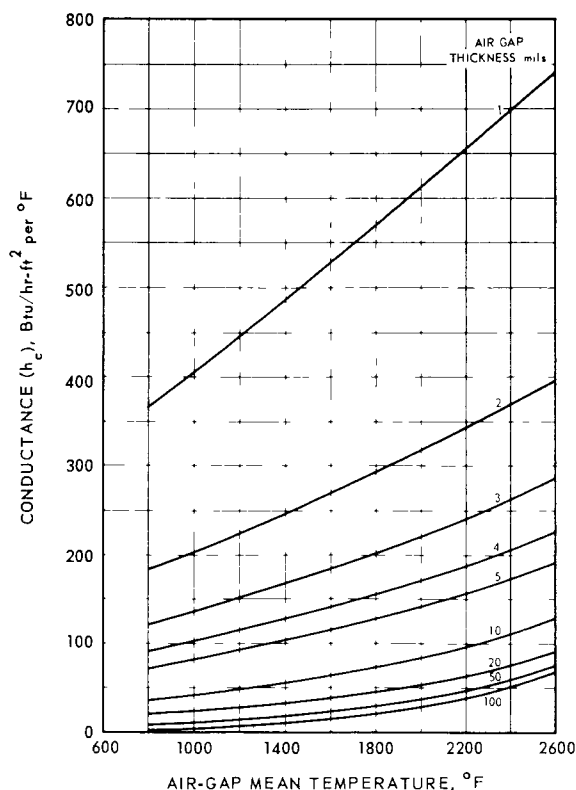


Fig. 4.91 - Reflector air-gap conductance

~~CONFIDENTIAL~~

The values obtained by the one-dimensional heat conduction analysis of a reflector segment were checked by a THTA (program 228) mockup for two-dimensional accuracy. Figure 4.92 compares the results of the one-dimensional analysis with THTA results and shows agreement within 2 percent. Figure 4.93 shows the ratio of k/k_{eff} as a function of air gap temperature for the reflector tubes with 0.001-inch and 0.002-inch air gaps. The effect of contact resistance on conductivity is shown in Figure 4.94 which gives a comparison of actual conductivity of BeO and effective conductivity based on 0.001-inch and 0.002-inch air gaps.

Detailed radial temperature distributions in the outer reflector were obtained for the following conditions:

1. Standard day, cruise
2. Hot day, emergency power setting
3. Locked rotor scram - intermediate-cold-day ITS transient

Figure 4.95 depicts the radial temperature distribution at different longitudinal locations for standard-day cruise and for conditions of maximum heating rate and perfect contact between tubes. Figure 4.96 is a similar plot for an effective conductivity of 0.001-inch and 0.002-inch air gaps. Corresponding reflector temperatures for the hot-day, emergency-power-setting flight condition were approximately 150°F higher.

Figure 4.97 shows the transient radial temperature distribution for the locked rotor scram and intermediate-cold-day, ITS ambient condition assuming perfect contact between tubes. These calculations were based on an assumed constant flow distribution. The results indicated that the radial arch temperature increased 200°F above the steady-state temperature during the first 600 seconds after shutdown. Pressure pad temperature increased

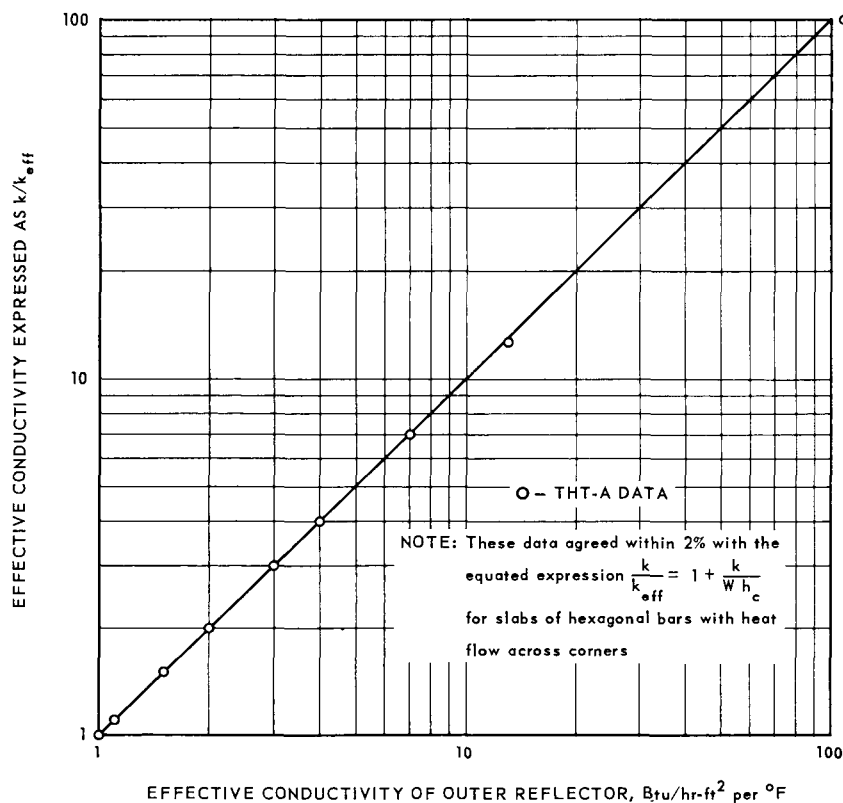


Fig. 4.92 - Effective conductivity of outer reflector region

~~CONFIDENTIAL~~

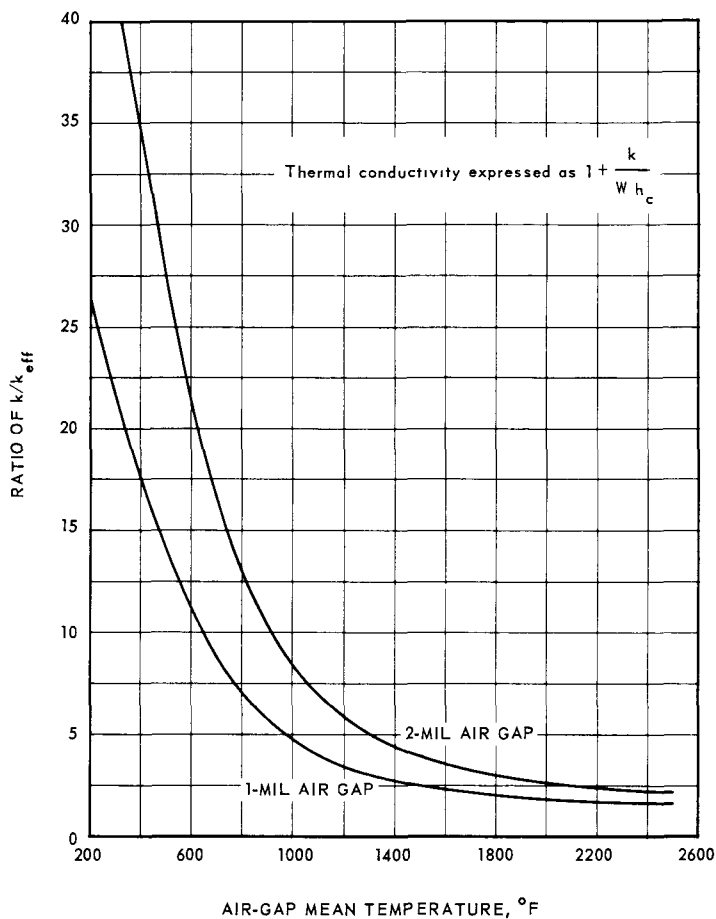


Fig. 4 93—Ratio of actual to effective conductivity of outer reflector tubes

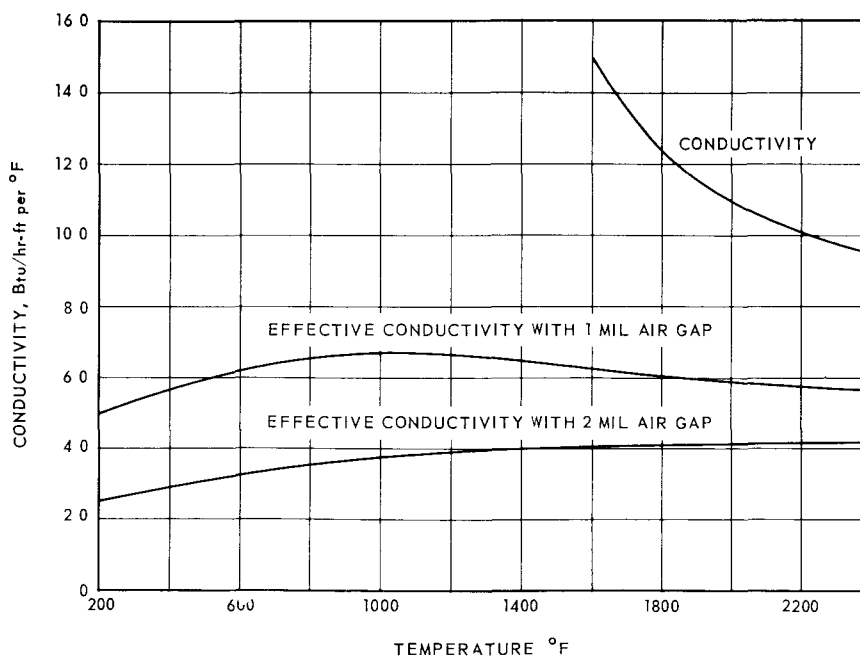


Fig. 4 94—Effect of contact resistance on conductivity of BeO

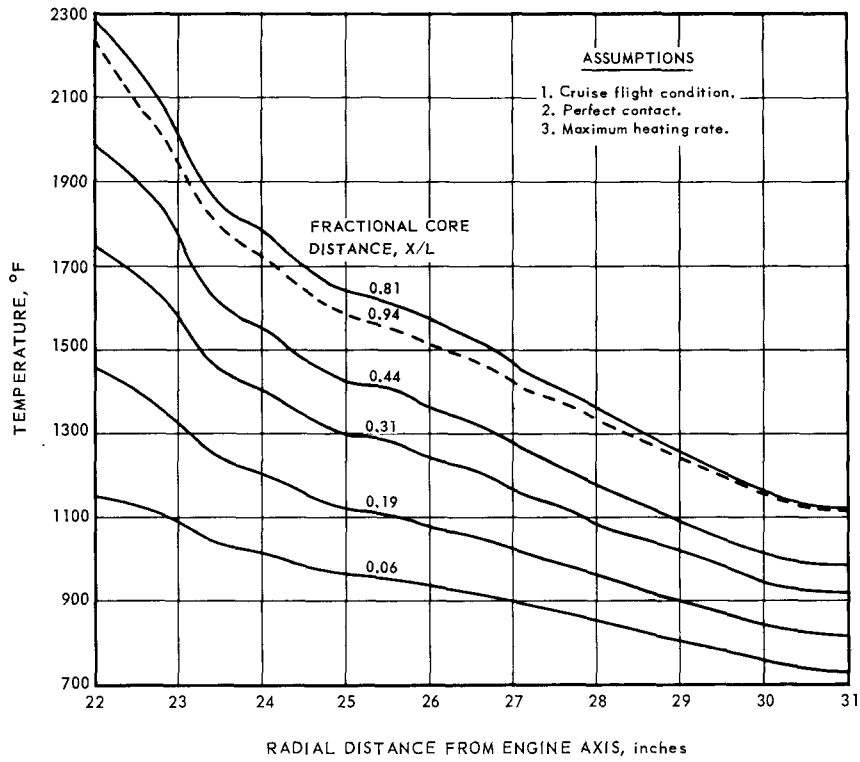
~~CONFIDENTIAL~~

Fig. 4.95 - Radial temperature distribution in outer reflector

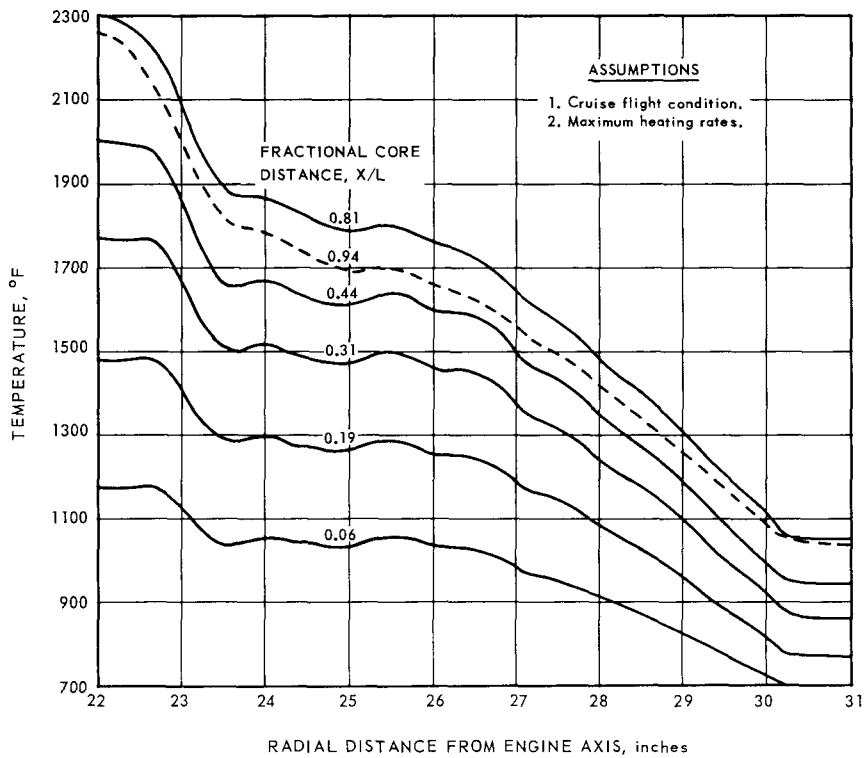


Fig. 4.96 - Effect of 0.001-inch air gap on radial temperature distribution in outer reflector

~~CONFIDENTIAL~~

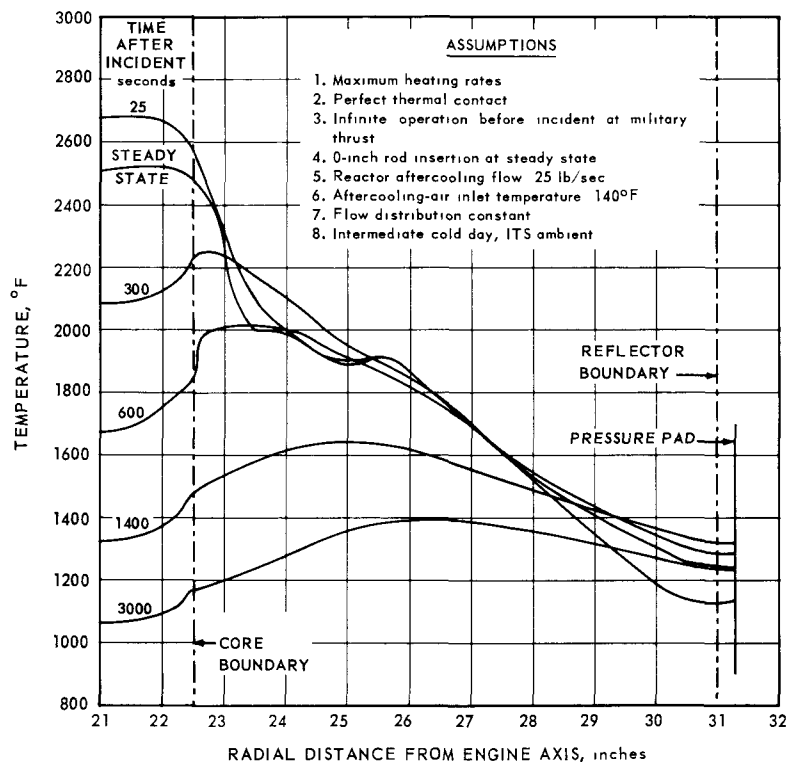


Fig. 4.97 - Outer reflector radial temperature distribution following locked rotor scram

200°F during the first 1400 seconds after shutdown. The temperature gradients across the outer reflector tubes at the reflector-core interface, immediately after scram, were slightly higher than the steady-state gradient.

Figure 4.98 presents longitudinal temperature distributions for the above transient condition at radial location 23.9 inch. A discontinuity is shown at a fractional core length of $X/L = 0.5$ at an extended time after scram. This discontinuity was due to the analysis procedure previously described in which the reflector was divided and analyzed in two longitudinal segments. The effect of conduction between the first and second half would have flattened the over-all longitudinal temperature profile at these later times. Similar calculations were completed for longitudinal locations 22.3 inches and 31.0 inches, and comparable results were obtained.

A summary of the thermal design data and criteria for the outer reflector is shown in Table 4.35.

4.7 INNER REFLECTOR COMPONENT DESIGN DATA

4.7.1 MECHANICAL DESIGN

The inner reflector was composed of aluminum oxide tubes and rods which formed an annular cylindrical region bounded by the inside diameter of the fuel region and the outside surface of the metallic core liner. Cooling channels formed by the tubes were dispersed throughout the inner reflector to remove the secondary heat generated within a number of rods surrounding each tube. The inside diameters of the tubes forming one cooling channel were the same; however, the inside diameter of the tubes varied from channel to channel to accommodate local cooling requirements. The inside diameters ranged from 0.117 to 0.155 inch.

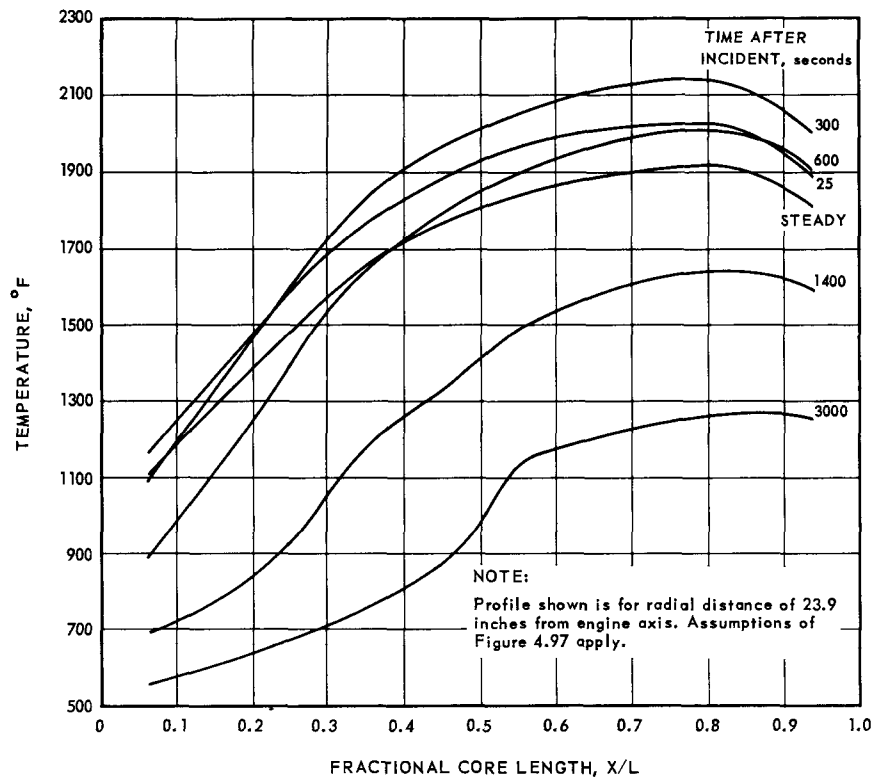
~~CONFIDENTIAL~~

Fig. 4.98 — Outer reflector longitudinal temperature profile following locked rotor scram

TABLE 4.35

SUMMARY OF THE THERMAL DESIGN DATA AND CRITERIA
FOR THE OUTER REFLECTOR

Nominal Average Heating Rate, w/gm-mw	0.008
Heating Rate Uncertainty Factor	
Average	1.50
Maximum	1.70
Minimum	1.45

Design Criteria

- (1) Perfect thermal contact between reflector tubes
- (2) Minimized radial arch temperature gradients
- (3) Pressure pad maximum inner surface temperature - 1250°F
- (4) Temperature limit of arch insulation - 2000°F (short time)
1900°F (1000 hours)

Thermal Design Parameters: Cruise Condition, Maximum Heating Rate.

Percent core power generated	1.41	
Percent core power absorbed	1.54	
Hydraulic diameter, in.	0.144	0.158
Number of tubes	642	438
Airflow, % $W_{a4.0}$	1.71	1.61
$T_{exit(max)}$, °F	1389	1026
$T_{exit(min)}$, °F	1126	1023

~~CONFIDENTIAL~~

The alumina elements also functioned as a gamma shield to reduce the secondary heat generated within the metallic components in the inner region of the reactor. Further, they provided thermal insulation for the metallic core liner.

In the hottest region of the core, the temperature was reduced radially through the inner reflector from 2300°F at the inner diameter of the core to 1200°F at the inner surface of the core liner. The gradient through the reflector was nearly linear, and equalled 500°F per inch. The radial gradient across one rod was approximately 140°F.

The thermal expansion of the inner reflector was less than that of the inside diameter of the fuel region during steady-state operation. Design dimensions of the core liner accounted for this difference to insure that the inner-reflector elements remained in intimate contact with the fuel tubes, and that radial pressure was transmitted through the tube bundle to the core liner.

Mechanical stresses were induced from the loadings resulting from the radial spring pressure. Bowing of the elements induced by thermal gradients across the element was resisted by the radial pressure which resulted in beam loading on the elements. This restraint, and its redistribution, produced ring loading. The stresses resulting from these loadings were calculated similar to fuel element calculations. Tangential and axial thermal stresses also were induced in the elements by the temperature gradients resulting from conducting secondary heat generated within the tubes and surrounding rods to the tube channel walls.

Each of these stresses was calculated individually and combined by the principle of superposition to provide the maximum tensile stress. Figure 4.99 shows the results of the stress analysis for the particular tube which results in the highest combined stresses for design point operation. Figure 4.100 shows the comparable stress analysis for the solid rods. Axial mechanical stresses were a function of the applied load since the elements were short (1.426 inches) and the stresses were independent of the thermal camber.

4.7.2 AEROTHERMAL DESIGN

4.7.2.1 Design Criteria

The following criteria were established for aerothermal design of the inner reflector:

1. The maximum material temperature was limited to 1400°F.
2. The temperature rise in the cooling air flowing in the annulus between the core liner and the shaft tunnel was limited to 50°F.
3. All radial temperature gradients were minimized.

Secondary heating rates are reported in reference 29. Figure 4.11 showed the distribution of gross secondary heating rates and indicated the degree of uncertainty in the design values.

Adequate cooling capabilities were provided for maximum predicted heating rate. The cooling configuration was based on the consideration of the most severe operating condition; namely, hot-day, emergency-power-setting. Perfect thermal contact was assumed to prevail between tubes and rods. The predicted heating rate uncertainty factor in the inner reflector region was 1.2.

The following aerothermal design assumptions were made:

1. The airflow friction factor was 1.15 times smooth tube friction factor.
2. The airflow inlet loss coefficient was 0.36; exit loss coefficient was 0.40.
3. Perfect thermal contact between tubes and rods.
4. Al₂O₃ properties were as given in reference 12.

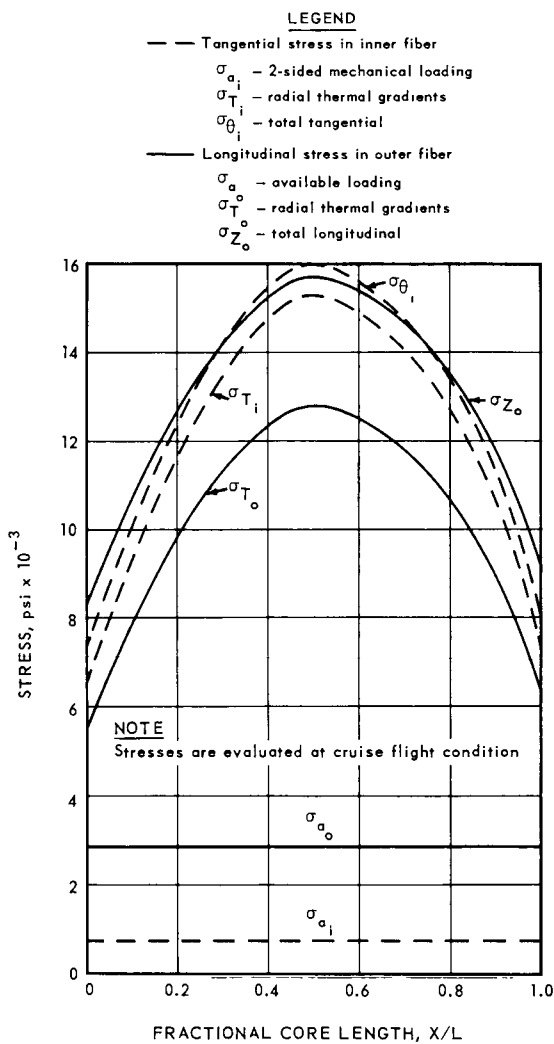
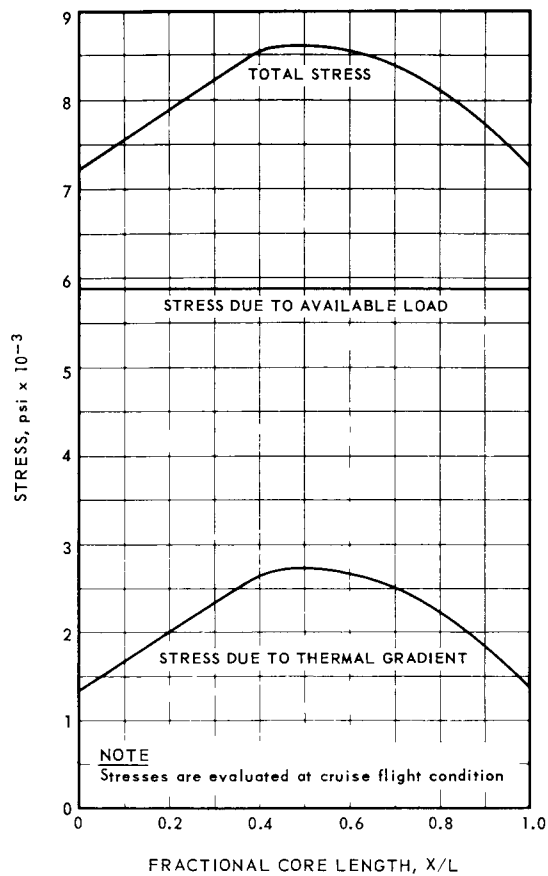
~~CONFIDENTIAL~~

Fig. 4.99 – Stress in inner reflector tubes

Fig. 4.100 – Stress in inner reflector rods

~~CONFIDENTIAL~~

The digital computer programs used in design analysis of the inner reflector were as follows:

1. Flow and Temperature Analysis Program (543) FANTAN
2. Modified Off-Design Program (443)

Figure 4.101 shows the nodal layout for a FANTAN analysis of an inner reflector segment. In this analysis the reflector was broken into 10 longitudinal segments which were analyzed simultaneously.

All other assumptions and analysis methods were similar to, or the same as, those used in the analysis of the outer reflector.

4.7.2.2 Design Results

The cooling channel configuration consisted of 456 tubes with hydraulic diameters ranging from 0.117 to 0.155 inch. The total coolant flow was 1.12 percent $W_{a4.0}$ for the maximum heating rate condition. For nominal heating rates, with orificed coolant channels, the flow requirements reduced to 0.96 percent $W_{a4.0}$.

The allowable upper temperature limit of the core liner was not reached during any steady-state or transient condition because the criterion of 50°F maximum temperature rise in the tunnel cooling-air was limiting. The tunnel cooling-air (3.6 percent $W_{a4.0}$) was used for cooling the front shield and rear shield central islands.

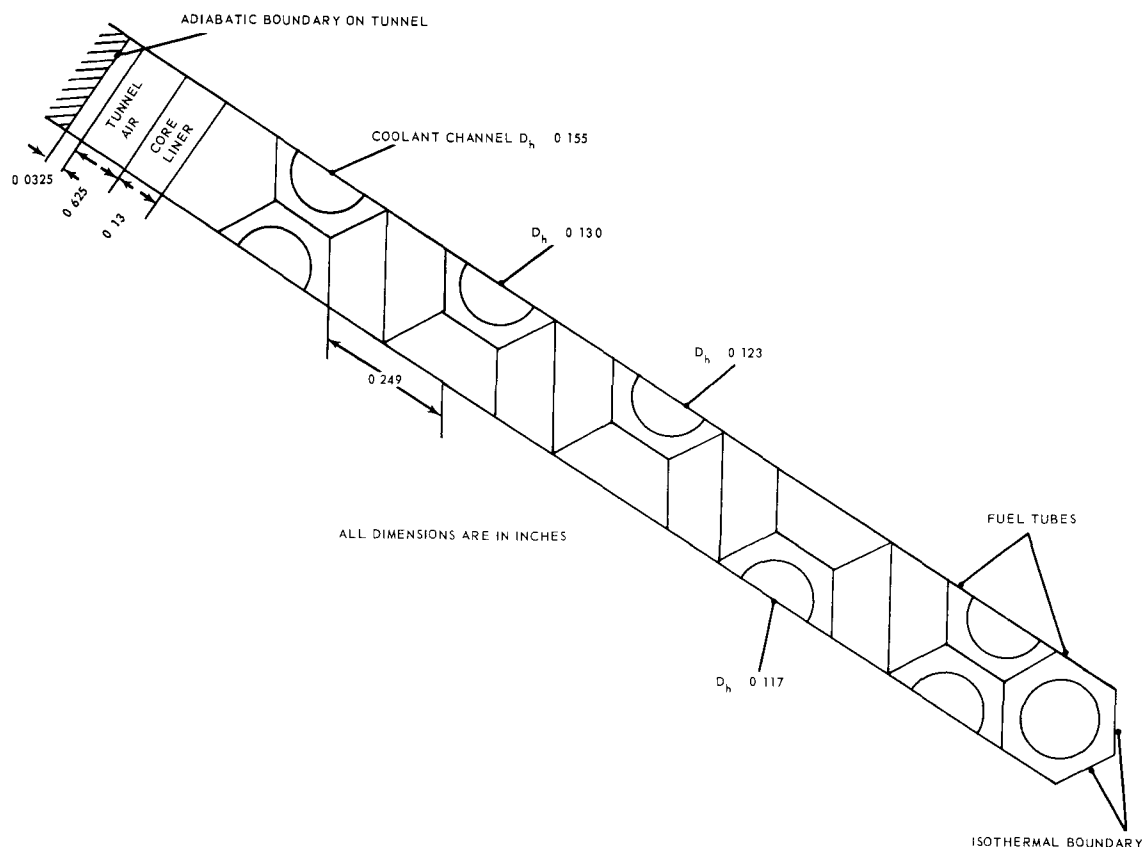


Fig. 4.101 - Inner reflector segment used in Fantan analysis

~~CONFIDENTIAL~~

As was the case in the outer reflector, a major uncertainty existed in the value of the surface contact resistance coefficient between adjacent tubes and rods in the inner reflector, and the same methods of analysis were used. Figures 4.102 and 4.103 show the actual and effective conductivity of Al_2O_3 and the ratio of actual k_{eff} versus temperature, respectively.

Material temperatures calculated on the basis of an effective conductivity were approximately the same as those calculated on the basis of perfect thermal contact. This similarity was due to the low thermal conductivity of Al_2O_3 and the high porosity of the inner reflector. Since the heat fluxes were low, the effects of the air gaps were secondary.

Detailed inner reflector temperature distributions for steady-state and transient design conditions were computed. Figure 4.104 shows the radial temperature distribution for steady-state design point conditions. Comparable plots for the hot-day, emergency-power-setting, and ITS intermediate-cold-day conditions are shown in reference 28. Approximately 20 further steady-state and transient temperature analyses also are shown in references 28 and 30.

A summary of significant aerothermal design criteria and data is shown in Table 4.36.

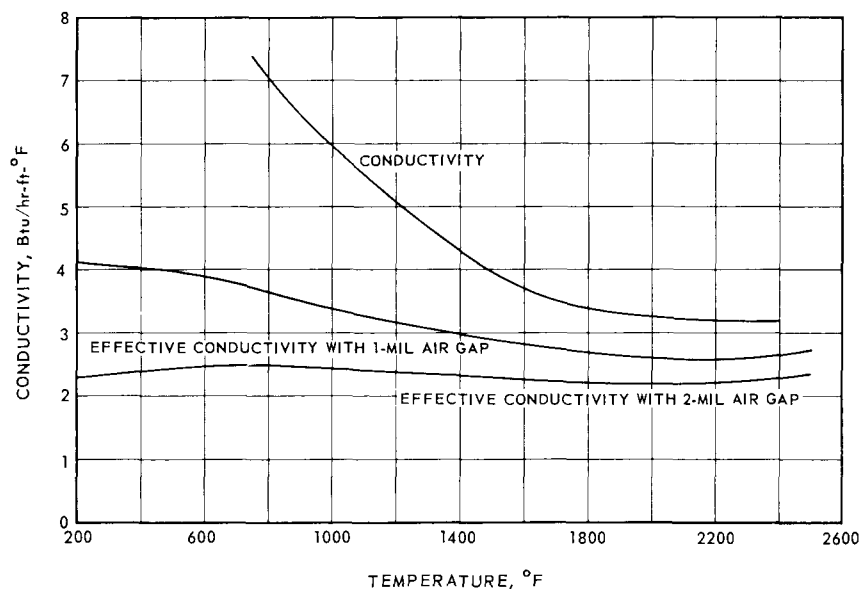


Fig. 4.102 – Effect of contact resistance on conductivity of Al_2O_3 inner reflector tubes

4.8 TRANSITION PIECES COMPONENT DESIGN DATA

4.8.1 MECHANICAL DESIGN

The transition pieces were BeO bodies that formed a 1 1/2-inch-thick reflector on each end of the tube bundle. Two configurations of transition pieces were used. The external shape of both configurations was the same and identical to the outer perimeter of 19 hexagonal fuel elements. Transition pieces on each end of the outer reflector region had a single hole through the center of each piece which was compatible with the outer-reflector cooling pattern (one cooling channel in the center tube of each bundle of 19 tubes and rods). Transition pieces on each end of the active core region had 19 small holes in

~~CONFIDENTIAL~~

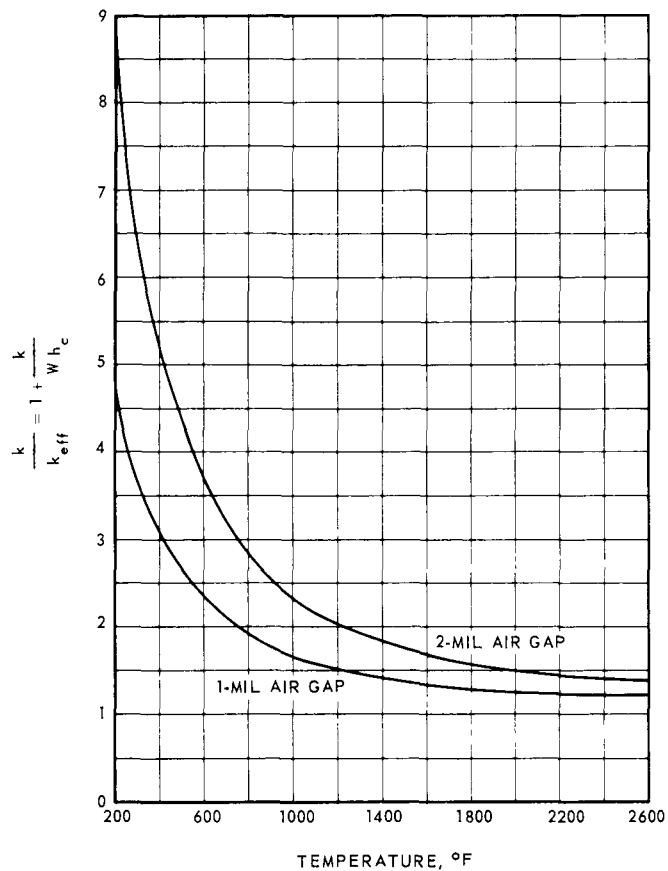


Fig. 4.103 – Ratio of actual to effective conductivity for Al_2O_3 inner reflector tubes

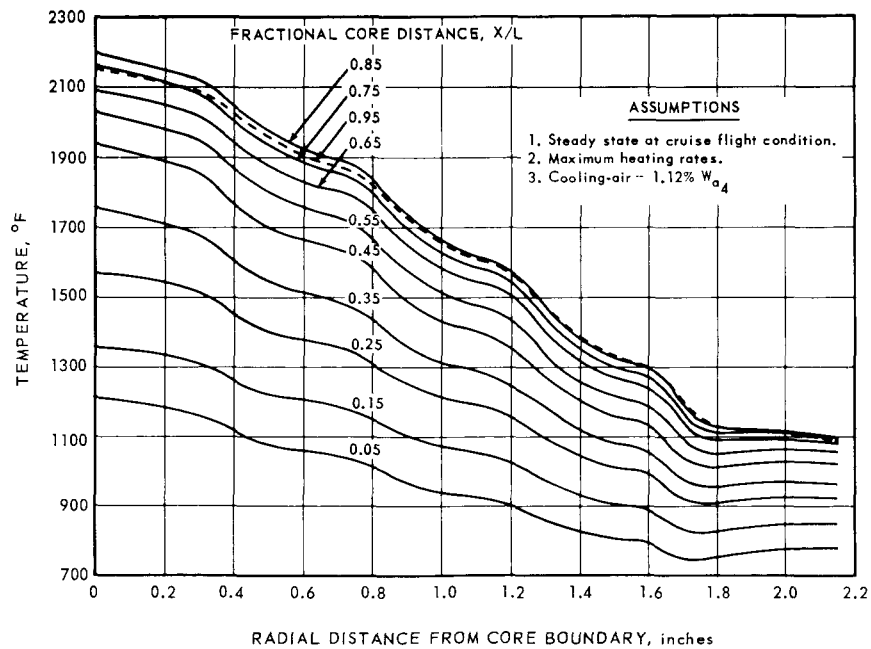


Fig. 4.104 – Radial temperature distribution in inner reflector

~~CONFIDENTIAL~~

TABLE 4.36

INNER REFLECTOR AEROTHERMAL DESIGN CRITERIA AND DATA

Nominal Average Heating Rate, w/gm-mw	0.035	
Heating Rate Uncertainty Factor	1.2	
Maximum Allowable Liner Temperature, °F	1400	
Air Temperature Rise through Annulus, °F	50	
Thermal Design Parameters Using Maximum Heating Rates		
Percent core power generated	0.74	
Hydraulic diameter range, in.	0.117 - 0.155	
Number of coolant channels	456	
Coolant void volume fraction	0.085	
Airflow, % W _{a4.0}	1.12	
Discharge-Air Temperatures, °F	<u>Cruise</u>	<u>Emergency Power Setting</u>
Maximum	1895	1990
Average	1382	1495
Minimum	1075	1145
Calculated Air Temperature Rise, °F	40	30

one end that converged into a large diameter hole in the opposite end of the piece, as shown in Figure 4.105.

The transition pieces at each end of the active core were orientated so that they served as a manifold for cooling-air entering and leaving the fuel element passages. At the forward end of the core, the air entered the large hole and was distributed to 19 fuel element air passages. At the aft end, the air from the same 19 passages was collected into the single large hole and discharged through the aft-retainer assembly. This permitted the use of larger diameter holes through the forward reflector and the aft-retainer assembly, and led to better structural and aerodynamic design of these components.

The transition pieces were designed in three lengths to stagger tubes axially throughout the reactor in bundles of 19. This prevented misalignment of the tubes forming each flow passage and maintained a shear plane across the diameter of the core. A typical arrangement of transition pieces is shown in Figure 4.106.

The operating temperature of the transition elements at the front face of the tube bundle was approximately that of core inlet-air. At the rear face of the tube bundle, the operating temperature of the transition pieces was approximately that of core exit-air. The exit-air temperature varied as much as 80°F in adjacent channels, and caused temperature gradients as high as 10°F in the web between adjacent holes in a transition piece.

Mechanical loading on the transition pieces resulted from the radial spring pressure. Two loading conditions were considered: (1) ring loading due to the radial pressure in the bundle, and (2) principal axial shear loading which developed when the central group of seven tubes transmitted a frictional load normal to the front face of the transition piece.

Ring loading was assumed to act on opposite slides of the transition piece, as shown in Figure 4.107. Using the radial spring pressure of 12 psi, a load path multiplier of 3, and an inertial factor of 4, similar to fuel element stress analysis, the tangential tensile stress was calculated to be 8500 psi.

~~CONFIDENTIAL~~

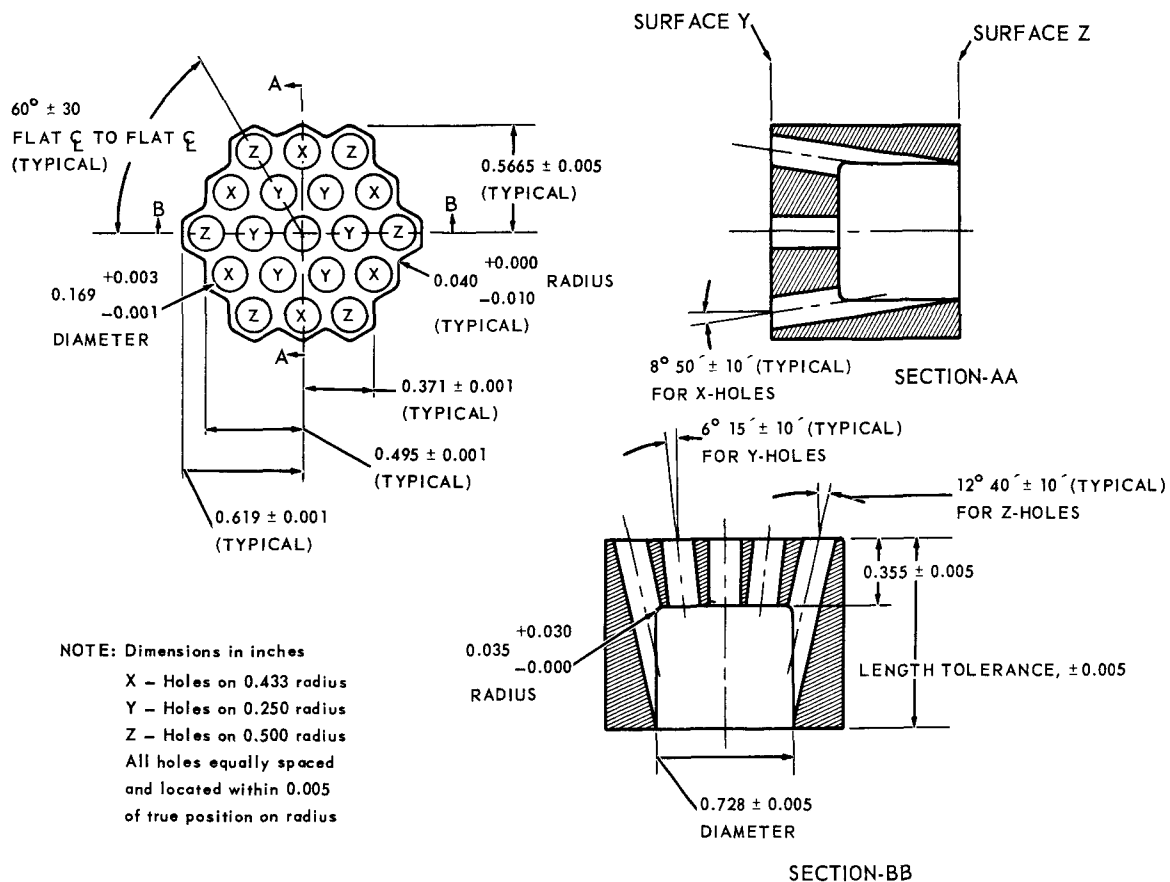


Fig. 4.105 - Fueled zone transition piece

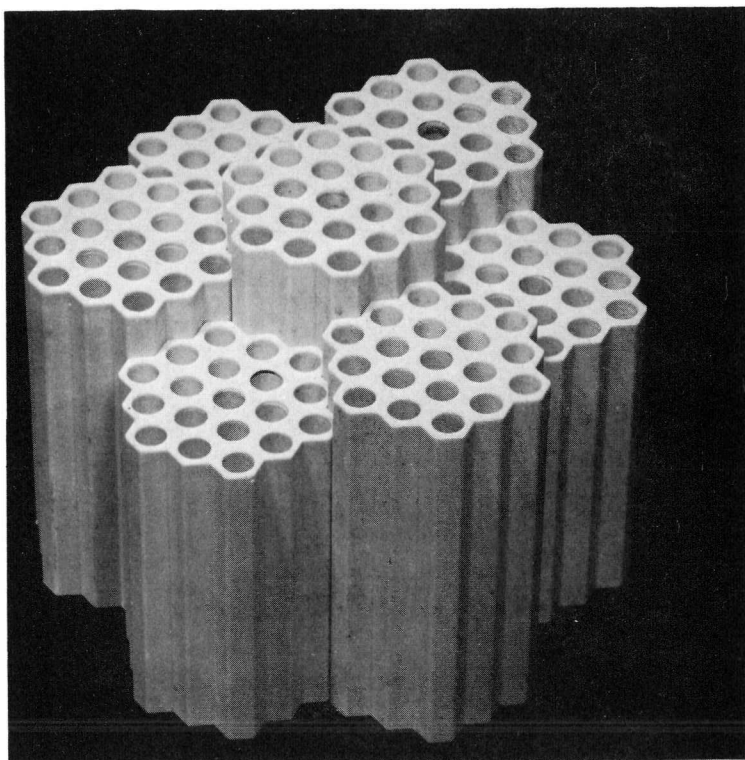
CONFIDENTIAL

Fig. 4.106 – Typical arrangement of transition pieces

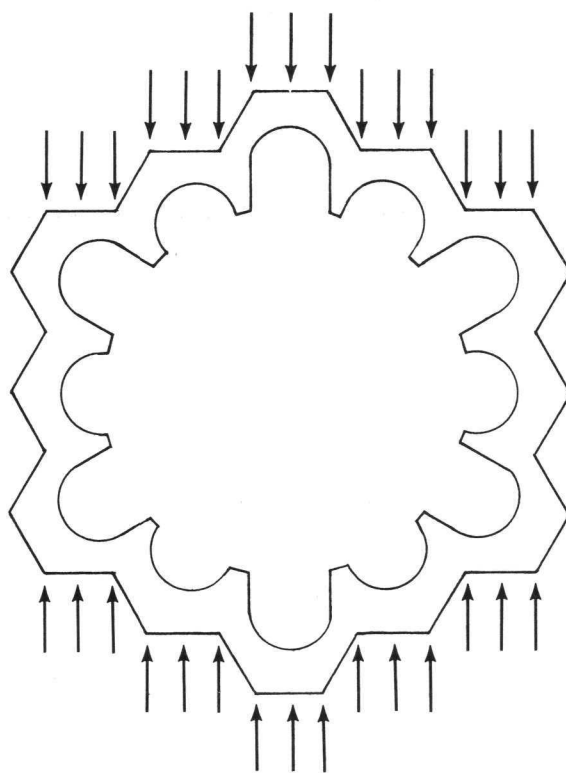


Fig. 4.107 – Transition piece ring loading

CONFIDENTIAL

The principal shear stress was due to the axial load of a bundle of fuel tubes acting on the shear area shown in Figure 4.108. The load was carried as shear on the periphery of this area. The axial load was obtained by using the formula $F = \mu N$ where:

F = Axial load on the transition piece in pounds

μ = Coefficient of friction

N = Total normal force on the fuel element

The shear stress was computed by dividing the axial load by the shear area, and was equal to 5740 psi.

The principal thermal stress was due to temperature gradients existing in the web between adjacent cooling holes. The ligament between the small holes was assumed fixed at all edges, and the minimum thickness of the ligament was used in stress calculations. The temperature gradient was assumed to be linear. The resulting stress was 2000 psi, and was calculated from the formula

$$\sigma = \frac{E \alpha \Delta T}{(1 - \nu)}$$

where: σ = stress due to linear temperature gradient, psi

α = instantaneous coefficient of thermal expansion, inches per inch per $^{\circ}\text{F}$

ΔT = temperature difference between opposite face of the ligament, $^{\circ}\text{F}$

E = modulus of elasticity, psi

ν = Poisson's ratio.

All stresses in the transition pieces were calculated from simplified models of the actual component. Although exact solutions were not available because of the geometric complexity, the results of the approximate solutions led to considerable margins of safety, and indicated safe stress levels for all operating conditions.

4.8.2 AEROTHERMAL DESIGN

There were no unique aerothermal design problems associated with the transition pieces.

4.9 RADIAL ARCHES COMPONENT DESIGN DATA

4.9.1 MECHANICAL DESIGN

4.9.1.1 Description of Component

Each individual radial arch was a large, hexagonal BeO tube 1.743 inches across flats and 0.741 inch long with an inside diameter of 1.435 inches, as shown in Figure 4.109. A column of 41 arches formed an axial cavity through the outer reflector to accommodate a control rod and guide tube. Forty-eight such cavities were provided within the outer reflector, equally spaced around the circumference of a diameter approximately 1.75 inches from the outside diameter of the active core.

The longitudinal temperature profile was approximately the same as that shown in Figure 4.48. The maximum operating temperature of the radial arch was 2000°F and occurred near the aft end of the core. The inside diameter of the radial arch was insulated to keep the control rod guide tube temperature within limits. Sufficient clearance was

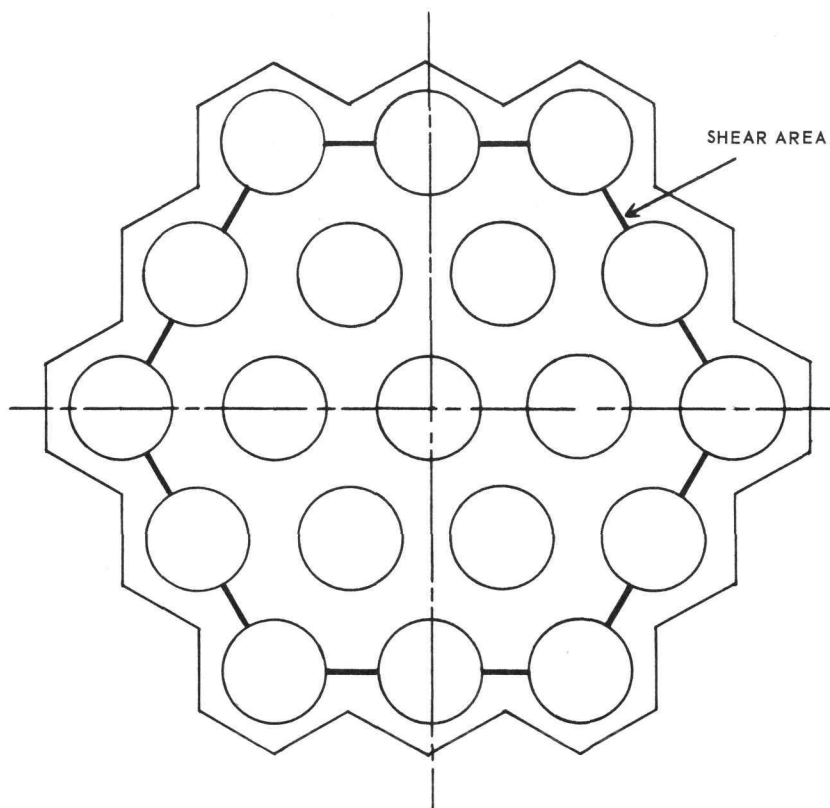
~~CONFIDENTIAL~~

Fig. 4.108 - Transition piece shear area

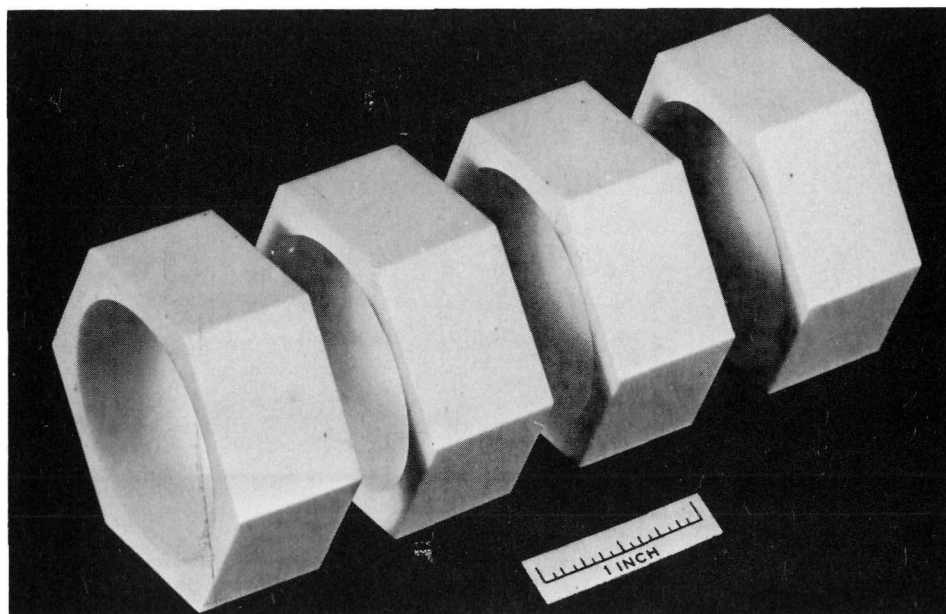


Fig. 4.109 - Radial arch pieces (C-23775)

~~CONFIDENTIAL~~

provided between the control rod guide tube and the insulation on the inside surface of the radial arch to insure a straight path for the control rod guide tube when the tube bundle assumed a barrel shape at operating temperatures. Secondary heat generated within the radial arch was conducted outward through its external surface to cooling passages in adjacent outer reflector tubes.

4.9.1.2 Mechanical and Thermal Stresses

Both mechanical and thermal stresses in the radial arch were calculated. Mechanical stresses resulted from the pressure load imposed by the radial springs. Thermal stresses resulted from thermal loads arising from temperature gradients produced by conducting secondary heat through the external surfaces to the convective boundary. Two temperature gradients were considered: (1) the radial temperature gradient through the thickness of the arch, and (2) the circumferential temperature gradient around the perimeter of the arch due to nonuniform heat removal and the exponential decrease in the heating rate across the arch.

The radial spring pressure on the radial arch resulted in a circumferential or ring-bending stress. The highest stress level was encountered when two opposite sides of the arch were loaded. The load was calculated by assuming that the maximum pressure in the core tangential direction acted on the projected area of the arch and caused a distributed pressure of 258 psi. The ratio of the inside diameter to the distance across flats, D/W , was 0.83. Using the data in Figure 4.77, the stress-to-pressure ratio, σ/p , was 20.4 for the outside fiber stress, and 40.4 for the inner fiber stress. Thus, the maximum mechanical tensile stress was 10,400 psi, and the outer fiber stress was 5270 psi.

Stresses due to radial thermal gradients were computed for an infinite cylinder with the same inner diameter and cross-sectional area as the arch. Corrections were then applied to account for the hexagonal outer surface and finite length. For the infinite circular cylinder case, cooled on the outside surface, insulated on the inside surface, with internal heat generation, the maximum tensile stress occurred at the outside surface of the cylinder. This thermal stress was equal in both the axial and tangential directions, and was calculated by the following equation:

$$\sigma_{\theta,z} = 43,200 \frac{E\alpha}{k(1-\nu)} q''' \left[\frac{(1.05W)^2}{32} \right] \left[1 - 3 \frac{D^2}{(1.05W)^2} - 4 \frac{\frac{D^2}{(1.05W)^2} \times \ln \left(\frac{1.05W}{D} \right)}{1 - \left(\frac{1.05W}{D} \right)^2} \right]$$

Where: D = Inside diameter of cylinder, inches
 W = Distance across flats of hexagon, inches
 E = Modulus of elasticity, psi
 K = Thermal conductivity, BTU per hour - feet - $^{\circ}\text{F}$
 q''' = Heat generation rate, BTU per second - inches³
 α = Instantaneous coefficient of thermal expansion, inch per inch - $^{\circ}\text{F}$

Combining the correction factors for both the hexagonal shape and the finite length yielded a correction factor of 1.55 for the end, and 1.25 for the middle of the arch. These correction factors were applied to the infinite cylinder stresses calculated above.

The circumferential thermal gradient resulted primarily from uneven cooling of the external surface of the arch. The temperature gradients were approximated by:

$$(T - T_{\text{avg}}) = T_0 \sin N\theta$$

~~CONFIDENTIAL~~

where: $(T - T_{avg})$ = Amplitude of sine wave at any point, °F
 T_0 = Maximum amplitude of sine wave, °F
 θ = Angular coordinate degrees
 N = Number of temperature waves in 360 degree circumference.

Radial arch stresses due to the circumferential temperature gradients were calculated by the following equation:

$$\sigma = \lambda \left(\frac{E}{1-\nu} \right) T_0 \sin N\theta$$

Where: σ = Stress, psi
 λ = Stress factor
 E = Modulus of elasticity, psi
 α = Coefficient of thermal expansion
 ν = Poisson's ratio
 $T_0 \sin N\theta$ = Magnitude of temperature fluctuation

The stress factor, λ , was a function of the ratio of the length to the inside diameter of the radial arch. An effort was made to optimize this ratio so as to minimize the stress. For this reason, the effect of varying the L/D ratio on the stresses arising from the circumferential temperature gradient was evaluated using the analysis of reference 31. Figure 4.110 shows the results of this analysis for a typical case with $N = 12$.

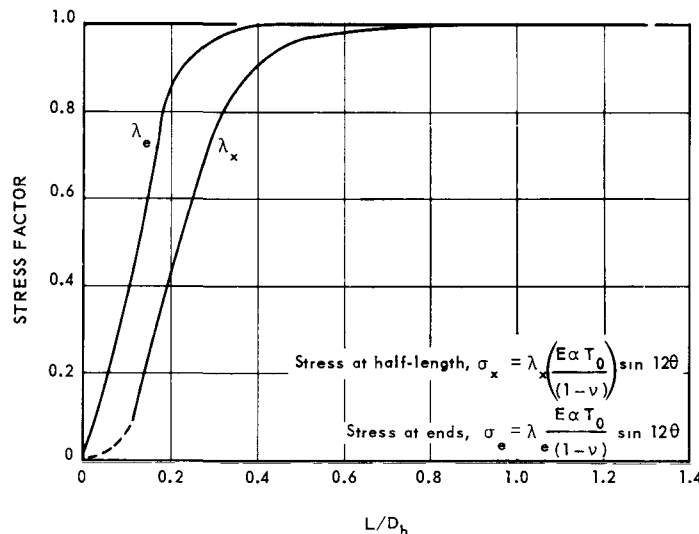


Fig. 4.110—Maximum thermal stress in radial arch due to circumferential temperature gradients

The length of the radial arch selected for the core was equivalent to a short cylinder (short in the sense that the full magnitude of the infinite length cylinder stresses was not developed).

Stress analysis was performed by computing and superpositioning the individual stresses discussed above, and combinations were obtained for the maximum tensile stresses. These combinations for design point operation are given in Table 4.37.

Similar calculations of the combined thermal stress in the radial arches during ground checkout operation on a cold day indicated that the outer fiber stress level, 19,200 psi

~~CONFIDENTIAL~~

TABLE 4.37
COMBINED STRESS IN RADIAL ARCHES DURING
DESIGN POINT OPERATION

	Inner Fiber, psi	Outer Fiber, psi
Mechanical stress	+ 10,200	+ 5,200
Thermal gradient stress	- 1,530	+ 3,000
Circumferential gradient stress	+ 3,200	+ 3,000
Combined stress	+ 11,870	+ 11,200

at 2000°F, exceeded the modulus of rupture (15,000 psi at that temperature). Methods of alleviating this problem were being developed.

4.9.2 AEROTHERMAL DESIGN

4.9.2.1 Design Criteria

The secondary heating rates are reported in reference 29. Figure 4.11 showed the gross radial secondary heating rate distribution through the reactor and indicated the uncertainty in the various components.

Perfect thermal contact between reflector cooling tubes and between the radial arch and its surrounding tubes was assumed to prevail in establishing the cooling configuration. This assumption yielded maximum heat flow from the core to the reflector and was the most conservative approach. Control rods were assumed to be fully withdrawn.

4.9.2.2 Design Results

The cooling configuration established for the radial arches consisted of 12 reflector tubes surrounding each arch. Six of these tubes had 0.195-inch-diameter channels, 4 had 0.155-inch channels, and 2 had 0.185-inch channels. Cooling-air supplied to the radial arch cooling tubes was equal to 2.45 percent $W_{a4.0}$, based on the maximum secondary heating rate. The coolant flow would have been reduced to 2 percent $W_{a4.0}$ for nominal heating rates and orificed flow channels.

Figure 4.111 shows the nodal layout for a FANTAN analysis of the radial arch region. The mockup included the outer row of fuel elements. All external boundaries were considered adiabatic as a simplifying, but slightly erroneous, assumption. All other assumptions and methods of analysis were similar to those used for the outer reflector.

Detailed circumferential and longitudinal temperature distributions were calculated for both hot day, emergency power setting and design point conditions with maximum heating rate. Both perfect thermal contact and effective conductivity conditions were analyzed. Circumferential temperature distributions for the design point and hot day, emergency power setting conditions at different longitudinal locations are shown in Figures 4.112 and 4.113, respectively. Corresponding longitudinal temperature distributions are shown in Figures 4.114 and 4.115. Figures 4.116 and 4.117 show circumferential and longitudinal temperature distribution for hot day, emergency conditions with an effective 0.001-inch air gap between unfueled tubes.

These data showed that, for the standard day cruise condition used as the design point for sizing cooling channel, the circumferential temperature variation did not exceed 50°F; however, during hot day, emergency power setting the variation was 150°F. Also, Figures

CONFIDENTIAL

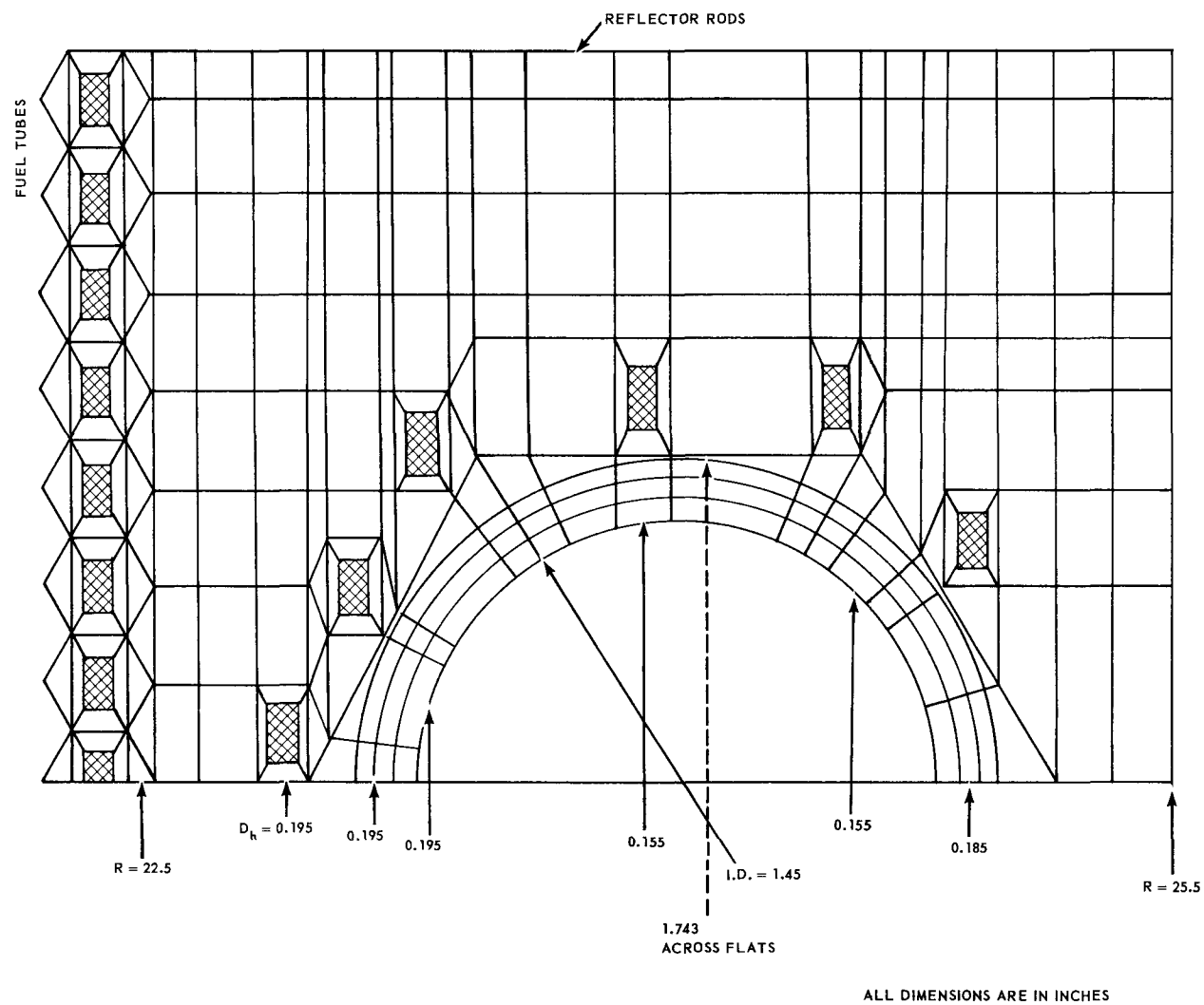


Fig. 4.111 - Nodal layout of FANTAN analysis of radial arch region

CONFIDENTIAL

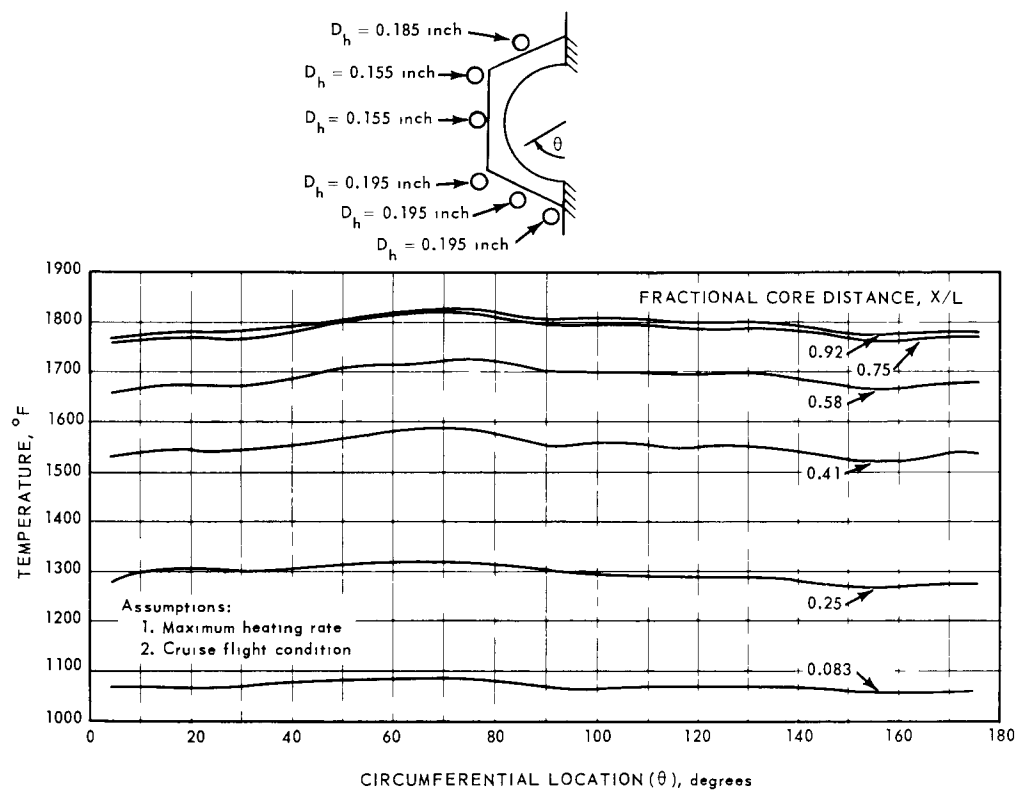


Fig. 4.112—Circumferential temperature distribution in radial arch

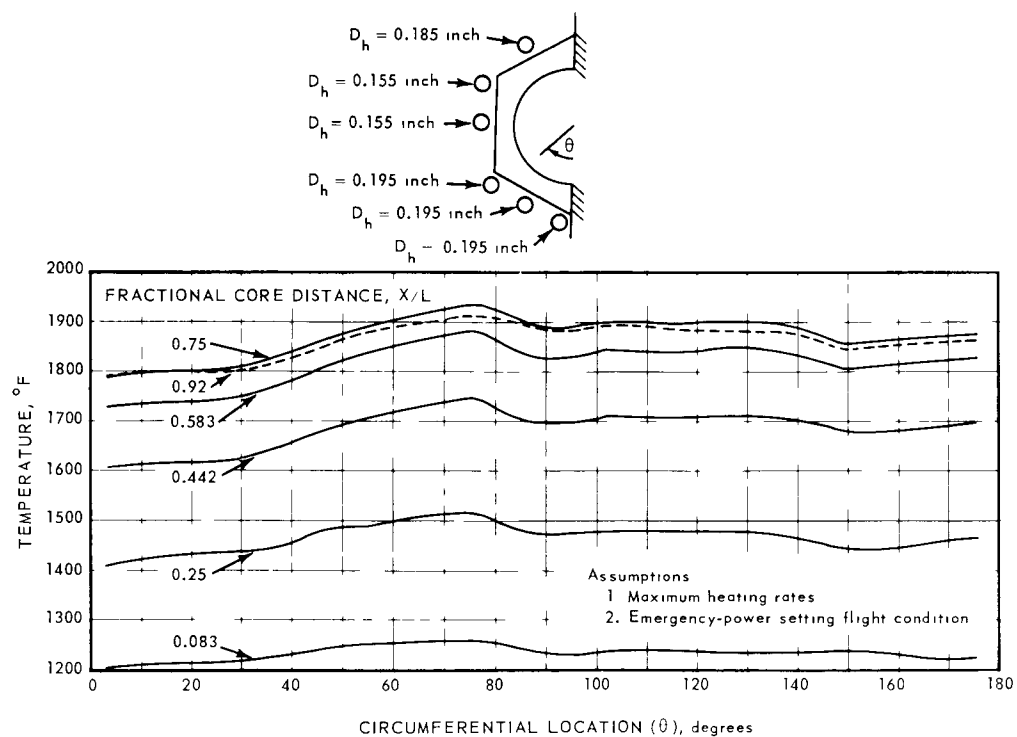


Fig. 4.113—Circumferential temperature profile in radial arch

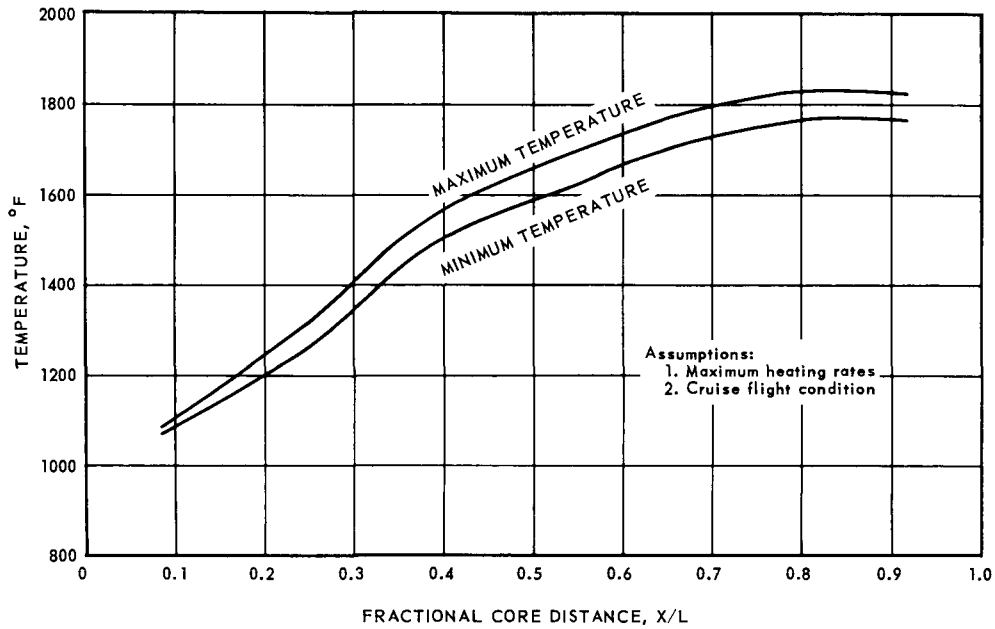
~~CONFIDENTIAL~~

Fig. 4.114 – Longitudinal temperature profile in radial arch

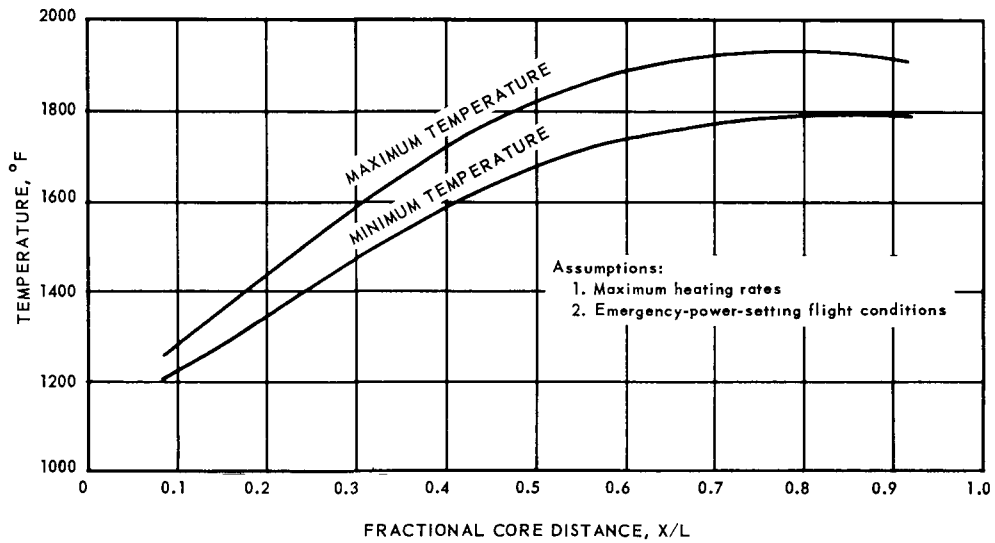


Fig. 4.115 – Longitudinal temperature profile in radial arch

~~CONFIDENTIAL~~

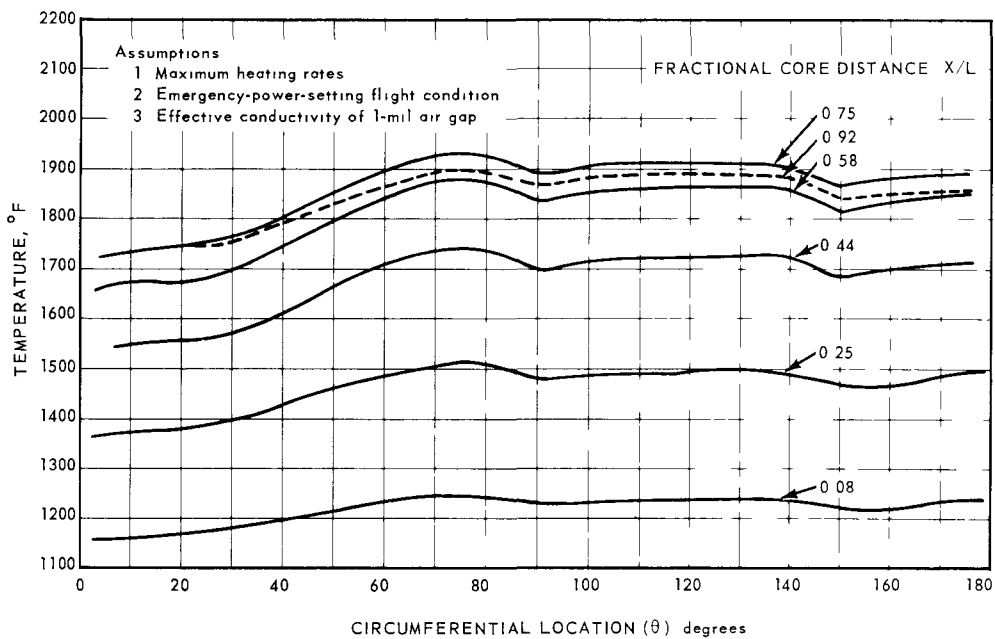


Fig. 4.116 - Circumferential temperature profile in radial arch

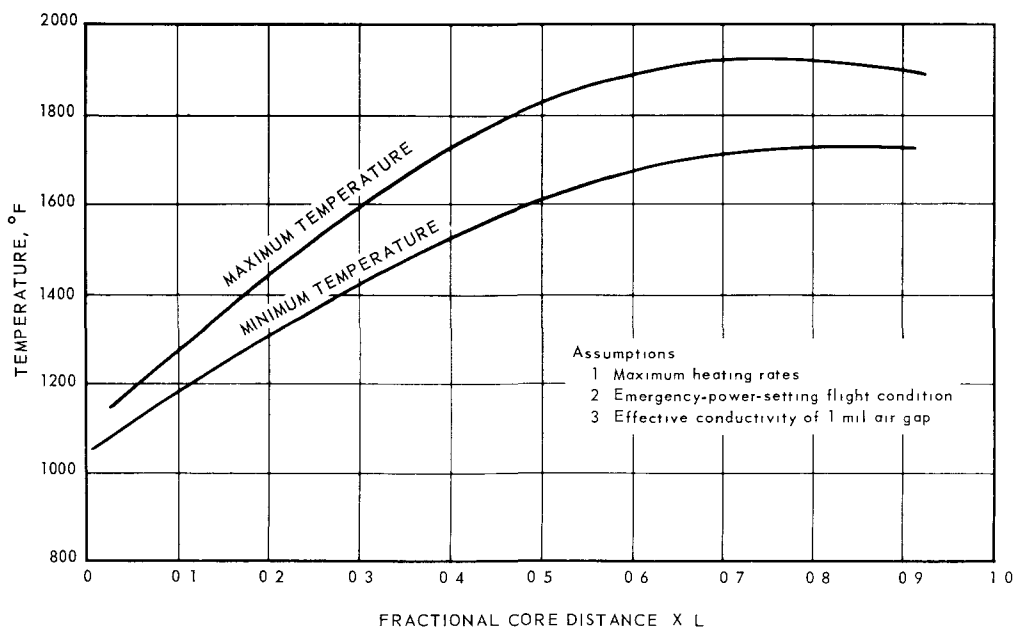


Fig. 4.117 - Longitudinal temperature profile in radial arch

~~CONFIDENTIAL~~

4.116 and 4.117 show that, when a 0.001-inch air gap was assumed to exist around reflector tubes, the circumferential temperature variation on hot day, emergency power setting increased to 200°F although the maximum temperature remained approximately the same as with perfect thermal contact.

A summary of significant aerothermal design data and criteria is shown in Table 4.38.

TABLE 4.38
RADIAL ARCH THERMAL DESIGN DATA AND CRITERIA

Nominal Average Heating Rate (w/gm-mw)	0.034		
Heating Rate Uncertainty Factor			
Average	1.30		
Maximum	1.35		
Minimum	1.20		
Design Criteria			
(1) Perfect thermal contact between reflector tubes			
(2) Minimize circumferential arch temperature gradients			
(3) Temperature limit of arch insulation - 2000°F short time			
	1900°F 1000 hours		
Thermal Design Parameters, Cruise Condition, Maximum Heating Rates			
Percent core power generated	1.72		
Percent core power absorbed	2.025		
Hydraulic diameter, in.	0.195	0.155	0.185
Number of tubes per arch	6	4	2
Total airflow, % $W_{a4.0}$	1.5	0.56	0.44
Texit, °F	1500	1625	1500

4.10 CORE LINER AND SHAFT TUNNEL COMPONENT DESIGN DATA

4.10.1 MECHANICAL DESIGN

4.10.1.1 Core Liner

Since the coupling shaft joining the compressor and turbine rotors passed through the center of the reactor, a core liner was provided as supporting structure to maintain the integrity of the tube bundle. The liner, shown in Figure 4.118, had a duodecagonal outside surface 13.36 inches across flats and a 13.23-inch inner diameter. Flanges on the forward end of the core liner supported the forward reflector sectors.

Due to differences in expansion at various operating conditions between the core liner and the tube bundle, the liner was oversized for a minimum of 75 percent contact area during reactor operation. At assembly, the core liner flats were 0.16 inch above the nominal size represented by 53 fuel tubes across each flat.

Ideally, the liner structure acted only as a substitute for rods and tubes removed from the tube bundle, and did not alter the magnitude or direction of pressures and load paths. However, with manufacturing tolerances, differential thermal growth, and dimensional variations within the core, perfect fit was not assured. Figure 4.119 is a plot of various stress conditions which could occur depending upon dimensional tolerances. All factors were normalized for simplification. The ordinate is the ratio of tangential pressures to

~~CONFIDENTIAL~~

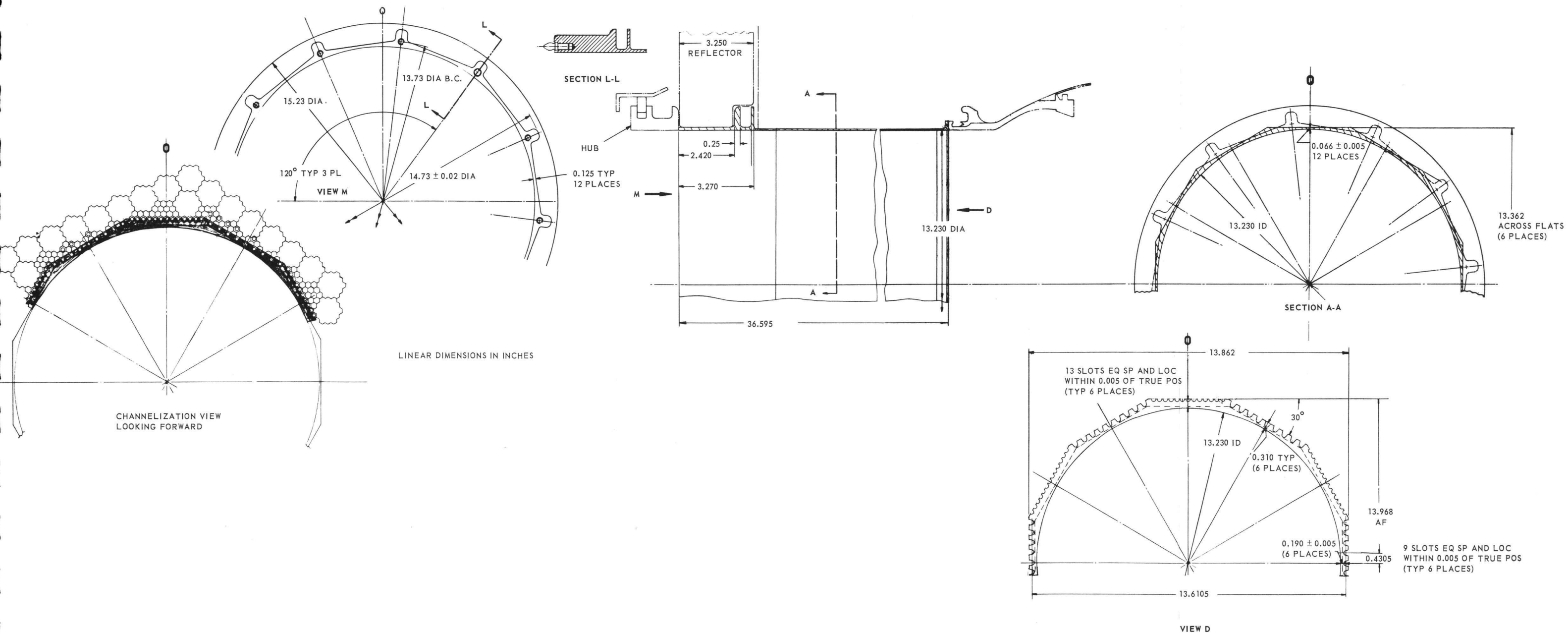


Fig. 4.118 - Core liner, XNJ140E-1 (Dwg. 207R906)

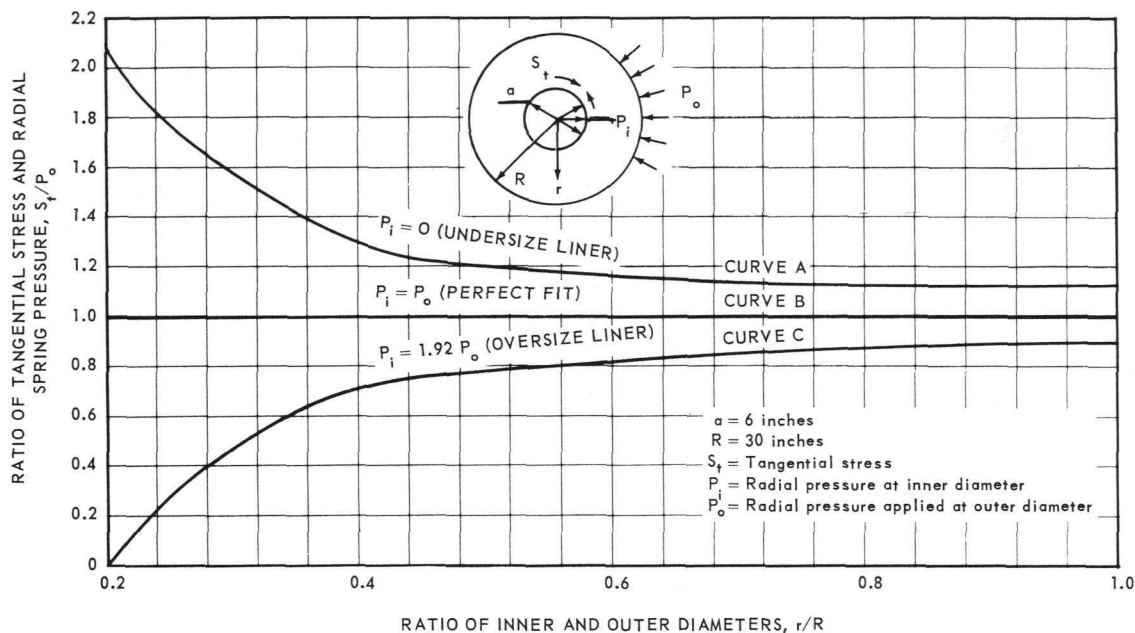
CONFIDENTIAL

Fig. 4.119—Tangential stresses in core due to core-liner fit and radial-spring loading

spring pressures; the abscissa denotes fractions of radial distances; and the parametric curves are the ratio of liner pressure to spring pressure.

Curve A represents the case in which the core liner was completely undersized so that it was actually free to ride within the void while imparting zero pressure against the tube bundle. Resulting tangential pressures within the bundle reached a maximum of 2.082 times the external pressure.

Curve B represents the ideal case of hydrostatic equilibrium where all pressures were equivalent to the external pressure.

Curve C represents the case of an oversize liner in which the tangential pressures at the liner interface approached zero but the radial pressure approached 1.92 times the spring pressure. Any increase in core liner pressure was impossible because the bundle, being unable to support tensile pressures, would begin to separate. This separation would move the apparent inner radius farther out until the internal pressure equaled the external pressure.

Mechanical design of the core liner primarily was concerned with buckling. The lowest possible mode of buckling failure was having three full sine waves since any lesser mode was fully restrained by the core geometry. External pressure was taken as the maximum spring force, increased by an oversized liner multiplier of 2, to which was added an air pressure differential which occurred at the forward end. These pressures were further increased by 1.5 since an ultimate type failure was assumed.

Stress levels in the thinnest wall sections were predicted to be approximately 15,000 psi compressive. Double-aged Inconel X was specified as the core liner material.

4.10.1.2 Shaft Tunnel

The shaft tunnel was a structural member transferring, by tension, the load reaction of the aft-retainer assembly to the front shield central island structure. It was a tubular

CONFIDENTIAL

member with an outer diameter of 12.00 inches and 0.120-inch wall thickness. A bolting flange on the forward end permitted remote replacement of the shaft tunnel without full disassembly of the reactor assembly.

Calculated tensile stresses in the shaft tunnel were low and were analyzed easily by conventional formulae.

Fine adjustment of a spacer ring in the front shield during final assembly virtually eliminated transverse loading at the forward flange due to manufacturing and assembly tolerance mismatch. Thus, bending stresses were confined to those caused by differential deflections of the core and front shield. Preliminary vibration analysis predicted as little as 0.04-inch differential deflection between the two components.

The wall thickness of 0.12 inch was chosen to increase the transverse natural frequency of the shaft tunnel to 7,000 rpm, well above the 5,000 rpm engine speed.

The annulus between the core liner and shaft tunnel was used to conduct cooling-air to the rear shield central island.

4.10.2 AEROTHERMAL DESIGN

The following temperature considerations were applied to the aerothermal design of these components:

1. The long-time temperature limit of the liner was 1400°F.
2. The long-time temperature limit of the tunnel was 1000°F.
3. The air temperature rise through the annulus was limited to approximately 50°F.

The secondary heating rates are reported in reference 29. Figure 4.11 showed the gross radial heating rate distribution through the reactor, indicating the uncertainty in the various components.

The thermal characteristics of the tunnel and liner were strongly dependent on the temperature of the inner reflector elements, and for this reason, the core liner, shaft tunnel, and inner reflector were analyzed as a single component.

The following assumptions were used in the aerothermal design:

1. Maximum heating rates prevailed.
2. Cooling-air flow rate between tunnel and liner was 3.6 percent $W_{a4.0}$.
3. Inlet-air temperature of annulus flow was 120°F above compressor discharge-air temperature for all design conditions.
4. Perfect thermal contact between liner and reflector elements was assumed.
5. Radiation (thermal) between tunnel and liner was negligible.
6. An adiabatic cylindrical boundary along the mean circumference of the tunnel wall was assumed.

The assumption of the adiabatic boundary along the mean circumference of the tunnel wall was justified on the basis of previous analysis which showed that, for steady-state conditions, the tunnel wall approached the temperature of the air flowing between the tunnel and liner. For transient conditions, the above assumption was not necessarily valid; however, at the time that the analysis was performed there were no data available concerning the boundary conditions on the shaft side of the tunnel which would have allowed an evaluation of this effect. Radiant heat exchange between the tunnel and the liner was neglected because of the limitations of the computer program used in the analysis (cf., section 4.7.2). However, for steady-state conditions the radiation effects were negligible. The effect of radiation during transient conditions was analyzed and is reported in reference 32. The analysis methods were the same as those reported in section 4.7.2.

~~CONFIDENTIAL~~

Calculations showed the following results for the cruise (design point) and emergency power setting flight conditions:

	Cruise	Emergency Power Setting
Temperature rise of tunnel air, °F	40	30
Maximum average liner temperature, °F	1090	1240
Maximum average tunnel temperature, °F	975	780

4.11 FORWARD REFLECTOR COMPONENT DESIGN DATA

4.11.1 MECHANICAL DESIGN

A forward reflector sector and mounting details are shown in Figure 4.120. The individual 30-degree sectors that formed the forward reflector were supported at their inside surface by a flanged support ring that was an integral part of the core liner. Each of the sectors was supported at its periphery by the structural shell and two leaf-spring assemblies. The leaf springs were keyed to both the structural shell and the sectors to affect a shear support similar to that used with the tube bundle, and were designed to give the reflector assembly approximately the same spring rate as that of the core. Accordingly, the core and reflector, although independent structures, exhibited similar deflections under inertia loads.

Cooling-air passage holes in the front reflector were aligned with the transition pieces to provide smooth airflow into the cooling passages. The resultant triangular hole pattern is shown in Figure 4.120. Large 1.30-inch-diameter holes in the outer reflector region provided passage for the control rod guide tube as well as the cooling-air for the channels surrounding the radial arch. Other small holes in the outer reflector region were necessitated by the partial transition pieces surrounding the radial arches.

Since transition pieces were not used at the forward end of the inner reflector, the inner portions of the sectors were slotted to supply cooling-air to a plenum formed between the double flanges at the front end of the core liner. Cooling-air was distributed to the inner reflector by small holes drilled through the inner of the two flanges.

The size of these slots and holes was governed by the required flow of cooling-air.

The tube bundle was supported axially by the longitudinal support system (front-reflector assembly, aft-retainer assembly, shaft tunnel, and minor hardware). Aft loads on the tube bundle, resulting from aerodynamic drag forces, friction and aft acceleration loads, were transmitted through the aft-retainer assembly to the balance of the longitudinal support system. Forward loads on the tube bundle, resulting from friction and forward acceleration loads, were transmitted through the forward reflector to the balance of the longitudinal support system. Clearance space was provided to permit the tube bundle and the metallic structure of the longitudinal support system to expand independently as dictated by temperatures and material properties without loading either the tube bundle or the longitudinal support system. Since the aerodynamic load was the principle load on the tube bundle in the axial direction, it was expected that the tube bundle would normally bear against the aft-retainer assembly. Clearance space would occur as a gap between the aft face of the forward reflector and the front face of the tube bundle. Therefore, the only loads that were expected to appear on the forward reflector were the aerodynamic drag and inertial loads of the reflector itself.

Two load-limiting conditions were considered in the mechanical design. The first of these occurred when the entire tube bundle pushed against the front reflector (as a uni-

~~CONFIDENTIAL~~

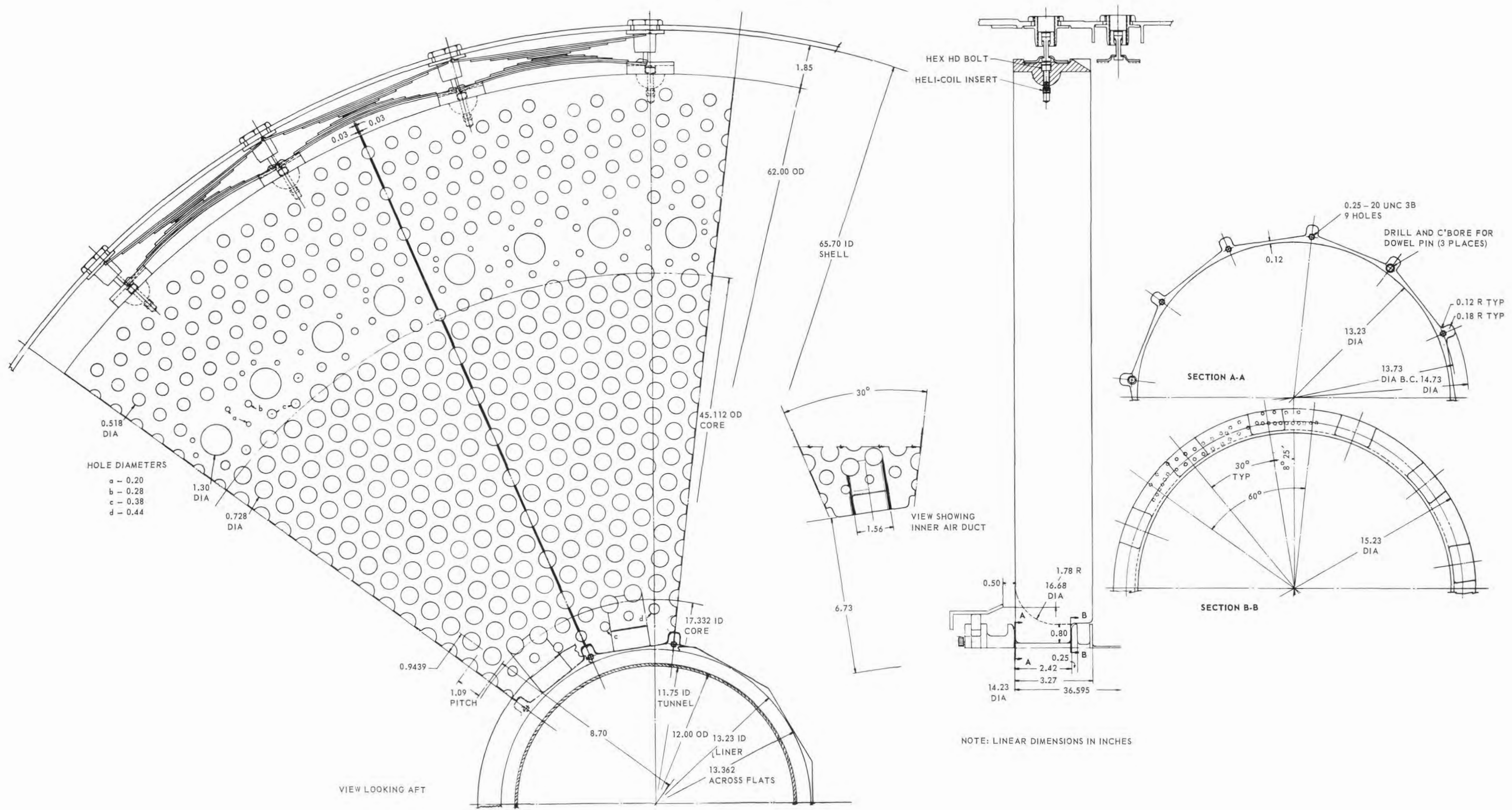


Fig. 4.120 - Sectors of forward reflector (Dwg. 207R935)

~~CONFIDENTIAL~~

form load) under an 8-G crash load. The second occurred when the entire tube bundle pushed against the front reflector and acted as a concentrated ring load through a circumferential row of transition pieces extending forward, consistent with friction, under a 2-G inertial load.

4. 11. 1. 1 Mechanical Stresses

Mechanical stress analysis assumed that each sector acted as a simply supported beam. First, the stresses were computed for a solid sector. Stress enlargement factors then were applied to the initial solution to obtain the maximum stresses in the ligaments of the perforated plate. A stress enlargement factor of 5.4 was derived from the geometry of the plate using methods discussed in reference 33.

Following are the results of the mechanical stress analysis:

Uniformly Distributed Load

Aerodynamic drag (1 psi)	Bending stress = 286 psi
8-G tube bundle load	Bending stress = 6580 psi

Concentrated Ring Loading on 22.5-inch Radius

2-G tube bundle load	Bending stress = 1360 psi
----------------------	---------------------------

The 0.2 percent yield strength of beryllium at 1000°F, the maximum temperature of the sectors, was 10,000 psi. Results of the stress analyses indicated that ample margins of safety in the sectors existed for both uniformly distributed and concentrated tube bundle loadings.

4. 11. 1. 2 Thermal Stresses

Approximate thermal stresses in the forward reflector were computed by assuming that each sector was a thin rectangular plate with a parabolic temperature distribution across its surface.

The assumed radial temperature profiles approximated the form $T = \Delta T \left(\frac{1 - 4y^2}{b^2} \right)$

For all temperature profiles investigated, the highest temperatures and gradients occurred in the region between the 6.75-inch radius and the 24-inch radius. Therefore, the sector was assumed to be a rectangular plate with a width of 12.6 inches (the width of the sector at the 24-inch radius) and a length of 17.25 inches (the length of the sector between the 6.75-inch and the 24-inch radii).

The maximum thermal stresses occurred at the edges of the plate, and were calculated in accordance with methods given in reference 34. Stresses computed from these equations applied to a solid plate, and were corrected by the stress enlargement factors given in reference 33.

Thermal stresses in the front reflector during steady-state conditions were negligible when compared to those for transient conditions. During scram transient conditions, radial temperature gradients in the front reflector were severe due to large variations in porosity and cooling-air flow between the active core and outer reflector regions. Temperature gradients and thermal stresses were reduced to acceptable levels by two methods: (1) lowering the temperature in the outer reflector region of the front reflector by increas-

~~CONFIDENTIAL~~

ing the porosity and heat transfer area in that region, and (2) introducing a time-temperature lag in the active core region of the forward reflector by insulating the cooling passages with metallic shields.

The results of the thermal stress analysis of the scram transient and the resulting margin of safety are shown as follows:

Time After Scram, sec	ΔT , °F	Temperature, °F	Ligament Stress, psi	Allowable Stress, psi	Margin Of Safety
50	21	574	2019	15,730	6.79
100	40	494	3729	17,060	3.56
400	50	244	3800	20,920	4.50

4.12 AFT-RETAINER ASSEMBLY COMPONENT DESIGN DATA

4.12.1 MECHANICAL DESIGN

The aft-retainer assembly provided longitudinal support of the tube bundle against aerodynamic drag forces, friction, and aft acceleration loads. The assembly was formed by 12 independent 30-degree sectors which were simply supported at the inside radius by the shaft tunnel and near the perimeter by the rear shield outer section. Individual sectors rather than a continuous plate were chosen for (1) compatibility with available brazing furnaces and (2) reduction of thermal stresses in the structure.

The assembly was a sandwich-type tube sheet having two parallel plates separated by tubes that served the dual purpose of providing shear ties for the plates and passages through the tube inside diameters for reactor discharge air. A diametric view of a sector complete with components is shown in Figure 4.121. Figures 4.122 and 4.123 show the aft-retainer assembly layout and sector drawings, respectively.

Sectors of the assembly were supported and oriented as indicated below.

<u>Location</u>	<u>Relative Motion</u>	<u>Method</u>
Center	Rotation	1. Keying sector to center hub 2. Keying center hub to liner
	Radial	1. Pin-connection between hub and sector 2. Hub moved inside liner
	Acceleration displacement	Supported by liner
Perimeter	Rotation and displacement due to acceleration	Supported in shear by springs and structural shell
	Radial	Radial springs allowed for differential thermal expansion

All components of the aft-retainer assembly were remotely removable for maintenance following nuclear operations. Handling lugs and data instrumentation lead disconnects were provided.

Rene' 41 was specified as the main structural material.

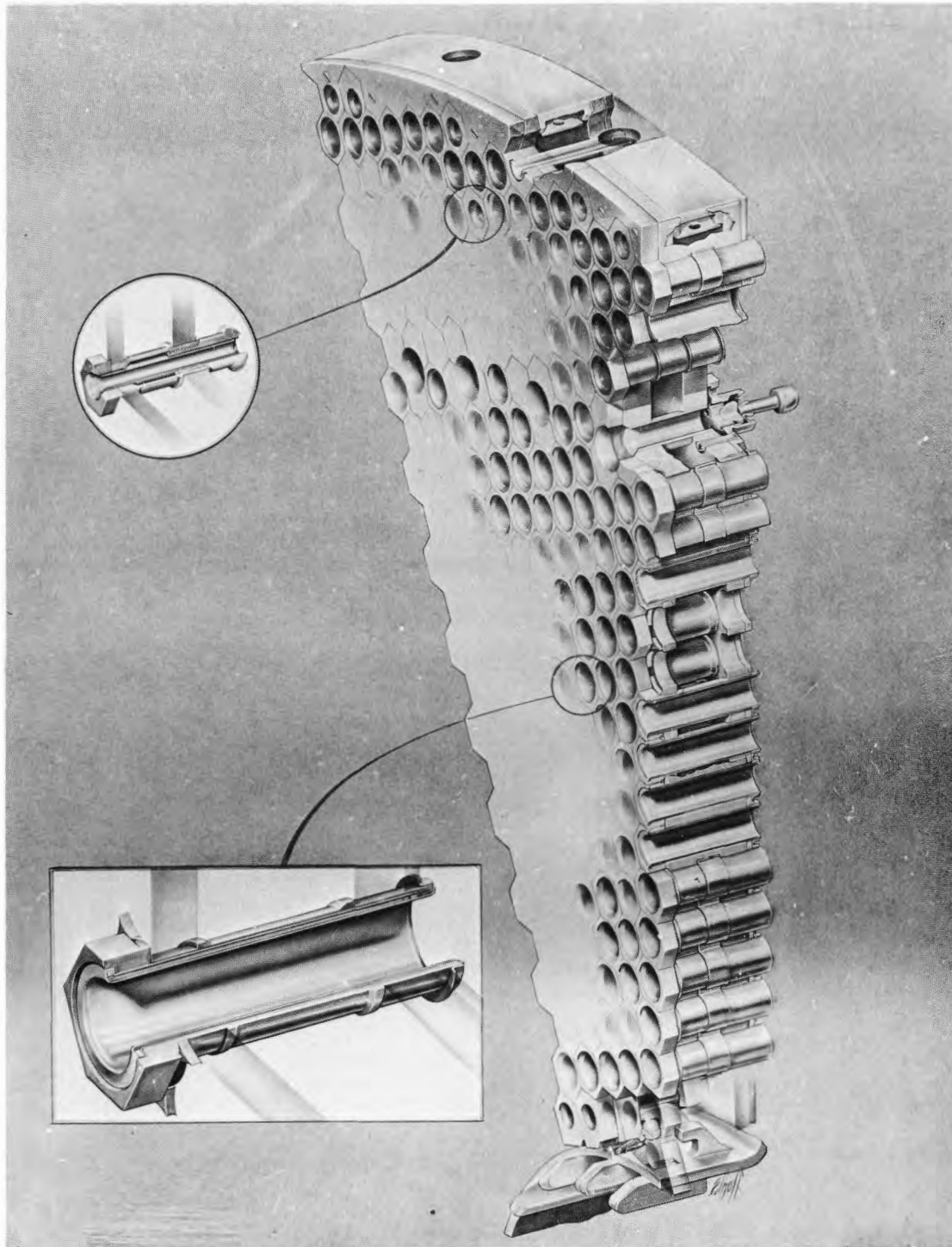
CONFIDENTIAL

Fig. 4.121 - Aft-retainer sector, XNJ140E-1 (DI-533)

CONFIDENTIAL

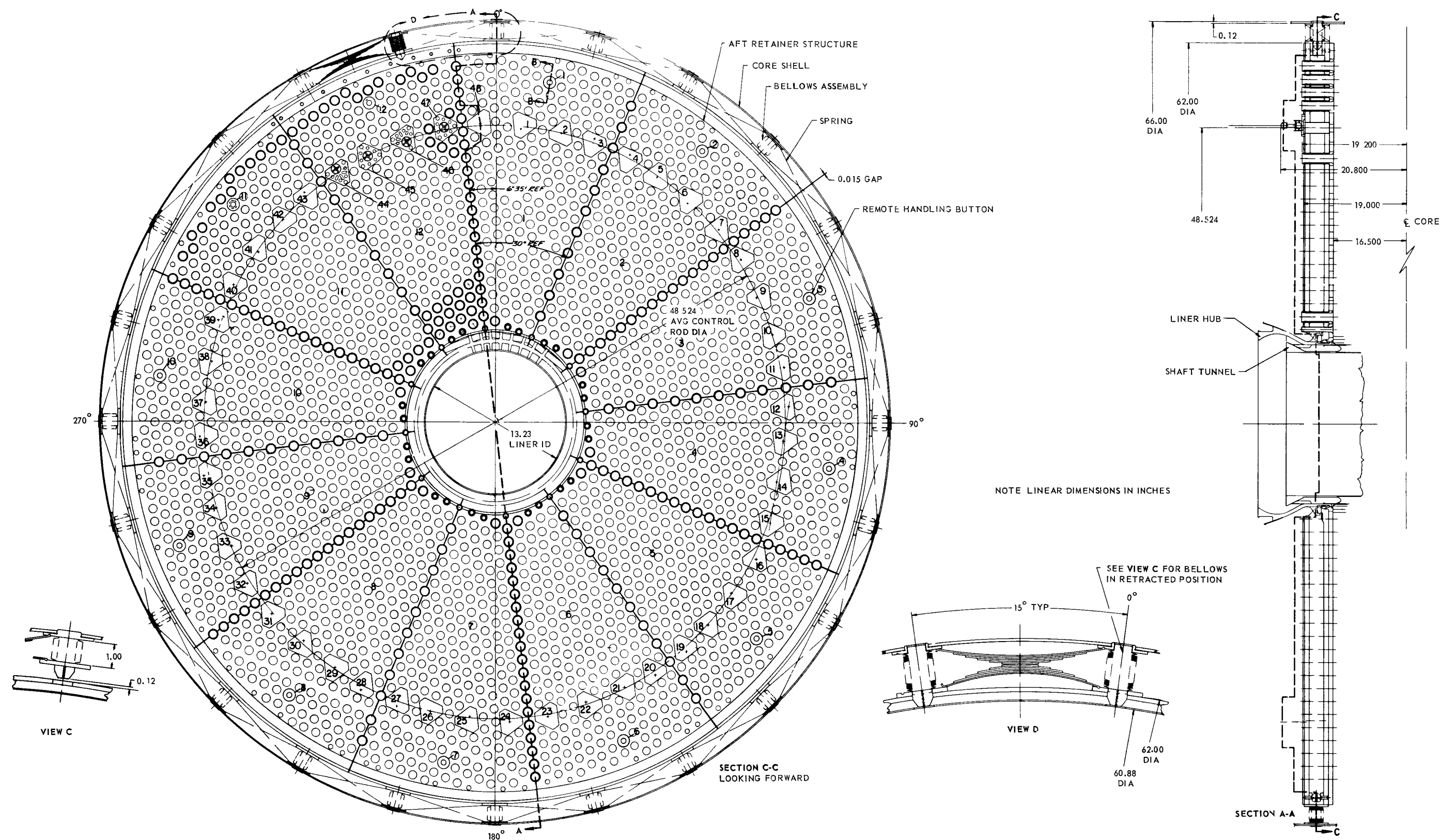


Fig. 4.12 - Aft-retainer assembly layout (Dwg. 206R691)

4. 12. 1. 1 Loading Criteria

Each sector was treated analytically as a simply supported radial beam with its outer end overhanging its support. The location of the inner support was dictated by the tunnel and liner diameters. The outer support was located to obtain approximately equal stresses due to positive and negative beam moments.

For purposes of gross analysis all stresses were assumed constant about any circumferential section and varied only with radius and loading. The structure was assumed to approach a sandwich concept having continuous shear ties. Secondary bending of the plate induced by the shear ties was negligible because the large tubes were located on close centers. Calculations assumed that the plate supported all bending stresses.

To obtain maximum calculated stresses in the perforated plate, a stress concentration factor of seven was used to allow for loss of material as well as stress concentration at the holes. This factor was conservative when compared with perforated plate stress enlargement factors presented in reference 33. An analysis determining stress magnification factors also showed that the assumed factor of 7 was conservative as indicated by Figure 4. 124.

Loading of the longitudinal support system was determined by (1) relative deflections of the supports for the aft-retainer sectors caused by thermal expansion, (2) pressure drop through the core, (3) inertial loads on the core, and (4) friction within the tube

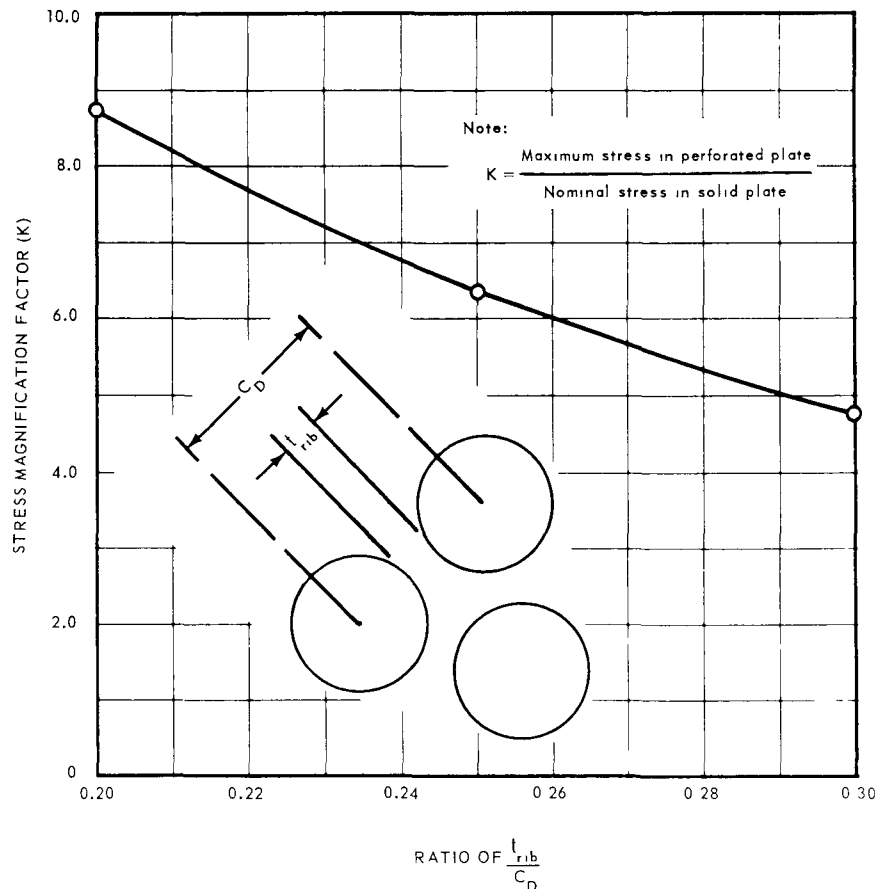


Fig. 4.124 - Stress magnification factor (theoretical) for maximum stress in a perforated plate

~~CONFIDENTIAL~~

bundle during deformation. The internal friction varied with the radial pressure (on the tube bundle) and the coefficient of friction. Analyses of a number of cases were necessary to determine maximum loads and most severe load distributions on the retainer sectors, inner support (tunnel), and on the outer support (rear shield). Load cases were selected that were physically possible. Other cases were analyzed for design changes that might relieve loading conditions. The most severe load conditions were established, and the various components were analyzed for these conditions.

4. 12. 1. 2 "Worst Case" Design Condition

A "worst case" design condition was derived to serve as the basis of mechanical design of the aft-retainer assembly. Reasoning and assumptions used to derive this worst case are presented in this section and are shown graphically in Figure 4. 125.

Earlier experimental evidence from hot airflow tests on the three-tier mockup indicated that the tube bundle moved in concentric rings when it deformed under load. For a given radial spring pressure, coefficient of friction, and length of core, the friction in pounds available at any radius r , Figure 4. 125a, was equal to

$$F = 2\pi r L f P_s.$$

For convenience, the pressure drop through the core and aft inertial load were treated as an equivalent pressure acting on the aft surface of the core. An aft inertial load of 1 G was equivalent to 3. 54 psi distributed pressure on the aft-retainer assembly. The shear at any radius was equal to the air load on the area inside of that radius, and was given by

$$V = P_o \pi (r^2 - r_i^2).$$

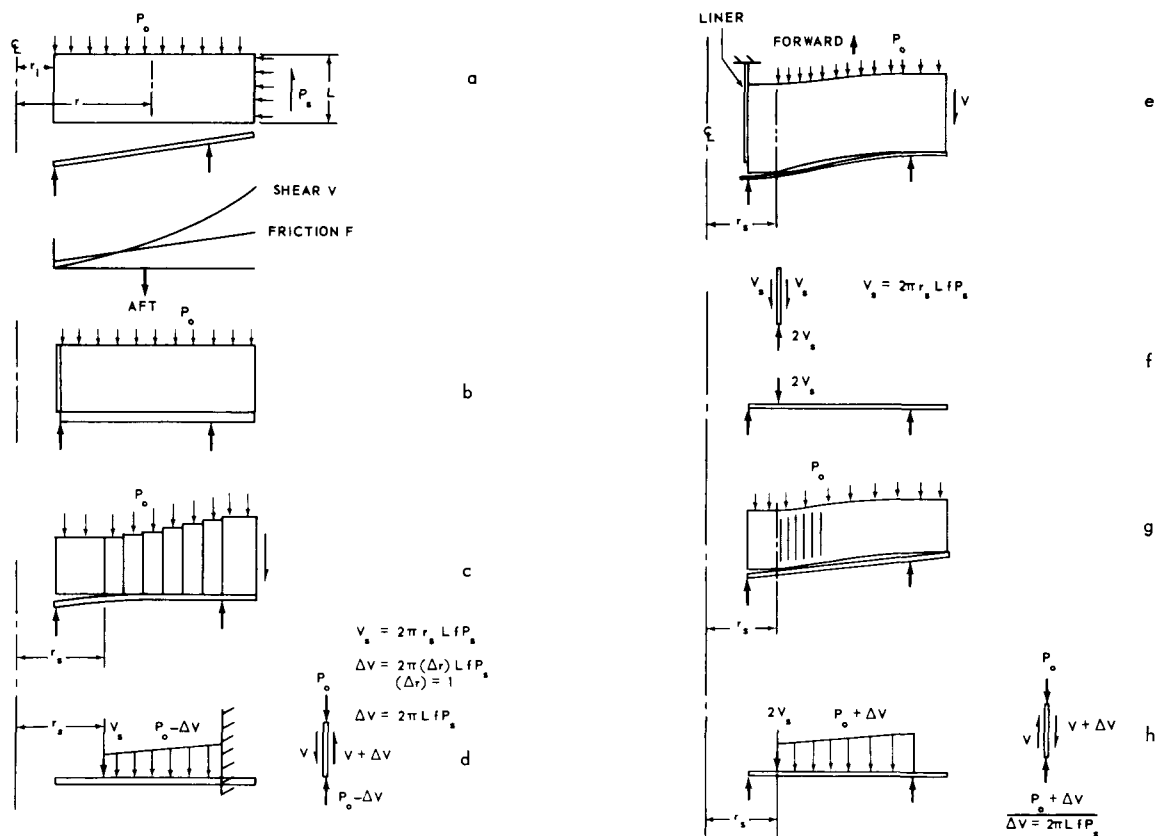


Fig. 4.125 - Aft-retainer-plate loading analysis

~~CONFIDENTIAL~~

The maximum shear occurred at the outer radius of the tube bundle. As the air load increased, the entire tube bundle moved against the retainer sectors, as shown in Figure 4. 125b. The inner support was assumed to have deflected aftward away from the retainer. If the air load on the tube bundle (now rigidly supported at the outer support) further increased, successive slip rings developed in the bundle as radii were reached wherein shear and friction forces were equal, Figure 4. 125c. The retainer acted as a cantilever fixed at the outer support and loaded as shown in Figure 4. 125d. The friction at the outside radius of the tube bundle and the air load on the bundle outside of the outer support served to keep the retainer sectors in equilibrium. This loading condition was investigated for several air loads (long and short time), and for the effects of varying radial pressure.

After the condition shown in Figure 4. 125d was reached, the inner support was assumed to move forward again (due to changes in temperature) and forced the retainer against the deflected shape of the core, Figure 4. 125e. The liner was assumed to be at a position forward against its stop so that friction to resist motion of the core was developed on both the inside and outside radii. Initially, the sectors touched the tube bundle and developed a concentrated load equal to $2 V_s$ (twice the frictional load on a single row of tubes). As the inner support continued to force the sectors forward, successive slip rings develop in the tube bundle as shown in Figure 4. 125g. The outer support deflected sufficiently to keep the sectors from picking up a balancing moment from the core and becoming a simple support. The limiting load case is shown in Figure 4. 125h wherein the sector was loaded by a concentrated load of $2 V_s$ plus a distributed load applied between the area of $2 V_s$ and the outer support. This condition was examined for (1) varying positions of the concentrated loads, (2) several air loads, and (3) the effect of varying radial pressure.

These maximum loads were combined with the appropriate maximum temperatures and time deviations to produce the equivalent life for a particular portion of the flight profile. A summation of these equivalent life spans then was compared with material properties for compatibility.

4. 12. 1. 3 Design Results

Since the structural integrity of the retainer sector was based on the stress-rupture strength of the Rene' 41 material, the total life was calculated for a composite mission. A maximum hot-spot temperature of 1600°F was assumed to exist over the entire life of the component. This condition occurred at a hot channel whose radial position was unknown and whose width could extend over an entire circumference. Since the maximum possible loading condition on the retainer also occurred as a ring load, the locations of maximum stresses and temperatures could have been coincident.

Certain flight conditions were lumped together for ease in design. These conditions represented a worst case, flight profile, as shown below.

Case	Flight Conditions ^a	Retainer Loading, psi	Time At Load, hr	Equivalent Life Versus Case 1	Allowable Stress, psi	Equivalent Life, %
1	d, e	12	905	905. 0	9, 000	12. 8
2	2	35	0. 1	31. 8	26, 300	0. 5
3	a, 4, f	27	75	5900. 0	20, 200	83. 4
4	c	19	20	237. 0	14, 250	3. 3
		Totals	1000. 1	7073. 8		100. 0

^aSee section 3. 2. 1.

When calculating tube stresses, the small change in shear across the diameter of the tube ends was neglected. Maximum tube bending stresses of 3580 psi indicated an adequate margin of safety, i.e., 1. 5.

~~CONFIDENTIAL~~

Shear stress on the braze connection was distributed the same as that for tube bending. A factor of 2 was applied to the braze stress to cover the uncertainty of braze penetration at the worst location. The maximum shear stress of 1080 psi, including the braze factor, indicated a margin of safety of greater than 1.³⁶

Center Hub - The center hub, Figure 4. 126, oriented the 12 retainer sectors and maintained them as a single unit. It resisted the interface friction between the tube bundle and the sectors resulting from differential radial thermal expansion. The hub also formed the inner longitudinal reaction for the retainer sectors, and, in turn, was held by the shaft tunnel.

The center hub of the aft-retainer assembly was analyzed for four general loading conditions. Each loading was applied individually and a stress factor was calculated at several stations in the critical area. No support from the adjacent members was considered and load distributions were treated to yield maximum stress values. The results of these loading studies are shown below.

<u>Loads Applied, lb</u>	<u>Resulting Stress, psi</u>
Axial load of 400 pounds per lug	-21,480
Radial load inward of 400 pounds per lug	-14,360
Radial load outward of 600 pounds per lug, eccentricity allowed for	+35,475
Radial load inward which was a radial component of a load of 833 pounds per lug. This is a load of 40,000 pounds per sector.	+38,310 (tension)

Other preliminary analyses, reference 37, indicated that an adequate margin of safety was present.

Outer Reactions - The outer reactions of the aft-retainer sectors were transmitted to the rear shield outer section through free-swiveling linkages of ball-and-socket design. These linkages permitted radial and tangential differential motion between the rear shield and retainer sectors to allow for differential thermal expansion as well as reactor deflection from G loads. The four linkages per sector were located on a chord perpendicular to the center radius to match closely the expected sector deflection. The worst case loading assumed that two of these linkages reacted the entire sector load. Discharge air from the control rod guide tubes maintained the linkage below 1200°F, the design temperature.

The mean temperature of the aft-retainer sectors was controlled by cooling-air flowing radially inward between the side plates and over the structural tubes. Each of the 12 sectors was a sealed, self-contained unit obtaining its cooling-air supply from the bleed-speed bypass annulus and discharging it at the center hub. Thin 0.010-inch foil, welded along radial edges of each sector, provided a seal for the coolant air. As shown in Figure 4. 122, two retractable bellows assemblies per sector formed the cooling passages from outside the structural shell to the perimeter of the retainer sectors. The bellows permitted differential motion between the structural shell and the retainer. A remotely adjustable orifice was provided in each bellows assembly. The orifice was located just outside the reactor structural shell and regulated the amount of cooling-air flowing into the sectors.

Thermal Insulation - Thermal insulation was used to isolate the retainer sectors from their surrounding sources of heat. The insulation consisted of (1) a zirconia spacer on the forward face, (2) an insulating tube within the structural tubes, and (3) a Thermoflex

~~CONFIDENTIAL~~

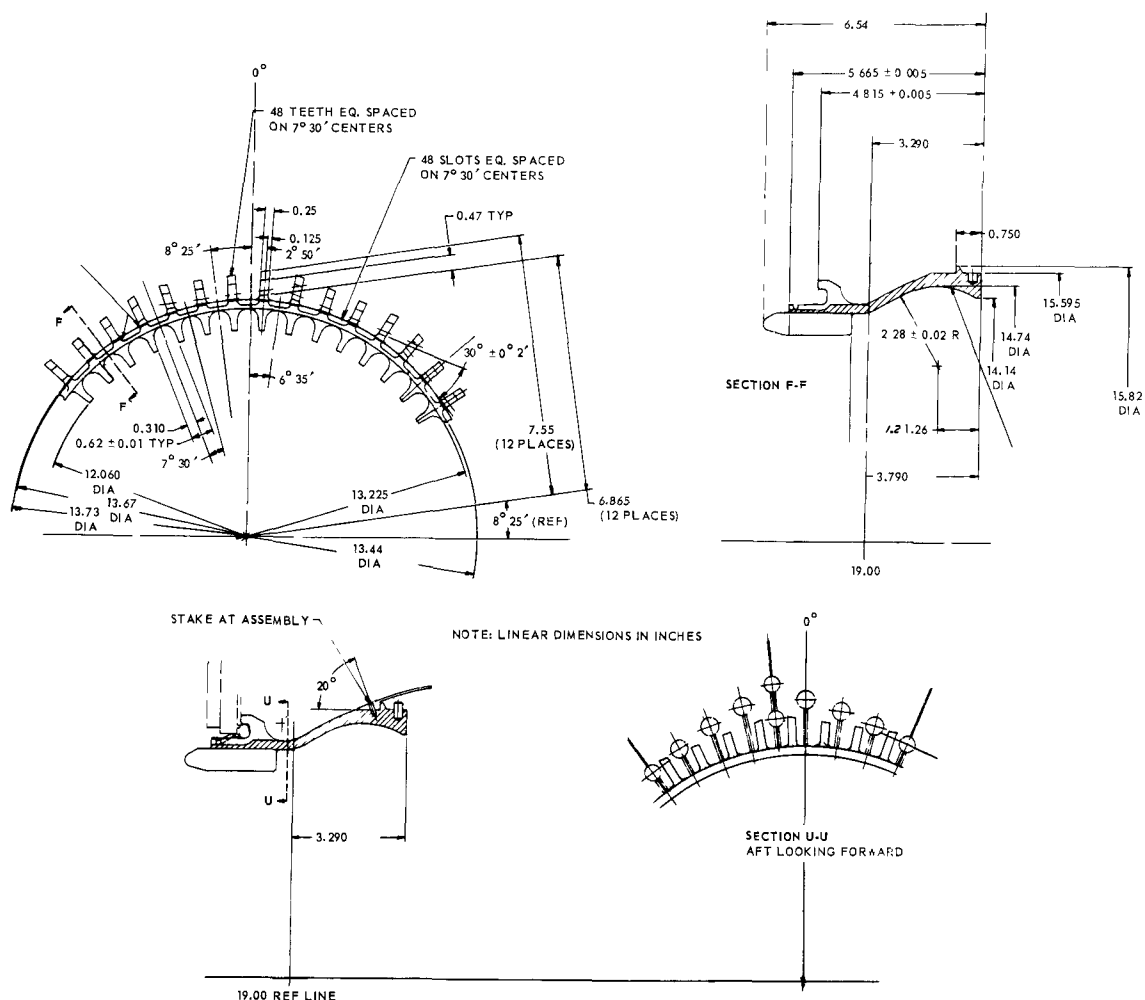


Fig. 4.126 - Aft-retainer assembly, center hub (Dwg. 207R910)

blanket on the aft surface. The hexagonal shaped zirconia spacer also transmitted compressive forces from the tube bundle transition pieces to the aft-retainer assembly. A shoulder on the zirconia spacer rested in a countersunk hole on the face of the retainer sectors, as shown in Figure 4.122, and resisted frictional loads arising from differential thermal expansions of the tube bundle and the retainer sectors.

The insulating tube was a self-contained unit made from a tube of high density insulation (24 lb/ft³ Johns Manville Company Thermoflex) sandwiched between two metallic foils. The inner foil was a 0.008-inch seamless tube while the cover sheet was a 0.002-inch foil wrapped around the outer surface of the insulation. Aft drag loads on the tubes were reacted by a forward ring welded to the sheathing foils, Figure 4.122. The resultant load on the tubes was less than 1 pound per tube.

Several 0.03-inch diameter holes were provided in the inner and outer sheaths to prevent external collapsing air pressure loads which might occur during a sudden depressurization caused by an engine stall or scram.

Those tubes carrying core discharge-air were made of palladium - 10 percent rhodium and an outer foil of palladium. Tubes used in the outer reflector region were exposed to relatively lower temperatures (<2000°F) and were made from Inco 702.

~~CONFIDENTIAL~~

Insulation on the aft face of the retainer was fabricated from a 0.12-inch-thick blanket of high density Thermoflex and a 0.025-inch cover sheet made of Inco 702, as shown in Figure 4.127. Each sector had five sections of insulation with overlapping edges on its back surface, held in position by cylindrical clips welded to the protruding structural tubes. Holes were provided in the cover sheet to allow for sudden depressurization.

Inco 702 was chosen as the cover material since the design temperature was in the 1800° to 1900°F range. Previous tests indicated that a 0.02-inch-thick foil of Inco 702 would operate 1000 hours without detrimental oxidation if kept below 2000°F.

4.12.2 AEROTHERMAL DESIGN

4.12.2.1 Methods of Analysis

Since the useful life of the aft-retainer assembly was a function of combined temperature level and stress (mechanical and thermal), configuration dimensions were established to provide an optimum design incorporating both thermal and mechanical stress analyses. Parameters which affected the aerothermal performance of the aft-retainer assembly were (1) core discharge-air temperature and flow rate, (2) transition piece temperature, (3) volumetric heating rate, and (4) aft-retainer cooling-air flow rate and inlet temperature. Core cooling-air flow rate, discharge-air temperature, and power level were fixed by the performance requirements; transition piece temperature and retainer volumetric secondary heating rate were dependent upon these factors. The aft-retainer assembly temperature level was controlled by the amount and inlet temperature of cooling-air supplied to the assembly.

Various studies investigated the possibility of using discharge-air from one or more other reactor secondary components for cooling the aft-retainer assembly. Combinations of control rod, outer reflector, radial spring, and pressure pad discharge-air were considered and eliminated for one or more of the following reasons: (1) discharge-air temperature was too high, (2) discharge pressure was insufficient to overcome pressure drop through the aft-retainer assembly, and (3) the method of cooling was physically impractical or impossible because of ducting and sealing problems. For these reasons, it was decided to cool the aft-retainer assembly by ducting compressor discharge-air, available in the bleed-speed duct between the structural shell and pressure vessel, through a bellows assembly connecting the annular duct and the retainer cooling passages.

Because of the complexities of the configuration and the number of aerothermal parameters which were considered simultaneously, analyses generated by hand calculations were limited. Most of the aerothermal analyses of the aft-retainer assembly incorporated the use of various digital computer programs.

Detailed temperature analyses were based on the consideration of a single structural tube and its associated pieces. The outer boundaries of these sections were assumed to be insulated, and circumferential effects were neglected. By analyzing several such isolated tube-plate sections at various radial positions, conservative values of maximum plate temperatures and gross radial temperature gradients were calculated. Each tube-plate section was analyzed by dividing it into relatively small nodes and incorporating the THTA digital computer program described in reference 38. For a given tube location, core airflow rate, discharge-air temperature, and transition piece temperatures were obtained from a core analysis and used as input to the computer program. Volumetric secondary heating rates and distributions were obtained from a nuclear analysis of the tube location.

A range of cooling-air flow rates was estimated, and an analysis was made for several flow rates within this range. The temperature increase of the cooling air as it flowed in-

~~CONFIDENTIAL~~

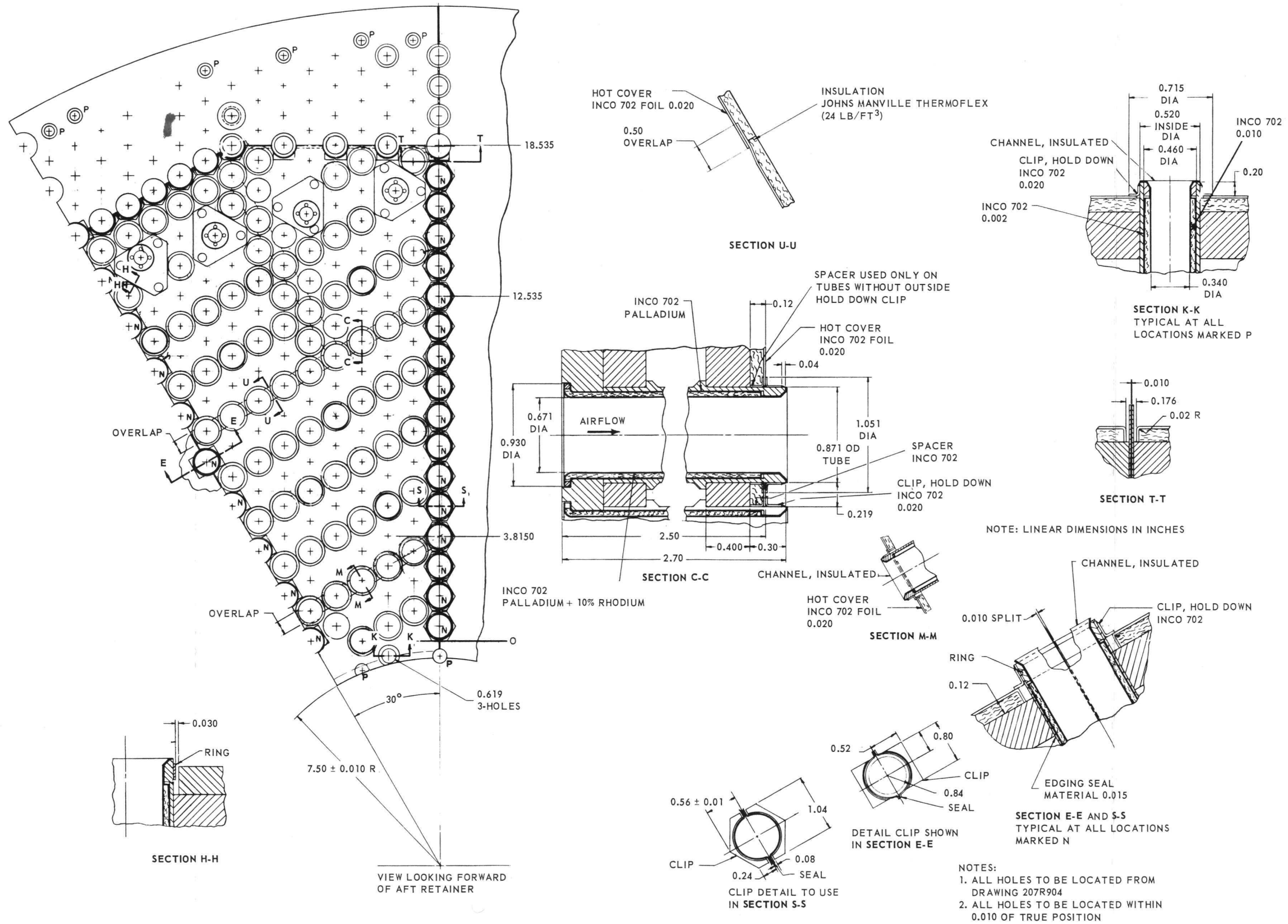


Fig. 4.127 - Insulation, aft face of aft-retainer assembly (Dwg. 196R707 Rev A)

~~CONFIDENTIAL~~

ward was due to heat input from (1) the reactor core through the transition pieces, (2) core discharge-air flow through the insulation assembly, and (3) secondary heat generated in the structural plates and tubes. Preliminary calculations were made assuming that every tube-plate section added equal amounts of heat to the air, based on a section of the first tube row where the local air temperature was known to be the inlet cooling-air temperature. This was a reasonable assumption because the increase in temperature as the air flowed radially inward essentially balanced the effect of the increase in heat transfer coefficient due to the converging passage. A more exact analysis was made by use of a specialized digital computer program, Exit Air Temperature program (EAT). The EAT program was used to make gross heat balances on tube-plate sections of successive tube rows to determine the exit-air temperature from each tube row. In addition, average temperatures of a structural tube, forward plate, aft plate, and zirconia spacers were computed for each tube row. With this information, detailed analyses were made for all tube rows of interest, usually the maximum temperature row as indicated by the EAT program.

An additional problem was the prediction of heat transfer coefficients within the retainer cooling passage. Grimison's data (reference 15, page 273) for flow across tube banks were used (with reservation because of the short tube length and the nonuniform, converging passage). Data for the side plates were practically nonexistent. Preliminary analyses were made using Grimison's data, based on local mass velocity, for the tube bank and arbitrarily assuming the actual local plate heat transfer coefficient to be one-half the computed coefficient. An experimental program, reference 39, determined both tube and plate heat transfer coefficients for the specific configuration.

The following design equations were used for computing minimum tube heat transfer coefficients:

$$\frac{h D_t}{k_f} = 0.0907 \left(\frac{D_t G_{L, M}}{\mu_f} \right)^{0.7} \left(\frac{C_p \mu}{k} \right)_f^{1/3}$$

and

$$\frac{h D_t}{k_f} = 0.000392 \left(\frac{D_t G_{E, M}}{\mu_f} \right)^{1.19} \left(\frac{C_p \mu}{k} \right)_f^{1/3}$$

where D_t = structural tube outside diameter

$G_{L, M}$ = mass velocity based on local minimum area

$G_{E, M}$ = mass velocity based on exit minimum area

subscript f = indicating properties evaluated at film temperature.

Four factors contributed to the total pressure loss in the cooling passages, (1) inlet and exit losses, (2) tube bank friction losses, (3) structural plate friction losses, and (4) heat addition losses. Pressure losses of 1.5 dynamic heads at the entrance and 1.7 dynamic heads at the exit were estimated by considering the various contraction, expansion, and turning losses. The tube bank friction losses were computed by the following equation, reference 40,

$$\Delta P = \frac{4fN G_{L, M}^2}{2 g_c \rho}$$

where $f = 0.635 \left[\frac{(S_t - D_t) G_{L, M}}{\mu_f} \right]^{-0.162}$

N = number of tube rows

S_t = transverse tube spacing.

~~CONFIDENTIAL~~

Since the mass velocity ($G_{L,M}$) increased from row to row through the passage, in the direction of airflow, a row-to-row analysis was made by letting N equal one in the above equation and employing the Off-Design digital computer program, reference 18. Heat addition, as computed by the EAT computer program, estimated loss coefficients, and constants in the above pressure loss equations were given as input to the Off-Design program. The result of the computer analysis was the total pressure loss of the configuration excluding the effect of friction due to the structural plates. The effect of friction was computed by the equation

$$\Delta P = \frac{4fL}{D_h} \frac{G_{L,M}^2}{2gc\rho}$$

$$\text{where } f = 0.046 \left(\frac{D_h G_{L,M}}{\mu_f} \right)^{-0.2}$$

L = plate length

D_h = twice the plate separation

and resulted in a 1.2 percent additional pressure loss.

The major problem in steady-state analyses was the determination of the cooling-air temperature rise, further complicated by the addition of heat storage terms in the heat balance equations. Since the method of analysis employed in the EAT program was not applicable to these conditions, a nodal-point solution, including a mockup of the cooling passage, was employed. In order to compute the cooling-air temperature rise, it was necessary that the nodal-point model include a tube-plate section of each tube row of the assembly. The large node capacity needed for such an analysis required the use of the THTB computer program, reference 41, which has a capacity of 1000 nodes as compared with the 200-node capacity of the THTA program.

4.12.2.2 Design Results

Design input data pertinent to aerothermal analysis of the aft-retainer assembly, at the design point, were as follows:

Turbine airflow rate = 157 lb/sec

Reactor power level = 51 mw

Core airflow rate = 132 lb/sec

Average core exit-air temperature = 1851°F

Maximum core exit-air temperature (hot streak) = 2016°F

Cooling-air inlet temperature = 538°F

Cooling-air inlet pressure = 70 psia

The longitudinal and radial volumetric secondary heating rate distributions are shown in Figures 4.128 and 4.129, respectively. The thermal conductivity of the Thermoflex insulation as a function of temperature is shown in Figure 4.130. The thermal conductivities of zirconia and Rene' 41 were assumed to vary linearly with temperature over the range shown below:

Temperature, °F	Zirconia Conductivity, Btu/hr-ft-°F	Rene' 41 Conductivity, Btu/hr-ft-°F
500	1.113	7.9
2500	1.428	20.0

Assuming the cooling-air flow rate to be 2.0 percent of W_{a4} , and using maximum secondary heating rates, typical results of the EAT computer program showing the variations of forward and aft plate inside surface temperatures and cooling-air temperature

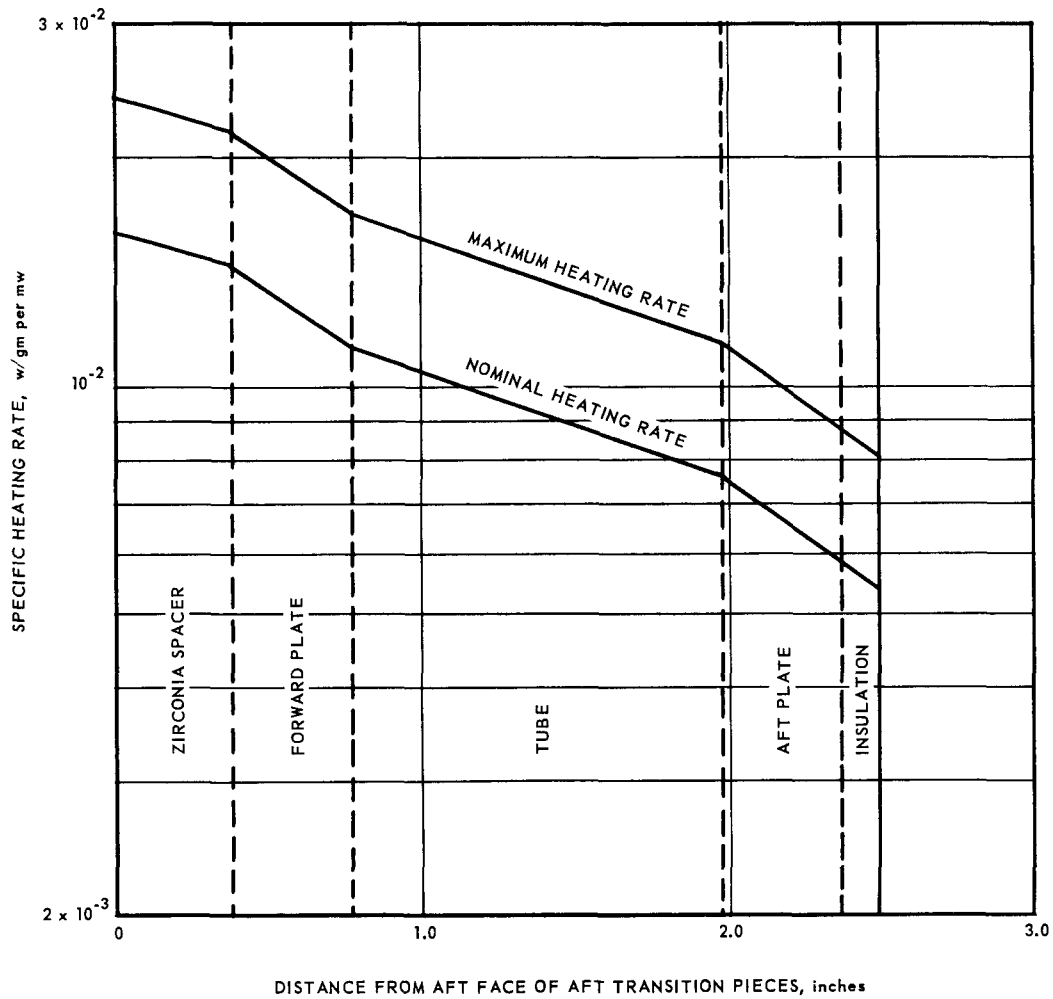
~~CONFIDENTIAL~~

Fig. 4.128—Longitudinal distribution of secondary heat generation in the aft-retainer assembly

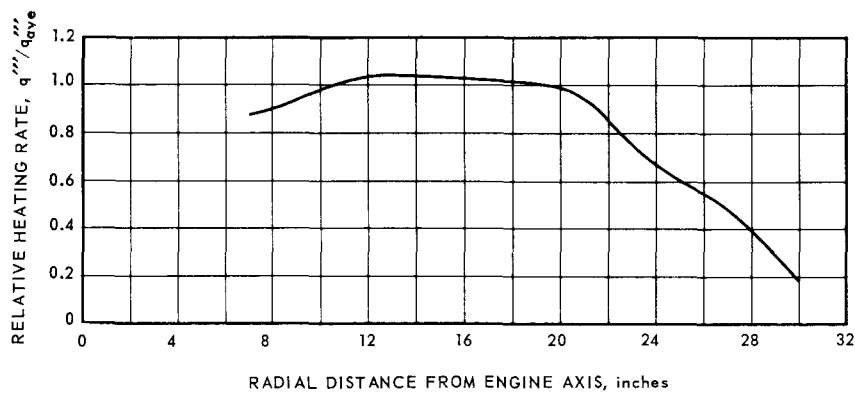


Fig. 4.129—Radial distribution of secondary heat generation in aft-retainer assembly

~~CONFIDENTIAL~~

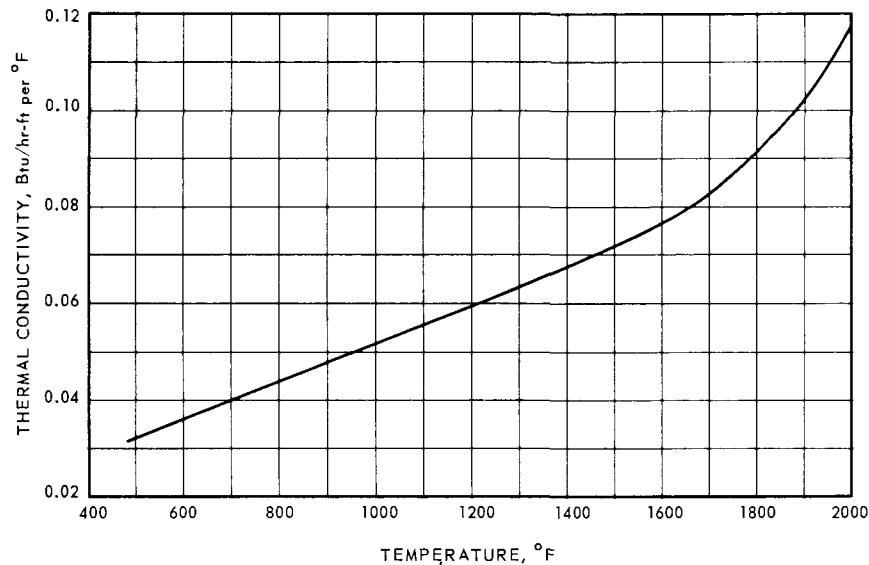


Fig. 4.130 – Thermal conductivity of Thermoflex insulation

with core radius (tube row) are presented in Figure 4.131. Figure 4.132 presents the detailed temperature distribution in the maximum-temperature-tube row for the above case with the additional boundary condition of maximum rather than average core exit-air temperature. Figure 4.133 shows the effect of varying the cooling-air flowrate for both nominal and maximum heating rates as well as average and maximum core exit-air temperature. The results of the pressure loss calculations are shown in Figure 4.134.

From an aerothermal design viewpoint, no further optimizing of the aft-retainer assembly was planned. A summary of the effects of design changes and the resulting design selection is presented in Table 4.39.

4.13 RADIAL-SUPPORT-STRUCTURE COMPONENT DESIGN DATA

4.13.1 MECHANICAL DESIGN

The system of radial leaf springs mounted inside the reactor structural shell constituted the radial support system for the tube bundle. The structural shell provided support for the springs as well as absorbing reactions from the longitudinal support system and, consequently, served a dual role as a member common to both support systems. The springs supplied the radial forces required to hold the tubes in intimate contact for all operating conditions and yet were sufficiently flexible to permit the tube bundle and metallic structures to expand independently as dictated by temperatures and materials properties without excessively loading the tube bundle. Loading from the springs was distributed to the tube bundle through metallic pressure pads to minimize local load concentrations under the springs.

The tube bundle was supported by a distribution of shear forces around its perimeter as previously shown in Figure 4.63. The leaf springs were designed to resist tangential loads so that the shell supported the reactor by supplying a shear reaction through the springs. This design concept was consistent with the ability of a thin shell (membrane) to furnish a shear reaction without distortion from out-of-round. The stiffness of the

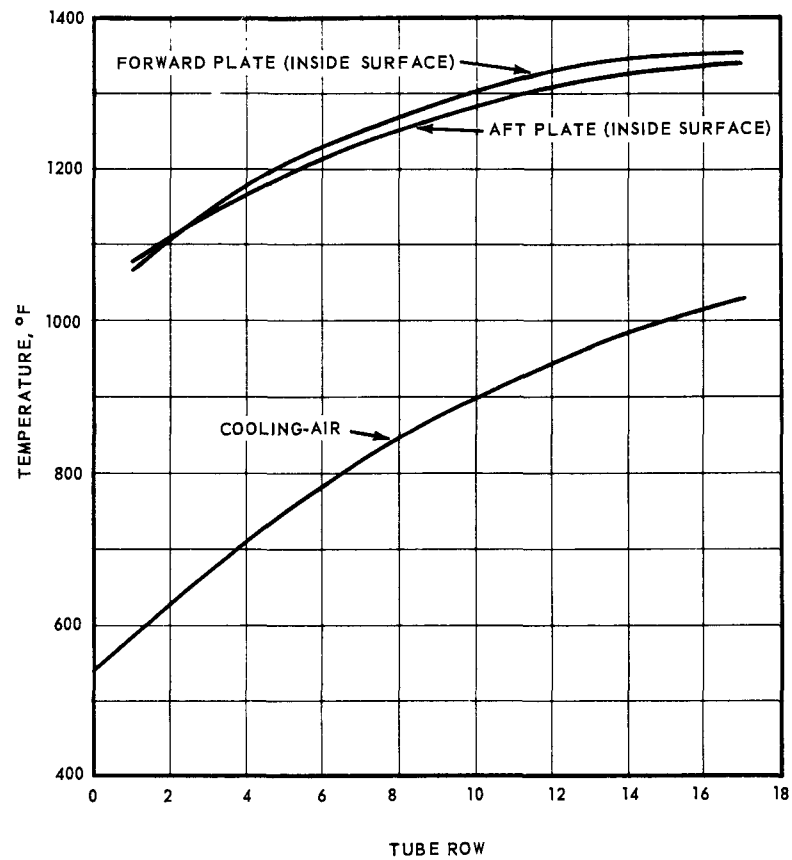
~~CONFIDENTIAL~~

Fig. 4.131 - Radial temperature distribution in components of aft-retain assembly

~~CONFIDENTIAL~~

CONFIDENTIAL

Overhead

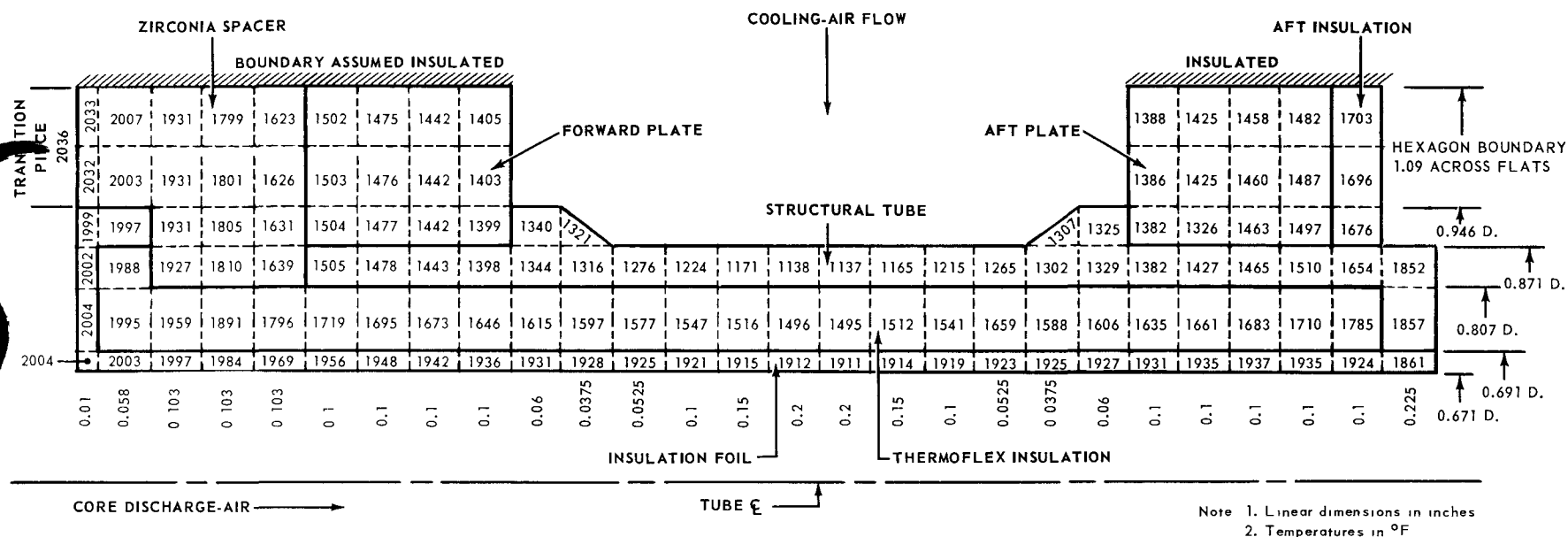


Fig. 4.132—Temperature distribution surrounding the hottest tube of the aft-retainer assembly.

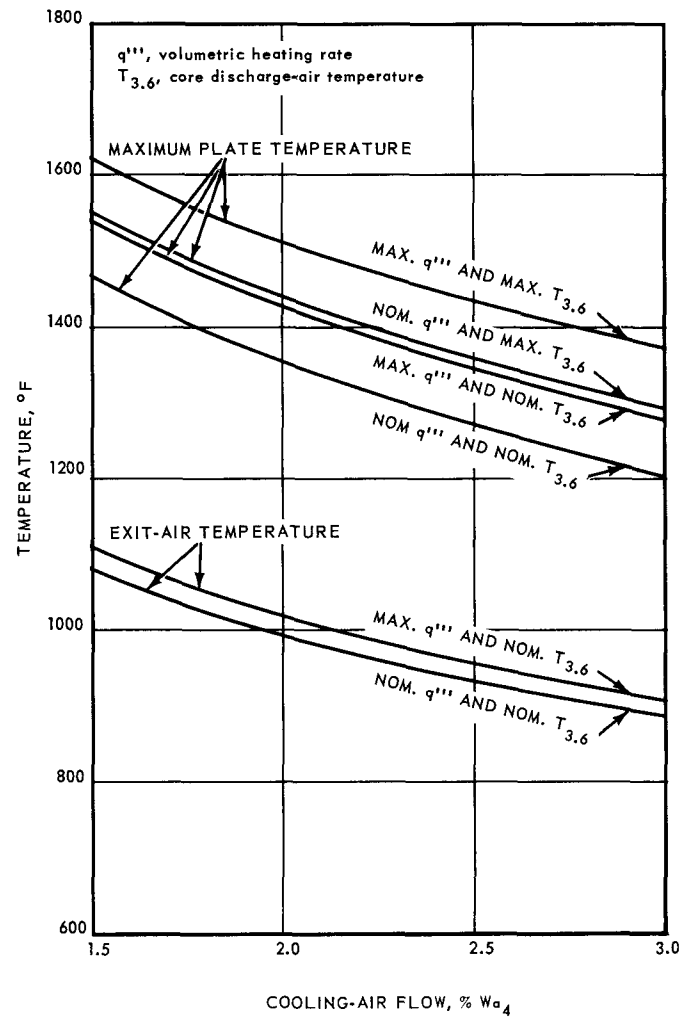
~~CONFIDENTIAL~~

Fig. 4.133—Parametric study of thermal performance, aft-retain assembly

~~CONFIDENTIAL~~

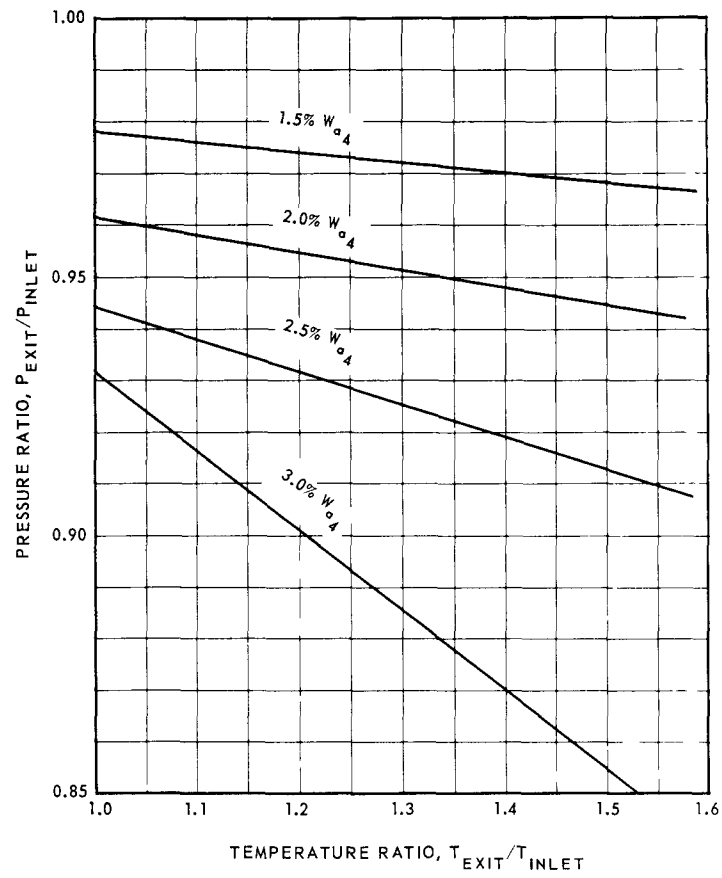


Fig. 4.134 - Parametric study of pressure-temperature relationship in aft-retainer assembly

~~CONFIDENTIAL~~

TABLE 4.39
EFFECTS OF DESIGN CHANGES, AFT-RETAINER ASSEMBLY

Design Change	Advantages	Penalties	Selected Dimensions, in.
Increase plate thickness.	Increases strength.	Increases heat generation volume. Increases temperature level. Increases internal temperature gradient. Increases core length.	Thickness = 0.4
Increase separation between plates.	Increases strength. Longer tube increases fin effect on plates.	Increases cooling flow to maintain heat transfer coefficient. Increases area exposed to core discharge air. Increases heat generation volume. Increases core length.	Separation = 1.2
Increase zirconia spacer thickness.	Increases temperature drop from transition pieces to forward plate.	Increases heat generation volume. Increases area exposed to core discharge air. Increases core length.	Thickness = 0.375
Increase tube outside diameter.	Allows thicker tube and/or insulation. Increases heat transfer area.	Increases cooling flow pressure loss.	Outside diameter = 0.871.
Decrease insulation liner diameter(s).	Allows thicker tube and/or insulation. Decreases temperature level.	Increases primary core flow pressure loss and heat transfer coefficient.	Inside diameter = 0.671.
Increase tube thickness.	Increases fin effect on plates. Increases strength.	Decreases insulation thickness. Increases heat generation volume.	Thickness = 0.030.
Increase insulation thickness.	Decreases heat flow from core discharge air.	Decreases tube thickness.	Thickness = 0.058.
Increase thickness of aft insulation.	Decreases heat flow from air in aft plenum.	Increases core length.	Thickness = 0.1.

leaf springs was much greater under tangential loading than under radial loading and virtually the entire support was furnished by the shear reaction. In addition to minimizing the relative deflections between the tube bundle and shell, this support method maintained radial spring loading nearly constant around the perimeter of the reactor, even under inertial loading. The tube bundle was semirigidly attached to the shell when considering displacement of the reactor axis relative to the axis of the shell, but was flexibly connected in the radial direction to provide for differential thermal expansion.

The spring rate of the combined tube bundle and radial support system was derived by integrating the spring resistance under inertial loading, as shown in Figure 4.135. The integration included both radial and tangential spring resistances.

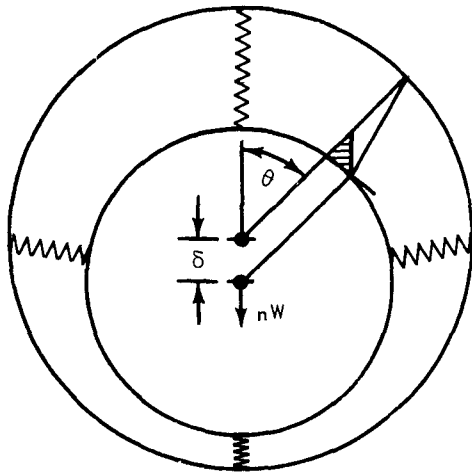
Positive shear ties between the shell and the pressure pads were provided. However, the large side frictional forces alone would have been sufficient to center the tube bundle during 2-G inertial loads. Figure 4.136 shows the deflection of the assembly for various conditions of shear ties and radial direction spring constants of the radial springs.

Each spring consisted of six 0.068-inch-thick leaves and five 0.76-inch-thick leaves, as shown in Figure 4.137. The leaves were welded together to form an 11-leaf assembly with a radial spring constant of 300 pounds per inch. The material was Rene' 41.

A summary of significant design criteria of the radial support system is shown in Table 4.40. A detailed description of the radial support system is contained in reference 42.

The structural shell is shown in Figure 4.138. The most important structural considerations in the design of the structural shell were the stability problems connected with

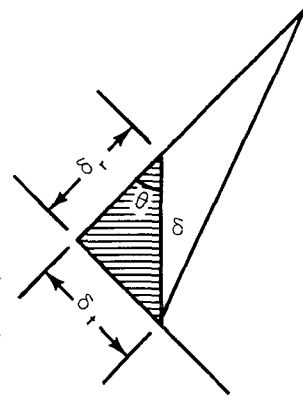
~~CONFIDENTIAL~~



Deflections

$$\delta_r = \delta \cos \theta$$

$$\delta_t = \delta \sin \theta$$



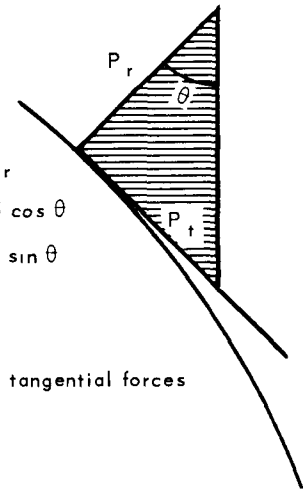
n = inertial load factor
 W = suspended weight
 L = length of tube bundle
 R = radius of tube bundle
 δ = deflection of tube bundle
 A_S = area of tube bundle loaded by a single spring
 subscript r = radial component
 subscript t = tangential component
 $S = \frac{\text{spring rate per spring}}{A_S}$

Forces

$$P_r = S_r \cdot A_S \cdot \delta_r$$

$$= S_r \cdot A_S \cdot \delta \cos \theta$$

$$P_t = S_t \cdot A_S \cdot \delta \sin \theta$$



Weight = summation of vertical components of radial and tangential forces

$$nW = \sum_0^{2\pi} [P_r \cos \theta + P_t \sin \theta]$$

$$= \sum_0^{2\pi} [S_r (R \cdot d\theta \cdot L) \delta \cos^2 \theta + S_t (R \cdot d\theta \cdot L) \delta \sin^2 \theta]$$

$$\frac{nW}{L} = R S_r \delta \int_0^{2\pi} \cos^2 \theta d\theta + R S_t \delta \int_0^{2\pi} \sin^2 \theta d\theta$$

$$= R S_r \delta \int_0^{2\pi} \frac{\theta}{2} + \frac{\sin^2 \theta}{4} + R S_t \delta \int_0^{2\pi} \frac{\theta}{2} - \frac{\sin^2 \theta}{4}$$

$$= \pi R \delta (S_r + S_t)$$

Fig. 4.135—Integration of radial support system spring rates

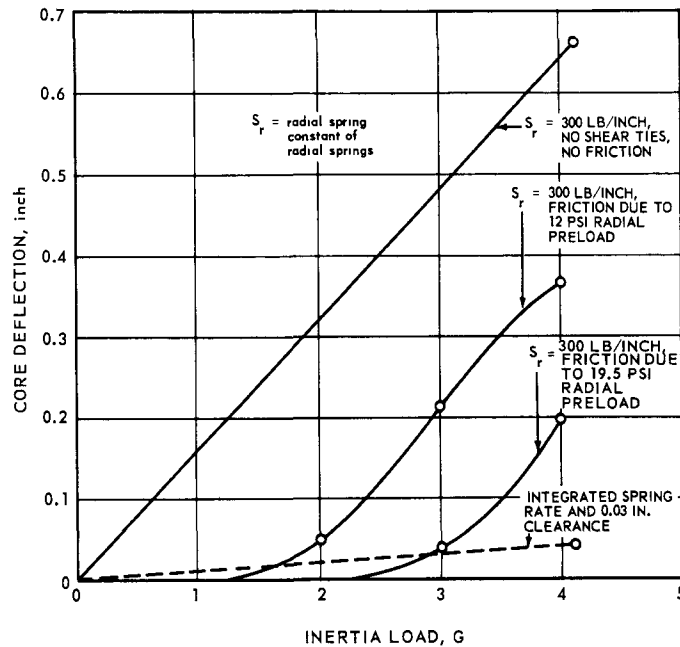
~~CONFIDENTIAL~~

Fig. 4.136—Calculated deflection of core for various conditions of shear ties and radial spring constants

TABLE 4.40
SUMMARY OF DESIGN CRITERIA OF
RADIAL SUPPORT SYSTEM

<u>Core Deflection</u>	
Maximum deflection of any part of core tube bundle from true position as determined by shell C_L , in.	0.12
<u>Radial Pressure</u>	
Spring supported weight, lb	10,409
Combined inertial loads, G	4.13
Minimum radial pressure to sustain core integrity, psi	12
<u>Spring Temperature</u>	
Maximum isothermal (chemical operation), °F	700
Standard day cruise (nominal heating rate), °F	750
Cruise (1.75 x nominal heating rate), °F	900
Hot day emergency (maximum heating rate), °F	1100
Pressure pad maximum longitudinal - average radial allowable temperature (hot day emergency), °F	1200
Structural shell maximum - average allowable temperature, °F	1000
<u>Heating Rates - Nominal Average</u>	
Shell, w/gm-mw	0.00165
Springs, w/gm-mw	0.00208
Pads, w/gm-mw	0.0215
Uncertainty factor	1.75 x nominal
<u>Spring Material</u>	
Maximum long time design stress	90,000 psi
Spring material (GE-ANPD 4203-06-R1)	Rene' 41
<u>Autoclaving</u>	
The maximum design autoclaving pressure radially on the tube bundle expressed as a percent of the reactor static pressure drop	10

~~CONFIDENTIAL~~

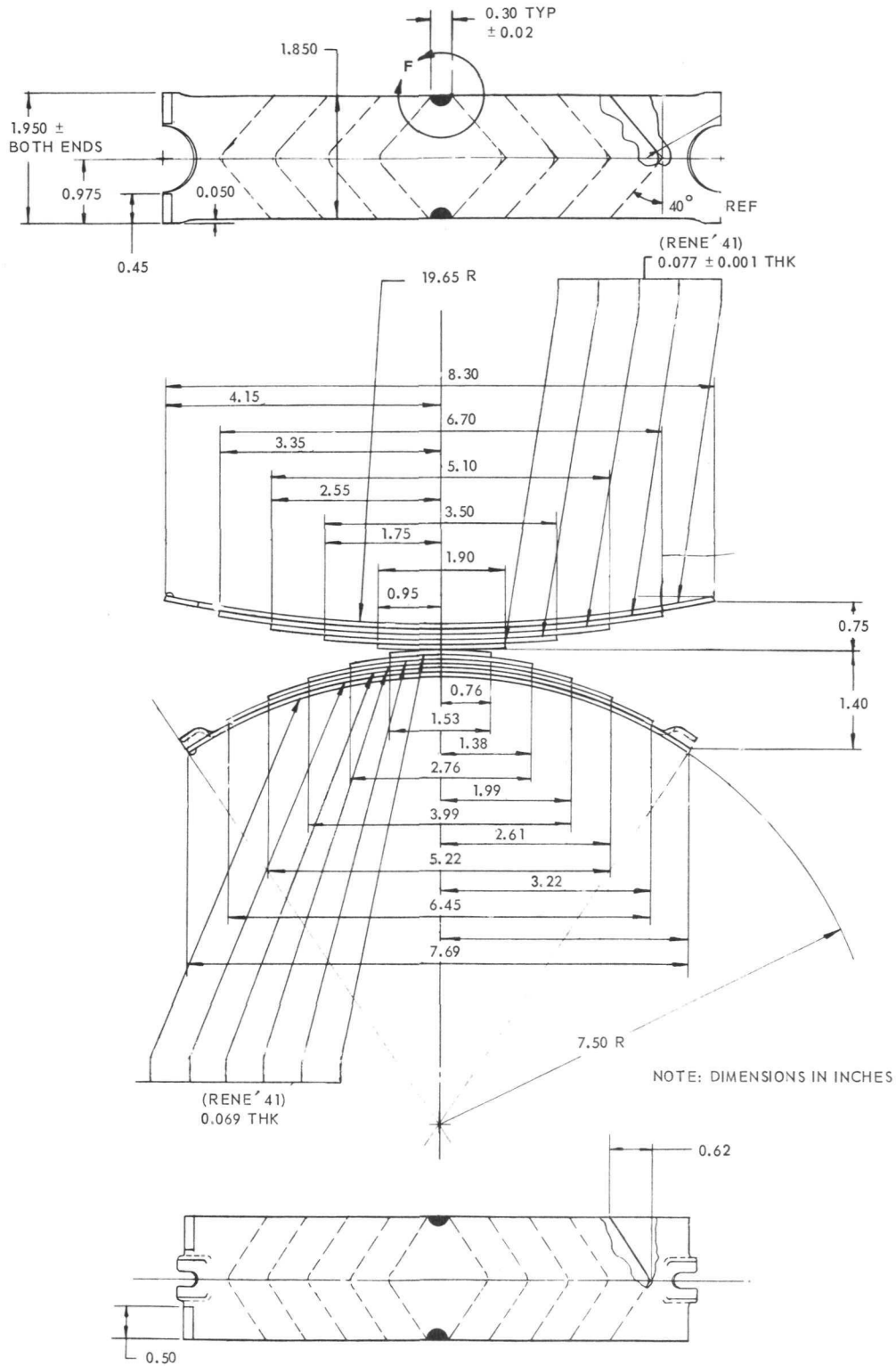


Fig. 4.137 - Leaf spring assembly

a perforated shell, and the thermal design of the flanges to avoid excessive thermal stresses. The mechanical stresses did not present major problems since the shell cross-section was ample, even with reductions due to perforations, to carry the pressure and flight maneuver loads with appreciable margins of safety. A summary of mechanical stresses at critical locations in the structural shell is given in Table 4.41. The maximum calculated stress was 55,000 psi, as compared with an allowable stress of 93,000 psi (0.2 percent yield strength) for Inconel X at 900°F.

TABLE 4.41
SUMMARY OF MECHANICAL STRESSES IN THE
REACTOR STRUCTURAL SHELL

Station ^a	Loading Conditions	Axial Stress, psi	Circumferential Stress, psi
4.5	4G vertical inertial load	13,029	
	Axial tensile load	15,806	
	Combined stresses	28,835	
24.0	Circular bending (4G front plug)		54,092
	4G vertical inertial load	8,078	
	Axial tensile load	17,780	
	Combined stresses	25,858	54,092
59.87	4G vertical inertial load	1,453	
	Axial tensile load	28,558	
	Discontinuous axial bending at base of rib	2,690	
	Hoop stress (radial springs)		16,760
	Circular bending (4G shear tie load)		10,000
	Combined stresses	32,701	26,760

^aInches aft from the forward face.

Because of the low spring rate, it was not necessary to provide for adjustment of the spring load. Retractors, however, were furnished for use during initial assembly to provide clearance between the shell-spring system and the assembled tube bundle. The retractors, Figure 4.139, also were employed at final remote teardown to release the spring load in increments. They provided a window in the structural shell where measurements of the net growth or relaxation of the reactor tube bundle could be made. These measurements would have been performed remotely in the hot shop without reactor disassembly.

4.13.2 AEROTHERMAL DESIGN

Aerothermal design criteria, methods, and results are covered in reference 42. Additional data are included in reference 43.

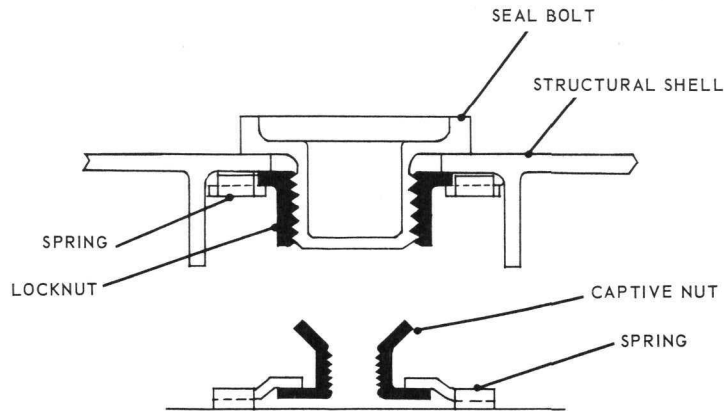
~~CONFIDENTIAL~~

Fig. 4.139 - Spring retractor

4.14 CONTROL ROD ASSEMBLY COMPONENT DESIGN DATA

4.14.1 MECHANICAL DESIGN

The control rod assembly consisted of the chain drive apparatus, the control rod guide tube, and the segmented control rod. It was treated as a simple beam, mounted at the front end by a spherical bearing in the front shield, and simply supported through the reactor.

The maximum normal operating load was established by the requirement that the rod negotiate a bend at which the slope changed from 0 to 0.9 inch per inch.

Details of the control rod are shown in Figures 4.140 and 4.141.

Since the chain drive was supported within two independent structures; i. e., front shield and reactor, it was necessary to determine the maximum long-time and short-time stresses imposed on the chain drive and control rod due to the displacement of these two structures relative to each other. Three primary displacements were investigated:

1. Thermal expansion
2. Manufacturing and assembly tolerances
3. Inertial deflections

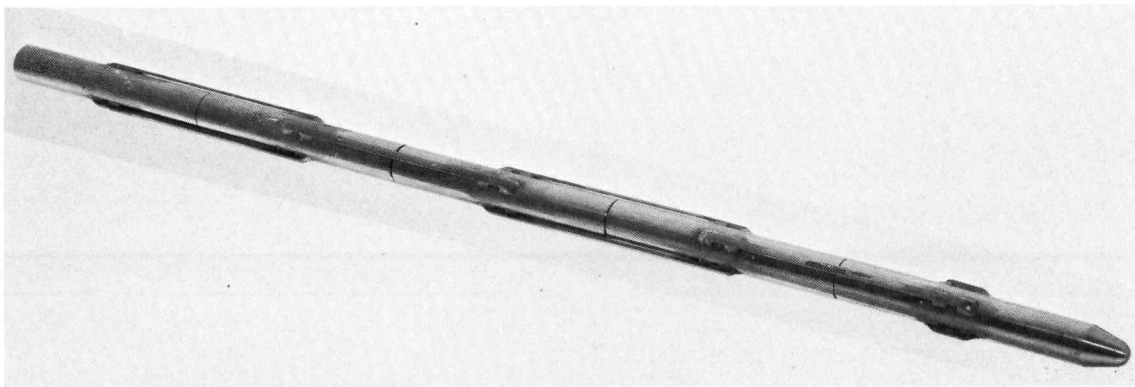


Fig. 4.140 - XNJ140E-1 control rod (U-38803B)

~~CONFIDENTIAL~~

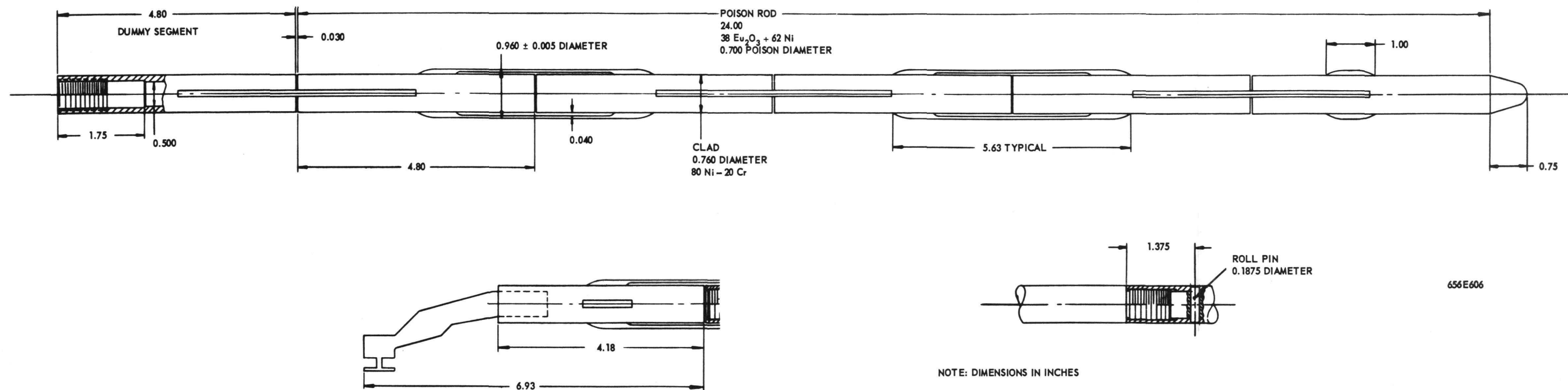


Fig. 4.141 - Details of control rod, XNJ140E-1 reactor

CONFIDENTIAL

Since only the maximum possible stresses were of interest, the top and bottom control rod locations on the vertical centerline were the most critical because only at these locations could all three primary displacement conditions produce the maximum resultant displacement, e. g.,

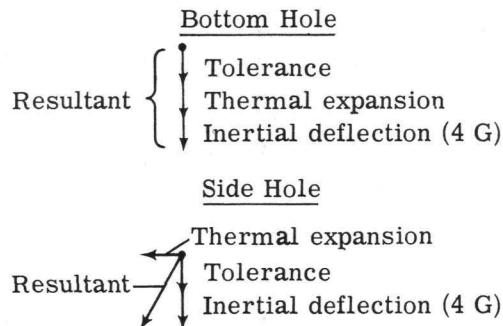


Figure 4.142 shows the axial locations within the engine that were considered critical to proper operation of the chain drive, i. e., flexibility of motion within the front shield and core without excessive interference.

Significant design criteria and data are summarized in Tables 4.42 and 4.43.

4.14.1.1 Design Results

The IBM 704 ASIST (Analysis of Statically Indeterminate Structures) program was used to analyze the control rod assembly. Friction forces, inertial loads, and joint deflections were used as inputs into the program. Three results were obtained from the program: (1) stress in the straps, (2) push-pull loads required to move the control rod, and (3) normal forces.*

Strap Stresses - At 1600°F the maximum strap stress, 19,460 psi, occurred in the maneuver flight condition with 0.0175 inch per inch guide tube slope change and scram (acceleration) rod operation. The stress increased as the temperature decreased, and reached a maximum value of 23,300 psi at 1200°F. Table 4.44 lists maximum stresses for various flight conditions, guide tube slope changes, and rod movements at 1600°F. Figure 4.143 illustrates the effect of temperature on strap stresses for the following conditions: maneuver flight, scram (acceleration); and extended flight, shims-in. Allowable stresses for Inconel X strap also are shown.

Push-Pull Load - The maximum push-pull load occurred in the extended flight condition with scram (deceleration) and was 33.89 pounds. Temperature and guide tube slope changes did not appreciably affect push-pull loads in any flight condition. Table 4.46 lists push-pull loads for various flight conditions, guide tube slope changes, rod movements, and temperatures.

Normal Force - At 1600°F with 0.0175 inch per inch guide tube slope change, the maximum normal force occurred in the maneuver flight condition and was 6.04 pounds. This normal force remained constant for various modes of rod operation (i. e., shim or scram). As temperature was decreased for the maneuver flight condition with scram acceleration, the normal force increased to 6.78 pounds at 1200°F.

Thermal stresses in the control rods due to secondary heat generation are shown in Figures 4.144 and 4.145 for the conditions of no clad bonding and complete clad bonding, respectively.

*The term *normal force* was used to represent the vertical load between the rod and guide tube at points where the two were in contact. This load was used to obtain the bearing forces on the straps for use in friction and wear studies.

CONFIDENTIAL

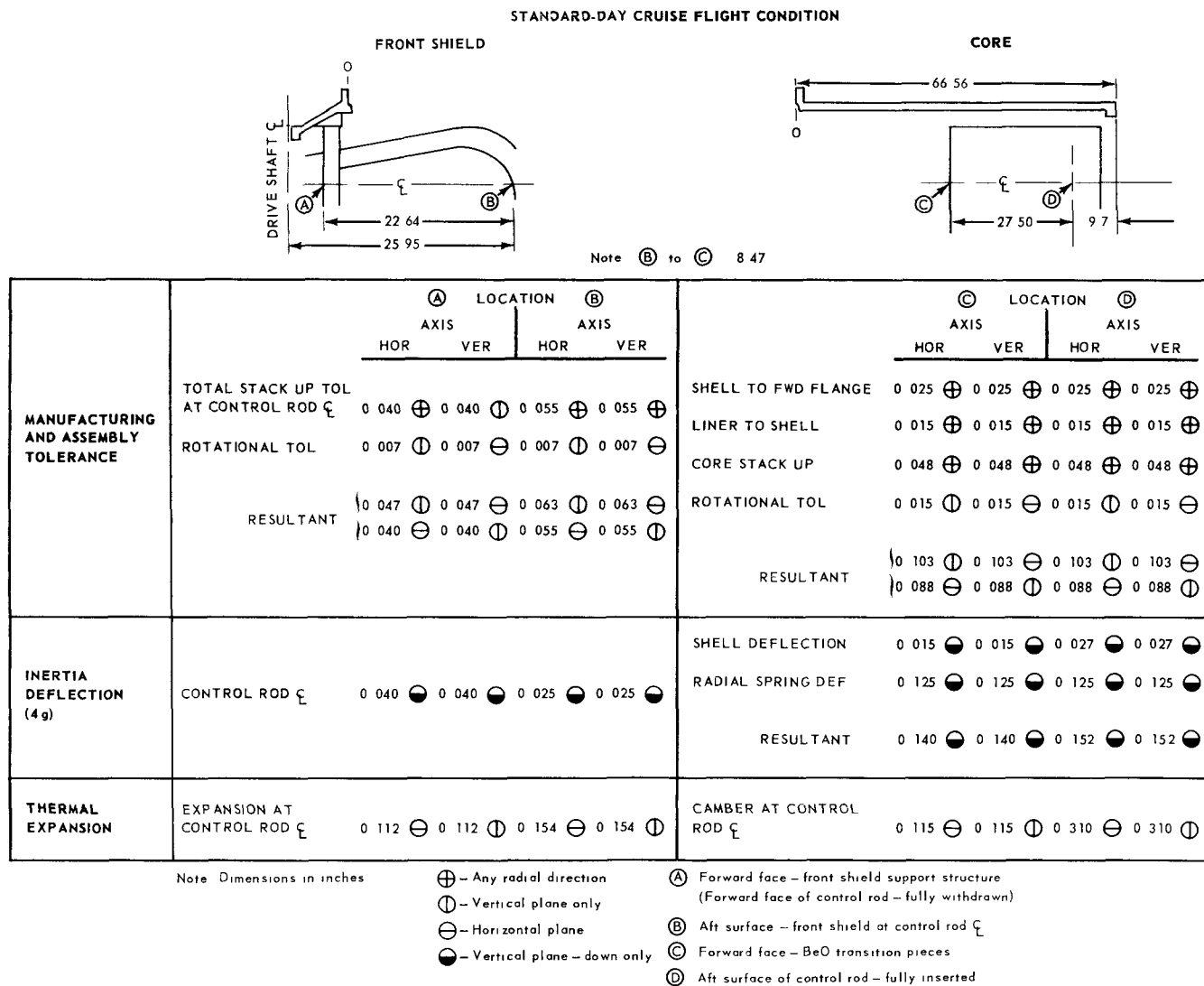


Fig. 4 142 - Control rod deflection stackup

~~CONFIDENTIAL~~

TABLE 4.42
CONTROL RODS DESIGN DATA

Flight Condition	Time, hr	Maximum Exposed Surface Temperature, °F	Maximum Surface Temperature (Under Strap), °F	Maximum Internal Temperature, °F	Total γ Heating Rate, w/gm	Thermal Flux (<0.25 ev), n/cm-sec
Cruise	885	1600	1680	1710	3.4	1.0×10^{14}
Emergency - hot day	5	1755	-	1975	7.4	2.7×10^{14}
Two-engine operation	50	1750	-	1770	6.7	2.4×10^{14}

TABLE 4.43

STRUCTURAL DESIGN CRITERIA FOR THE CONTROL ROD AND GUIDE TUBE

Flight Condition	Combined Load Factors	Rod Load, lb	Stress Criteria
Cruise on station	1	100	1000-hour life, 80% of stress-rupture strength; 0.2% yield strength
Emergency hot day	1	100	100-hour life, 80% of stress-rupture strength; 0.2% yield strength
Flight maneuver	4.13	233	0.2% yield strength
	6.19	350	Ultimate or column strength
Ground operation of aircraft	2.24	233	0.2% yield strength
	3.35	350	Ultimate or column strength
Crash	4.5 down 8 forward	350	Ultimate or column strength
Normal rod operating loads		15 lb, long time 30 lb, short time	
Total rod travel		10,000 ft/1000 hours	
Shim rate		7.7 in./min	
Scram rate		First 5 inches in 300 milliseconds; balance at shim rate	
Scram acceleration		3.45 G	
Scram deceleration		10.0 G	

~~CONFIDENTIAL~~

TABLE 4.44
CONTROL ROD AND GUIDE TUBE MECHANICAL DESIGN RESULTS^a

Flight Condition	Operating Mode	Operating Temperature, °F	Maximum Normal Force, lb	Strap Bearing Load, lb	Maximum Strap Stress, psi	Push-Pull Load, lb
Maneuver on Station	Scram	1,200	6.78	4.79	23,300	26.8
Maneuver on Station	Scram	1,400	6.40	4.53	21,340	26.8
Maneuver on Station	Scram	1,500	6.21	4.39	20,310	26.8
Cruise	Shim	1,200	4.47	3.16	20,300	3.7
Cruise	Shim	1,400	4.18	2.96	18,720	3.39
Cruise	Shim	1,500	4.04	2.89	17,890	3.15

^aDirection of rod motion into core, and traversing a change of slope of 0.0175 in./in.

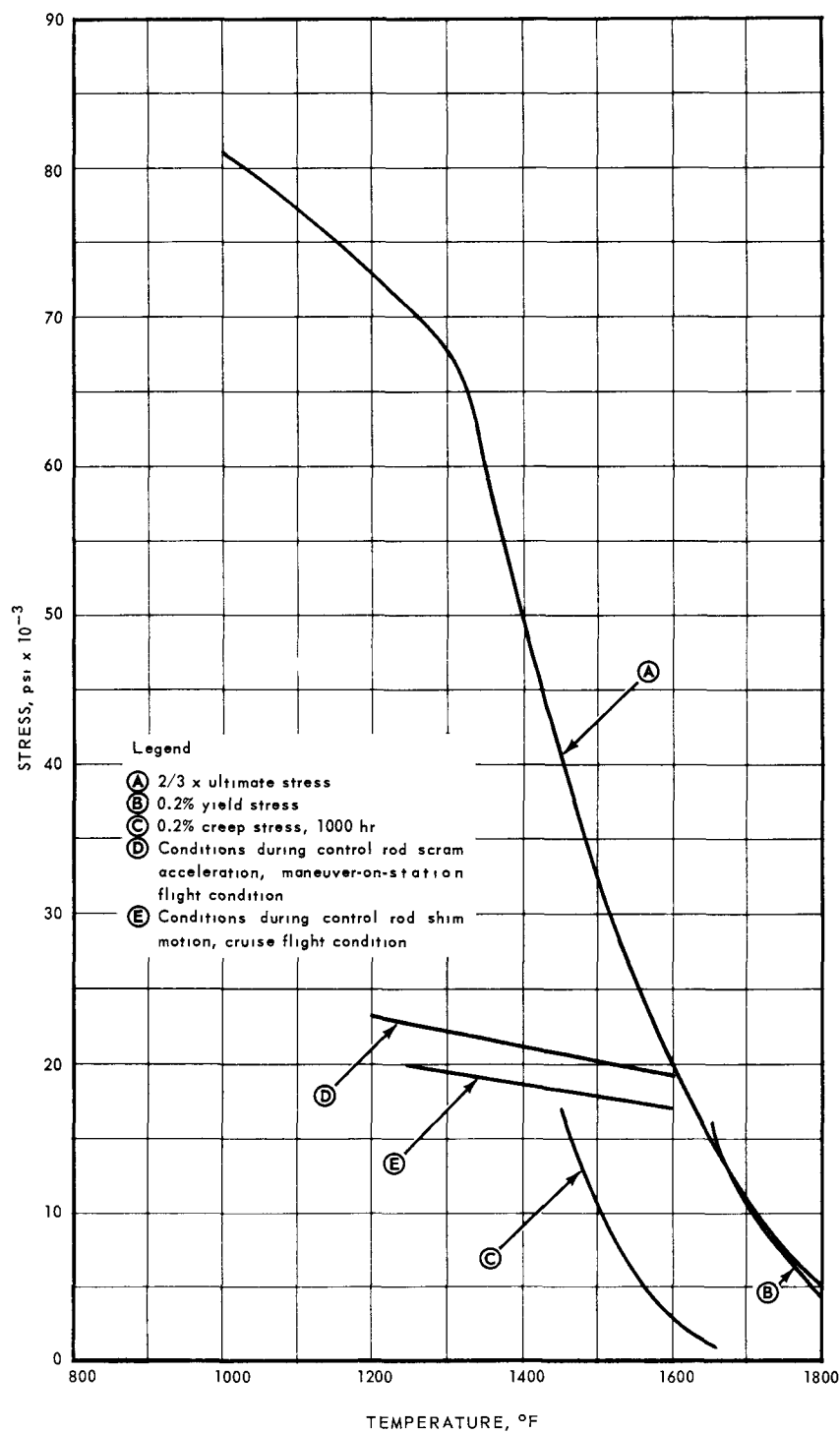
~~CONFIDENTIAL~~

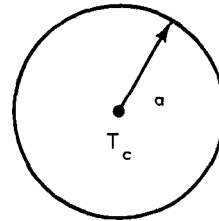
Fig. 4.143 - Comparison of operating and allowable stresses in control rod straps

~~CONFIDENTIAL~~

Assuming no bonding, the presence of cladding material does not effect the conditions within the matrix. Then, circumferential stress (σ_θ) = axial stress (σ_z) = maximum stress at outer fibers.

ASSUMPTIONS :

Radius, inch	0.35
α , inch/inch per $^{\circ}\text{F}$	7.87×10^{-6}
k , Btu/hr-ft per $^{\circ}\text{F}$	21
E , psi	30×10^6
q''' , Btu/ft ³ per hour	2.6×10^6
Temperature (T_c), $^{\circ}\text{F}$	1800 $^{\circ}$



$$\sigma_z = \frac{\alpha E q''' a^2}{8k(1-\nu)} = \frac{75.19 \times 10^6}{0.016934 \times 10^6}$$

$$= 4,440 \text{ psi tension}$$

Fig. 4.144—Thermal stresses in segment of control rod for case of no bond between matrix and clad, cruise flight condition

The control rod was assembled from five 4.8-inch segments by semiflexible straps to prevent bowing and seizure due to unequal heating across the diameter. Eccentricity within the guide tube, nonuniform material distribution, and variation in heat flux density across the rod could contribute to the unequal heating. A limiting case temperature differential across the rod was estimated to be 330 $^{\circ}\text{F}$ and the resulting camber of a single segment is shown in Figure 4.146.

Neutron Source - A startup source of polonium-beryllium replaced the first segment on the forward, cooler end of one of the control rods. The source strength would have been 10 to 12 curies, with a theoretical neutron yield of 2.85×10^6 n per second per curie and a practical range (percent of theoretical) of 75 to 90.

Fabrication details and development tests are described in reference 44.

4.14.2 AEROTHERMAL DESIGN

4.14.2.1 Design Results

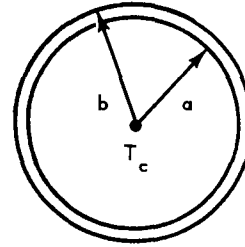
General aerothermal design studies were based on a single static control rod, inserted to a 24-inch depth. The objectives were to design the control rod, guide tube and cooling flow passage in a manner that rod and guide tube temperatures were held within limits required for structural integrity and, at the same time, restricted the flow in the coolant channel to the amount required by the imposed temperature limitations in order to optimize reactor performance.

Studies were conducted to determine the effect on control rods of variations in airflow, rod insertion, and internal heat generation rate. These calculations were based upon design point performance, summarized as follows:

1. Reactor power level, 50 megawatts
2. Nominal specific secondary heating rate of guide tube and radial arch, 0.024 watt per gram per megawatt
3. Volumetric secondary heating rate of guide tube, 0.152 Btu per second per cubic inch
4. Volumetric secondary heating rate of radial arch, 0.054 Btu per second per cubic inch

~~CONFIDENTIAL~~**ASSUMPTIONS:**

	Matrix (m)	Clad (c)
Radius, inch	$a = 0.35$	$b = 0.38$
α , inch/inch per $^{\circ}\text{F}$	7.87×10^{-6}	10.37×10^{-6}
k , Btu/hr-ft per $^{\circ}\text{F}$	21	16.5
E , psi	30×10^6	20×10^6
q''' , Btu/ft ³ per hr	2.6×10^6	2.6×10^6
Temperature, $^{\circ}\text{F}$	$T_c = 1800$	

**1. STRESS IN CLAD**

$$\sigma_{z_b} = \sigma_{\theta_b} = \frac{-E\alpha_m q''' a^4}{8(1-\nu)k_m b^2} + \frac{E\alpha_c q''' a^4}{4(1-\nu)k_m b^2} + \frac{E\alpha_c q''' a^4}{4(1-\nu)k_c} \left(a^2 - \frac{a^4}{b^2}\right) + \frac{ET_c}{(1-\nu)} \left[\frac{a^2}{b^2}(\alpha_m - \alpha_c)\right] + \frac{E q''' \alpha_c}{8(1-\nu)k_c} \left[\frac{a^4}{b^2} + b^2 - 2a^2\right]$$

Assuming no heat generation within clad, the last term of this equation is neglected. Then,

$$\begin{aligned}\sigma_{z_b} = \sigma_{\theta_b} &= -2511 \text{ psi} + 6618 \text{ psi} + 1500 \text{ psi} - 109,032 \text{ psi} \\ &= -103,425 \text{ psi compression}\end{aligned}$$

2. STRESS IN MATRIX

$$\begin{aligned}\sigma_{\theta_a} &= \frac{-E q''' \alpha_m}{16(1-\nu)k_m} \left(\frac{a^4}{b^2} - 3a^2\right) - \frac{E q''' \alpha_c}{8(1-\nu)k_m} \left(a^2 - \frac{a^4}{b^2}\right) \\ &\quad - \frac{E q''' \alpha_c}{8k_c(1-\nu)} \left(2a^2 \ln \frac{b}{a} - a^2 + \frac{a^4}{b^2}\right) + \frac{E q''' \alpha_c}{16k_c(1-\nu)} \left(\frac{a^4}{b^2} - b^2 + 4a^2 \ln \frac{b}{a}\right) \\ &\quad + \frac{ET_c}{2(1-\nu)} \left(\frac{a^2}{b^2} - 1\right) (\alpha_m - \alpha_c)\end{aligned}$$

Assuming no heat generation within the clad,

$$\begin{aligned}\sigma_{\theta_a} &= +4771.8 \text{ psi} - 874.2 \text{ psi} - 94.9 \text{ psi} + 14,420 \text{ psi} \\ &= 18,223 \text{ psi tension}\end{aligned}$$

Fig. 4.145—Thermal stresses in segment of control rod for case of perfect bond between matrix and clad, cruise flight condition

~~CONFIDENTIAL~~

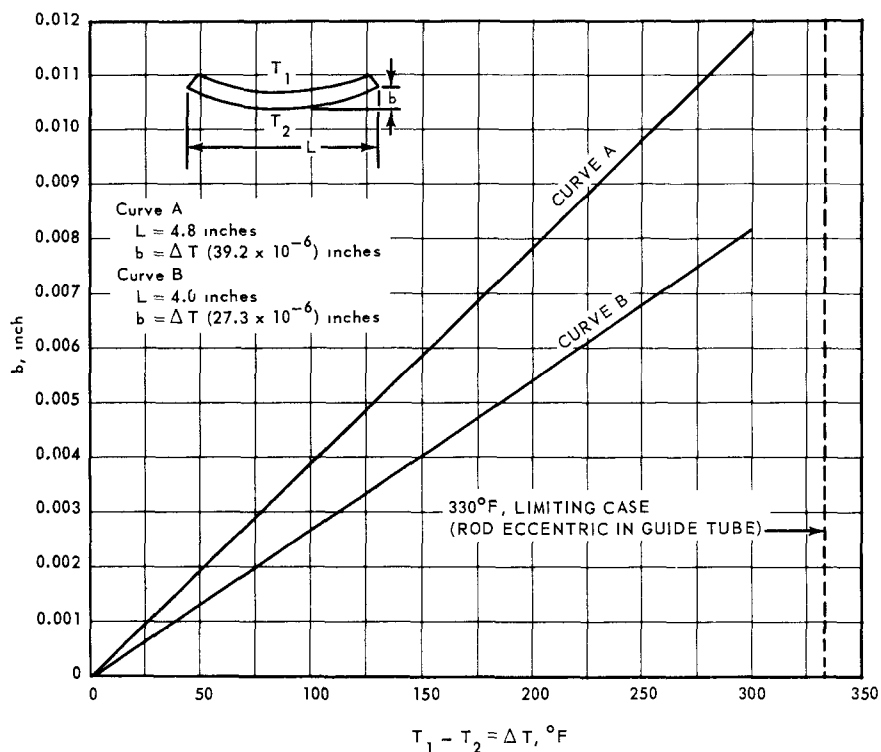


Fig. 4.146—Control rod segment thermal bowing due to temperature differential between sides

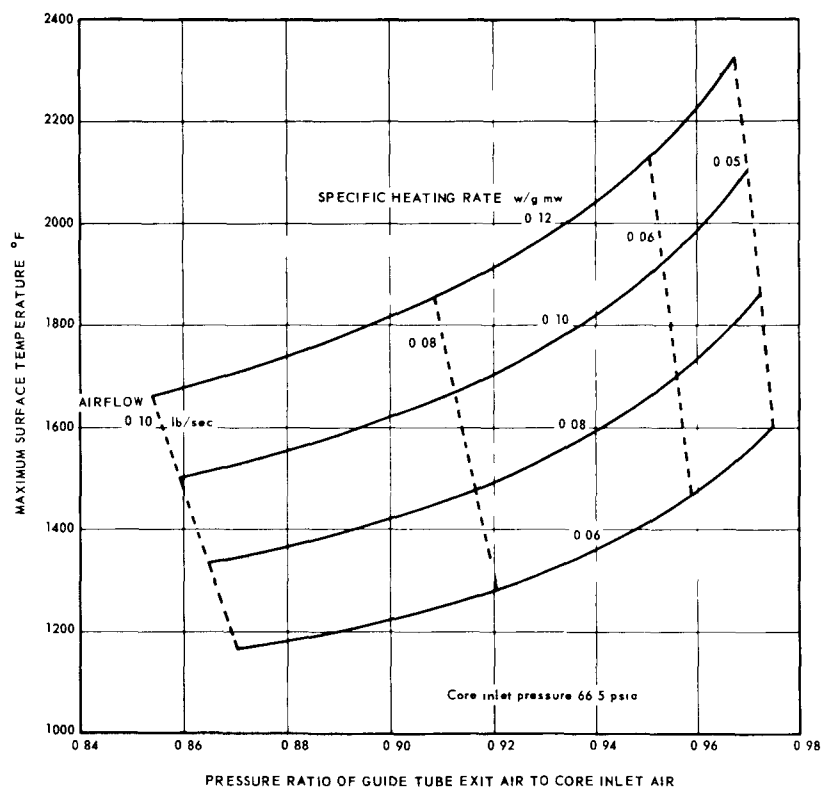


Fig. 4.147—Results of parametric study of control rods with heating rate and airflow as parameters

~~CONFIDENTIAL~~

5. Temperature of inlet air, 583°F
6. Airflow to turbine, 155 pounds per second
7. Total pressure at core inlet, 66.5 psia
8. Total pressure at guide tube inlet, 67.7 psia.

All heating rates were longitudinal average values as defined in reference 29. Pressure losses were computed from guide tube inlet to guide tube exit. The assumed pressure ratio of the guide tube exit air to the core inlet air was 0.94. Temperature limit for the rod surface was assumed to be 1600°F. The nominal airflow for one control rod was 0.05 pound per second. For 48 control rods, this amounted to 1.5 percent of the total airflow to the turbine. Figure 4.147 shows rod surface temperature versus pressure ratio with rod heating rate and airflow as parameters.

Variation of control rod surface temperature with rod insertion, for the nominal control rod heating rate and a range of airflows is shown in Figure 4.148. The maximum temperature occurred when the rod was inserted approximately 18 inches, but was less than 30 degrees higher than when the rod was inserted 24 inches. With 0.05 pound per second airflow, the maximum surface temperature was estimated to be 1625°F. When the rod insertion was 18 inches or less, the longitudinal maximum temperature occurred at the downstream end of the rod. However, when the rod was inserted further, the maximum temperature position remained at 18 inches. The increase in maximum surface temperature when the rod was withdrawn from 24 to 18 inches was caused by additional heat added to the airstream in the forward direction.

In these calculations, all secondary heat generated in the radial arch was assumed to be added to the guide tube airstream. The resultant temperatures of the radial arch were higher than those assumed in the thermal design of the outer reflector coolant channels and indicated that some of the heat generated in the radial arch flowed from the arch into

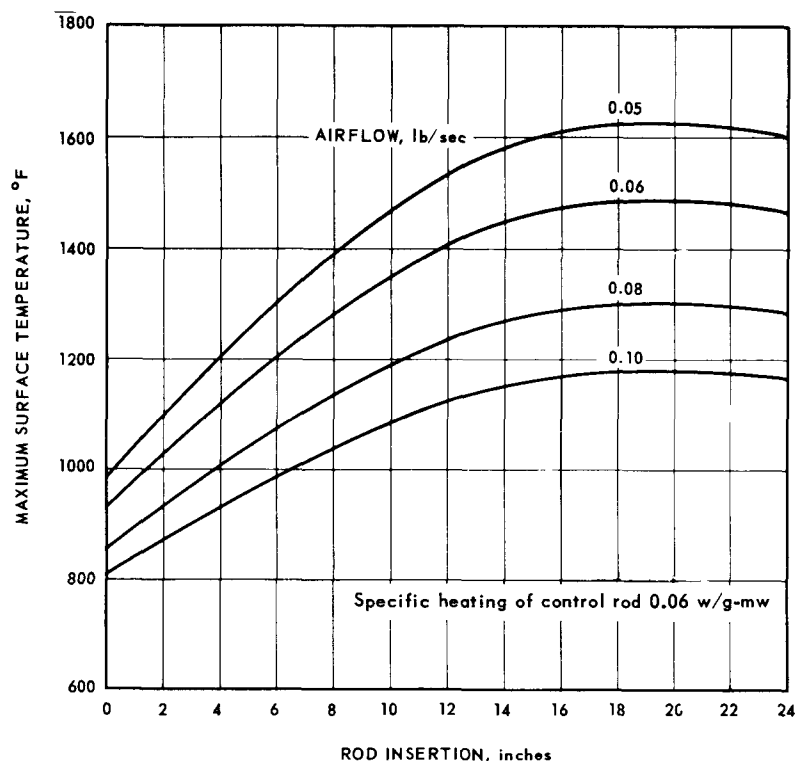


Fig. 4.148 — Variation of maximum surface temperature of control rod as rod is inserted.

~~CONFIDENTIAL~~

the reflector cooling channels. Consequently, the guide tube did not receive as much heat as was assumed in these analyses and the calculated temperatures were conservative.

Additional studies were based on the longitudinal temperature profile of the radial arch as a boundary condition, assuming that all heat generated in the arch was added to the reflector coolant channels. Maximum heat generation rates were assumed for the guide tube and arch. The specific heating rate for both was 0.031 watt per gram per megawatt. Figures 4.149, 4.150, and 4.151 show variations of control rod, guide tube, and exit air temperatures, respectively, with rod insertion and airflow as parameters. Temperatures are shown for both nominal and maximum heating rates. The trends were the same as in the initial studies, but the temperature level was somewhat lower. With nominal heating rate and an airflow of 0.05 pound per second, the maximum surface temperature of the control rod was estimated to be 1560°F.

General studies were based on the assumption that the control rod was perfectly centered within the guide tube. Actually, the rod could lie eccentrically along some portion of its length within the guide tube. Figure 4.152 shows two extreme cases which were studied. In each case, the rod was assumed to be uniformly eccentric along its entire length. The estimated effects of eccentricity on rod temperatures are shown in Figure 4.153 for a range of cooling-air flowrates. The temperature differential across the rod was estimated to be 330°F in the limiting case. With an airflow of 0.05 pound per second, the maximum surface temperature was estimated to be 1820°F.

If airflow leakage occurred between the guide tube and arch, the most significant effect would be the amount of heat drawn inward from the arch. This effect was most pronounced when there was no insulating material between the arch and guide tube. Figure 4.154 shows the relative heat flow from the arch for a series of leakage flow

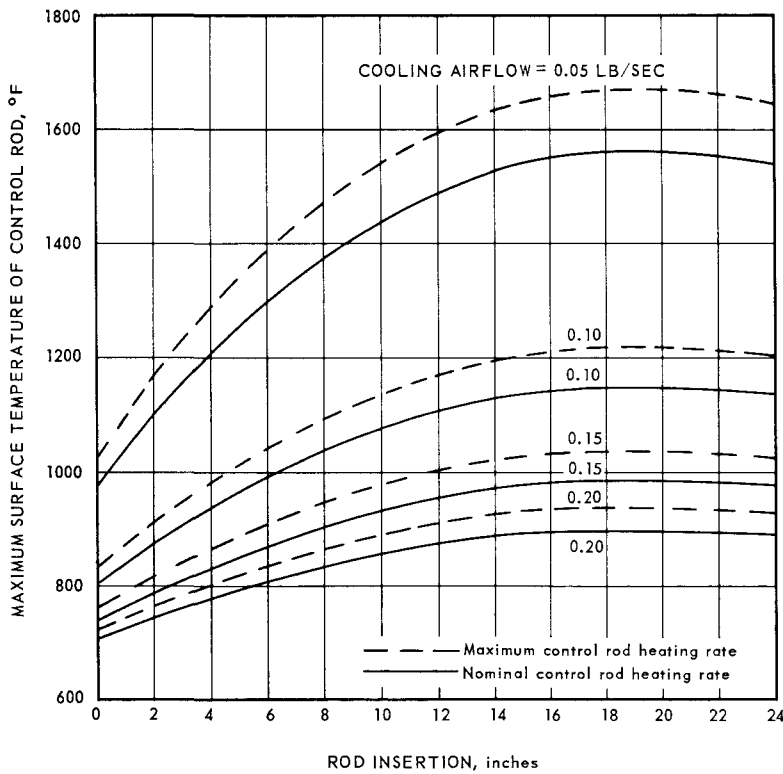


Fig. 4.149 - Effect of rod insertion on maximum surface temperature of control rod

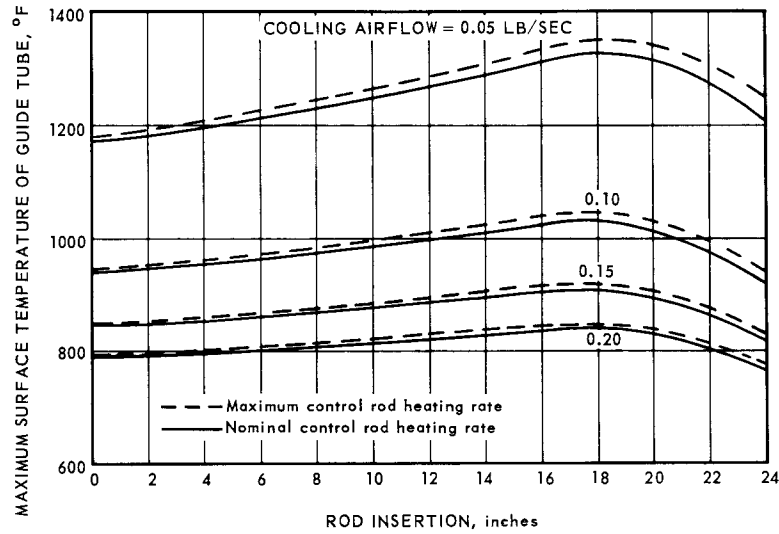
~~CONFIDENTIAL~~

Fig. 4.150 – Effect of rod insertion on maximum surface temperature of guide tube

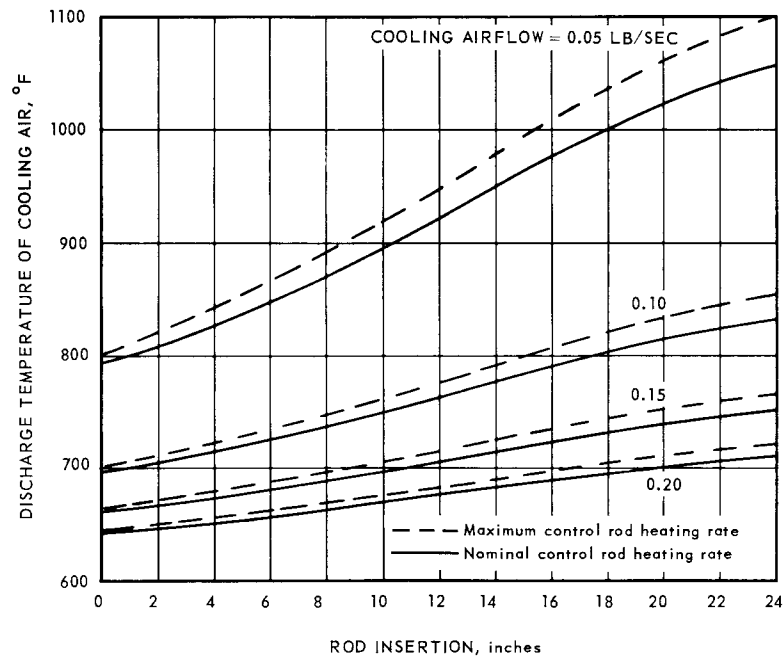


Fig. 4.151 – Effect of rod insertion on cooling-air discharge temperature

~~CONFIDENTIAL~~

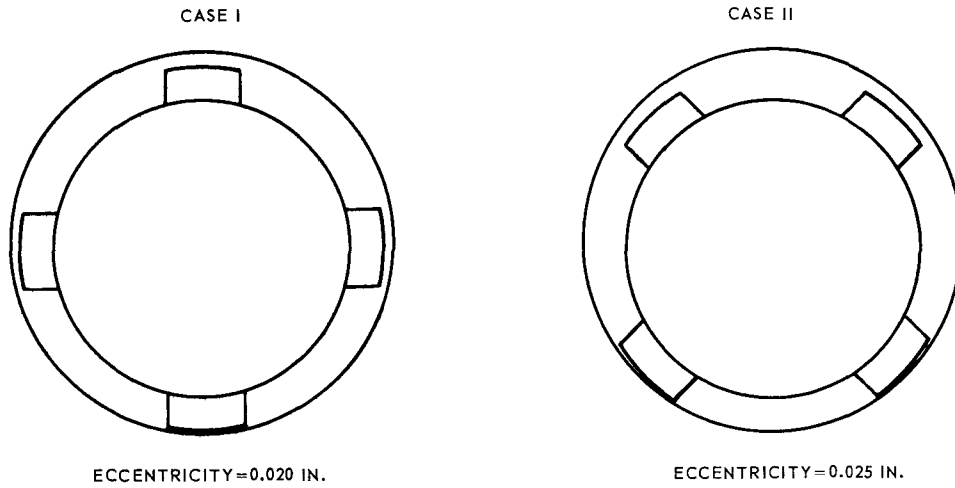


Fig. 4.152—Two extreme cases of eccentricity of a control rod within a guide tube

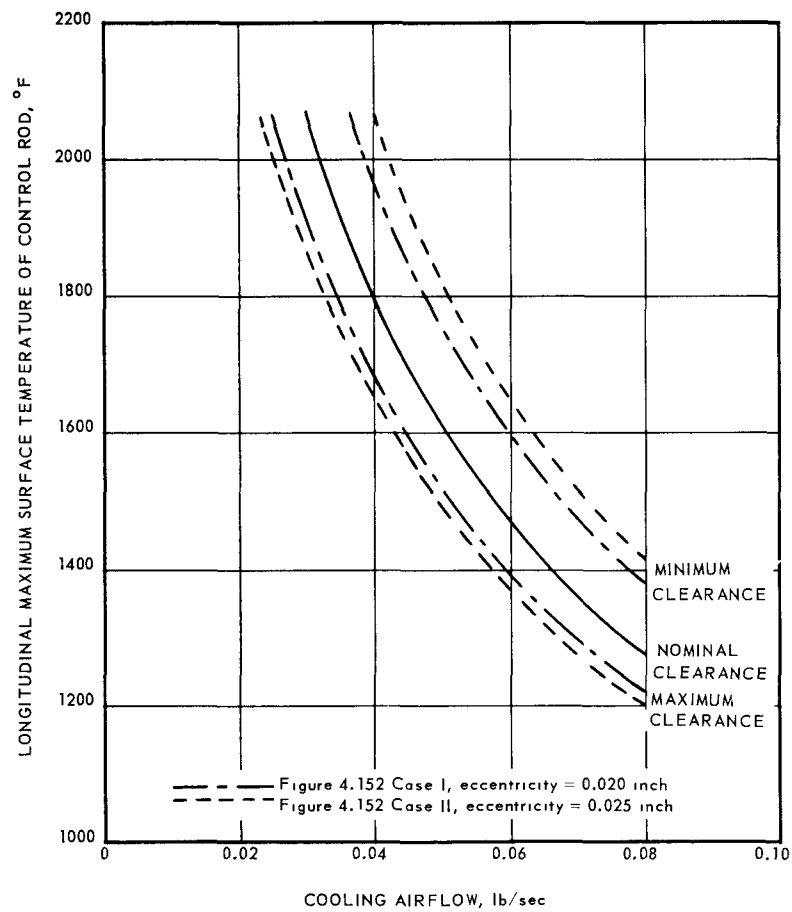


Fig. 4.153—Effect of eccentricity of the control rod within the guide tube on control rod surface temperature

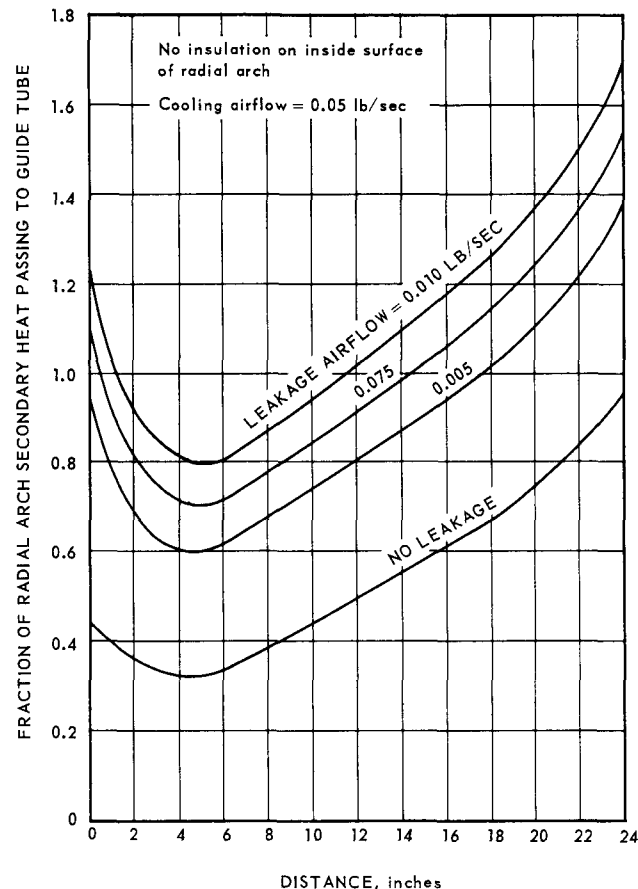
~~CONFIDENTIAL~~

Fig. 4.154 — Relative heat flow from radial arch to guide tube airflow leakage

rates. With insulation on the arch, the effect of leakage upon heat flow from the arch became insignificant.

Longitudinal temperature distributions for the control rod guide tube passage are shown in Figure 4.155. Variations in depth of rod insertion are shown to indicate their effect on longitudinal temperature profiles. Nominal airflow and control rod heat generation rates were assumed.

Detailed temperature distributions for the control rod straps are given in Figure 4.156. These temperatures were for straps on a control rod segment at the longitudinal maximum temperature location, with no air flowing under the straps. The rod was assumed to be perfectly centered within the guide tube. The hottest portion of the strap was at its point of contact with the control rod, and was at the same temperature as the rod surface at that point.

4.14.2.2 Pressure Loss Calculations

Pressure loss calculations were based on cooling-air entering the guide tube at its forward end, and discharging into the aft-retainer assembly. An entrance loss of 2.3 percent into the guide tube was estimated for the assumed range of airflow. The contraction and expansion loss coefficients, $\Delta P/q$, as defined in reference 45, were as follows:

- Contraction into annular passage, 0.27
- Contraction into strap region, 0.025
- Expansion into open guide tube, 0.39
- Expansion into aft-retainer, 1.0

~~CONFIDENTIAL~~

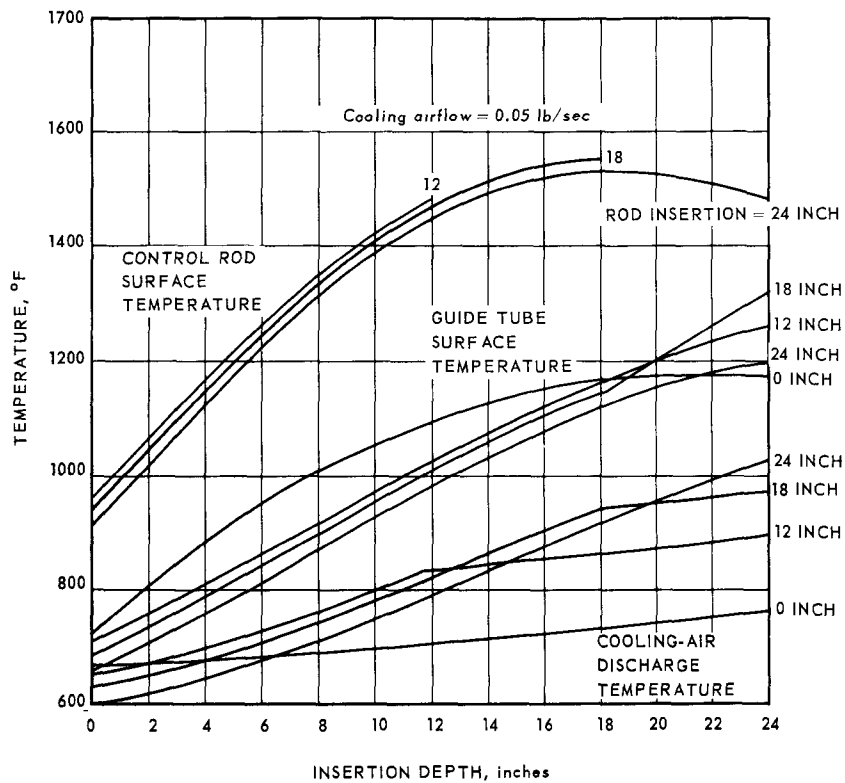


Fig. 4.155—Effect of depth of control rod insertion on longitudinal temperature profiles along control rod channels

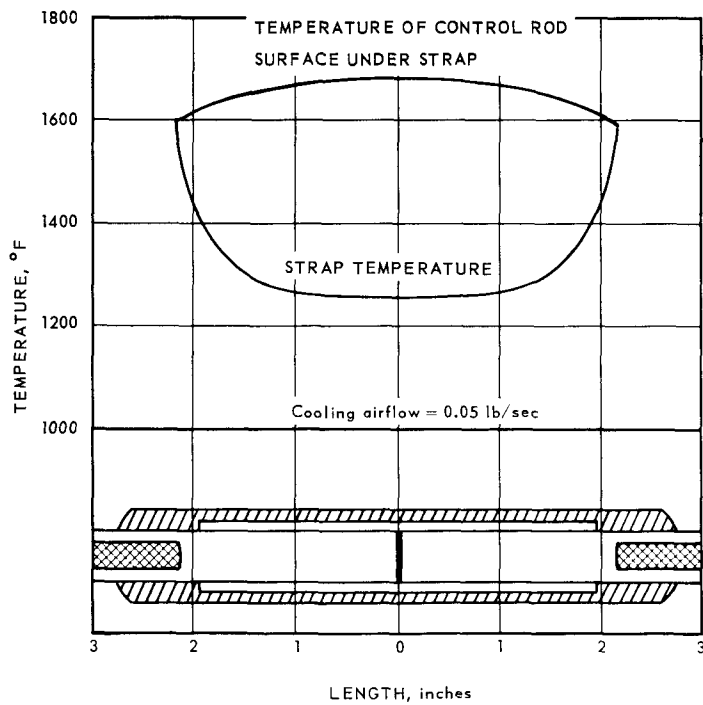


Fig. 4.156—Control rod surface and strap temperatures

~~CONFIDENTIAL~~

The smooth tube friction factor was defined by the equation:

$$f = 0.046 \text{ Re}^{-0.20}$$

The assumed friction factor for the open guide tube and annular passage was 5 percent above the reference smooth tube friction factor. This assumed value was confirmed by cold flow testing to within ± 3 percent.⁴⁶

The assumed value for the friction factor in the region of the control rod straps was 38 percent above the reference smooth tube value. Subsequent experimental data indicated a friction factor approximately 45 percent greater than the reference value, or 7 percent greater than the assumed value.

4.14.2.3 Computer Programs

Heat transfer calculations for general studies and design perturbations were carried out with the Control Rod Cooling Program, ANP 438. This is a special purpose computer program which computes longitudinal and radial temperature distributions for a series of concentric cylinders with one or two flow passages. It is suitable for general parametric studies because of the ease of varying input data and the small amount of computer time required. The original analysis for the program is given in reference 47.

A modified version of the Off-Design Core Pressure Loss Program, ANP 99, was used to compute pressure losses in the control rod cooling passage. Reference 18 explains the details of the program. In addition to the pressure losses due to friction and increase in temperature, the program is capable of computing contraction and expansion losses between segments. Pressure loss coefficients are given as input.

Detailed strap temperature distributions were obtained using the Transient Heat Transfer Program (THT-A), ANP 228. This is a general three-dimensional heat transfer computer program for transient or steady state conditions. Usage of the program is explained in reference 38.

The Flow and Temperature Analysis Program (FANTAN), ANP 542, was used to study transient conditions. The FANTAN program is similar to the THT program except that it does not include heat transfer by radiation. One advantage of using this program is that it can compute film heat transfer coefficients rather than having them entered as boundary conditions. It also makes pressure loss calculations and redistributes flow between passages, if necessary. The latter features were not used for the transient analysis. Reference 48 explains the program in detail.

4.15 REACTOR AFTERCOOLING STUDIES

4.15.1 BASIS OF STUDIES

The results of studies pertaining to the transient thermal characteristic of the XNJ140E-1 reactor following shutdown from nuclear operation are reported in this section. Although primary interest was focused on the fuel elements, several limiting cases for nonfueled regions of the reactor were investigated. Nonfueled regions of particular interest were the outer reflector and the inner reflector because of their relatively high rates of secondary heat deposition.

A special reactor computer program, the CTPP (Program No. 330) was chosen to serve as the basic analytical tool. The primary reason for selecting this program was its versatility insofar as relatively few restrictions were placed on fuel element parameters, and relatively small amounts of input data were required.

~~CONFIDENTIAL~~

The following parameters identify the analytical model used for these studies:

1. Geometry was that of the average channel in the core.
2. Longitudinal power profile was a 2:1 chopped cosine, symmetrical about the reactor mid-plane.
3. Convection heat transfer equations used were:

Turbulent flow

$$N_{Nu} = 0.0205 (N_{Re})^{0.8} (N_{Pr})^{0.4}$$

(All properties were evaluated at the film temperature.)

Laminar flow

$$N_{Nu} = 1.86 (N_{Re})^{1/3} (N_{Pr})^{1/3} \left(\frac{D_H}{L} \right)^{1/3} \left(\frac{\mu_B}{\mu_S} \right)^{0.14}$$

(All properties were evaluated at the film temperature except the last term which is the ratio of viscosity at bulk temperature divided by the viscosity at surface temperature.)

4. Pressure-loss friction factors used were:

Turbulent flow

$$f = 1.15 [(0.046) (N_{Re})^{-0.2}]$$

Laminar flow

$$f = 16 (N_{Re})^{-1.0}$$

5. Core free flow area was 3.87 square feet.
6. Fuel element hydraulic diameter was 0.167 inch.
7. Core solid cross-sectional area was 5.64 square feet.
8. Core length was 30 inches.
9. Total wetted perimeter of heat transfer surface was 1100 feet.

The CTTTP program required that the thermal properties of solid materials be entered into the program as power functions. The equation used for thermal conductivity k was

$$k_T = k_{1000^{\circ}} \left(\frac{T^{\circ}}{1000^{\circ}} \right)^b$$

and, for thermal diffusivity " α ," was

$$\alpha_T = \alpha_{1000^{\circ}} \left(\frac{T^{\circ}}{1000^{\circ}} \right)^c$$

where the constants b and c depend upon the material. All temperatures were absolute ($^{\circ}R$). The program then assumed that the properties were valid over the temperature range involved. Figure 4.157 shows the values of thermal conductivities used in these studies, and compares these values to reported data.⁴⁹ Figure 4.158 shows the corresponding values for thermal diffusivity.

Unless specifically stated otherwise, all transients were assumed to start from the following conditions:

Power history	- 100 hr (equilibrium)
Power level	- 128 mw (Military Power)
Ambient	- 5000 ft, static, intermediate cold day ($-14^{\circ}F$)

Steady-state operating parameters through the engine prior to shutdown are shown in Table 4.45 for intermediate cold, standard, and Air Force hot day conditions.

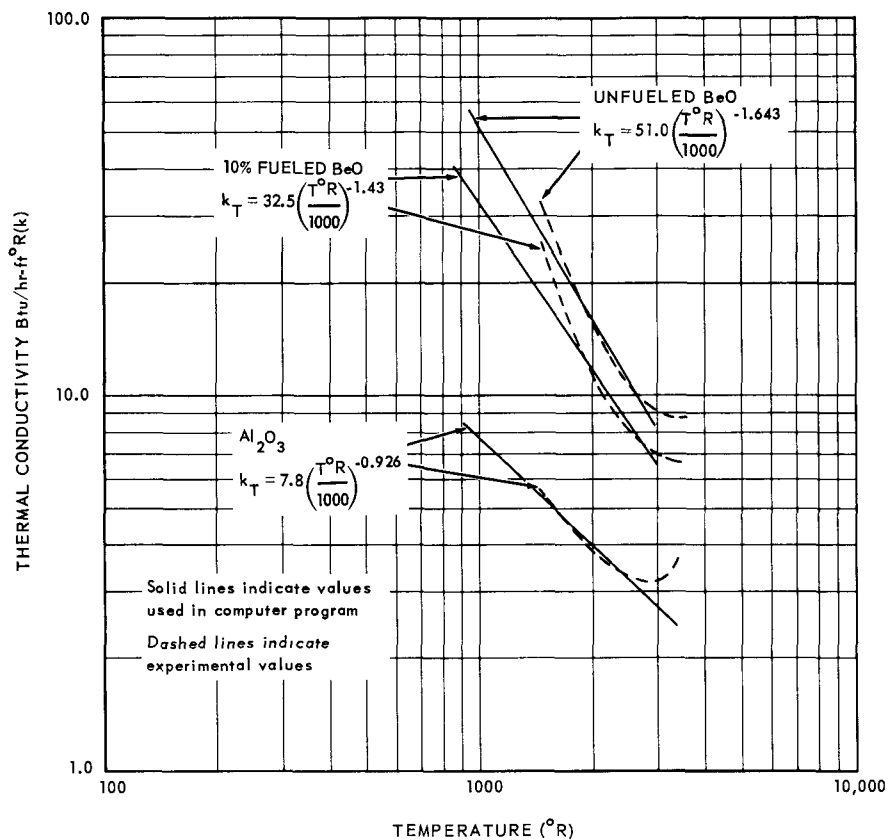
~~CONFIDENTIAL~~

Fig. 4.157—Thermal conductivities used in computer program number 330
(values in Btu/hr-ft-°R)

TABLE 4.45
STEADY-STATE OPERATING PARAMETERS USED FOR
REACTOR AFTERCOOLING STUDIES

Parameter	Ambient Day		
	Intermediate	Standard	Hot
Ambient air temperature, °F	Cold		
Reactor inlet-air temperature, °F	590	665	715
Reactor exit-air temperature, °F	1960	1970	1970
Turbine inlet-air temperature, °F	1800	1800	1800
Reactor inlet pressure, psia	165	146.7	131.5
Airflow through fuel elements, lb/sec	315	280	252
Airflow through turbine, lb/sec	375	333	300
Fuel element average-channel maximum surface temperature, °F	2360	2315	2314
Power, mw	128	107	92

~~CONFIDENTIAL~~

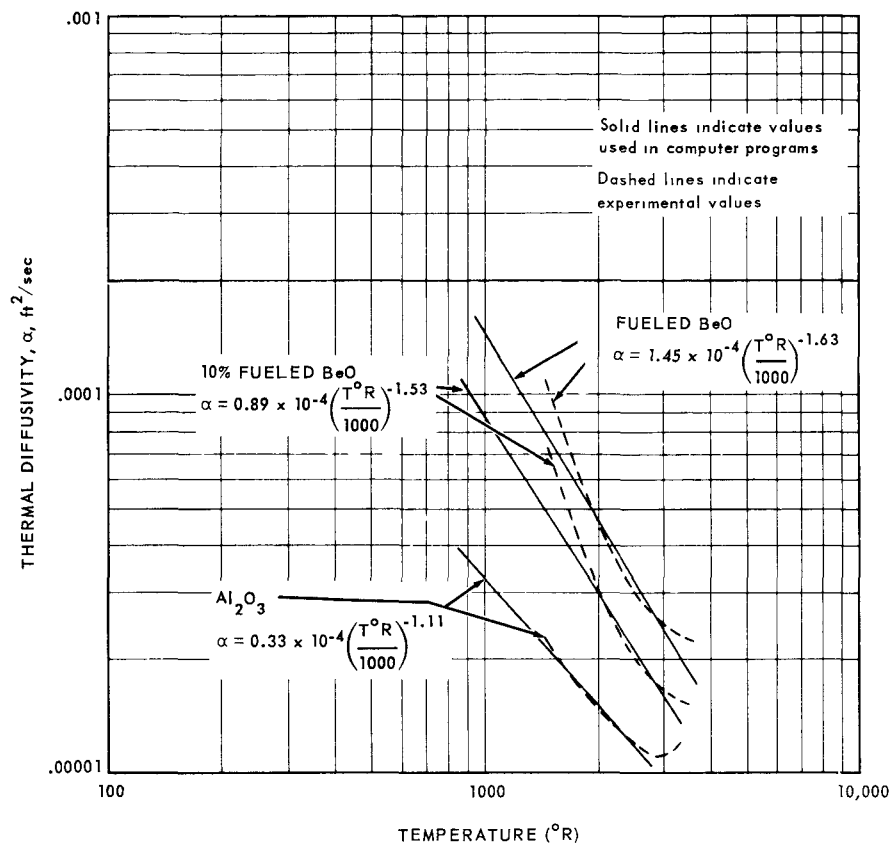


Fig. 4.158 – Thermal diffusivities used in computer program number 330 (values in ft^2/sec)

Since cold-day operation yielded the highest surface temperature as well as the highest power level, most of the aftercooling studies were based on this condition.

All engine shutdowns were assumed to be scrams initiated by the normal power plant protective circuits. Scram consisted of fast insertion of -2 percent $\Delta k/k$, followed by shim rod insertion.

Figures 4.159, 4.160, and 4.161 show the transient rates of power generation, following scram, in various reactor components. Values of power generation are expressed as fractions of the power generation at equilibrium nuclear operation, and are relative values. Figure 4.159 shows the values for the fuel elements, the outer reflector, and the radial-spring pressure pads. Figure 4.160 shows values for the forward reflector, forward transition pieces, aft transition pieces, and the aft-retainer assembly. Figure 4.161 shows values for the coupling shaft, the core liner, and the inner reflector.

4.15.2 ROTOR SEIZURE

The first type of transient considered was the case of rotor seizure. Engine coastdown was assumed to cease 2 seconds after the incident, and the reactor was scrammed within 1 second. Aftercooling air from the afterheat removal system started flowing 2.5 seconds after the incident.

Figure 4.162 shows the fuel element average-channel maximum surface temperature ($T_s \text{ max-avg}$) as a function of time following the incident. Two families of curves are

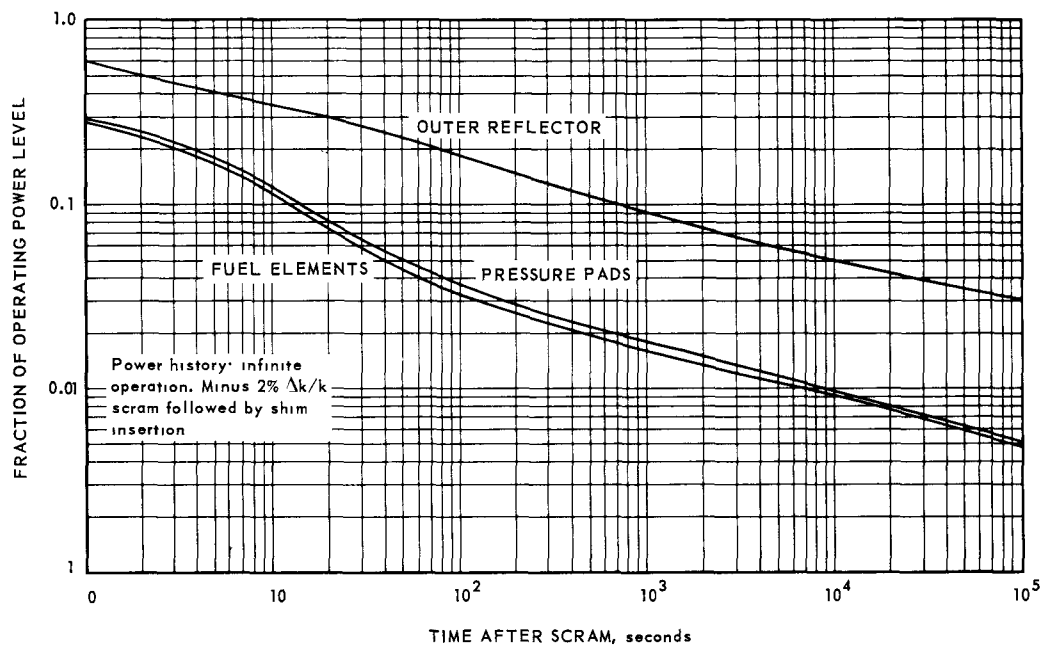
~~CONFIDENTIAL~~

Fig. 4.159 -- Transient power generation following scram

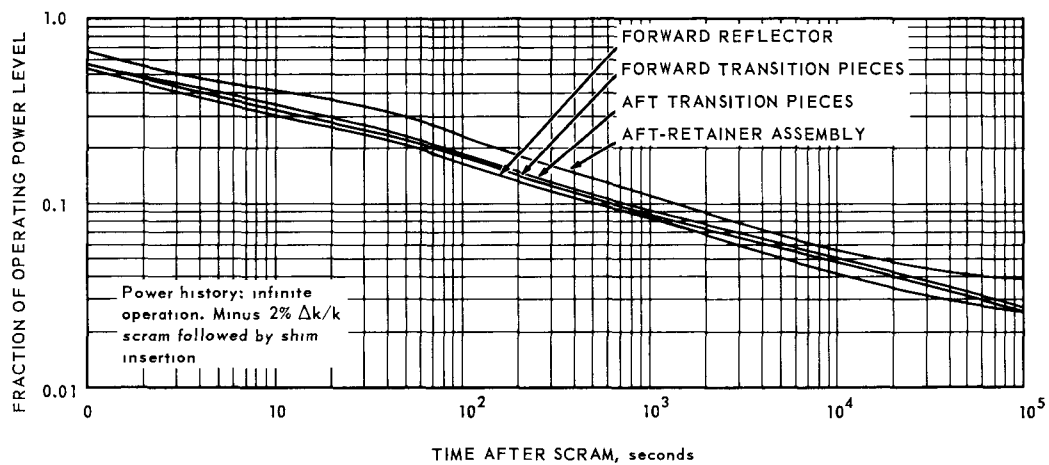


Fig. 4.160 -- Transient power generation following scram

~~CONFIDENTIAL~~

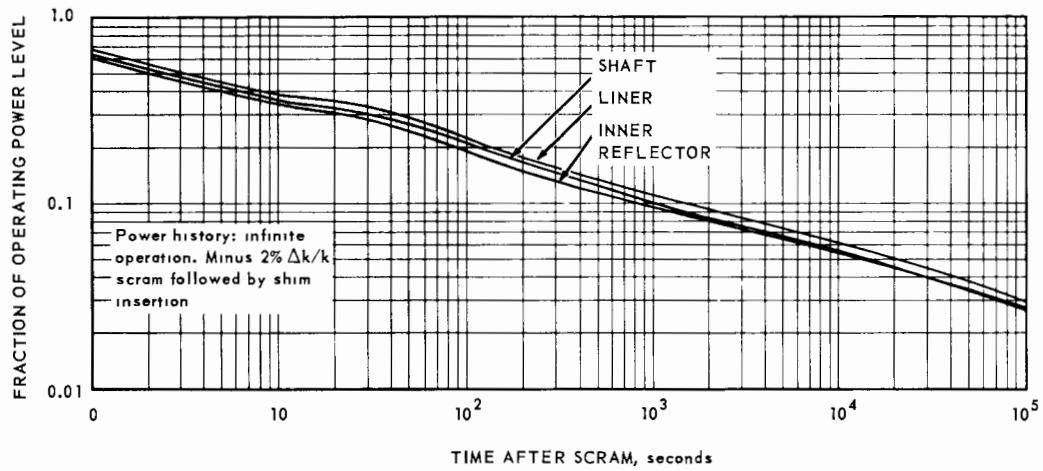


Fig. 4.161 – Transient power generation following scram

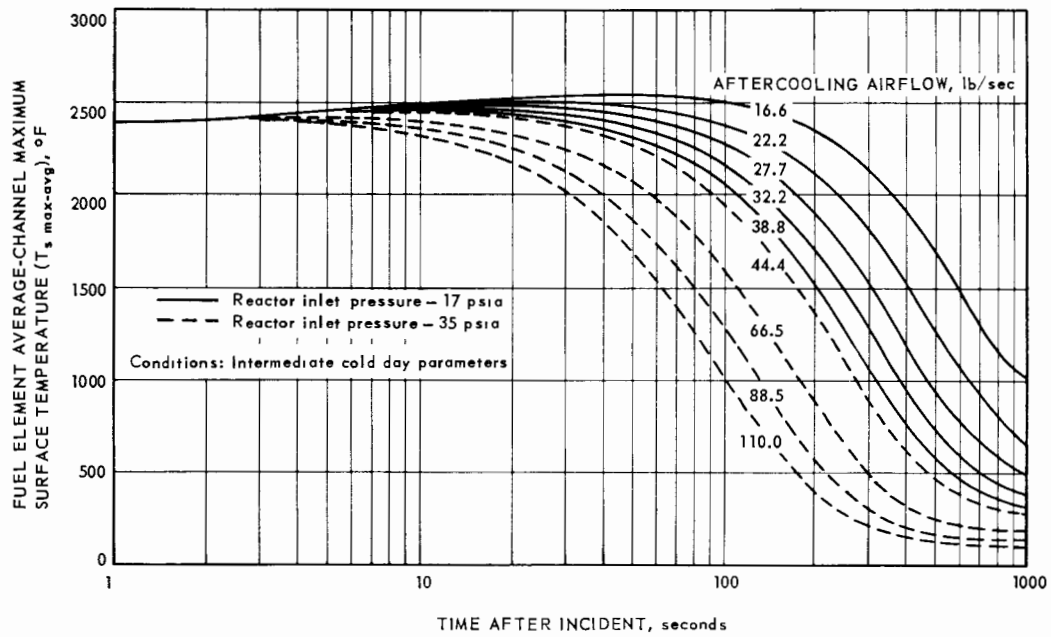


Fig. 4.162 – Fuel element average-channel maximum surface temperature following scram caused by rotor seizure

~~CONFIDENTIAL~~

shown, one for 17 psia reactor inlet-air pressure and one for 35 psia reactor inlet-air pressure. The family-variable parameter was airflow through the reactor, expressed as $W_{a4,0}$ (the relationship between $W_{a3,2}$ and $W_{a4,0}$ was fixed at 0.896 and the use of $W_{a4,0}$ simplified the calculations). It was assumed that the exhaust nozzle could be driven shut so as to cause a throttling restriction uniquely yielding the desired reactor inlet-air pressure for each rate of airflow. The increased level of air pressure was introduced into the study to avoid sonic velocity being developed at the fuel-element-channel discharge for the higher airflow rates. Figure 4.162 shows that the fuel element surface temperature did not exceed approximately 2500°F for the airflow rates of interest, i. e., 15 to 20 pounds per second at 17 psia.

Comparable data for the fuel element exit-air temperature ($T_{a3,6}$) are shown in Figure 4.163. The discontinuity in the curves at 2.5 seconds represents the initiation of after-cooling air flow. The exit-air temperature did not exceed 2400°F for the range of interest of cooling-air flow rates.

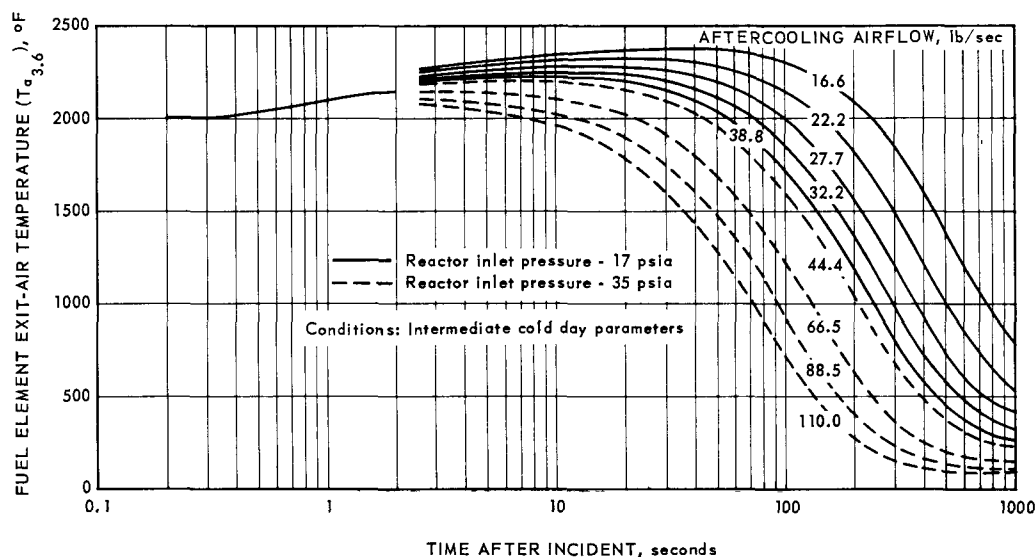


Fig. 4.163—Fuel element exit-air temperatures following scram caused by rotor seizure

Figure 4.164 shows fuel element surface temperatures through the average channel for various fractional distances along the core length and at various times after the incident. Although the surface temperatures were rapidly dropping, thermal gradients and thermal stresses in the fuel elements were no greater than those at steady state conditions because of the significantly lower rates of heat generation.

Fuel element surface temperatures, T_s max-avg, and fuel element discharge-air temperatures for the hot-day ambient condition are shown in Figure 4.165 and Figure 4.166, respectively. These sets of data are comparable to Figure 4.162 and Figure 4.163, respectively, for the ambient intermediate-cold-day condition. In spite of higher ambient-air temperatures, both fuel element surface temperatures and exit-air temperatures were lower for the hot-day condition because of the lower rates of power generation.

Figure 4.167 shows fuel element average-channel maximum surface temperatures following rotor lock during cold-day conditions for lower cooling-air flow rates between 4 pounds per second and 15 pounds per second. Since approximately 16 pounds per second airflow represented the transition between turbulent flow and laminar flow, laminar flow correlations were used as the basis of calculations for all data shown in Figure 4.167.

~~CONFIDENTIAL~~

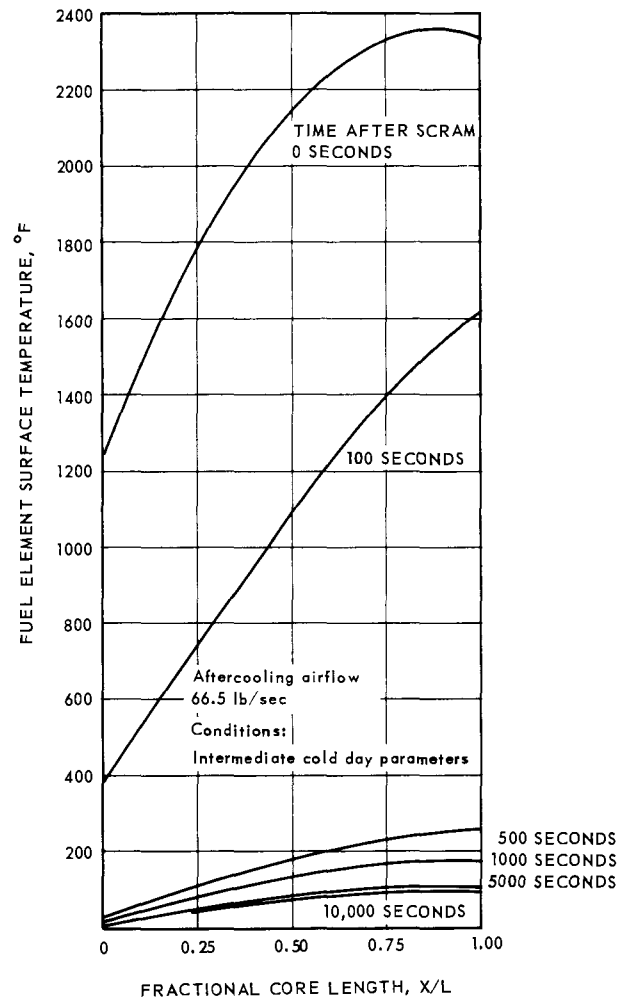


Fig. 4.164 – Fuel element surface temperature along average-channel following scram caused by rotor seizure

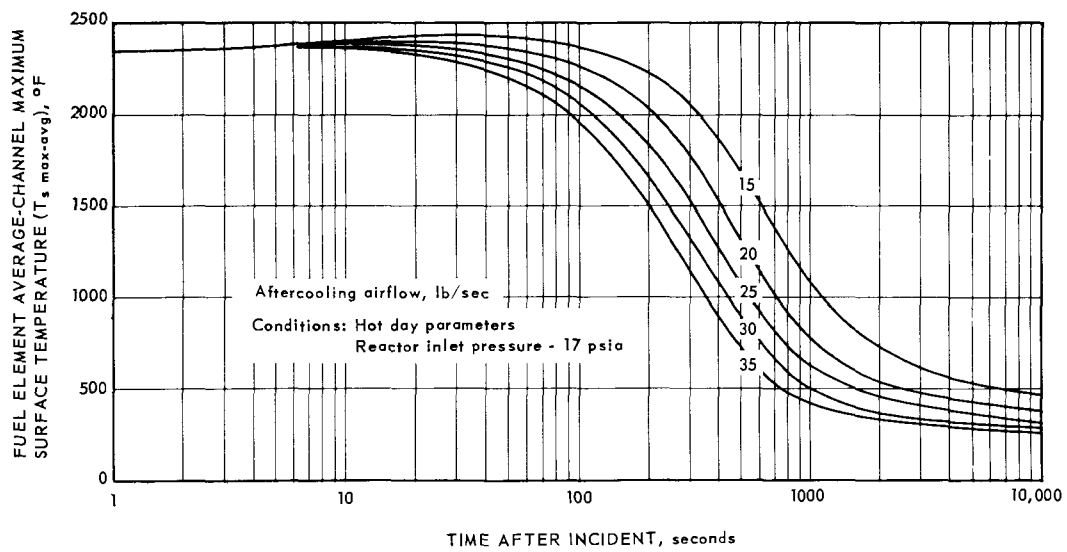


Fig. 4.165 – Fuel element average-channel maximum surface temperature following scram caused by rotor seizure

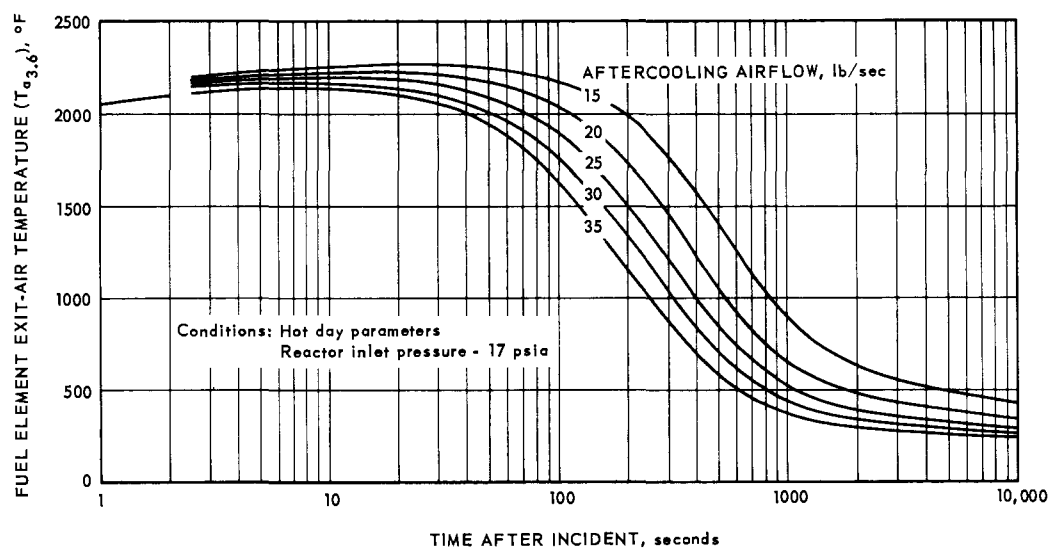
~~CONFIDENTIAL~~

Fig. 4.166 – Fuel element exit-air temperature following scram caused by rotor seizure

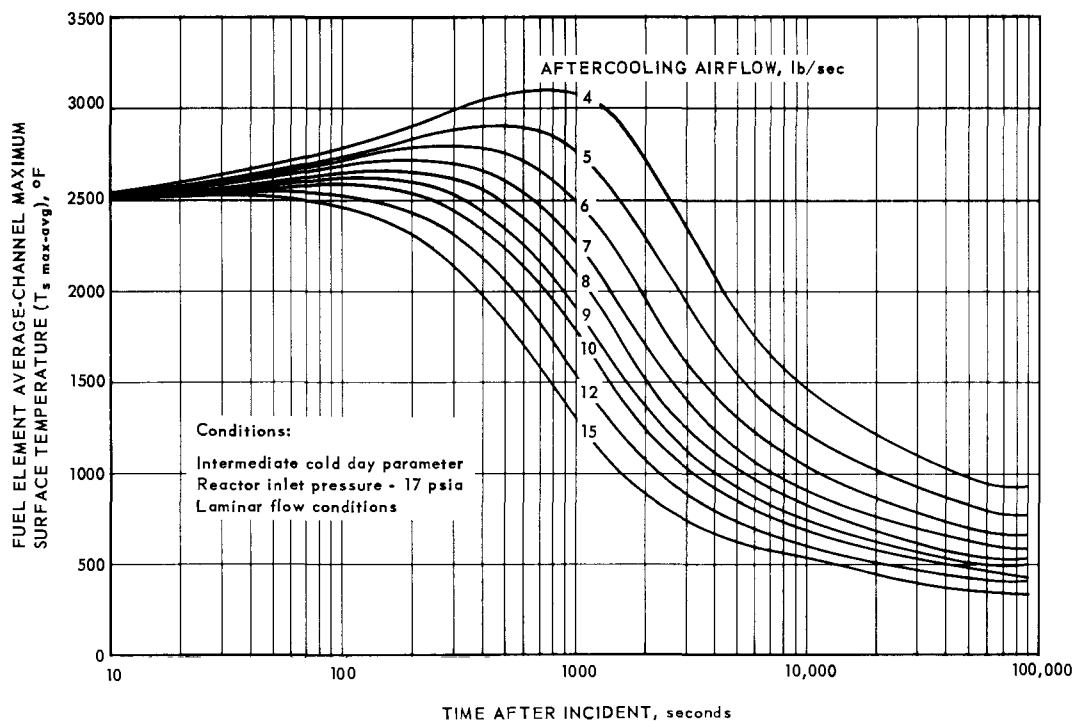


Fig. 4.167 – Fuel element average-channel maximum surface temperature following scram caused by rotor seizure (low airflows)

~~CONFIDENTIAL~~

Figure 4.168 shows a comparison of calculated fuel element average-channel maximum surface temperatures for a cooling-air flow of 15 pounds per second when using both laminar-flow and turbulent-flow correlations. Temperature data calculated on the basis of these different flow correlations began to diverge as the time increased beyond 500 seconds. This divergency was due to the fact that cooling-air temperature decreased with time, and the Reynolds number increased (for a constant flow rate) because of the decreased viscosity.

4.15.3 ENGINE COASTDOWN

4.15.3.1 NORMAL ENGINE COASTDOWN

Fuel element average-channel maximum surface temperatures are shown in Figure 4.169 for the case of engine scram followed by unperturbed engine coastdown. Auxiliary aftercooling-air from the AHR system was assumed to start 120 seconds after shutdown. A family of curves is shown for a range of aftercooling-air flows. Figure 4.170 shows the reactor discharge-air temperature ($T_{a3,6}$) for the same transient condition.

These data showed that the fuel element surface temperature decreased to 900°F by the time engine coastdown ceased, and increased thereafter by a negligible amount for the lowest aftercooling-air flow shown, i. e., 15 pounds per second.

4.15.3.2 Engine Coastdown Following Compressor Stall

Fuel element average-channel maximum surface temperatures are shown in Figure 4.171 for the case of engine scram caused by compressor stall and followed by normal engine coastdown. Auxiliary aftercooling-air from the AHR system was assumed to start 120 seconds after the incident. A family of curves is shown as a function of aftercooling-air flow. Figure 4.172 shows the reactor discharge-air temperature for the same transient condition. The engine was assumed to scram four seconds after the incident, and aftercooling-air started 120 seconds after the incident. The temperature peak occurring in Figure 4.172 was caused by the surging airflow characteristic of a compressor stall.

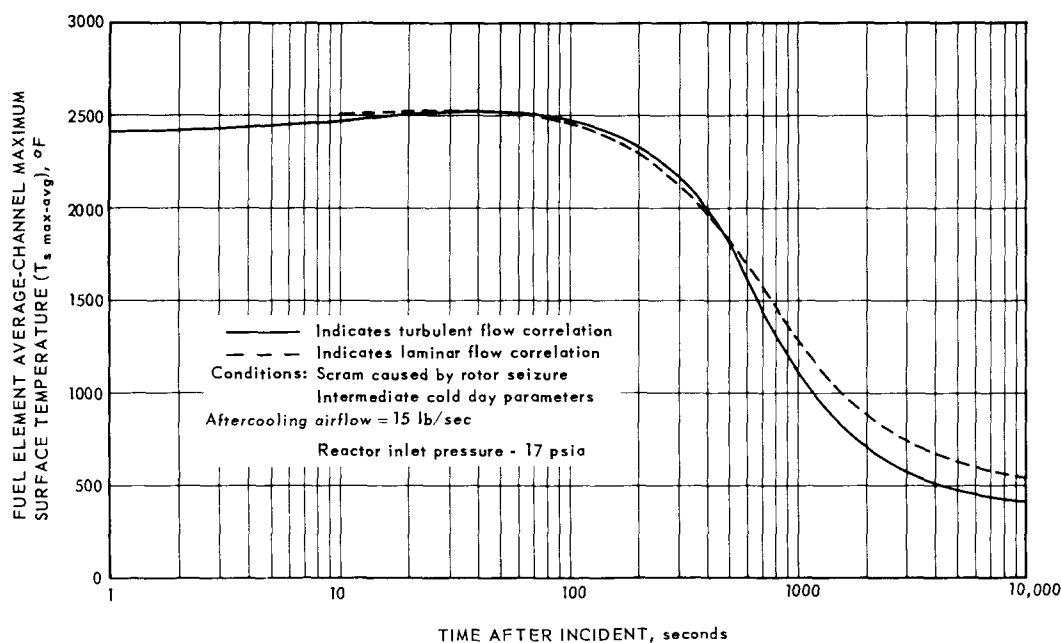


Fig. 4.168—Comparison of fuel element average-channel maximum surface temperature using laminar and turbulent flow correlations

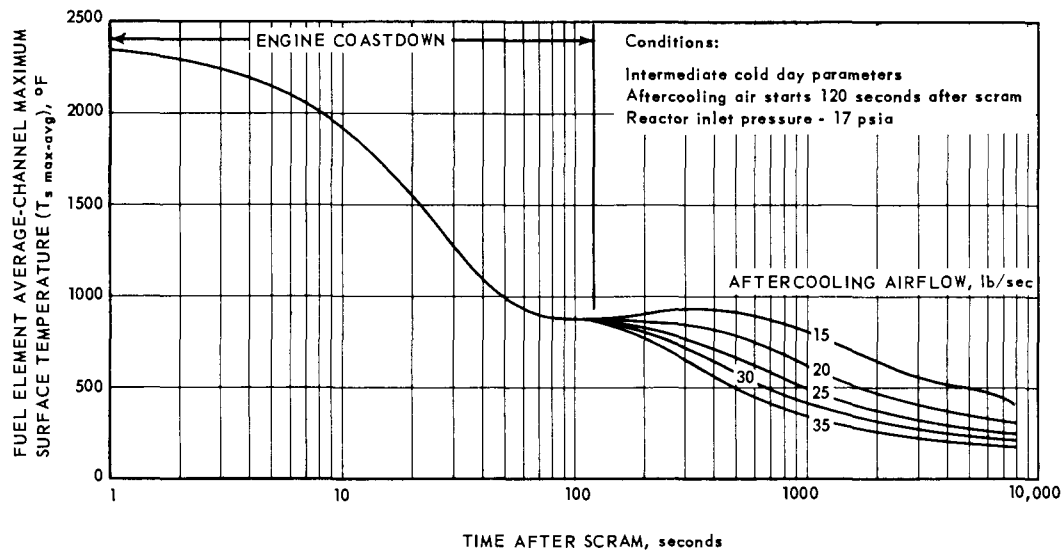
~~CONFIDENTIAL~~

Fig. 4.169 -- Fuel element average-channel maximum surface temperature following scram followed by engine coastdown

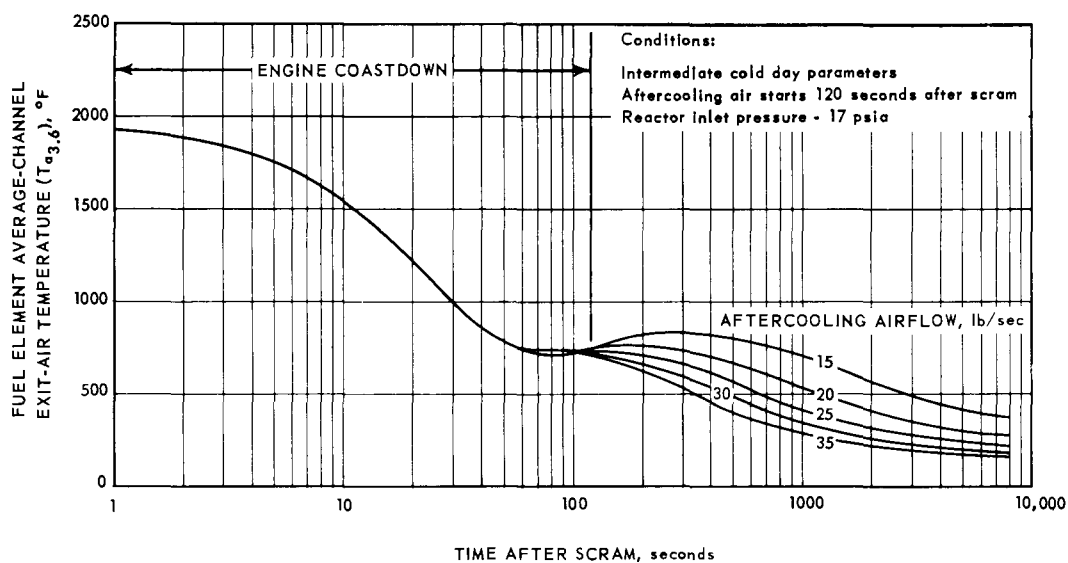


Fig. 4.170 -- Fuel element discharge air temperature following scram followed by engine coastdown

~~CONFIDENTIAL~~

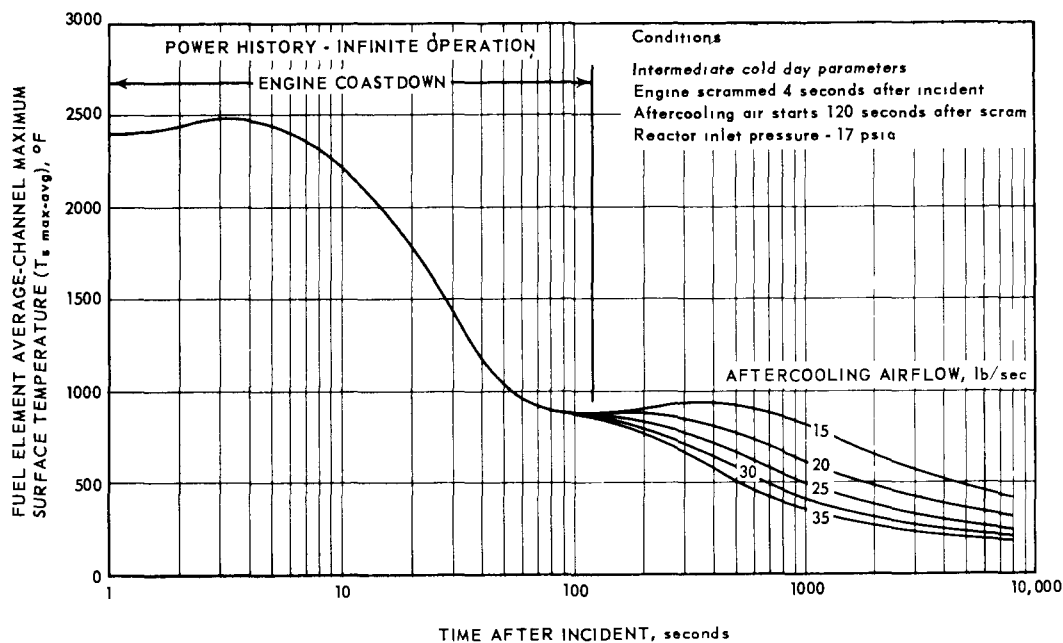


Fig. 4.171—Fuel element average-channel maximum surface temperature following scram caused by compressor stall

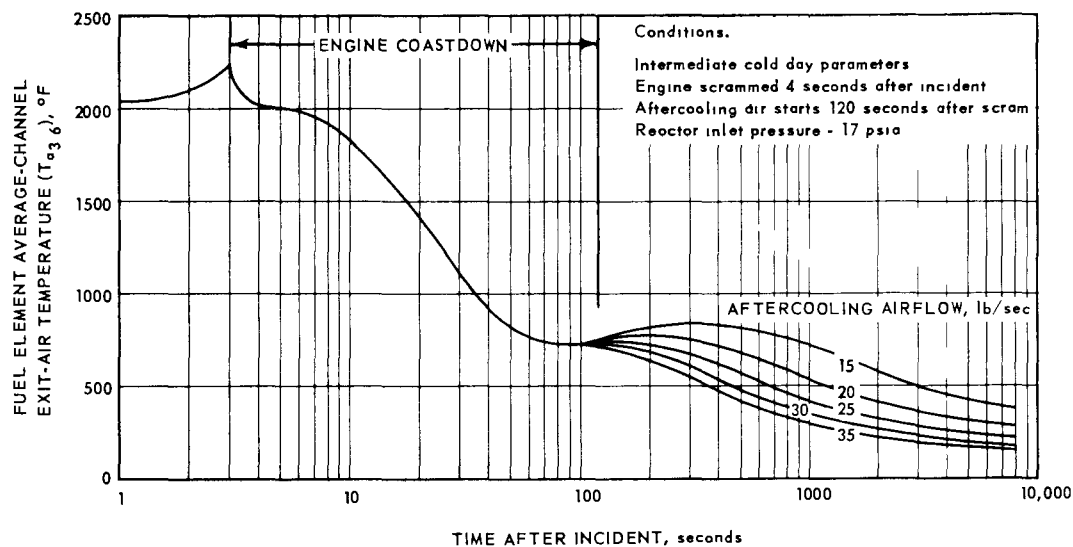


Fig. 4.172—Fuel element exit-air temperature following scram caused by compressor stall

~~CONFIDENTIAL~~

As in the case for the unperturbed engine scram followed by engine coastdown, the lowest aftercooling-air flow shown, 15 pounds per second, satisfactorily protected the reactor.

4.15.4 REACTOR PRESSURE DROP

The maximum transient pressure drop across the reactor during aftercooling for a given rate of airflow occurred in that transient leading to maximum fuel element discharge-air temperature. Accordingly, the maximum pressure drop occurred during locked rotor transients. Pressure drops under this condition are shown in Table 4.46 for several aftercooling-air flows with both 17 psia and 35-psia reactor inlet-air pressure levels. Furthermore, the pressure drop decreased with decreasing fuel element discharge-air temperature, and progressively decreased as the time after the incident increased.

TABLE 4.46
PRESSURE DROP ACROSS REACTOR
DURING AFTERCOOLING^a

Reactor Inlet Air Pressure, psia	Airflow Through Turbine, lb/sec	Reactor Pressure Drop, psi
17	16.6	0.66
	22.2	1.12
	27.2	1.70
	32.2	2.41
	38.8	3.31
35	44.4	1.83
	66.5	3.97
	88.5	7.18
	110.0	12.34

^aLocked Rotor Condition

4.15.5 FUEL ELEMENT TEMPERATURE RISE WITH LOW AFTERCOOLING-AIR FLOW

Fuel element average-channel maximum surface temperatures with low aftercooling-air flows were calculated. Figure 4.173 shows the results of these calculations for the conditions of both normal engine coastdown and initial rotor seizure (no engine coastdown). Considering the severe case of no engine coastdown, an aftercooling-air flow of 5 pounds per second limited the fuel element average-maximum surface temperature to 2900°F at 450 seconds (7.5 minutes) after the incident. The normal steady-state temperature of 2300°F was restored within 2000 seconds (33.3 minutes) after the incident. With engine coastdown, an aftercooling-air flow of 5 pounds per second limited the average-maximum surface temperature to 1700°F at its peak.

Figure 4.174 shows the increase in fuel-element average-channel maximum surface temperature in the absence of aftercooling-air following shutdown from three equilibrium power levels; 50 megawatts, 100 megawatts, and 128 megawatts. The values shown were valid for periods up to one hour after shutdown. Following the initial decay of short-lived fission products, the rate of temperature rise leveled out; for example, 89°F per minute for shutdown from the sustained power level of 128 megawatts.

The rate of temperature rise decreased to 40°F per minute when considering the operating power level of 50 megawatts (corresponding to simulation of the cruise flight condition).

~~CONFIDENTIAL~~

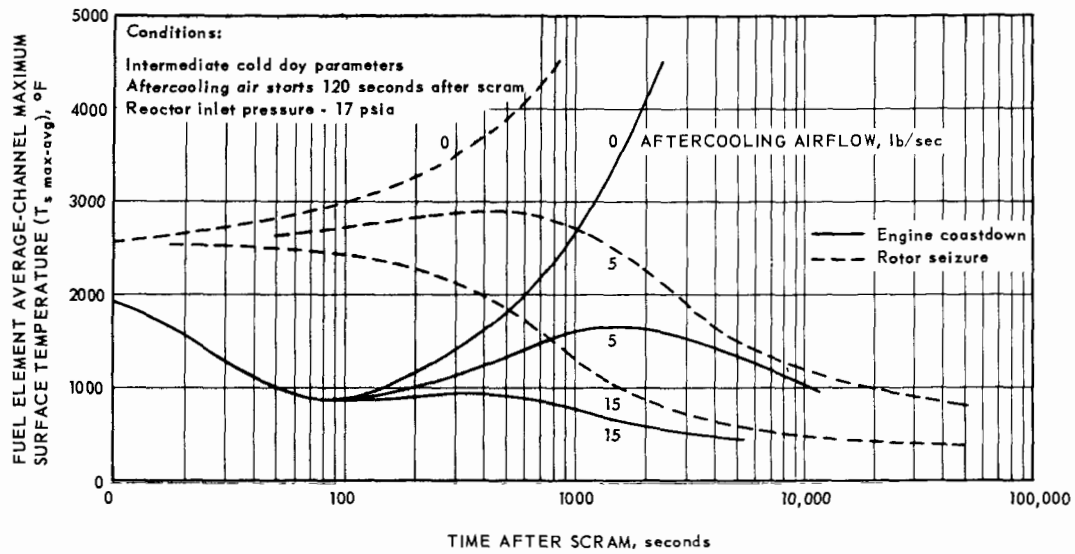


Fig. 4.173 - Fuel element average-channel maximum surface temperature following scram with low aftercooling airflow rates

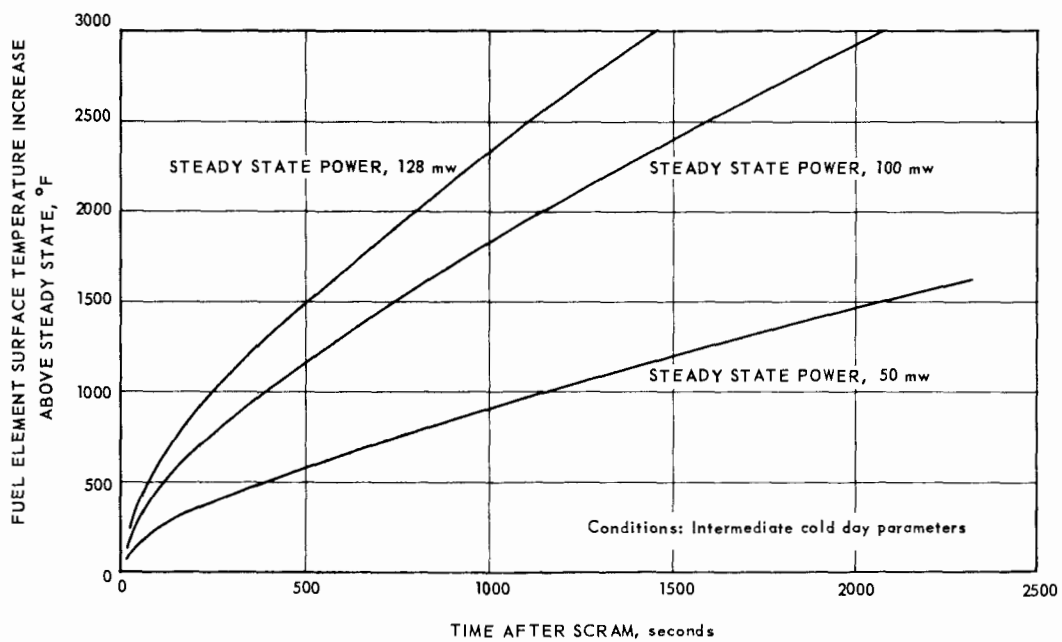


Fig. 4.174 - Increase in fuel element average-channel maximum surface temperature in absence of aftercooling air

~~CONFIDENTIAL~~

4.15.6 EFFECTS OF DELAY IN ENGINE SCRAM TIME

In the foregoing analyses of transient conditions, it was assumed that the engine was scrammed one second after the occurrence of the incident. Table 4.47 shows the rate of temperature rise in selected reactor components if scram was delayed and the reactor continued to operate at a steady-state power level of 128 megawatts in the absence of cooling-air flow.

TABLE 4.47
TEMPERATURE RISE IN REACTOR COMPONENTS IN ABSENCE
OF COOLING-AIR^a

Component	Rate Of Temperature Rise, °F/sec
Fuel Elements	
Up to 17 seconds, X/L = 0.8	75
After 17 seconds, X/L = 0.5	90
Inner reflector, near core	7.3
Outer reflector, near core	3.1

^aPower at 128 mw.

4.15.7 CONTROL ROD AFTERCOOLING CONSIDERATIONS

An analysis was made of the transient case of control rod aftercooling for the severe condition of reactor scram following rotor lock after 100 hours of operation at Idaho intermediate-cold-day conditions. The steady-state conditions before scram were defined as follows:

Turbine inlet-air temperature, 1800°F
Reactor power level, 128 megawatts
Temperature of reactor inlet-air, 590°F
Airflow to turbine, 375 pounds per second

The control rod surface temperature before scram was 1730°F. Figure 4.175 shows the power decay curves for the control rod and guide tube.

Results of the study showed that, when 25 pounds per second of air was used for cooling the reactor and secondary components, the control rod surface temperature increased for a period of 90 seconds, peaking at 1910°F. The maximum surface temperature of the rod exceeded 1800°F for 390 seconds. Figure 4.176 shows the transient temperature response of the control rod for this extreme condition. Without aftercooling air, the initial rate of temperature rise was approximately 6 degrees per second, with the rate decreasing to 4 degrees per second after 10 seconds and to 2 degrees after 100 seconds.

4.15.8 LONG DURATION REACTOR AFTERCOOLING CONSIDERATIONS

Figure 4.177 shows fractional rates of afterheat generation at extended periods of time after shutdown. A family of curves is given for various periods of operating time followed by 2 percent $\Delta k/k$ scram and shim rod insertion. The specific heat of fueled BeO, as used for calculations in this section, is given in Table 4.48. The average fuel loading in the core was 8.4 weight percent UO₂, and the average specific heat in the temperature range of 100° to 200°F was 0.24 Btu per pound per °F. The weight of fueled material in the core was 2920 pounds, which, when combined with the specific heat given above, meant that the

~~CONFIDENTIAL~~

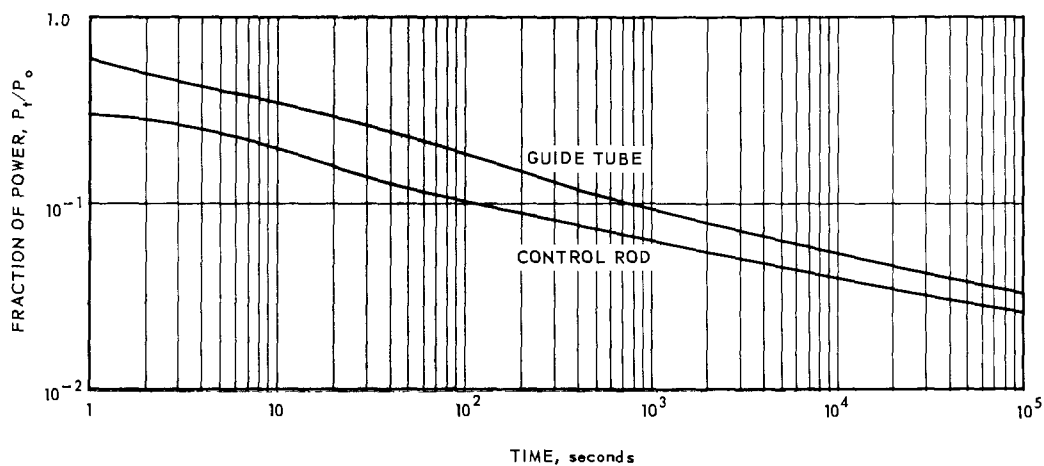


Fig. 4.175 - Power decay curves following scram after 100 hour operation

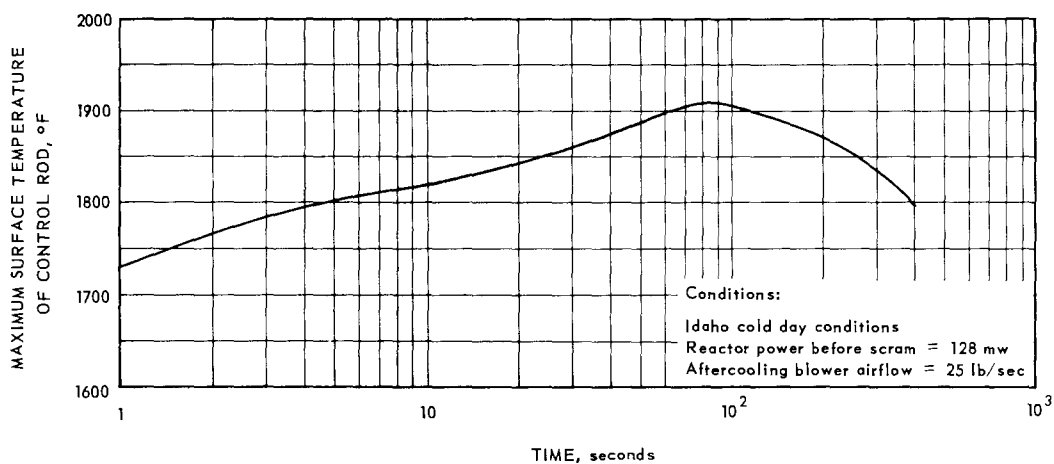


Fig. 4.176 - Control rod transient temperature response for reactor scram without engine coastdown

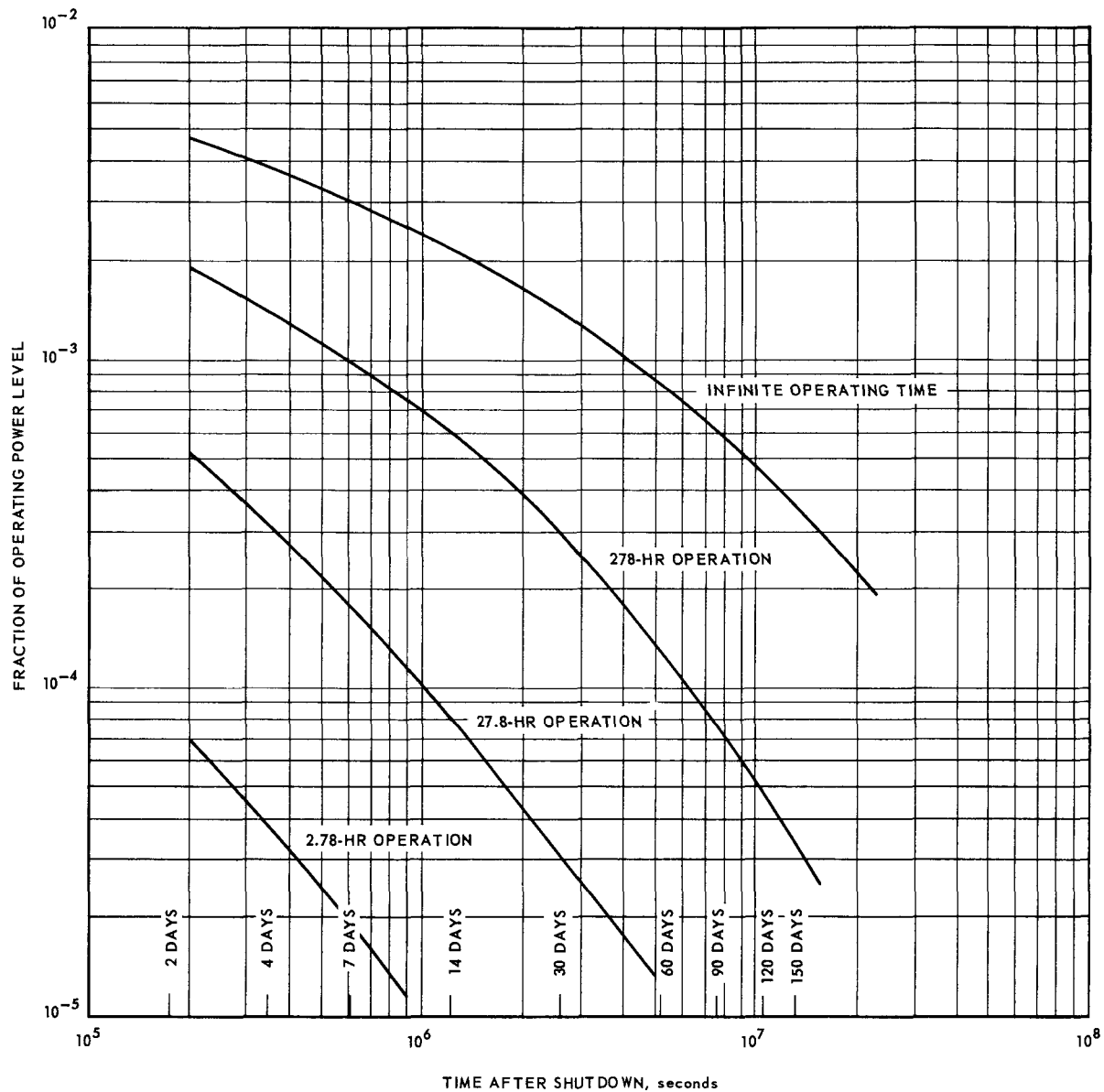
~~CONFIDENTIAL~~

Fig. 4.177 – Afterheat generation rate as a fraction of operating power level versus time after shutdown for various periods of operating time

heat capacity of the core was 700 Btu per $^{\circ}\text{F}$. Assuming that the reactor has operated at 128 megawatts for 278 hours, and that 90 percent of the afterheat was stored in the core, the rate of afterheat generation 7 days after shutdown was approximately 127 kilowatts and the temperature rise was approximately 56°F per hour. Similarly, for these same conditions, the rate of temperature rise in the core 150 days after shutdown was approximately 23°F per hour.

4.15.9 RESULTS OF AFTERCOOLING STUDIES

The transient aftercooling studies reported in this section indicated that the AHR system requirements were satisfied if 25 pounds of aftercooling-air per second was assured. This aftercooling-air requirement was established by the fuel element temperature rise in the event of engine rotor seizure or other sudden loss of cooling-air. The delay time between

~~CONFIDENTIAL~~

TABLE 4.48
SPECIFIC HEAT OF
FUEL ELEMENT MATERIAL

Temperature, °F	Specific Heat, Btu/lb-°F		
	6% UO ₂	8% UO ₂	10% UO ₂
100	0.238	0.226	0.215
200	0.262	0.250	0.237
400	0.310	0.300	0.282
800	0.390	0.373	0.356
1200	0.434	0.412	0.395

loss of cooling-air and reactor scram was critical since the fuel elements increased in temperature at the rate of 75°F per second in the absence of airflow at a power level of 128 megawatts. For a scram followed by engine coastdown, the airflow of 25 pounds per second was more than adequate for cooling the fuel elements. Other reactor components, such as the core tunnel, inner reflector, outer reflector, and pressure pads were relatively insensitive to scram delay time. However, considering the allowable temperature limits of all components, the aftercooling-air flow of 25 pounds per second was required to satisfy all transient conditions of normal engine shutdown and was adequate in the case of no engine coastdown.

4.16 PRODUCT HANDBOOK

The Reactor Handbook for 140E1²⁸ is identified in section 1.6. Material contained in this handbook is illustrated by the following Table of Contents.

<u>Section</u>	<u>Title</u>
A	Table of Contents
B	Distribution
C	Responsibility
D	Introduction
E	Reactor Product Breakdown Numbers
1-2000-0.0	Design
1-2000-1	Over-all Reactor Description & Requirements
1-2000-2	Over-all Reactor Mechanical Design
1-2000-4	Over-all Reactor Aerothermal Design Data
1-2000-5	Over-all Reactor Nuclear Design Data
1-2000-8	Over-all Reactor Drawing Planning List
1-2210-1	Fuel Element Assemblies Description & Requirements
1-2210-2	Fuel Element Assemblies Mechanical Design
1-2311-1	Side Reflector Tubes & Rods Description & Requirements
1-2311-2	Side Reflector Tubes & Rods Mechanical Design
1-2340-1	Central Island Reflector Elements Description & Req.
1-2341-1	Central Island Tubes Description & Requirements
1-2341-2	Central Island Tubes Mechanical Design
1-2342-1	Central Island Rods Description & Requirements
1-2342-2	Central Island Rods Mechanical Design
2-2000-0.0	Materials Development
2-2000-0.1	Over-all Reactor Materials

~~CONFIDENTIAL~~

<u>Section</u>	<u>Title</u>
2-2000-0.2	Reactor Ceramic Materials
2-2000-1.1	Beryllium Oxide
2-2000-1.2	Beryllium Oxide Coefficients of Static Friction Data
2-2000-2.1	Beryllium Oxide Plus Fuel
2-2000-2.2	Beryllium Oxide Plus Fuel Compressive Creep of BF116
2-2000-3.1	Aluminum Oxide
2-2000-4.1	ZrO ₂ + Y ₂ O ₃
2-2000-4.2	ZrO ₂ + Y ₂ O ₃ Modulus of Elasticity for Cladding
2-2000-5.1	Europium Oxide
2-2000-21.1	Inconel X
2-2000-22.1	Rene 41
2-2000-23.1	304 Stainless Steel + 1 W/O B ¹⁰
2-2000-24.1	Beryllium
2-2000-25.1	Nichrome V
2-2000-26.1	316 Stainless Steel
2-2000-41.1	Thermoflex
2-2000-42.1	Zirconia
3-2000-0.0	Manufacture, Assembly, Shipment
4-2000-0.0	Component Testing
4-2000-0.1	Over-all Reactor Testing
4-2000-1.1	Three-Tier Mockup Testing
4-2000-2.1	Three-Tier Mockup Hazards Testing
4-2000-3.1	Three-Tier Mockup Hyge Deformation Test
4-2000-4.1	Three-Tier Mockup Vibration Tests
4-2000-5.1	Three-Tier Mockup Assembly Procedures
4-2000-6.1	Three-Tier Mockup Longitudinal Structure
4-2000-21.1	Two-Tier Mockup Testing
4-2000-22.1	Two-Tier Mockup Hazards Test
4-2000-23.1	Two-Tier Mockup Core Integrity Test
4-2000-24.1	Two-Tier Mockup Simulated Reflector
4-2000-31.1	Single Cell Testing
4-2000-32.1	Clad Cell Testing
4-2110-1.1	Reactor Radial Structure Testing
4-2112-1.1	Radial Springs Relaxation Test
4-2112-2.1	Radial Springs Heat Transfer Test
4-2112-3.1	Radial Springs Photo-Stress Process
4-2112-4.1	Radial Springs Loading Tests
4-2112-5.1	Radial Springs Fatigue Life Test
4-2112-6.1	Cold Flow Radial Support System Test
4-2120-1.1	Aft Retainer Assembly Testing
4-2121-1.1	Aft Retainer Deflection
4-2121-2.1	Tube Plate Stress
4-2121-3.1	Brazed Tube to Plate
4-2121-4.1	Air Flow Tests
4-2125-1.1	Linkage Assembly Friction Test
4-2130-0.1	Forward Reflector Assembly Testing
4-2133-1.1	Spring Assembly - Forward Reflector
4-2140-1.1	Inner Island Structure Testing
4-2141-1.1	Liner Spring Rate Test
4-2143-1.1	Shaft Tunnel Testing - Natural Frequency Test

~~CONFIDENTIAL~~

<u>Section</u>	<u>Title</u>
4-2200-0.1	Reactor Core Element Testing
4-2210-0.1	Fuel Element Testing
4-2210-1.1	MTR-HT-1 Testing
4-2210-26.0	ETR 99 Testing
4-2210-26.1	ETR 99CR19
4-2210-27.1	ETR 99CR20
4-2210-28.1	ETR 99CR35
4-2210-29.1	ETR 99CR33
4-2210-51.1	Non-Nuclear Environmental Testing
4-2300-0.1	Reactor Reflector Elements Testing
4-2311-1.1	Side Reflector Tubes
4-2312-1.1	Thermal Tests
4-2312-2.1	Side Radial Arches Proof Tests
4-2312-3.1	Side Radial Arches Size Factor Tests
4-2321-1.1	Transition Pieces Thermal Test
4-2400-0.1	Reactor Control Rod Elements Testing
4-2400-1.1	Control Rod Element Dynamic Nuclear Test #1
4-2400-2.1	Control Rod Element Dynamic Nuclear Test #2
4-2400-3.1	Control Rod Element Mechanical Friction Test
4-2410-0.1	Poison Rod Assembly Testing
4-2410-1.1	Poison Rod Assembly Cold Flow Test
4-2410-2.1	Poison Rod Assembly Static Nuclear Test #1
4-2410-3.1	Poison Rod Assembly Static Nuclear Test #2
4-2410-4.1	Poison Rod Assembly Static Nuclear Test #3
5-2000-0.0	Operations
6-2000-0.0	Schedules

~~CONFIDENTIAL~~

4.17 REFERENCES

1. Lapides, M. E., "Summary of Aerothermal Nuclear Analysis for the Advanced Configuration Study," GE-ANPD, DC 60-3-201, 1960.
2. Moon, C. W., "Fuel Element Bypass Flow," GE-ANPD, DCL 61-3-95, 1961.
3. Trussell, J. I., "Minutes of Meeting - Mr. D. Shaw's Office October 19, 1960," GE-ANPD, DCL 60-11-68, 1960.
4. Flitner, D. P., "Reactor Performance Estimates for Zero Stage Compressor Utilization," GE-ANPD, DCL 60-12-42, 1960.
5. Flitner, D. P., "140E2 Power Plant Configuration Study - Reactor Sizing," GE-ANPD, DCL 61-2-128, 1961.
6. Orr, W. L. and White, E. R., "D140E1 Fuel Element Nuclear Design," GE-ANPD, DC 61-6-41, 1961.
7. "Project 101 Quarterly Task Report, April through June, 1960," GE-ANPD, DC 60-6-1, 1960.
8. Deissler, R. G., and Eian, C. S., "Analytical and Experimental Investigation of Fully Developed Turbulent Flow of Air in a Smooth Tube with Heat Transfer with Variable Fluid Properties," NACA-TN-2629, 1952.
9. Lapides, M. E., and Goldstein, M. B., "Heat Transfer Source File Data," GE-ANPD, APEX 425, 1957.
10. Taylor, M. F., and Kirchgessner, T. A., "Measurements of Heat Transfer and Friction Coefficients for Helium Flowing in a Tube at Surface Temperatures up to 5900°R," NACA-TN-D-133, 1959.
11. Hobbs, J. L., and Lapides, M. E., "Physical Properties and Flow Characteristics of Air," GE-ANPD, APEX 527, 1956.
12. Cole, J. M., "A Review of the Structure for the Proposed Core for the D141-A1 Test," GE-ANPD, DC 59-10-65, 1959.
13. Turney, G. E., "Experimental Determination of Pressure Loss Characteristics for Various Types of Ceramic Tubes," GE-ANPD, DC 60-4-173, 1960.
14. Jay, D. J., and Morgan, W. R., "Minutes of Subcommittee Meeting for Preparation of Fuel Element Specifications," GE-ANPD, DC 52-27-90 (DC 52-24), 1952.
15. McAdams, W. H., "Heat Transmission," Third Edition, McGraw-Hill Book Co., New York, 1954, p. 157.
16. Layman, D. C., "Temperature Relaxation in Ceramic Fuel Elements," GE-ANPD, DC 61-11-4, 1961.
17. "Engineering Progress Report No. 37," GE-ANPD, APEX-37, September, 1960.
18. Delaney, J. A., Dyer, P. A., and Skirvin, S. C., "Off Design and Modified Off Design Programs," GE-ANPD, DC 60-7-12, 1960.
19. Flitner, D. P., and Smith, A. D., "ETR 99CR19 Pretest Evaluation," GE-ANPD, XDC 60-8-112, 1960.
20. Orr, W. L., and White, E. R., "D140E1 Fuel Element Nuclear Design," GE-ANPD, DC 61-6-41, 1961.
21. Roark, R. J., "Formulas for Stress and Strain," Third Edition, McGraw-Hill Book Co., New York, 1954.
22. Williams, R. P. and Gjertsen, R. K., "Stresses in a Hexagonal Ring and Chipped Corner Hexagonal Ring Due to a Two Sided External Pressure Loading," GE-ANPD, DC 60-11-153, 1960.
23. Redmond, R. F., Pollack, H., Klickman, A. E., Hogan, W. S., Epstein, H. M., and Chastain, J. W., "Numerical Solution of Fuel Element Thermal Stress Problems," B. M. I. -1422, February 26, 1960.
24. Melan, E., and Parkus, H., "Warmespannungen," Springer, Vienna, 1953.
25. Carslaw, H. S., and Jaeger, J. C., "Conduction of Heat in Solids," Second Edition, Clarendon Press, Oxford, 1959.

~~CONFIDENTIAL~~

26. Boley, B. A., and Weiner, J. H., "Theory of Thermal Stresses," John Wiley and Sons, Inc., New York, 1960.
27. Timoshenko, S., and Goodier, J. N., "Theory of Elasticity," Second Edition, McGraw-Hill Book Co., New York, 1951.
28. Minnich, S. H., "Reactor Design Data Handbook for 140E," GE-ANPD, DC 60-9-21, 1960.
29. Lacey, P. G., "Secondary Heating and Flux Bulletin 140E-1," GE-ANPD, DC-60-10-108, 1960.
30. Layman, D. C., "Temperature Distributions in the XNJ140E-1 Inner Reflector," GE-NMPO, DC 61-12-2, 1961.
31. Dunholter, R. J., and Riley, D. R., "Solution of Flugge's Cylinder Equations for a Non-Axisymmetric Load," GE-ANPD, XDC 59-12-164, 1959.
32. Layman, D. C., "Aerothermal Design Results of Core Liner, Shaft Tunnel, and Inner Reflector," GE-ANPD, DC 61-12-11, 1961.
33. Horvay, G., "The Plane Stress Problem of Perforated Plates," Journal of Applied Mechanics, September, 1952.
34. Ross, A. L., "Thermal Stress Analysis of Finite Sections," GE-ANPD, APEX-480, January 20, 1959.
35. Layman, D. C., "Development Tests Supporting the Design of the XNJ140E-1 Aft Retainer Assembly," GE-ANPD, DC 61-12-12, 1961.
36. Mobley, P. R., "Development of a High Strength Brazing Alloy for the Aft Retainer," GE-ANPD, DC 61-3-34, 1961.
37. Myers, R. T., "Stress Analysis Aft Hub Retainer," Allstate Design and Development Co., AS-4049-R3, February 27, 1961.
38. Anderson, J. T., et al, "User's Manual for IBM 704 Transient Heat Transfer Program," GE-Flight Propulsion Division, DF58AGT674, 1958.
39. Eckard, S. E., "D140 Aft Retainer Experimental Heat Transfer Evaluation," GE-ANPD, DC 61-4-27, 1961.
40. Lapides, M. E., "Preliminary Design Notes," GE-ANPD, DC 61-4-37, 1961, p. 148.
41. Stephans, G. L., et al, "Program THTB for Analysis of General Transient Heat Transfer System," GE-Flight Propulsion Division, R60FPD647, 1960.
42. Woike, O. G., "140E-1 Radial Support System," GE-ANPD, APEX-733.
43. Layman, D. C., "Aerothermal Design of the XNJ140E-1 Radial Support System," GE-ANPD, DC 61-12-13, 1961.
44. Layman, D. C., "Fabrication and Development Tests of the XNJ140E-1 Control Rods," GE-ANPD, DC 61-12-14, 1961.
45. Cliffe, R. T., et al, "Pressure Losses Within Ducting Systems and Components for Incompressible Flow," GE-ANPD, DC 59-1-156, January 5, 1959.
46. Turney, G. E., "Experimental Evaluation of Pressure Losses in D140E-1 Control Rod Cooling Passage," GE-ANPD, DC 60-12-52, 1960.
47. Dilley, R., and Reynolds, M. B., "Analysis for Control Rod Cooling Program" GE-ANPD, DC 59-12-161, 1959.
48. Anderson, J. T., et al, "User's Manual for Flow and Temperature Analysis Program," GE-Flight Propulsion Division, R59FPD837, 1959.
49. Cole, J. M., "Review of the Structure for the Proposed Core for the D-141-A1 Test," GE-ANPD, DC 59-10-65, 1959.